Seismic Body Wave Attenuation in the Upper Mantle beneath the Australian Continent

by

Hai-Xu Cheng

A thesis submitted for the degree of Doctor of Philosophy

of

The Australian National University

October 2000

Author's Declaration

Except as noted throughout the text and in the acknowledgments, the research described in this thesis is solely that of the author.

Hai-Xu Cheng

The Australian National University

October 2000

Author's Declaration

Except as noted throughout the text and in the acknowledgments, the research described in this thesis is solely that of the author.

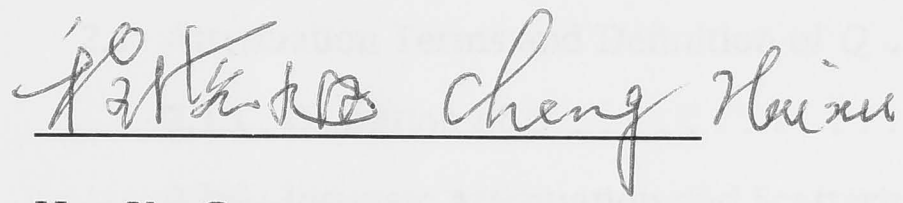

HAI-XU CHENG

The Australian National University

October 2000

Contents

Acknowledgments

Heartfelt thanks go to my wife, Huai Qing, for her unwavering support. I wish to thank my parents who understood and tolerated me going overseas to undertake my PhD research. I wish also thank my brother and my sisters for looking after my parents when I was on leave. The successful conclusion of this research is founded on the selfless and generous concordance of my family. Thank you!

Prof. Brian Kennett, my supervisor, has been a thorough and thoughtful guide throughout my candidature. Most of the strands of the ATTENUATION project have grown from Brian's seminal ideas. His keen insight and appreciation of the broad issues have helped bind this wide-ranging project into a cohesive unit. I have appreciated Brian's generosity with his time and energy, and I have benefited enormously from the depth and breadth of his understanding. Brian, my sincere gratitude.

Dr. Olafur Gudmundsson, my advisor, has been an active collaborator in the differential attenuation measurement. The initial differential attenuation measurement method based on the spectral theory which was first used by Teng [1968], which forms the basis for the construction of attenuation model developed in this project, was provided by Olafur. Olafur has given generously of his time and suggestions during my work on differential attenuation measurement. He also allowed me to use and modify his plotting library in C. Olafur also assisted in reading and correcting my mid-term report. This was a time-consuming task which Olafur undertook willingly. Additionally, Olafur has been a regular sounding board for new ideas and developments in many aspects of this project.

Dr. Malcolm Sambridge, my advisor, provided the inversion programme with NA algorithm used in Chapter 7 and 9 for constructing the Q models, and gave ready assistance in response to questions relating to its implementation. Malcolm introduced me to statistical analysis of my differential attenuation observation results which is the start point of inverting Q from δt^*_{sp} . Malcolm also assisted me in computing problems and introduced me to use the plotting programme *xvgr*.

Dr. Ian Jackson, my advisor, introduced me their laboratory observation of seismic wave attenuation and provided the references of the laboratory measurement of attenuation and gave many discussions on how to interpret my results.

I am pleased to acknowledge the contribution to this research of members of my advisory panel, Prof. Kurt Lambeck, Prof. Brian Kennett, Dr. Olafur Gudmundsson, Dr. Ian Jackson, Dr.

Malcolm Sambridge, and Dr. Jean Braun, particularly at the time of my mid-term appraisal.

To colleagues in the Seismology and Geomagnetism Group, led by Prof. Brian Kennett, I am grateful for regular assistance with computing, technical and scientific issues.

Prof. Alan Douglas and Dr. David Bowers, University of Reading, UK, provided me the references on seismic wave attenuation by their research, and gave many useful discussions in the IUGG meeting in UK in 1999.

Dr Adrian Hitchman answered many initial queries about LaTeX, *xvgr* and *GMT*.

Dr Yuka Kaiho answered many enquiries regarding the velocity models used in this thesis. Yuka also assisted me producing the figures 6.1, 6.9 and 6.10.

Dr Eric Debayle provided the data of surface velocity models to produce the figure 3.2. Kazunori Yoshizawa also helped me in producing this figure.

Dr Geoff Clitheroe provided the topographic data to produce the figure 1.1(b).

Dr Stephen Billings answered many initial questions on using *Matlab*.

The production of figures in this thesis has been accomplished using Prof. Brian Kennett's plotting package *ps_rpost* in *f77*, Olafur Gudmundsson and author's plotting package in *c*, the *xvgr* package, the *Matlab* package and the Generic Mapping Tools (GMT) package [Wessel and Smith, 1991, 1995].

My experience has been enriched by attendance at a number of conferences and workshops. I am grateful to the Research School of Earth Sciences at the ANU, and the International Association of Seismology and Physics of the Earth's Interior (IASPEI), for financial assistance which made such attendance possible.

The opportunity to have been a research student in the fertile environment of RSES is appreciated. I gratefully acknowledge the receipt of an OPRS scholarship and the ANU PhD scholarship, which made it financially possible.

HAI-XU CHENG

The Australian National University

October 2000

Abstract

Because the Earth is not perfectly elastic, propagating seismic waves attenuate with time due to various energy-loss mechanisms, such as movement along mineral dislocations or shear heating at grain boundaries. The attenuation can be characterised by a quality factor Q which generally has a weak frequency dependence below 1 Hz. This thesis constructs a 3-D structure of body wave attenuation and its frequency dependence in the upper mantle beneath the Australian continent.

In the epicentral distance range of up to 45°, the body wave field is very complex due to the velocity discontinuities in the upper mantle. As a first step, in order to understand the wave field in this distance range, I have simulated the travel time and differential attenuation δt^*_{sp} and particularly paid attention to the effects from the velocity discontinuities, low and high velocity zones.

The dense set of observations of body waves turning in the upper mantle which has previously been exploited in studying the velocity distribution provides a good coverage for studying attenuation, particularly under northern Australia. A significant challenge in attenuation studies is the separation of anelastic effects from both propagation and source effects. The spectral ratio between the P and S wave arrival provides a means of cancelling the frequency dependent factors common to the two wave types. Based on the successful forward modelling of δt^*_{sp}, I developed the δt^*_{sp} measurement method based on the spectral ratio between P and S waves. I picked the P and S wave arrival which is required by estimating spectra by using a coding scheme. The P and S arrival windows and P and S wave spectra windows were selected by looking at around 2000 three components seismograms to achieve robust estimation of δt^*_{sp}.

Over a narrow band in frequency, Q can be treated as nearly frequency independent and then the slope of the logarithm of the spectral ratio is directly related to the difference in attenuation between P and S in the passage from source to receiver. This spectral ratio approach was systematically applied to the estimation of the differential attenuation between P and S (δt^*_{sp}) from the broadband data recorded at portable stations of SKIPPY project in Australia. The estimation of δt^*_{sp} from the SKIPPY data provides measurements along nearly 2000 refracted raypaths, mostly sampling the northern part of the continent for fixed frequencies centred around 1 Hz. The measurements clearly delineate major variations in attenuation between the cratonic structures in the centre and west and the eastern part of Australia, with

much stronger attenuation in the east.

The differential attenuation correlates well with the velocity structure. Weak attenuation of S waves was found in central and western Australia where the S velocity is high. But strong attenuation of S waves was found in eastern Australia and the Coral Sea where the S wave velocity is low.

The broad-band seismic observations also allow the examination of a wider frequency range (up to 6.0 Hz) to look for frequency dependence of attenuation. With the assumption of a simple power law dependence of frequency, the spectral ratio information can again be used and a frequency dependence parameter can be extracted from the rate of change of the logarithmic slope of the spectral ratio with frequency. The frequency dependence parameter estimated directly from the spectral ratio represents the average dependence of frequency attenuation along the whole path. Thus I call it γ to distinguish it from the α which I obtained from frequency dependent δt^*_{sp} by nonlinear inversion. γ was estimated from the SKIPPY data set for a broad frequency band up to 6 Hz. There turns out to be a strong correlation between γ and δt^*_{sp}.

There is significant geographic variation in γ. The raypaths covering the north-west part of the Australian continent show γ close to zero with a small error in γ; so that the frequency dependence of Q in this area is relatively weak. In the eastern part of Australia and Coral Sea area, there is a mixture of paths with small and larger γ so that the frequency dependence in those areas is more complex and depends on the depth of penetration of the waves.

The wide range of differential attenuation measurements from the SKIPPY data set can be exploited to invert for attenuation structure, by making use of the velocity information extracted from stacked body wave arrivals. The differential attenuation data have been organised into azimuthal corridors and have been inverted to produce a set of 1-D Q profiles. Then a 3-D Q model at fixed frequency was constructed by combining these 1-D Q profiles weighted by ray density. The inversion has been accomplished by using the neighbourhood algorithm (NA) approach for parameter space exploration, which allows an assessment of the properties of a group of models with good fit to the data as well as just the best fitting model. From the inversion, a set of 1-D Q profiles at fixed frequency around 1 Hz was obtained from the robust estimation of δt^*_{sp} at lower frequency band.

I have performed forward modelling on the effect of frequency on the δt^*_{sp}. I discovered the curvature of the δt^*_{sp} as a function of frequency is controlled by α. When α is 0, the relation between δt^*_{sp} and frequency is a linear straight line with no frequency dependence of attenuation. As α increases, the curvature of δt^*_{sp} as a function of frequency increases, and the frequency dependence of attenuation is stronger. I have also investigated the effect of dispersion on δt^*_{sp}. I concluded that the dispersion is not an important influence on δt^*_{sp}, because the velocity is affected by less than 0.5%.

Based on successful forward modelling on frequency dependent δt^*_{sp}, I have estimated a set of frequency dependent δt^*_{sp} in a broad frequency band up to 6 Hz. I divided the broad frequency band into six sub-frequency bands by using a Golden section. Then I have estimated

the δt^*_{sp} in each sub-frequency band. Hence, I obtained a surface of δt^*_{sp} as a function of frequency and distance. This surface was used to construct a set of 1-D Q_0 and α profiles for each azimuthal slice and corridor across the Australian continent. This set of 1-D Q_0 and α profiles also allows me to synthesise a 3-D frequency dependent attenuation model of Q and α as a representation of the attenuation structure beneath the Australian region by combining the various 1-D profiles. My estimation of 3-D Q and α suggests there is strong spatial variation in seismic body wave attenuation in the upper mantle. My investigation of 3-D Q and α have also suggested a spatial correlation among Q, α and velocity.

Part I

Introduction

Chapter 1

Introduction

1.1 The SKIPPY and KIMBA Projects

The SKIPPY project consists of 73 temporary broadband three-component seismic stations evenly distributed across the Australian continent to supplement the sparse network of permanent broadband stations (Figure 1.1(b)). Arrays of up to 12 stations have been deployed, covering the continent in 6 major deployments (stations SA-SF, Figure 1.1(b)). The first array was deployed in northeastern Australia in May 1993. The last array, in far north Western Australia was completed in September 1996. The KIMBA project consists of a deployment of 10 closely spaced broadband stations in the Kimberley block deployed from July to October 1997 (Figure 1.1(b)).

Recorders used in SKIPPY and KIMBA projects are Refraction Technology units with 24-bit Analogue-to-Digital Conversion (ADC) and an internal Global Positioning System (GPS) corrected clock. Data are continuously recorded using a Digital Audio Tape (DAT) drive. The DAT drive was replaced by external disc drives for KIMBA and latter projects. The sensors in the field are three-component broadband Güralp CMG-3ESP seismometers that are flat in velocity response from 30 mHz to 30 Hz. Four seismometers are flat to 0.016 Hz (62.5 s period) (type 1) while the remaining eight are flat to 0.033 Hz (30 s period) (type 2). Data is digitised at 25 samples per second and with the flat velocity response of the sensors and 24-bit ADC ensures very high data quality. During the fifth and sixth deployments of the SKIPPY project (stations SE and SF, Figure 1.1(b)) internal memory errors in the recorders have led to intermittent data loss. This has affected the analysis of surface waves for Western Australia and has also adversely affected the studies discussed here. Because of the poor data quality recorded at stations SE and SF, I have lost many paths in those area. However, I still have good path coverage in this area from data recorded at Warramunga and KIMBA stations.

Data are extracted for selected earthquakes (based on simple magnitude-distance criteria) from the Preliminary Determinations of Epicenters (PDE) catalogue, published by NEIC. Over

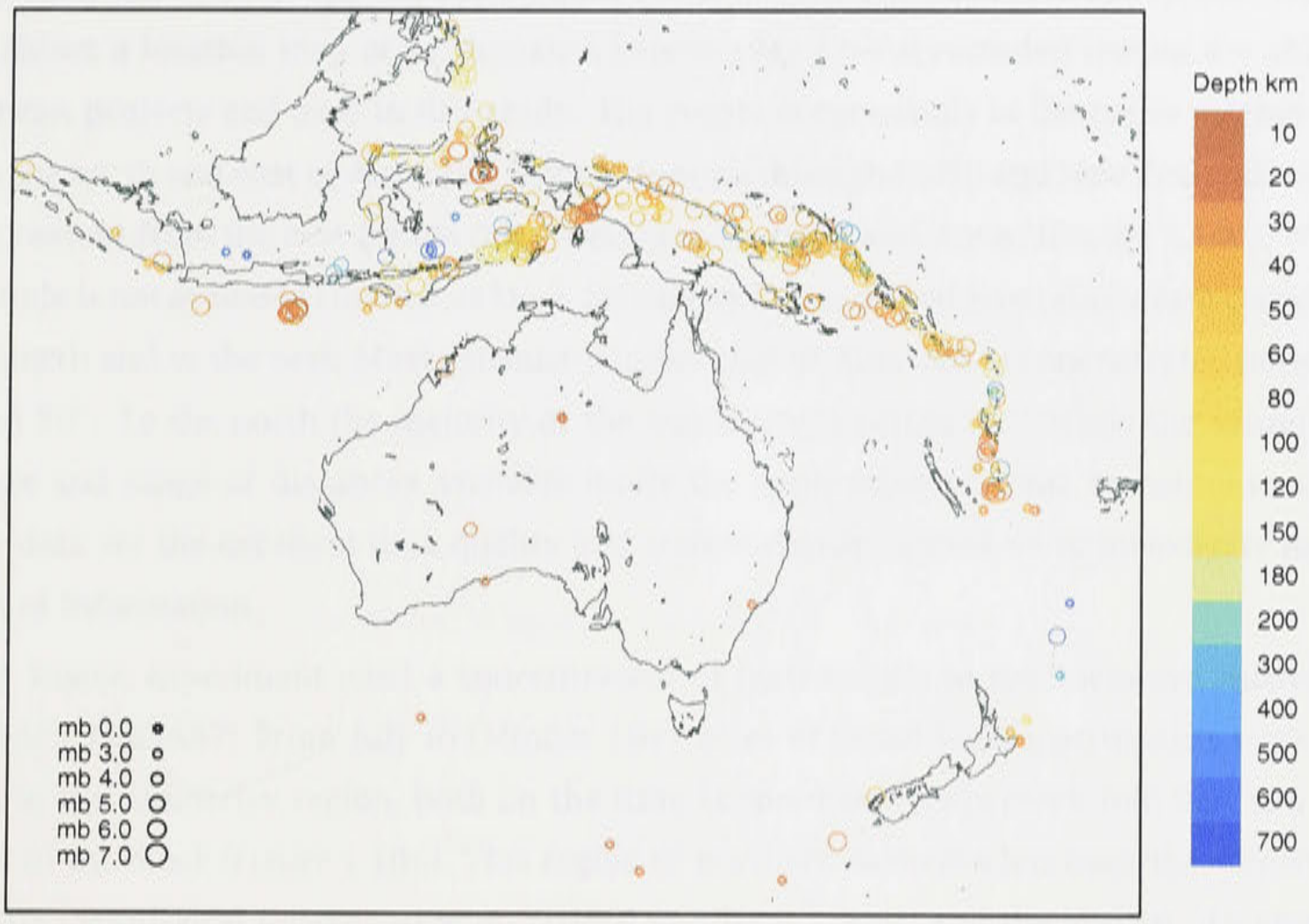

(a) SKIPPY Events

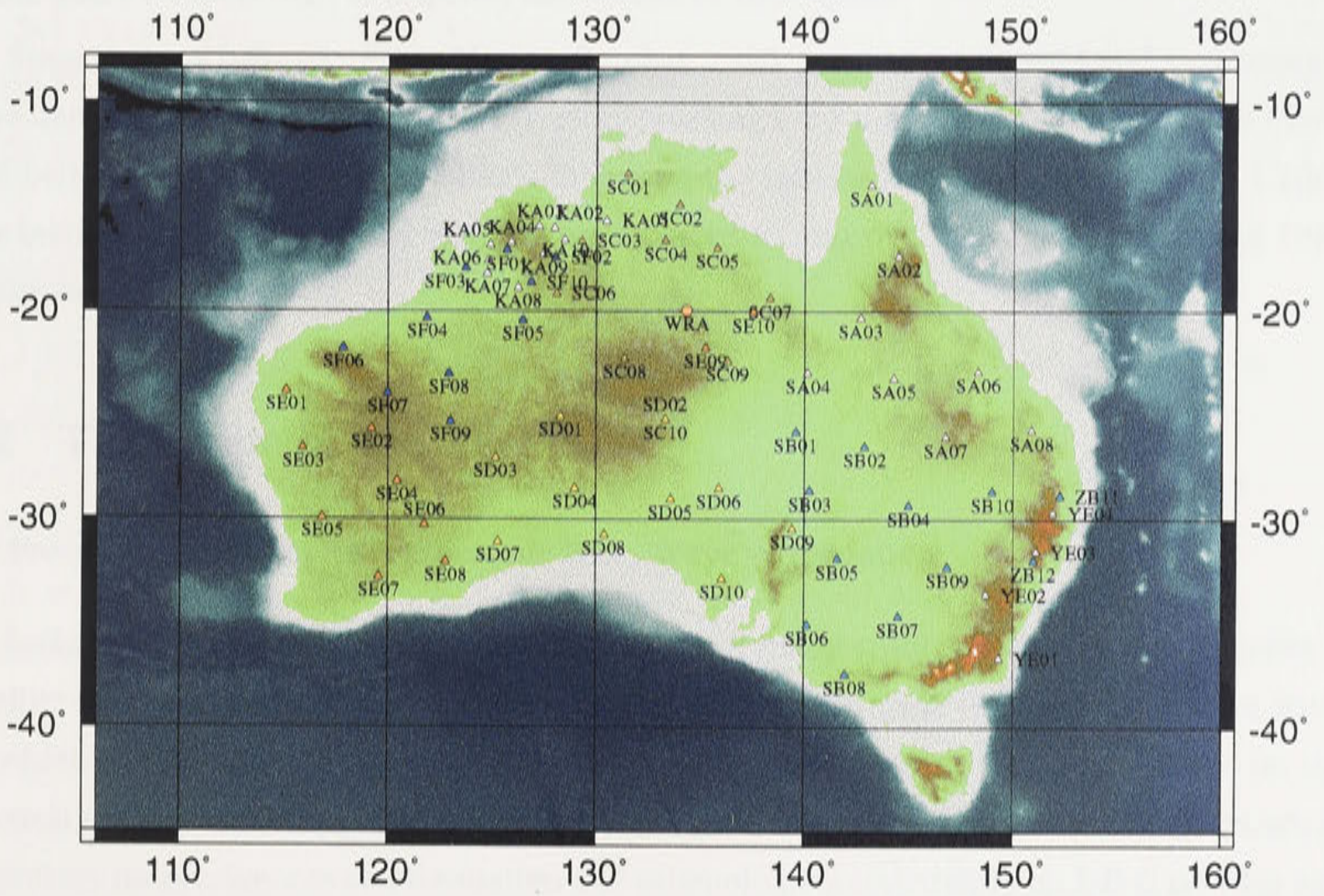

(b) SKIPPY Stations

Figure 1.1: (a) Events in the range of M_b 4.0-7.0 recorded at stations of the SKIPPY and KIMBA projects. When magnitude is not available, I mark it as M_b 0. (b) Portable and permanent stations used in this study. The six deployments (SA-SF) of the SKIPPY project are shown as coloured triangles. The stations of the KIMBA project are shown as white triangles. One permanent station (WRA array) is shown as red circle.

2500 events have been archived for stations from the SKIPPY and KIMBA projects. Figure 1.1(a) shows a location map of earthquakes between M_b 4.0-7.0 recorded during the SKIPPY and KIMBA projects and used in this study. The events occur mainly in the major earthquake belt to the north and east of Australia, from Indonesia through to Fiji and New Zealand and to a lesser extent from the east-Indian ridge, between Australia and Antarctica (fig 1.1(a)). When magnitude is not available I mark it as M_b 0. Seismicity falls into two general azimuth corridors to the north and to the east. Most seismicity to the east of Australia is concentrated between 30° and 50°. To the north the majority of the seismicity is within 70°. While the azimuthal coverage and range of distances available limits the application of some techniques to the SKIPPY data set the excellent data quality and station density allows us to investigate many classes of information.

The KIMBA experiment used a concentration of instruments in northwestern Australia. Stage one - KIMBA97: From July to October 1997 a set of broad-band instruments were deployed in the Kimberley region, both on the King Leopold and Halls creek fold belt and the interior of the block (Figure 1.1(b)). This region of northern Australia has been the subject of very little geophysical investigation on crustal and large scales, and the station placements were designed to build on the information obtained from the stations in the SK3 and SK6 legs of the SKIPPY experiment to improve knowledge of the region.

Stage two - KIMBA98: From May to October 1998 a set of 14 broad-band instruments were deployed through the Kimberley region, crossing both the King Leopold and Halls Creek fold belts and the interior of the block including the remote northern region (Figure 1.1(b)). The instruments deployed in 1998 (KB) were placed to improve the coverage from the 1997 deployment (KA).

1.2 The Scope of the Thesis

Review of Previous Studies on Seismic Body Wave Attenuation

Seismic wave attenuation has been the subject of many studies in the last few decades. I briefly review the progress in the determination of Q structure in the Earth both from studies of laboratory and seismological constraints on seismic wave attenuation. I focus on the physical mechanism of seismic wave attenuation, the frequency dependence of attenuation, laboratory measurements on attenuation and seismological constraints on 1-D Q profiles and 3-D Q structures in the upper mantle on global and local scales.

Numerical Simulation of Seismic Wavefield, Travel Time and t^*

The upper mantle has a relatively complex structure. Beneath the continental areas the lithosphere commonly extends to 100 km depth and reaches 200 km in some cratonic areas

[Kennett, 1998]. There is usually a low velocity zone beneath the lithosphere and a rapid increase in velocity with depth below 250 km. Due to phase transition in the silicate minerals of the mantle, there are noticeable jumps in seismic wavespeed near 410 and 660 km depth. Those velocity discontinuities lead to triplications in the travel time curves for P and S and produce complex seismic phases in the epicentral distance range from 15-28°.

In order to provide a background to understand and interpret the differential attenuation measurement from SKIPPY data, I need to understand the seismic wave field in regional scale up to 50°. For this purpose, I have simulated the raypath distribution, travel time curve, slowness variation and t^*.

Theory and δt^* Measurement Techniques

I have developed a method to estimate the differential attenuation δt^*_{sp} based on the spectral ratio between P and S. I have investigated the effects of dispersion and frequency dependence of attenuation. The wavespeed and Q both depend on frequency, but the effect of dispersion is very small. Stable estimates of Q can be found for frequency less than 1 Hz. For the broad frequency band up to 6 Hz, Q is a function of frequency, latitude, longitude and depth. In other words, Q is a 4-D parameter. The frequency parameter of Q is also dependent on depth and position. I develop the techniques which allow us to estimate the δt^*_{sp} in a series of sub-frequency bands within a broad frequency band. Thus I am able to construct a 3-D frequency dependent Q model in chapter 9.

Measurement of the Path Average Properties of Attenuation

Although Q is a 4-D parameter of frequency and space, it is very difficult to model it in 4-D for a number of reasons. From Warramunga data I found that the differential attenuation between P and S show relatively constant low values at shorter epicentral distance, a steep increase for medium distances, and a gradual decrease at relatively large distance. The differential attenuation variation with distance reveals the attenuation variation with depth. From the work of Gudmundsson et al. [1994] and my successful experiments on Warramunga and SKIPPY data, I found that I have good constraints on the measurement of δt^*_{sp} over a narrow frequency range near 1 Hz. The frequency dependence of attenuation may be significant across a wide range of frequencies nevertheless its impact will be small across a narrow band. Based on the successful experiments on Warramunga and a few SKIPPY data, the SKIPPY data set was analysed to determine the detailed attenuation structure in upper mantle under the Australian continent.

To estimate the δt^*_{sp} from the SKIPPY data set, the P and S wave arrivals needed to measure the spectra. As a first step, the P and S wave arrival times were estimated by using a coding scheme described in section 6.2.3. The P and S wave arrivals contain the information of

average value of P and S velocity along the raypath. The estimation of P and S wave arrivals reveals the lateral variation of the velocity along the whole path.

Then I systematically applied my approach of the measurement of spectral ratio in the narrow frequency band to the SKIPPY data set. From the spectral ratios of P and S wave, a set of measurement of differential attenuation δt^*_{sp} from nearly 2,000 raypaths was obtained which covers the upper part of the mantle beneath the Australian continent. The measurements clearly delineate major variations in attenuation between the cratonic structures in the central and western and the eastern part of Australia. To visually display the lateral variation of attenuation, the raypaths were plotted with colour scaled by δt^*_{sp}. As a result, clear geographical variation in attenuation across the Australian continent was revealed. This result was presented by the author at the 1999 IUGG meeting at Birmingham, UK.

In a broad frequency band, the attenuation is dependent on the frequency. The path average parameter of attenuation dependence on the frequency γ was estimated from the spectral ratio. It is different from the 3-D attenuation frequency dependence parameter α which could be inverted from the frequency dependent δt^*_{sp} in chapter 9. The estimation of γ is also shown clear lateral variation.

Comparing the variations in velocity structure, δt^*_{sp} and γ across the continent, it was found that they are correlated with each other quite well. In the area of high velocity, the attenuation is weak and the attenuation dependence on frequency is also weak. Meanwhile, the strong attenuation corresponds to the low velocity zone. Weak attenuation of S waves was found in central and western Australia where the S velocity is high. But strong attenuation of S waves was found in eastern Australia and Coral Sea area with low S wave velocity.

The correlation between attenuation, attenuation dependence on frequency and velocity provides a good background for inverting a 3D attenuation model in the upper mantle.

3-D Attenuation Structure in the Upper Mantle

Based on the robust measurement of differential attenuation δt^*_{sp} in the narrow frequency band below 1 Hz, I have constructed 3-D attenuation structure in the upper mantle beneath the Australian continent. First I sorted my raypaths into a set of azimuth corridors at the step of 20° from 0° to 80° clockwise and 0° to -80° anticlockwise. I have also divided every corridor into 4 slices. I have undertaken inversion for Q from the estimates of δt^*_{sp} by using a recently developed nonlinear inversion method with neighbourhood algorithm [Sambridge, 1999a,b]. Thus a set of 1-D profiles of Q at fixed frequency around 1 Hz was obtained. The 1-D Q profile with azimuth 0 derived by nonlinear grid search was presented by the author at the 1999 IUGG meeting at Birmingham, UK.

I have derived a pseudo 3-D Q model by combining the set of 1-D Q profiles. First, I estimated three raypath density functions by undertaking raytracing for each slice. One of the

function represents the depth dependence of raypath density. Other two functions represents the lateral variation of raypath density at certain depth. Then I undertook a grid search across the whole area within my data coverage. The grid search was undertaken layer by layer. Because the slices from different azimuth corridors are overlapped, I obtained a Q value for each point by averaging the Q^{-1} values from the slices which cover the point weighted by three sets of raypath density functions of each slice which represents the raypath density vary with vertival and lateral variation raypath density.

Numerical Simulation and Measurement of δt^*_{sp} at Broad Frequency Band

The δt^*_{sp} estimation from the SKIPPY data set at centre frequency of 1 Hz reveals the lateral variation of attenuation. The measurement of path average frequency dependence of attenuation reveal the depth dependence of frequency dependence of attenuation. Temperature dependence of frequency dependence of attenuation has been found in laboratory studies.

For better understanding the δt^*_{sp} measurement, I calculated the δt^*_{sp} based on the formulation $\delta t^* = t^*_0 (f/f_0)^{-\alpha}$. I also simulated the δt^*_{sp} from real velocity and attenuation models based on $Q(f) = Q_0(f_0)(f/f_0)^{\alpha}$. The results suggested that the α are very small at the lithosphere, corresponding to distances less than 16°. There are dramatic changes in δt^*_{sp} from 16° to 18°. The changes in δt^*_{sp} at this distance range contributed by the big jump in velocity at 410 km discontinuity. The changes in δt^*_{sp} at this distance range suggested a significant difference between the frequency dependence of attenuation in the lithosphere and the asthenosphere.

3-D Frequency Dependent Attenuation Structure in the Upper Mantle

Because of raypath coverage and/or data limitations, all the previous studies on frequency dependence of attenuation have focused on modeling the mean value of Q dependent on frequency along a raypath. The quality and dense broadband SKIPPY data allows me to obtain a set of measurements of δt^*_{sp} as a function of distance and frequency in a broad frequency band up to 6 Hz. A set of 1-D profile of Q and α were obtained by inversion using NA from estimates of frequency dependent δt^*_{sp} with same parameterisation as I undertook the inversion for Q model at fixed frequency.

By using the same method when I derived the 3-D Q model at fixed frequency, I have constructed the pseudo 3-D α model in the upper mantle which has not been done before. Considering the error with δt^*_{sp} estimation, the Q derived from frequency dependent δt^*_{sp} is consistent with Q model derived from δt^*_{sp} estimated at fixed frequency. My estimation of 3-D Q and α reveal the spatial variation of the seismic body attenuation and its frequency dependence in the upper mantle beneath the Australian continent.

Chapter 2

Q

The attenuation structure of the upper mantle has been the subject of many studies in the last 30 years. Useful reviews on attenuation theory, observation techniques, and results have been given by Gordon and Nelson [1966], Anderson [1967], Sato [1967], Jackson and Anderson [1970], Smith [1972], Kennett [1975, 1983], Dziewonski [1979], Minster [1981], Priestley and Chavez [1985]; Chavez and Priestley [1986]; Priestley [1988], Anderson [1989], and more recently by Douglas [1992], Nakanishi [1993], Gudmundsson et al. [1994], Sharrock [1995]; Sharrock et al. [1995], Bahttacharyya et al. [1996], Roth et al. [1999], Romanowicz and Durek [2000]. The studies on seismic wave attenuation and scattering in shallow part of lithosphere, particularly in the crust has been thoroughly reviewed and summarised by Aki [1980a,b], Johnston and Töksoz [1981], Wu and Aki [1988b, 1989, 1990] and more recently by Sato and Feher [1998]. The recent progress on laboratory studies on seismic wave attenuation and attenuation mechanism was reviewed by Karato and Spetzler [1990]; Karato et al. [1995], Jackson [1991, 1993, 2000].

A special issue of *Pure and Applied Geophysics* in 1998 has included a variety of perspectives on Q. It includes papers pertaining to a dislocation model for seismic wave attenuation and creep [Karato, 1998]; the state of global Q tomography [Romanowicz, 1998]; on teleseismic body waves, both observational results [Der, 1998; Morozov et al., 1998] and methodology [Bahttacharyya, 1998; de Lorenzo, 1998]; and on subduction zones [Sato et al., 1998; Flanagan and Wiens, 1998]. The issue also includes studies that cover a broad range of scales and distances. These include papers on laboratory studies of crustal rock [Lu and Jackson, 1998]; surface waves [Cong and Mitchell, 1998b]; and L_g coda [Cong and Mitchell, 1998a; de Souza and Mitchell, 1998; Baqer and Mitchell, 1998; Mitchell and Cong, 1998a,b] over distances of 100 to 1000 or more km, on regional body waves [Sarker and Abers, 1998; Tselentis, 1998; Ugalde et al., 1998; Gupta et al., 1998], and local frequency dependent attenuation structure of P and S waves in the upper crust [Yoshimoto et al., 1998];

In this chapter, I summarise the definition of Q and review physical mechanisms and

laboratory measurements on seismic wave attenuation, the limitations and improvement of seismological attenuation observation techniques and attenuation tomography.

2.1 Attenuation Terms and Definition of Q

2.1.1 Definition of Q

Real Earth materials are not perfectly elastic. Any anelastic processes will lead to the dissipation of seismic energy as seismic waves propagate through the Earth; in other words, seismic waves attenuate or decay as they propagate. The anelastic behaviour can be included in the constitutive law for the material by introducing the assumption that the stress at a point depends on the time history of strain.

The most commonly used measures of attenuation found in the literature are the quality factor Q and its inverse Q^{-1}, which may be defined as:

$$Q^{-1}(f) = \Delta E(f)/(2\pi E_0(f)), \tag{2.1}$$

Here $\Delta E(f)$ is the energy loss in one cycle at frequency f, and E_0 is the elastic energy stored in the oscillation. If I use the amplitude instead of energy in equation (2.1), then I get

$$\frac{\Delta A}{A} = \frac{\pi}{Q} \quad \text{(per cycle)}. \tag{2.2}$$

Considering the attenuation, the amplitude has to take the form

$$\begin{aligned} A &\sim A_0 \exp(-\frac{\pi}{Q}\frac{l}{\lambda}), \\ &= A_0 \exp(-\frac{\pi f}{Q} l). \end{aligned} \tag{2.3}$$

Other parameters used to measure attenuation are the attenuation coefficient γ which is the exponential decay constant of the amplitude of a plane wave traveling in a homogeneous medium, and the logarithmic decrement δ. These quantities are related as follows [Johnston and Töksoz, 1981]:

$$Q^{-1} = \frac{\mathrm{Im}\mu}{\mathrm{Re}\mu} = \frac{\gamma V}{\pi f} = \frac{\gamma(dB/\lambda)}{8.686\pi}, \tag{2.4}$$

where:

Q = quality factor,

γ = attenuation coefficient,

$\mathrm{Re}\mu$, $\mathrm{Im}\mu$ = real and imaginary parts, respectively of complex modulus μ,

V = velocity,

f = frequency.

The attenuation coefficient may be expressed in nepers/unit length (or simply inverse length) or in dB/unit length. The relationship between the two is given by γ(dB/unit length) = 8.686γ (nepers/unit length), and as noted in equation (2.12), $\gamma(\mathrm{dB}/\lambda = 8.686\pi/Q$.

The energy dissipation δE is just associated with the imaginary parts of the elastic moduli. For purely dilational disturbances:

$$Q_\kappa^{-1}(f) = \mathrm{Im}\{\kappa_1(f)\}/\kappa_0, \tag{2.5}$$

and for purely shear effects

$$Q_\mu^{-1}(f) = \mathrm{Im}\{\mu_1(f)\}/\mu_0. \tag{2.6}$$

For the Earth it appears that loss in pure dilatation is normally much less significant than loss in shear, and then $Q_\kappa^{-1} \ll Q_\mu^{-1}$ (Kennett, 1983).

2.1.2 Intrinsic Attenuation and Scattering

Seismic attenuation is caused by either intrinsic anelasticity or scattering attenuation. The is intrinsic anelasticity characterised by attenuation quality factor, Q_{in} associated with small-scale crystal dislocations, friction, and movement of interstitial fluids. The scattering attenuation, associated with an elastic process of redistributing wave energy by reflection, refraction, and conversion at irregularities in the medium, is often characterised by an exponential attenuation quality factor, Q_{sc}. The latter process is not true anelasticity but has virtually indistinguishable effects that are not accounted for by simple Earth models. Unlike Q defined for anelastic processes, Q_{sc} is not a measure of energy loss per cycle but, rather, a measure of energy redistribution. Q_{sc} depends very strongly on frequency and is very path dependent, since it depends on the particular heterogeneity spectrum encountered by a wavefield propagating through the Earth. Q_{sc} is usually modeled with stochastic operators, or randomisation coefficients. According to Kennett [1983] and Richards and Menke [1983], the scattering contribution to attenuation may be accounted for by

$$Q_{ob}^{-1} = Q_{in}^{-1} + Q_{sc}^{-1}. \tag{2.7}$$

In order to separate the scattering effect from intrinsic attenuation, Wu and Aki [1985] developed a multiple scattering model for seismic wave propagation in random heterogeneous media. In their research, a radiative transfer theory was applied to seismic wave propagation and the energy density distribution in space for a point source was formulated in the frequency domain. It is possible to separate the scattering effect and the absorption based on the measured energy density distribution curves. By comparing the theory with data from two digital stations of 53 events distributed for depths down to 350 km, they found that the

scattering is not the dominant factor for the measured apparent attenuation of S waves in the frequency range 2-20 Hz. From estimations at high frequency ($f > 20$ Hz), they suggest the existence of a strong-scattering surface layer with small scale heterogeneities in the crust, at least for the Hindu Kush region which they studied [Wu and Aki, 1988a].

More recently, the P and S wave scattering was investigated by Tilmann et al. [1998] from mantle plumes. Sato and Feher [1998] thoroughly summarised the intrinsic attenuation mechanism and scattering for crustal propagation and discussed various mechanism for intrinsic attenuation and their frequency characteristics. They have also discussed the scattering of seismic waves caused by random heterogeneities as a mechanism to explain the excitation of incoherent S-coda waves. Taking scalar waves as an example, Sato and Feher [1998] introduce an approach for calculating the amount of scattering attenuation in agreement with conventional seismological attenuation measurements.

At frequencies with wavelengths much larger than the heterogeneities in the medium, intrinsic attenuation dominates; so that the energy loss through nonelastic processes is usually measured by intrinsic attenuation and parameterised with Q. Large values of Q imply small attenuation. In this research, I will focus on the intrinsic attenuation in the upper mantle.

2.1.3 Frequency Dependence of Intrinsic Q

Because the real Earth is not perfectly elastic, propagating seismic waves will attenuate with time due to various energy-loss mechanisms, such as movements along mineral dislocations or shear heating at grain boundaries. Those processes are generally described as internal friction and are difficult to model because the microscopic processes are complex. The attenuation of seismic waves is commonly characterised by a Q value which is observed to be largely independent of frequency in the range from 0.001 to 1.0 Hz, [see e.g. Sipkin and Jordan, 1979]. At higher frequencies, Q depends on frequency and, in general, increases with frequency.

An absorption band model is commonly used to explain both the absorption and associated dispersion of seismic waves in the mantle [Liu et al., 1976; Anderson and Given, 1982]. The behaviour of this mechanical model explains discrepancies between long- and short-period seismic observations so that the apparently weaker damping observed for higher frequency waves [e.g. Sipkin and Jordan, 1979] is likely to be a rheological property of mantle materials.

Over the frequency band 0.001-10 Hz in seismological studies, the intrinsic loss factor Q_μ^{-1} appears to be essentially constant, but in order for there to be a physically realisable loss mechanism, Q_μ^{-1} must depend on frequency outside this band (Kennett, 1983). Many observed results confirm this conclusion, such as, Q for seismic waves is observed to be largely independent of frequency in this frequency range [Sipkin and Jordan, 1979]. At higher

frequency, Q depends on frequency and, in general, increases with frequency. To explain the frequency dependence of Q I follow the discussion by Kennett [1983]. In order to express the macroscopic characteristics of the material within the Earth, a constitutive relation between the stress and strain is needed. For linear elastic media, the stress field τ_{ij} is related to the displacement u by,

$$\tau_{ij} = c_{ijkl}\partial_l u_k. \tag{2.8}$$

with $\partial_l = \partial/\partial x_l$. The tensor of incremental adiabatic elastic moduli c_{ijkl} has the symmetries

$$c_{ijkl} = c_{jikl} = c_{ijlk} = c_{klij}. \tag{2.9}$$

On a fine scale the Earth material will have a relatively chaotic assemblage of crystal grains with anisotropic elastic moduli. However, the overall properties of a cube with the dimensions of a typical seismic wavelength (a few kilometres in the mantle) will generally be nearly isotropic. In consequence the elastic constant tensor may often be approximated in terms of only the bulk modulus κ and shear modulus μ

$$c_{ijkl} = (\kappa - \frac{2}{3}\mu)\delta_{ij}\delta_{kl} + \mu(\delta_{ik}\delta_{jl} + \delta_{il}\delta_{jk}). \tag{2.10}$$

The rheology of mineral assemblages is very complex in the crust and mantle. The rheological behaviour depends on the time scale. Over geological time scale they can sustain flow. However, on the relatively short time scales appropriate to seismic wave propagation (0.01s-1000s), the behaviour will be nearly elastic with a modest influence of the long-term rheology. The small incremental strains associated with seismic disturbances suggest that departures from constitutive relations (2.8) should obey some linear law [Kennett, 1983].

The anelastic behaviour could be included in the constitutive laws by introducing the assumption that the stress at a point depends on the time history of strain, so that the material has a 'memory' [Kennett, 1983] . The theory of such linear viscoelasticity has been reviewed by Hudson [1980]. The isotropic constitutive law which describes linear viscoelasticity is [Hudson, 1980; Kennett, 1983]:

$$\begin{aligned} \tau_{ij} &= \lambda_0\partial_k u_k\delta_{ij} + u_0(\partial_i u_j + \partial_j u_i) \\ &+ \int_0^t ds[\dot{R}_\lambda(t-s)\delta_{ij}\partial_k u_k(s) + \dot{R}_\mu(t-s)(\partial_i u_j(s) + \partial_j u_i(s)]. \end{aligned} \tag{2.11}$$

Here $\lambda_0 = \kappa_0 - \frac{2}{3}\mu_0$ and μ_0 are the instantaneous elastic moduli which define the local wavespeeds and R_λ, R_μ are relaxation functions specifying the dependence on the previous strain states.

Taking the Fourier transform of (2.12) with respect to time, in terms of stress and displacement at angular frequency ω I get

$$\tau_{ij}(\omega) = [\lambda_0 + \lambda_1(\omega)]\delta_{ij}\partial_k\bar{u}_k + [u_0 + u_1(\omega)](\partial_i\bar{u}_j(\omega) + \partial_j\bar{u}_i(\omega)), \tag{2.12}$$

where λ_1 and μ_1 are transforms of the relaxation terms:

$$\lambda_1(\omega) = \int_0^\infty dt \dot{R}_\lambda(t) e^{i\omega t} \qquad \mu_1(\omega) = \int_0^\infty dt \dot{R}_\mu(t) e^{i\omega t}. \tag{2.13}$$

The form of the stress-strain relation at frequency ω (2.12) is as for an elastic medium, but now with complex moduli.

Because the relaxation contribution to (2.9) depend only on the past history of the strain, $\dot{R}_\mu(t)$ vanishes for $t < 0$, so that the transform $\mu_1(\omega)$ must be analytic in the upper half plane ($\mathrm{Im}\omega \geq 0$). In consequence the real and imaginary parts of $\mu_1(\omega)$ are the Hilbert transforms of each other [see, for example Kennett, 1983; Titchmarsh, 1937]

$$\mathrm{Re}\{\mu_1(\omega)\} = \frac{1}{\pi} P \int_{-\infty}^{\infty} d\omega' \frac{\mathrm{Im}\{\mu_1(\omega)\}}{\omega' - \omega}, \tag{2.14}$$

where P denotes the Cauchy principal value. From the definition of Q_μ^{-1}, (2.14) can be rewritten in a way which shows the dependence of $\mathrm{Re}\{\mu_1(\omega)\}$ on the behaviour of the loss factor with frequency.

$$\mathrm{Re}\{\mu_1(\omega)\} = -\frac{2\mu_0}{\pi} P \int_0^\infty d\omega' \frac{\omega' Q_\mu^{-1}(\omega')}{\omega'^2 - \omega^2}. \tag{2.15}$$

When I wish to use observational information for the loss factor $Q_\mu^{-1}(\omega)$ I am faced with the difficulty that this only covers a limited range of frequencies, but the detailed form of $\mathrm{Re}\{\mu_1(\omega)\}$ depends on the extrapolation of $Q_\mu^{-1}(\omega)$ to both high and low frequencies. If Q_μ^{-1} is not too large, the approximate relation:

$$\mathrm{Re}\{\mu_1(\omega)\} = 2\mu_0 \ln(t_a f) Q_\mu^{-1}/\pi. \tag{2.16}$$

for some time constant t_a, fits a number of classes of model with approximately constant Q_μ^{-1}.

Kennett [1983] also developed the complex bulk modulus $\kappa_0 + \kappa_1(\omega)$ in terms of the loss factor Q_κ^{-1}. For a locally uniform region, at a frequency f, as in a perfectly elastic medium, two sets of plane waves exist. The S waves have a complex wave speed $\bar{V}_S$ given by

$$\bar{V}_S^{\,2}(\omega) = [\mu_0 + \mu_1(\omega)]/\rho, \tag{2.17}$$

influenced only by shear relaxation process. In terms of the wave speed $V_{S0} = (\mu_0/\rho)^{1/2}$ calculated for the instantaneous modulus, (2.17) may be rewritten as

$$\bar{V}_S^{\,2}(\omega) = V_{S0}^2 (1 + \frac{\mathrm{Re}\{\mu_1(\omega)\}}{\mu_0} - \mathrm{isgn}(\omega) Q_\mu^{-1}(\omega), \tag{2.18}$$

when I have used the definition of Q_μ^{-1} in equation (2.6). Even if Q_μ^{-1} is frequency independent in the seismic band, my previous discussion shows that $\bar{V}_S$ will have weak frequency dispersion through $\mathrm{Re}\{\mu_1(\omega)\}$.

For a small loss factor ($Q_\mu^{-1} \ll 1$) the ratio of complex velocity at two different frequencies f_1 and f_2 will from (2.18) be approximately

$$\frac{\bar{V}_S(\omega_2)}{\bar{V}_S(\omega_1)} = 1 + \frac{Q_\mu^{-1}}{\pi} \ln(\frac{\omega_1}{\omega_2}) - \mathrm{isgn}(\omega) \frac{1}{2} Q_\mu^{-1}(\omega). \tag{2.19}$$

The problem of the unknown constant t_a can be overcome by fixing a reference frequency most commonly 1 Hz and then,

$$\bar{V_s}(\omega) \approx V_{s1}[1 + \pi^{-1}Q_\mu^{-1}(\omega)\ln(\omega/2\pi) - i\mathrm{sgn}(\omega)\frac{1}{2}Q_\mu^{-1}(\omega)]. \tag{2.20}$$

where V_{s1} is the velocity at 1 Hz. The real part of this equation is the velocity dispersion contributed by attenuation with the condition of Q_μ^{-1} is independent of frequency [see also Kanamori and Anderson, 1977].

When $Q_\mu^{-1}(\omega)$ has some significant frequency dependence, the nature of the frequency dependence $\mathrm{Re}\{V_s(\omega)\}$ will vary. Under the condition of power low relationship between Q and frequency as $Q(f) = Q_0 f^\alpha$ and at reference frequency 1 Hz, the dispersion takes the form (2.21), (see also equation (2.36) and Jackson, 1993).

$$\bar{V_s}(\omega) \approx V_{s0}\left[1 - \tan((1-\alpha)\pi/2))Q_0^{-1}\left(\frac{\omega}{2\pi}\right)^\alpha\right] \tag{2.21}$$

I simulated the effect of dispersion based on (2.21) in section (8.2.4). I found the effects of dispersion to be very small in general. The δt_{sp}^* calculated with dispersion are slightly smaller than δt_{sp}^* calculated without dispersion at smaller distances and lower frequencies. They are identical at higher frequency and larger distance (see (8.2.4) for details).

For P waves the situation is a little more complicated since anelastic effects in pure dilatation and shear are both involved. The complex wave speed $\bar{V_p}$ is

$$\begin{aligned}\bar{V_p}^2(\omega) &= [\kappa_0 + \frac{4}{3}\mu_0 + \kappa_1(\omega) + \frac{1}{3}\mu_1(\omega)]/\rho \\ &= V_{p0}\{1 + A(\omega) + i\mathrm{sgn}(\omega)Q_p^{-1}(\omega)\},\end{aligned} \tag{2.22}$$

where

$$V_{p0} = [(\kappa_0 + \frac{4}{3}\mu_0)/\rho]^{1/2}, \tag{2.23}$$

and I have introduced the loss factor for the P waves.

$$Q_p^{-1} = \mathrm{Im}\{\kappa_1 + \frac{4}{3}\mu_1\}/(\kappa_0 + \frac{4}{3}\mu_0). \tag{2.24}$$

The real dispersive correction to the wave speed $A(\omega)$ will have a rather complex form in general but under the conditions leading to a linear relationship between Q_p^{-1} and Q_s^{-1}, there is a similar form to (2.16).

$$A(\omega) = 2(\kappa_0 + \frac{4}{3}\mu_0)Q_p^{-1}\ln(t_a\omega)/\pi. \tag{2.25}$$

and again for the complex wave speed has the form in terms of the wave speed at 1 Hz

$$\bar{V_p}(\omega) \approx V_{p1}[1 + \pi^{-1}Q_p^{-1}\ln(\omega/2\pi) - i\mathrm{sgn}(\omega)\frac{1}{2}Q_p^{-1}]. \tag{2.26}$$

It is believed that intrinsic attenuation in the Earth mantle occurs almost entirely in shear associated with lateral movement of lattice defects and grain boundaries 2.2.1.

The above discussion can be simplified by introducing stress and strain relaxation times. Following Lay and Wallace [1995], a standard linear solid can be used to explain and simplify the above discussion of the frequency dependence of Q. For this model, the constitutive law is written

$$\sigma + \tau_\sigma \dot{\sigma} = \mu_0(\varepsilon + \tau_\varepsilon \dot{\varepsilon}) \tag{2.27}$$

where μ_0 is called the relaxed elastic modulus, and τ_σ and τ_ε are called the stress and strain relaxation times, respectively. τ_σ implies constant strain, and τ_ε implies constant stress. Equation (2.27) is a special case of (2.12).

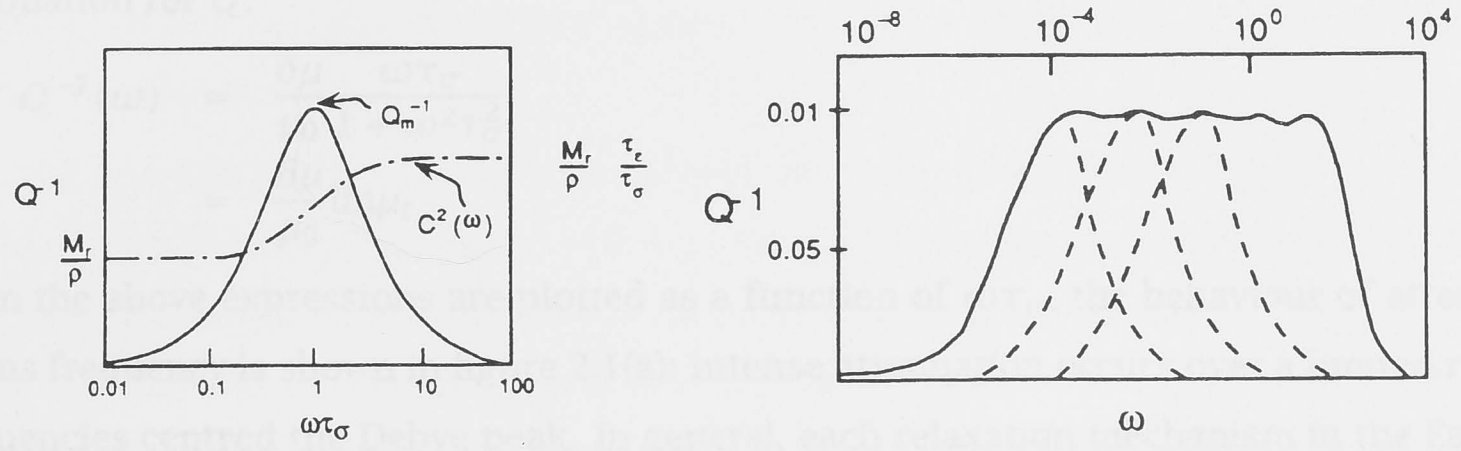

(a) Single Debye peak **(b)** Superposition of Debye peaks

Figure 2.1: (a) Q^{-1} as a function of frequency for a standard linear solid. The peak in Q^{-1} is know as a Debye peak. (b) Superposition of numerous Debye peaks results in an absorption band—nearly constant Q over a range of frequencies. After Lay et al. 1995.

The behaviour of (2.27) can be investigated by looking at the ratio of harmonically time-varying stress to strain:

$$\sigma(t)/\varepsilon(t) = \mu \tag{2.28}$$

μ is called the complex elastic modulus and is given by

$$\mu = \mu_0 + \mu_c \tag{2.29}$$

and

$$\mu_c = \delta\mu \left(\frac{\omega^2\tau_\sigma^2}{1+\omega^2\tau_\sigma^2} + i\frac{\omega\tau_\sigma}{1+\omega^2\tau_\sigma^2} \right) \tag{2.30}$$

where $\delta\mu = \mu_1 - \mu_0$, $\mu_1 = \tau_\varepsilon\mu_0/\tau_\sigma$ is the unrelaxed elastic modulus. The real part $\mathrm{Re}\mu_c$ and imaginary parts $\mathrm{Im}\mu_c$ of μ_c are also the Hilbert transform of each other as in (2.14).

$$\mathrm{Re}\mu_c = \frac{\omega^2\tau_\sigma^2}{1+\omega^2\tau_\sigma^2} \tag{2.31}$$

$$\mathrm{Im}\mu_c = \frac{\omega\tau_\sigma}{1+\omega^2\tau_\sigma^2} \tag{2.32}$$

This complex elastic modulus has several significant differences from simple elastic modulus; most importantly, the behaviour of a standard linear solid depends on frequency (ω).

This implies that waves traveling through such a solid will be dispersed. In other words, the different frequencies in a seismic wavelet will travel with different velocities. I can write the phase velocity as

$$\begin{aligned} V_p(\omega) &= \sqrt{\frac{\mu_0}{\rho}}\left(1+\frac{1}{2}\frac{\delta\mu}{\mu_0}\right)\frac{\omega^2\tau_\sigma^2}{(1+\omega^2\tau_\sigma^2)} \\ &= \sqrt{\frac{\mu_0}{\rho}}\left(1+\frac{1}{2}\frac{\delta\mu}{\mu_0}\right)\mathrm{Re}\mu_c \end{aligned} \tag{2.33}$$

This equation is valid only for small $\delta\mu$. Note that if $\delta\mu = 0$, the V_p is independent of frequency and is, of course, just the velocity in the elastic case. For small $\delta\mu$ I can also write an equation for Q:

$$\begin{aligned} Q^{-1}(\omega) &= \frac{\delta\mu}{\mu_0}\frac{\omega\tau_\sigma}{1+\omega^2\tau_\sigma^2} \\ &= \frac{\delta\mu}{\mu_0}\mathrm{Im}\mu_c \end{aligned} \tag{2.34}$$

When the above expressions are plotted as a function of $\omega\tau_\sigma$, the behaviour of attenuation versus frequency is shown in figure 2.1(a): intense attenuation occurs over a limited range of frequencies centred the Debye peak. In general, each relaxation mechanism in the Earth has a distinct Debye peak. These relaxation processes may involve grain boundary sliding, the formation and movement of crystal lattice defects, and thermal currents.

Because of the great variety and scale of attenuation processes in the Earth, no single mechanism dominates [Lay and Wallace, 1995]. The sum or superposition of numerous Debye peaks for the various relation processes, each with a different frequency range, produces a broad, flattened absorption band. Figure 2.1(b) shows the superposition effect. The Q^{-1} is basically constant for frequencies of 1.0 Hz to 2.8×10^{-4} Hz [Lay and Wallace, 1995]. This is likely the reason why the observation of attenuation from seismic wave indicates that Q is frequency independent over a large range of seismic frequencies. However, my estimation of frequency dependent δt^*_{sp} in a broad frequency band up to 6 Hz allows me to invert Q and α as a function of depth at same time. Hence, both depth dependence of Q and the depth dependence of frequency dependence of Q were obtained in thesis (see details in chapter 9).

2.1.4 Previous Seismological Studies on Frequency Dependence of Body Wave Attenuation

The frequency dependence of Q has been investigated in the last few decades for regional, teleseismic distances and global scale sampling of the crust and mantle by various authors [Anderson and Minster, 1979; Sipkin and Jordan, 1979; Aki, 1980a,b; Clements, 1982; Der et al., 1982, 1986; Roecker et al., 1982; Ulug and Berckhemer, 1984; Douglas, 1992; Bahttacharyya et al., 1996; Flanagan and Wiens, 1998; Martynov et al., 1999].

Sipkin and Jordan [1979] investigated the frequency dependence of Q_{ScS} using data from HGLP instruments at KIP and MAT and WWSS, LP and SP instruments at KIP and GUA and found

that Q_{ScS} is frequency dependent and takes the form of power law relationship between Q_{ScS} and frequency $Q_{ScS} \propto f^{\alpha}$ with $\alpha = 0.35$ in the frequency range 0.01-2 Hz. Der et al. [1982] investigated the regional variations and frequency dependence of anelastic attenuation in the mantle under the United Sates in the 0.5-4.0 Hz band. They found a large variation in the attenuative properties of the upper mantle under the United States. Their data indicate that attenuation is greatest under the south-western United States and the lowest attenuation prevails under the north central shield regions. They have found that the Q is frequency dependent and doubles in value somewhere in the range of 0.01-2.0Hz. They also indicated the form of frequency dependence may change from region to region, and the depth distribution of Q may be different at various frequencies. But these uncertainties can only be resolved by further detailed studies.

Ulug and Berckhemer [1984] summarised the range of studies on the frequency dependence of Q up to 1982. For a model with a power law dependence on frequency, $Q(f) = Q_0 f^{\alpha}$, the value of α for the whole Earth is 0.2-0.4 in the frequency range $10^{-8} - 10^{-2}$ Hz, for mantle, α is 0.15-0.6 in the frequency range 0.001 - 2.0 Hz, for crust, α is 0.25 - 1.0 in the frequency range 0.025 - 48 Hz. Laboratory data suggest α is 0.25 - 0.3 in the range $10^{-4} - 30$ Hz. Ulug and Berckhemer [1984] also investigated the frequency dependence of attenuation of P and S waves using 17 earthquakes at 40° - 90° range recorded at CSO, Germany and compared their results with previous investigations. They found their results are in good agreement with Sipkin and Jordan [1979]. Their Q model can probably best be represented by a power law absorption band $Q(f) = Q_0 f^{\alpha}$ with a slope of $0.25 < \alpha < 0.4$ and a cut-off relaxation time $0.2 < \tau < 0.5s$. This model is of the type proposed by Anderson and Given [1982] for absorption in the mantle.

A more thorough summary of values of α and Q_0 in the shallow lithosphere estimated from short distance seismic waves was given by Sato and Feher [1998]. The frequency dependence of the attenuation in the form of a power law as $Q_S \approx Q_{S0} f^{\alpha}$ for the frequency dependence higher than 1 Hz. Values of the exponent α range from 0.2 to 1. Q_{S0} is of the order of 10^2 at 1 Hz and increase to the order of 10^3 at 20 Hz. Based on the Q_S to be of 10^3 at 0.01 Hz from surface wave analysis, Sato and Feher [1998] described that Q has a peak of the order of 10^3 at 0.5 Hz and decays for both increasing and decreasing frequencies as conjectured by Aki [1980a]. The frequency dependence near 1 Hz remains poorly understood because seismic measurements are difficult to make at this frequency and, since most of the events that provide the best data have S wave corner frequencies near 1 Hz, it is difficult to discriminate attenuation effects from source effects. Compared to the S wave attenuation, the P wave attenuation is poorly constrained. For frequencies lower than 0.05 Hz, the ratio of Q_p/Q_S has been taken to be constant at 2.0-2.5 by many authors. Sato and Feher [1998] argue that recent observations have clearly shown that the ratio ranges between 1, 1/2 and 1/3 for frequencies higher than 1 Hz. But this only for very short distance records travelling

in the crust, in the case of scattering is dominant. For the long distance events which traverse in the upper mantle, the Q_p/Q_s ratio, should be only slightly affected by scattering. So that the intrinsic attenuation is dominant in the upper mantle and the Q_p/Q_s ratio will be around 2.25.

Flanagan and Wiens [1998] have summarised recent progress in attempting to quantify the frequency dependence of attenuation in the upper mantle, they also investigated the frequency dependent Q in upper mantle beneath Tonga region by a spectral-ratio method using *sS-S* and *pP-P* pairs. The spectral ratio between *sS-S* and *pP-P* pairs allow them to estimate the compressional wave attenuation Q_α and shear wave attenuation Q_β independently. Their measurements suggest substantial frequency dependence of Q in the upper mantle beginning at frequencies less than 1.0 Hz and consistent with the power law form: $Q(f) = Q_0 f^\alpha$ with α between 0.1 and 0.3.

By using the *Pg*, *Sg*, and *SmS* body waves and *S* coda waves from analysing 243 three-component broadband digital seismograms of aftershocks from the $M_s = 7.3$ Suusamyr, Kyrgyzstan earthquake, Martynov et al. [1999] investigated the high frequency (1.2-30 Hz) attenuation in the crust and upper mantle of the Northern Tien Shan. By taking the power law model $Q_j(f) = Q_{j0} f^{\alpha_j}$ for multiple layers, they found the Q_{j0} increases with depth from 76 (upper crust) to 1072 (upper mantle), and the value of α_j decrease from 0.99 to 0.29 over the same range. The Q coda results also demonstrated an azimuthal dependence. There is a strong 2ϕ dependence on azimuth for high frequencies (> 1.2 Hz). The depth and azimuth dependence of the quality factor show that Q is complicated and three dimensional. They also indicated that the lateral variation of Q_0 can be connected with azimuthal anisotropy in the upper mantle related to current deformation under the Tien Shan.

Multiple-frequency bands techniques similar to those I have developed in chapter 9 were reported in the AGU 2000 spring meeting by Mamada and Takenaka [2000]. Mamada et al. [2000] studied the *S* -wave attenuation in the focal regional of the 1997 northwestern Kagoshima earthquake, Japan. They used the coda normalisation method to estimate Q_s^{-1} for five frequency bands centered at 1.5, 3.0, 6.0, 12.0 and 24.0 Hz. They obtained the frequency dependence of Q_s is $Q_s^{-1} = 0.1673 f^{-0.84}$ in the focal area, and $Q_s^{-1} = 0.0146 f^{-0.69}$ for the crust of the whole western Kyushu including the focal area they studied. Mamada et al. explain the main reason for this extremely low Q is due to the focal region fractured completely with mainshock and a large number of aftershocks (personal communication). They did not use an inversion method.

2.2 Physical Mechanisms of Seismic Wave Attenuation

2.2.1 Physical Mechanisms of Attenuation

The mechanisms of attenuation have been reviewed by Gordon and Nelson [1966], Johnston and Töksoz [1981]. Seismological observations relevant to discussions of microscope mechanisms of attenuation were summarised by Anderson [1989]:

1. The frequency dependence of Q is weak over most of the seismic band and the weak frequency dependence can be explained by involving a distribution of relaxation times.

2. There has been no evidence to prove that seismic attenuation is amplitude or stress dependent. Laboratory measurements of attenuation are independent of amplitude at strains less than 10^{-6}.

3. The radial and lateral variations of Q in the mantle are our best clues to the effects of temperature and pressure. The lower Q regions of the mantle are in those areas where the homologous temperatures are highest.

4. The variation of Q with depth in the mantle covers a range of less than two orders of magnitude. This means that the effects of temperature and pressure are relatively modest or that they tend to compensate each other.

5. Losses in shear are more important than losses in compression. This is consistent with stress-induced motion of defects rather than a thermoelastic mechanism or other mechanism involving bulk dissipation.

The mechanisms of intrinsic attenuation (such as grain-boundary sliding and crystal-defect migration) are very sensitive to pressure and temperature conditions. This means that Q will vary within the Earth as a function of temperature. Tectonically active regions typically have relatively high heat flow and are more attenuative than "colder" regions. It has also been observed that Q variations correlate with travel-time variations as expected from the theory reviewed in section 2.1. Fast travel-time paths are typically high Q, slow paths typically low Q. This is a manifestation of the thermal activation of the attenuation mechanisms. Thus, mapping Q can reveal thermal processes at depth.

The actual physical mechanism of attenuation in the mantle is uncertain, but it is likely to be a relaxation process involving a distribution of relaxation times. Many of the attenuation mechanisms that have been identified in solids occur at relatively low temperatures and high frequencies. These include point-defect and dislocation resonance mechanisms, which typically give absorption peaks at kilohertz and megahertz frequencies at temperatures below about half the melting point [Anderson, 1989]. However, even in the laboratory it is often difficult to identify the mechanism of a given absorption peak. The effects of amplitude,

frequency, temperature, irradiation, annealing, deformation and impurity content must be studied before the mechanism can be identified with certainty.

Among phenomena which may be of importance are the migration of crystal defects, grain boundary processes and some thermoelastic effects [see e.g. Jackson and Anderson, 1970]. Anderson and Minster [1979] have suggested that the dislocation microstructure of mantle materials can account for both long-term steady-state creep and also for seismic wave attenuation. In this model the glide of dislocations within grains leads to attenuation, which climb and defect annihilation processes in the grain boundaries account for the long term rheology. For the upper mantle the most likely mechanisms are partial melting, grain-boundary diffusion, and intergranular thermoelastic relaxation [Kennett, 1983].

2.2.2 Laboratory Measurement of Attenuation and Dispersion

For experimental research, the main difficulties are to reproduce both the mantle conditions of temperature and pressure and the low-frequency range of seismic observations [Romanowicz and Durek, 2000]. During the last 20 years, a couple of experimental techniques operating in the seismic frequency band were developed matching the mantle conditions of temperature (1200-1500K) [Berckhemer et al., 1982; Gueguen et al., 1989; Kampfmann and Berckhemer, 1985] or pressure (0.3 GPa) [Jackson et al., 1984; Jackson and Paterson, 1987]. It is only recently that both relatively high temperature (1000°C) and high pressure (0.3 GPa) have been achieved simultaneously [Jackson et al., 1992]

A comprehensive review of attenuation measurements in the laboratory by Karato and Spetzler [1990] has given the solid-state mechanisms of relaxation processes of seismic wave attenuation in mantle rocks, showing that dislocation and/or grain boundary mechanisms can have a significant effect on seismic anelasticity. Anelastic behaviour is characterised by two parameters: the relaxation strength Δ (= (anelastic strain)/elastic strain)) and the relaxation time τ. The internal friction Q^{-1} has a maximum at the frequency $f_0 (= 1/\tau)$, and the modulus M changes with frequency, resulting in the dispersion of elastic wave velocities (section 2.1, fig 2.1). Karato [1998] developed a dislocation model of seismic wave attenuation and microcreep in the Earth. The model is based on the dynamics of dislocation motion in minerals with high Peierls stress. The frequency and temperature dependences of attenuation depend on the geometry and dynamics of dislocation motion, both of which affect the distribution of relaxation times. The distribution of relaxation times is largely controlled by the distribution in distance between pinning points of dislocations, L, and the observed frequency dependence of Q, $Q \propto f^{\alpha}$, is shown to require a distribution function $P(L) \propto L^{-m}$ with $m = 4 - 2\alpha$. Karato also indicated that a physically more sensible analysis of lateral variation in Q^{-1} should include the frequency dependence of Q^{-1} which is well documented in laboratory studies.

From anelasticity measurements on single crystals and relatively coarse-grained rocks at

high temperature and one atmosphere, dislocation relaxation mechanisms have been proposed for seismic wave attenuation in the upper mantle [e.g. Berckhemer et al., 1982; Kampfmann and Berckhemer, 1985; Gueguen et al., 1981, 1989]. An alternative view in which attenuation is dominant by diffusional process associated with grain boundary sliding has also been advocated by Sato et al. [1989]. From the relationship between Q and homologous temperature, Sato and Sacks [1989] proposed a connection between Q and the properties of the grain boundaries; that is, the major loss of seismic energy occurs at grain boundaries.

An experiment to measure anelasticity of rocks at seismic frequency under high pressure was made by Jackson et al. [1984]; Jackson and Paterson [1987]. They constructed an apparatus that facilitates the study of rock anelasticity under conditions which closely approach those of teleseismic wave propagation: simultaneous high temperature, low frequency, low strain amplitude and potentially controlled pore pressure of volatiles through observation of torsional forced oscillation and creep within an internally heated gas-filled pressure vessel. Measurement on granitic and calcite rocks showed that due to crack closure both the shear modulus and the quality factor Q_s increase sharply with increasing pressure below ~0.1 GPa, beyond which pressure both parameters become markedly less pressure sensitive. Further, Jackson et al. [1992] have extended their pressure and temperature ranges of anelasticity measurement to 0.3 GPa and 1000° C, respectively, and have confirmed the amplitude independence of Q^{-1} for seismologically mantle relevant strains ($< 10^{-6}$). Under these conditions, substantial dispersion of the shear modulus of dunite occurred and Q increased mildly with frequency as $Q \propto f^{1/6}$. The distinctive features of this approach and some recent modifications providing routine access to temperatures as high as 1300° has been discussed by Jackson [2000].

Detailed descriptions and a review of the status of experimental studies of seismic attenuation were given by Jackson [1993]. Experimental results indicate a frequency and temperature dependence of Q^{-1} of the form

$$Q^{-1} = Af^{-\alpha}\exp(-\alpha E^*/RT) \tag{2.35}$$

f frequency, E the activation energy, R the gas constant and T the temperature, with $\alpha = 0.15 - 0.25$, compatible with seismological results, and activation energies ranging from 440 kJ/mole to 700 kJ/mole. Such behaviour confirms the need for a distribution of relaxation times proposed in particular by Minster [1981]; Minster and Anderson [1981]. Most experimental data on the amplitude and the frequency dependence of Q^{-1} for olivine and olivine rich rocks have been summarised by Karato and Spetzler [1990]. Most data show a monotonic increase of internal friction with decreasing frequency. Internal friction peaks of the Debye type associated with a relaxation mechanism having a unique relaxation time, or a narrow distribution of relaxation times, are generally not observed [Jackson, 1993]. It was found that Q^{-1} increases monotonically with increasing oscillation period and temperature. Over very wide ranges of temperature and oscillation period, a variety of relaxation mechanisms

will be operative [Jackson, 1993]. Different temperature sensitivities observed from different studies indicate that several distinct mechanisms (probably including both dislocation- and melt-related processes) must be contributing to the variability of Q^{-1} under widely varying experimental conditions [Jackson, 1993].

A more thorough discussion of the current status of the art in experimental measurements of attenuation was given by Jackson [2000]. Relatively fine-grained synthetic materials, which have the advantages of controlled microstructure and resistance to thermal cracking, have been the focus of much of the recent experimental work with the low frequency torsional forced oscillation and microcreep methods [see also Gribb and Cooper, 1998b,b]. Based on the experiments at ANU by Jackson and his colleague, a number of the general characteristics of high temperature behaviour was illustrated by Jackson [2000]. The linearity of the stress-strain relationship is demonstrated by its amplitude insensitivity, the adherence of the observed dissipation (Q^{-1}) and modulus dispersion $\mu(f)$ to the Kramers-Krönig relation, approximated for $Q^{-1} \ll 1$, by

$$\mu(T)/\mu(T^{ref}) = 1 - \tan[\pi(1-\alpha)/2][Q^{-1}(T) - Q^{-1}(T^{ref})] \tag{2.36}$$

and by the close consistency between the results of torsional forced oscillation and microcreep tests. α is previously defined as power-law exponent.

The dissipation and associated modulus dispersion both increase monotonically with increasing temperature and decreasing frequency, as is characteristic of the 'high-temperature internal fiction background' in a wide variety of materials [Jackson, 2000]. The extent of departure from elastic behaviour in these generally fine-grained materials appears to be sensitive to both grainsize and impurity content. Much of this viscoelastic behaviour is compatible with an origin in elastically accommodated diffusion-accommodated grain-boundary sliding [Jackson, 2000]. The anelastic relaxation of internal stresses caused by elastic anisotropy must also be a significant contributor in some situations. There is some evidence of the grainsize sensitivity expected of such phenomena in the results of Tan et al. [1997] where a marked reduction in the intensity of the viscoelastic relation accompanies grain growth from 10 to ~ 150 μm in one initially fine-grained Fo_{90} specimen.

More recently, several fine-grained polycrystalline specimens of Fo_{90} olivine have prepared by hot-isostatic-pressing and used for laboratory study of seismic wave attenuation and dispersion by Jackson et al. [2000]. Torsional forced oscillation and complementary microscreep methods have been used to measure the shear modulus and associated strain energy dissipation Q_{-1} as function of frequency ω, temperature T and grainsize d. Q_{-1} varies with ω (0.01-1 Hz), T (1000 - 1300°C) and d (2 - 30 μ m) as $Q^{-1} = AX^{-\alpha}$ with $X = \omega\tau = B\omega d \exp(E/RT)$. The form of this expression for the relaxation time τ is suggestive of elastically accommodated grain-boundary sliding. The optimal values for the parameters α, which determines the frequency dependence of Q_{-1} within the absorption band,

and E are respectively 40.25 ± 0.024 and 420 ± 30 kJ/mol, the latter being comparable with the activation energy for diffusional creep. Extrapolation of the observed relatively mild grainsize sensitivity to the mm grainsizes thought to be representative of the suggesting that much of the seismic wave dissipation might be attribute to such diffusional process.

2.2.3 Application to Seismological Models for the Earth's Interior

Attenuation measurements done in the laboratory which are helpful to understand the attenuation in the upper mantle were recently summarised by Sato [1995]. He also reviewed the thermal and mechanical structure inferred from seismic data. A good correlation between surface-wave slowness and high heat flow was indicated by Nakanishi and Anderson [1984]. Global earth structure obtained from surface waves by Yomogida and Aki [1987] and Tanimoto and Zhang [1990] shows deviations from simple boundary layer theory for the thickening of oceanic lithosphere, which may be accounted for by the presence of thermal anomalies in the upper mantle caused by heterogeneous distribution of hotspots. Bock [1991] determined a 7% P wave velocity contrast between the subducting slab and the overlying mantle beneath the Lau basin, indicating the presence of at most minor amount of partial melt in the upper mantle. Some seismic studies have indicated changes in both chemical composition in low (or high) velocity regions. A joint inversion of travel time residuals, geoid height and bathymetry along the Mid-Atlantic ridge indicated to Sheehan and Solomon [1988] that temperature variations of ± 50°C and compositional variations of ± 0.5-3% Mg/(Mg+Fe) over the upper 300 m of the mantle provide good fits to both geoid and travel time data. The presence of 1-4 vol.% melt was estimated in the low velocity upper mantle beneath the Salton Trough, whereas ~ 500°C colder temperature and 1% higher than average densities were indicated for the high velocity subcrustal lithosphere beneath the Transverse Ranges in southern California [Humphreys and Hager, 1990]. Q and velocity structures determined by Halderman and Davis [1991] indicated average melt fractions of 1 and 3 vol.% with corresponding homologous temperatures of 1.015 in the asthenosphere beneath the Rio Grande and East African rifts, respectively. Global lateral variations in the elastic and anelastic structure studied by Suda et al. [1991], for example, indicate that regions of high hotspot density overlap with high attenuation anomalies in the transition zone and with regions of low P wave velocity in the lower mantle.

Robust quantitative extrapolation of the results of experimental studies of seismic wave dispersion and attenuation to the conditions of seismic wave propagation is clearly not yet possible with a useful level of confidence [Jackson, 2000], however, the discussion above highlights the fact that there are beginning to emerge experimental data of high quality for classes of well-characterised materials broadly relevant to discussions of seismic wave propagation within the Earth.

Recent work suggests that grainsize sensitive diffusional processes could conceivably be responsible for seismic wave attenuation in the upper mantle. The grainsize sensitive of

shear modulus $G(f)$ and dissipation Q^{-1} were calculated by Tan et al. [1997]. Their results show that the relatively mild grainsize sensitivity in the extrapolation yields value of Q^{-1} in the range 0.002-0.01 at 5 mm grainsize which is close to the levels of dissipation from seismological studies of the upper mantle.

Gribb and Cooper [1998b,a] have concluded instead that grainsize extrapolated values of Q^{-1} are substantially lower than seismological observations, and speculated that sub-grain size rather than grainsize might be the controlling factor. Alternatively, it is possible that at larger grainsize representative of the Earth's upper mantle and at the low stresses of teleseismic wave propagation, linear dislocation migration mechanisms perhaps of the type discussed by Karato [1998] will dominate the transient creep and the associated phenomena of seismic wave dispersion and attenuation [Jackson, 2000].

2.3 Q Models in the Upper Mantle on Global and Regional Scales

2.3.1 Introduction

In the last thirty years, much work has been done on both the attenuation structure of the upper mantle from the inversion of body waves and surface waves [Anderson and Archambeau, 1964; Mills, 1977; Anderson and Hart, 1978a,b; Lay and Helmberger, 1981; Anderson and Given, 1982; Masters and Gilbert, 1983; Der et al., 1986; Woodward and Masters, 1991a; Bussy et al., 1993; Romanowicz, 1995], and on free oscillations [Sailor and Dziewonski, 1978; Roult et al., 1990; Suda et al., 1991; Widmer et al., 1991; Woodward and Masters, 1991b]. This has led to numerous attenuation models for the Earth. The attenuation models have been summarised, compared and displayed in several figures by Romanowicz and Durek [2000] which include 1-D profiles of Q from the upper mantle to the inner core, 3-D structure in the upper-mantle and anisotropy in the inner core. Goes et al. [2000] obtained models of temperature at 50 to 200 km depth beneath Europe from the global P velocity model [Bijwaard et al., 1998] and the regional S wave velocity model [Marquering and Snieder, 1996]. For a 100° increase in temperature, a decrease of 0.5-2% in V_p and 0.7-4.5% in V_s is predicted, where the strongest decrease is due to the large effect of anelasticity at high temperature. At shallower depths, variation in crustal thickness

and possibly the presence of partial melt appear to have an additional effect, mainly on S wave velocity. The temperature inferred from the V_p and V_s derived thermal models agree well with each other and with temperatures determined from surface heat flow observations in the regions where both P and S are well resolved.

2.3.2 1-D Q Models in the Earth

Early studies of Q models were based primarily on normal mode and surface wave data which identified a few characteristics that are valid to this day: the dominance of attenuation in shear over attenuation in compression, high Q in the lithosphere, the existence of a low Q zone in the uppermost mantle and a rapid transition to high Q around the upper mantle to lower-mantle boundary [Romanowicz and Durek, 2000]. The common feature among the models is the steep gradient in the transition from upper to lower mantle. There are large variation among models in the lower mantle, although some indication for a maximum, placed at different depths by different authors.

Romanowicz and Durek [2000] also undertook a comparison of recent Q profiles in the upper mantle. The surface wave based models show a pronounced low Q zone in the uppermost mantle, under a lid that has very high Q, but lower Q than PREM. The fundamental spheroidal mode Q models can be classified into two groups of incompatible data and corresponding models. There is an apparent discrepancy between the measurements of fundamental mode Q obtained using a standing wave approach and those obtained using a surface wave traveling approach [Romanowicz and Durek, 2000]. Standing wave Q estimates have been found to be systematically larger than surface wave Q by about 10-15% in the period range where both can be measured with some confidence (200-300 sec). This discrepancy translates into higher Q in the transition zone and at the bottom of the upper mantle. The discrepancy could be due to measurement techniques, with the presence of noise leading to an overestimation of Q for normal modes.

Recent studies have not attempted to fit body wave data and have therefore poor depth resolution in the lower mantle [Romanowicz and Durek, 2000]. This thesis is supplementary to the contribution of the body wave attenuation in the upper mantle. Recent attenuation models have also been reviewed by [Jackson, 2000]. [Jackson, 2000] summarised that the radial variation of Q^{-1} features a low-loss 'lid' in the uppermost mantle (Q^{-1} usually < 0.002), overlying a zone of very high average attenuation ($Q^{-1} \sim 0.015$) at depths of 80-220 km in the upper mantle. Q^{-1} is markedly lower at greater depths, averaging 0.006 between 200 and 700 km depth, and 0.003 for most of the lower mantle, although some what higher values are found for the layer in the lowermost mantle ($2600 < z < 2900$ km) .

2.3.3 3-D Tomographic Q Models in the Earth

The existence of large lateral variations in attenuation in the upper mantle, reaching and exceeding 50-100%, has long been documented using a variety of techniques. Regional variation in the attenuation of fundamental modes measured using a standing wave approach [Roult et al., 1990] or a surface wave approach [Dziewonski and Steim, 1983].

In recent years, a tomographic approach was applied to determine 3-D models of atten-

uation in the upper mantle from low frequency surface wave data [Romanowicz, 1995; Bahttacharyya et al., 1996], but the resulting models still suffer from low lateral resolution (compared to their equivalent elastic 3-D models) and large uncertainties [Romanowicz and Durek, 2000]. The primary reason why attenuation tomography is currently at the level of resolution at which velocity tomography was in the early 1980's is related to the extreme complexity of seismic wave amplitudes, which depend not only on intrinsic attenuation effects, but also on the focusing/scattering effects due to wave propagation in a laterally varying elastic medium, which are controlled by the transverse gradients of elastic structure [Romanowicz et al., 1987; Romanowicz and Durek, 2000]. Those transverse gradients depend on high order terms in spherical harmonics expansions of elastic structure and are not well constrained at present, even in the latest generation of elastic tomographic models [Li and Romanowicz, 1991; van der Hilst et al., 1997]. Such unmodelled effects, combined with very noisy attenuation datasets, mean sophisticated methods have to be devised to get around these difficulties [Romanowicz and Durek, 2000].

Mitchell and Cong [1998a] investigated and summarised the tomographic maps of L_g coda Q which maps crustal perspectives, and its relation to the structure and evolution of continents in a global scale in which covers the entire African, Eurasian, South American, and Australian continents as well as for the United States. $Q_{L_g}^c$ at 1 Hz (Q_0) varies from less than 200 to more than 1000 and $Q_{L_g}^c$ frequency dependence η varies between 0.0 and nearly 1.0.

2.3.4 Previous Studies of Attenuation Structure in the Upper Mantle beneath the Australian Continent

Clements [1982] investigated the intrinsic Q and its frequency dependence from *P*, *S*, *PcP* and *ScP*, phases recorded at the Warramunga array in the Northern Territory of Australia from earthquakes located in the Japan Arc, Mariana Arc, Sunda Arc, New Hebrides Arc, Kermadec and Tonga trench zones. Clements [1992] suggested that the values of Q for compressional and shear waves are frequency dependent, because it was found that the attenuation parameter t^* for short period waves were much smaller than estimates from published free-oscillation Q models at the time. The short period t^* values and the free oscillation Q model could be made consistent with each another by assuming that $Q = Q_0(1 + \tau f)$, where Q_0 and τ are constants.

A Q model for the attenuation structure in the upper mantle under the north of the Australian continent was obtained by Gudmundsson et al. [1994] from the analysis of 22 seismograms. Assuming that shear dissipation dominates over bulk dissipation, their measurements are consistent with an average quality factor for *S* waves in the lid of the order of $Q_s = 1400$ ($Q_p = 2800$), a highly attenuative asthenosphere of 200km thickness with $Q_s = 100$ ($Q_p = 200$), and the transition zone with $Q_s = 600$ ($Q_p = 1200$). These results are generally

Table 2.1: The QNA1 model of Q_s and Q_p in the upper mantle beneath Australian continent (After Gudmundsson et al. [1994]).

Layer Description	*Depth* (km)	Q_s	Q_p
Lithosphere	0-210	1400 ± 400	2800
Upper mantle	210-410	100 ± 20	200
Transition zone	410-660	600 ± 300	1200
Lower mantle	660-2660	1300	2600

It is assumed $Q_p = 2Q_s$.

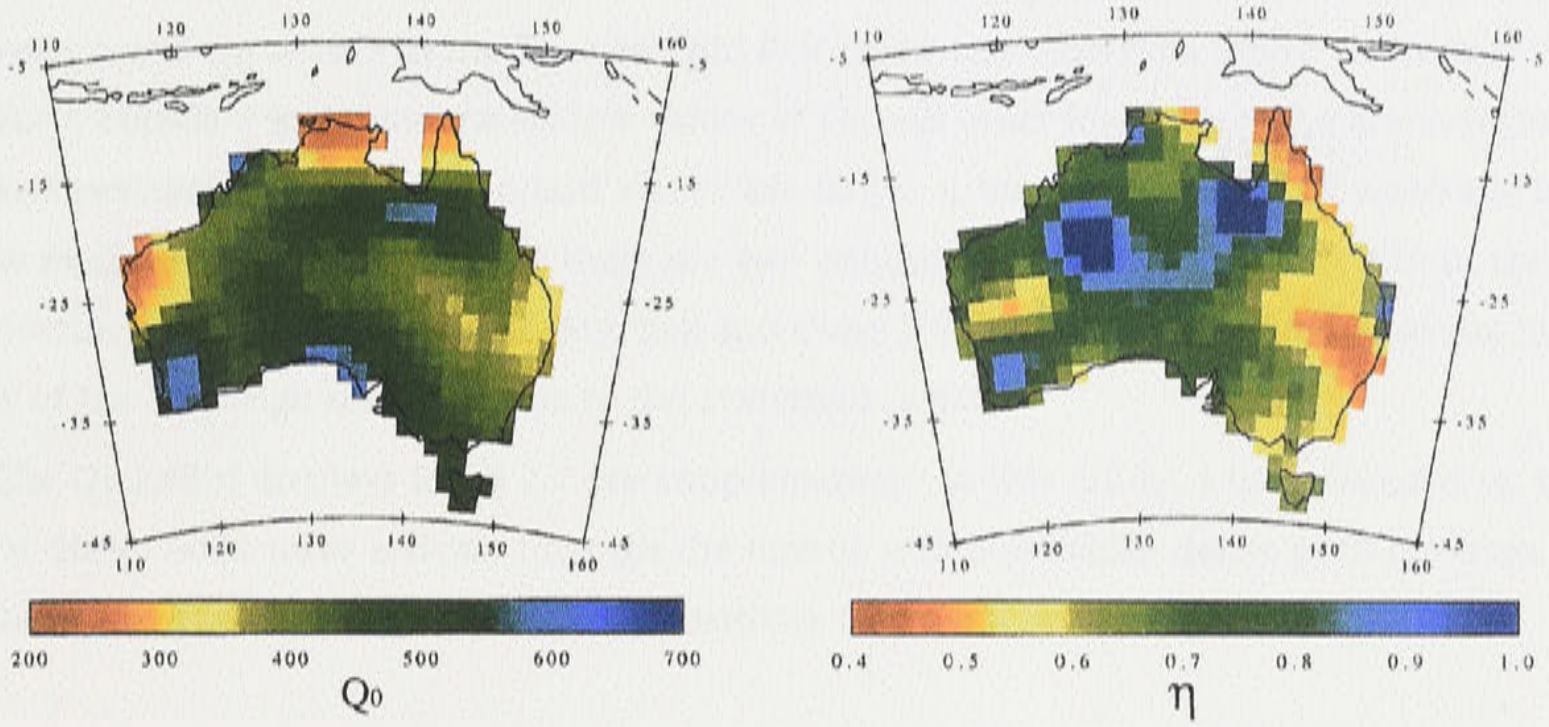

Figure 2.2: Tomographic map of L_g coda Q at 1 Hz for all of Australia and the regional variation of the frequency dependence of $Q_{L_g}^c$ at 1 Hz (η). Each cell is 1.5° by 1.5° in area, After Mitchell and Cong [1998b].

comparable with published results from 0.3 Hz body-wave observations under the Eurasian shield (Der et al. 1986), but a lower value for Q_s in the asthenosphere and a much higher value in the lid was obtained in the research of Gudmundsson et al. [1994]. This difference can be explained by a significant thermoelastic contribution to attenuation, or it may be a reflection of the difference between the two shields.

L_g coda Q in Australian has been determined by Mitchell and Cong [1998b] from ground motion recorded at seven broadband stations in Australia by using a stacked spectral ratio method. $Q_{L_g}^c$ at 1 Hz in Australia varies between 330 and 600. They have also discussed the relation between L_g coda Q and the crustal structure and evolution of the Australian continent. They argue that lowest values of L_g coda Q (330-400) characterise the Tasman Fold Belt in eastern Australia; these Fold Belts may be associated with fluids produced by orogenic activity that occurred during the Devonian and Carboniferous periods or by sedimentation that occurred in Jurassic and Triassic times. Smaller reductions of $Q_{L_g}^c$, relative to maximum values, in central and western Australia, may be associated with sedimentation that occurred over a long-time interval between late Precambrian time and the Carboniferous period or with deformation that occurred in the Central Australian Mobile Belts during the Carboniferous.

Bowman and Kennett [1991] proposed a velocity gradient model rather than a sharp

boundary for the crust-mantle transition zone in the entire of the Australian continent. Mitchell and Cong [1998b] have found that up to a 20% reduction in $Q_{L_g}^c$ can be produced by using the velocity gradient model derived by Bowman and Kennett [1991]. The lateral variation in the thickness, depth, and severity of the velocity gradient lead to additional L_g energy to leak into the mantle. The $Q_{L_g}^c$ through out most of Australia is 30 to 60% lower than it is in most stable continental regions (Mitchell and Cong, 1998b). The lateral variation of Q_0 is displayed on the left side of fig 2.2. The regional variation of the frequency dependence of $Q_{L_g}^c$ at 1 Hz (η) in the Australia is shown in the right side of fig 2.2. The only clear correlation between η and Q_0 occurs in the Tasman Fold Belt of eastern Australia where the lowest values for η correlate with moderately low values of Q_0. All other low values of η are in regions where resolution is poor or standard errors are large. η throughout most of Australia lies in the range 0.65 to 0.75, however there are two regions of very high η (about 1.0) in the in the northern part of the continent. Mitchell and Cong [1998b] have commented that the high value of the very high η may be due to the systematic errors.

The Q_0 and η displays in fig 2.2 are supplementary to this study. I have focused on the use of direct body wave arrivals through the mantle which provides dense path coverage in northern Australia but has very limited sensitivity to crustal prospectives.

Chapter 3

P and *S* Velocity Structure under Australian Region and their Geological Background

3.1 Geological Background of the Australian Continent

The large scale elements of the geology of the Australian continent are marked by the outcrop of Precambrian material in the center and west and an extensive zone of Phanerozoic rocks in the east. The eastern extent of Precambrian outcrop is marked by the "Tasman line" whose location is guided by gravity and magnetic lineations through those regions with substantial regolith cover [Veevers, 1984].

The Australian continent has evolved during a long geological history, with the tectonic processes that have most recently influenced the lithosphere becoming younger from west (Archaean) to east (Proterozoic). Proterozoic cratons lie in the central part of the continent. The lateral boundaries between the major tectonic divisions are not well constrained, and, in particular, their depth extent is uncertain [Kennett and van der Hilst, 1998]. Studies over the past 10 year using global seismic data suggest that the Archaean shields have high velocity roots extending to as much as 400 km depth. A number of methods e.g. Jordan [1975], have suggested that Archaean cratons would have very deep roots to 400 km or more. The results of Kennett and van der Hilst [1998] suggest that the cratonic roots lie mostly above 250 km, although there may be some isolated regions with greater thickness. These results are in good general agreement with the work of van der Lee and Nolet [1997] in Northern America and the work of Priestley et al. [1997] in Southern Africa and the work of James et al. [2000] where the high velocity also lies above 250 km.

The continental upper mantle has more complex seismic structure which reflects its long

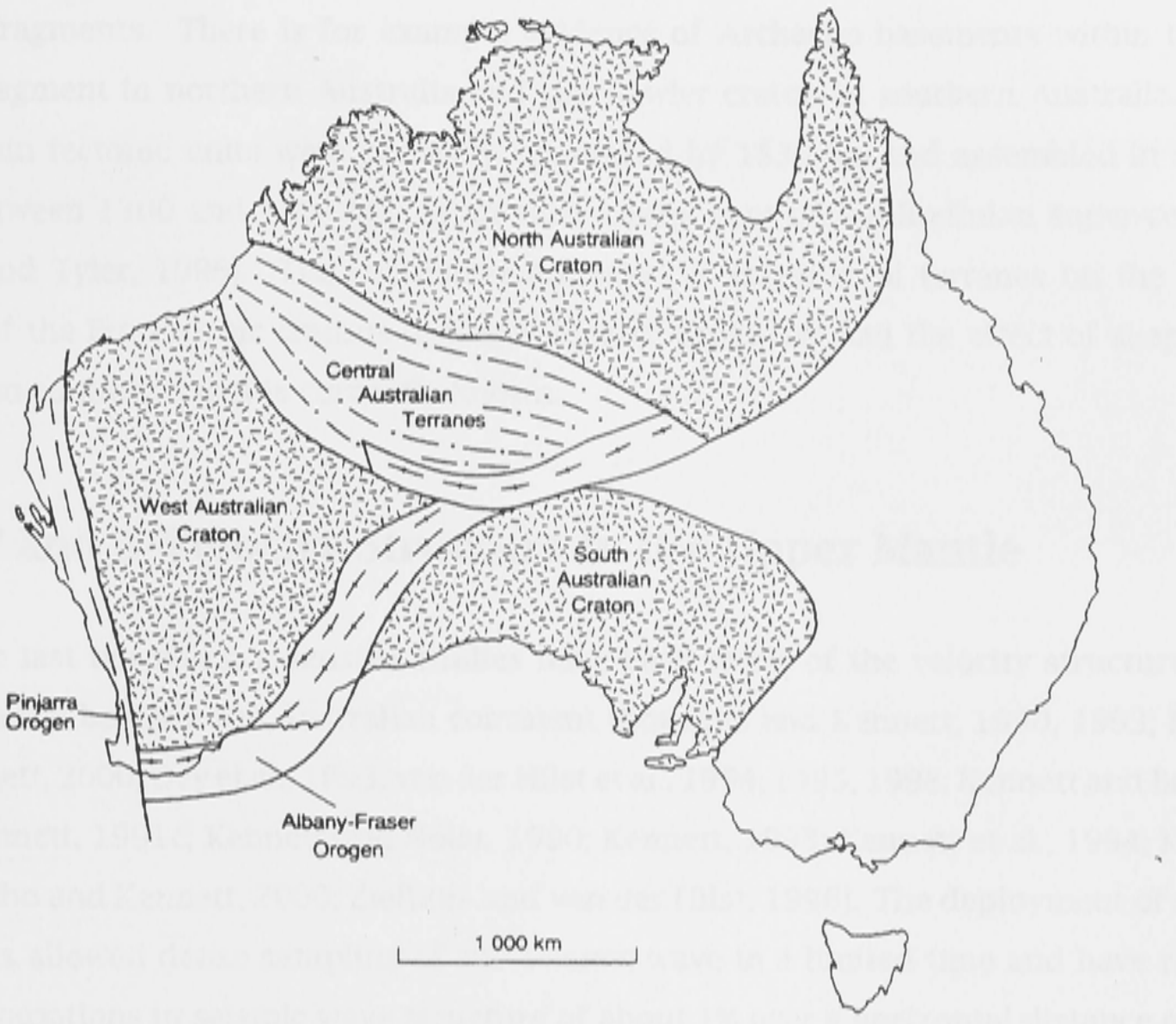

Figure 3.1: The main Precambrian tectonic units of Australia: ~ 1830 Ma cratons; ~ 1900 to 1300 Ma central Australian terranes; and the ~ 1300 Ma Albany-Fraser orogen. The central Australian terranes were accrued onto the North Australian Craton prior to its ~ 1300 Ma suturing with the West and South Australian cratons, After Myers and Tyler [1996].

history. Generally, high seismic velocities are found beneath the oldest Precambrian cratons while the more recent Phanerozoic regions display lower velocities [Zielhuis and Nolet, 1994; Zielhuis and van der Hilst, 1996; van der Lee and Nolet, 1997; Debayle and Kennett, 2000], but the depth extent of these continental high velocity anomalies is still controversial. If the lithosphere thickens gradually with age, a thickness of 250 km has been predicted for Archaean cratons [Fleitout and Yuen, 1984]. The existence of thicker continental roots would require the presence of compositional heterogeneities in the mantle. In this thesis, I focus on the upper mantle structure beneath Australia, a continent which has experienced a long tectonic history since the Archaean. The continent is the result of the assemblage of numerous fragments of continental crust by plate tectonic processes [Myers and Tyler, 1996], which are likely to have left a lasting imprint on the lithospheric mantle. It is generally assumed that two thirds of the Australian crust is Precambrian while the remaining third has been accreted during the Paleozoic. According to Myers and Tyler [1996] Precambrian Australia comprises three main tectonic units called the North, West and South Australian cratons (Fig. 3.1). The West Archaean craton has been accreted from two main Archaean blocks, the Pilbara and Yilgarn cratons, well exposed in Western Australia (Fig. 3.3(a)). The North and South

Australian cratons are probably the results of the assemblage of Proterozoic and Archaean crustal fragments. There is for example evidence of Archaean basements within the Pine Creek fragment in northern Australia and the Gawler craton in southern Australia. These three main tectonic units were probably cratonised by 1830 Ma and assembled in a single piece between 1300 and 1100 Ma, as an early component of the Rodinian super-continent [Myers and Tyler, 1996]. The successive accretion of continental terranes on the eastern margin of the Proterozoic cratons during Paleozoic times has had the effect of shaping the Australian continent as it is currently known.

3.2 *P* and *S* Velocity Structure in the Upper Mantle

In the last ten years, extensive studies have been made of the velocity structure in the upper mantle beneath the Australian continent [Bowman and Kennett, 1990, 1993; Debayle and Kennett, 2000; Dey et al., 1993; van der Hilst et al., 1994, 1995, 1998; Kennett and Bowman, 1990; Kennett, 1991c; Kennett and Nolet, 1990; Kennett, 1993; Kennett et al., 1994; Kennett, 1997; Kaiho and Kennett, 2000; Zielhuis and van der Hilst, 1996]. The deployment of seismic arrays has allowed dense sampling of the seismic wave in a limited time and have revealed regional variations in seismic wave structure of about 1% over a horizontal distance of 1,000 km [Dey et al., 1993].

Kennett and Bowman [1990] have suggested the presence of heterogeneity with about 1% fluctuations in P-wave speeds on scales of 200-300 km, superimposed on larger scale variations. This analysis was based on amplitude and waveform variability for individual events recorded in a number of portable-array experiments with different array dimensions and spacings. The scale length is small enough to be difficult to resolve directly (particular using refracted waves), and this style of heterogeneity may need to be represented in a stochastic manner. The influence of medium- and small-scale heterogeneity is likely to be particularly important for the regions where radial velocity gradients can then dominate the behaviour of the seismic wave field [Kennett, 1993].

Surface wave studies have revealed three dimensional variation in shear wave structure beneath the continent by exploiting the records from SKIPPY stations [Zielhuis and van der Hilst, 1996; van der Hilst et al., 1998; Debayle and Kennett, 2000]. In general, low velocities are found on the eastern Phanerozoic margin of the continent, whilst west of 140°E the Precambrian cratons which characterise central Australia are underlain by high velocities.

Waveform inversion [Zielhuis and van der Hilst, 1996] reveals large lateral variations in shear-wave speed in the upper mantle beneath the eastern Australian region. The mantle beneath easternmost Australia, and marginal basins between Australia and the Indo-Australia-Pacific-plate boundary, are marked by a pronounced low-wave-speed anomaly. On the continent, the lateral distribution of these low wave speeds correlates closely with the location

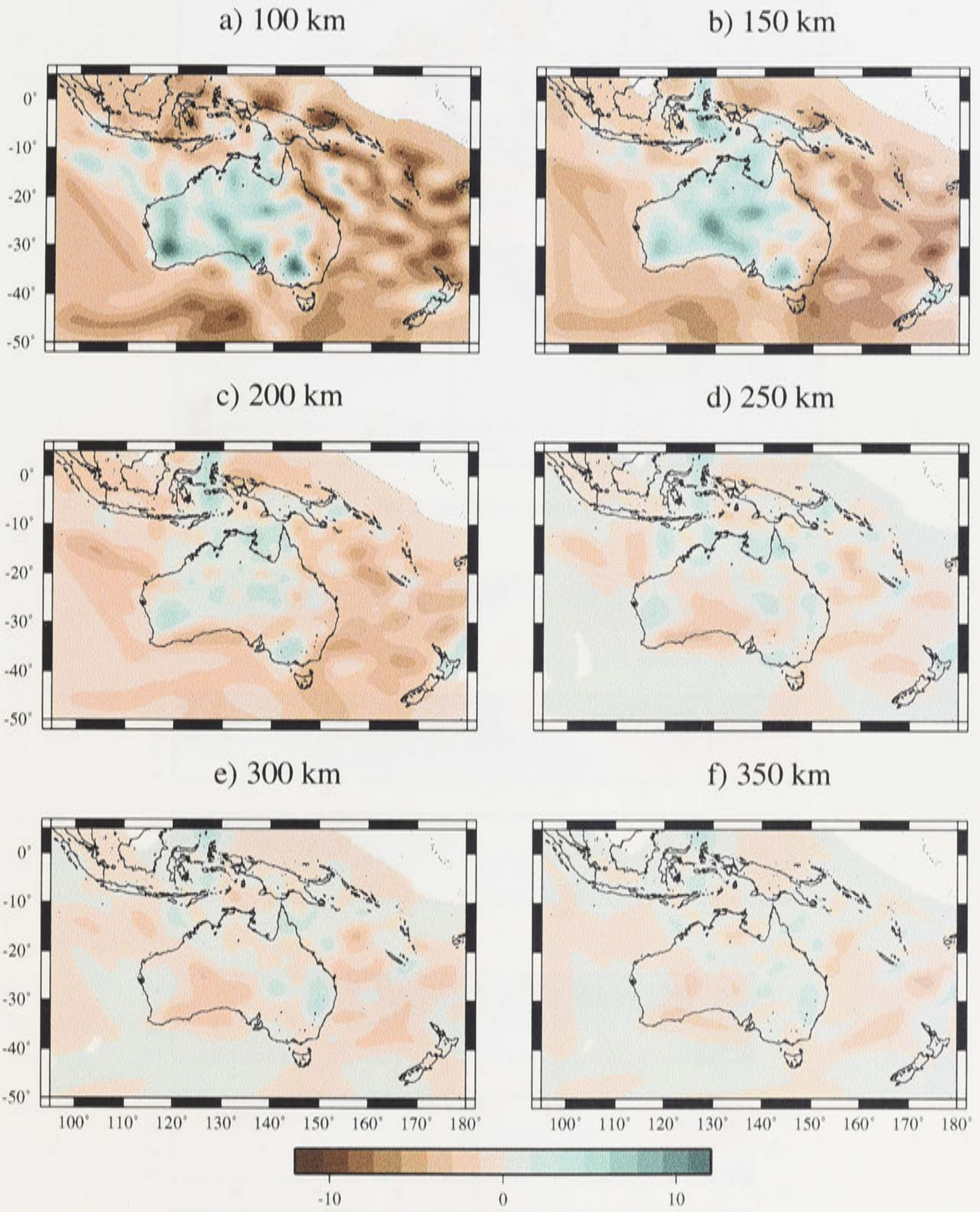

Figure 3.2: Lateral variation of surface wave velocity at different depths. *SV* perturbations are shown in percent using the tone scale with respect to the average velocity values, of which are 4.50 km.s^{-1} for 100 km, 150 km and 200 km, 4.6 km.s^{-1} for 250 km, 4.69 km.s^{-1} for 300 km and 4.73 km.s^{-1} for 350 km. The area in gray on the border of each map correspond to the regions where an a posteriori error close to the a priori error indicating a total lack of resolution. The maps were plotted by GMT based on the data from Debayle and Kennett, 2000

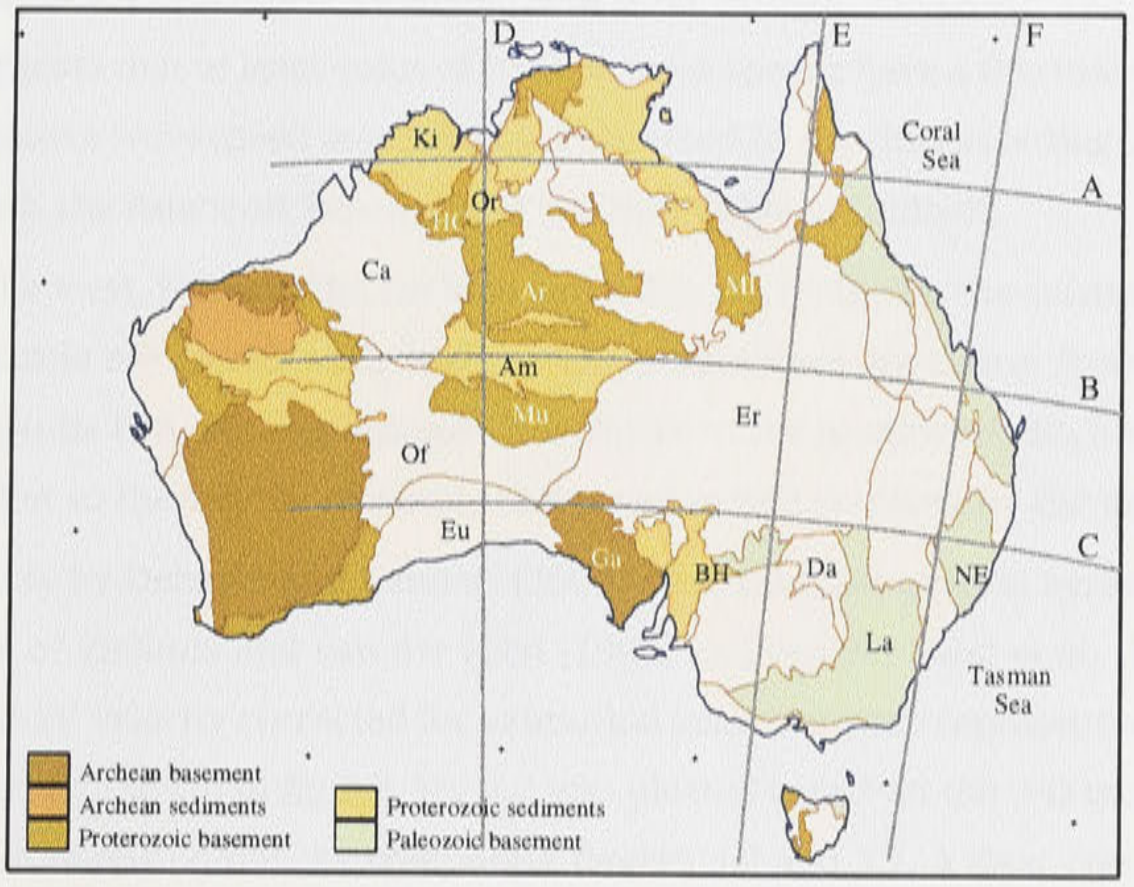

(a) Australian Geology

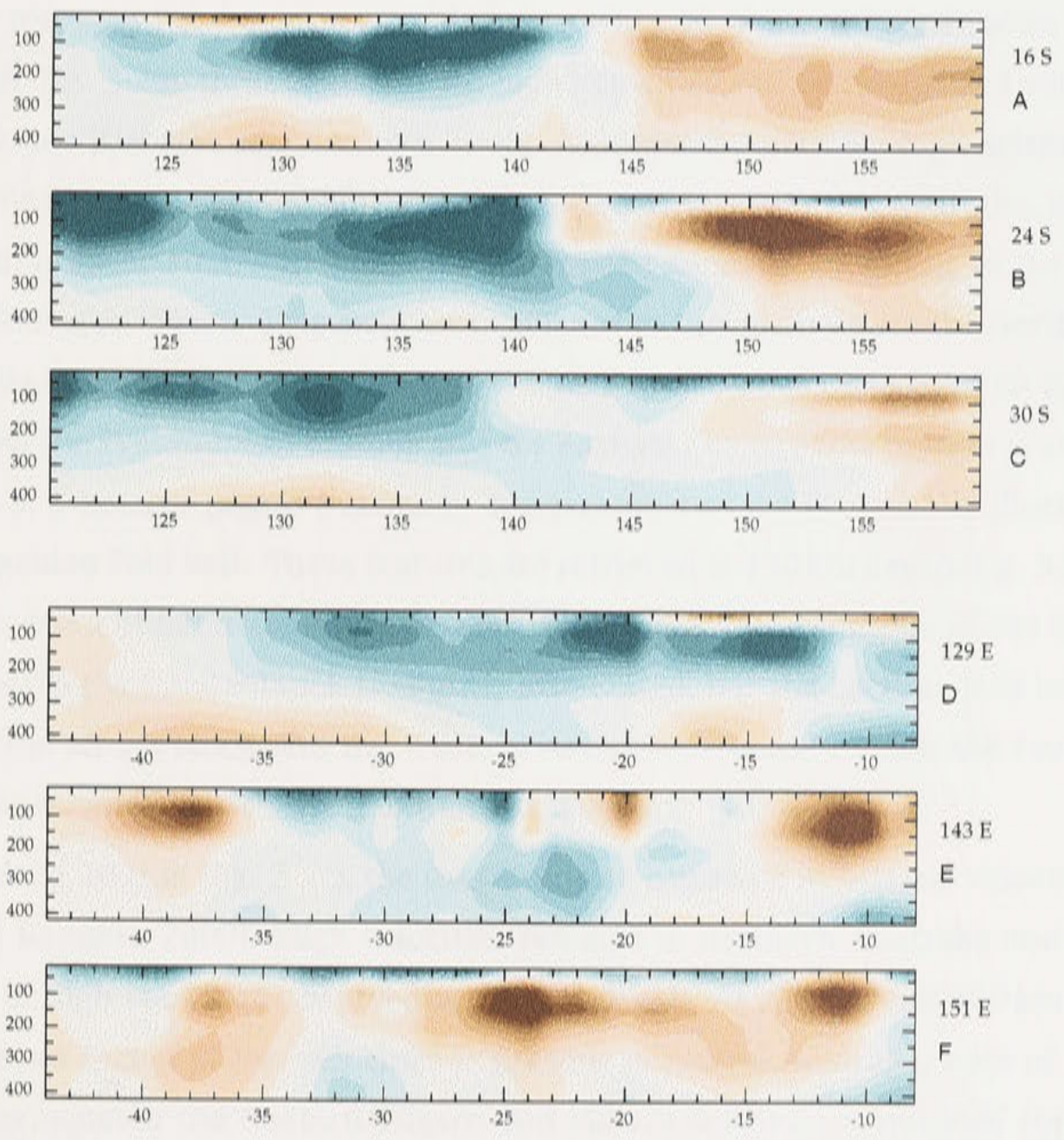

(b) Velocity Cross Sections

Figure 3.3: (a) Australian geology and (b) vertical cross sections through the 3-D shear wavespeed in the upper mantle derived from partitioned waveform inversion from the SKIPPY experiment in eastern and central Australia. Cross sections at A 16°S, B 24°S and C 30°S, and north-south sections at D 129°E, E 143°E and F 151°E, After van der Hilst et al., 1998.

of Neogene volcanos, particularly strongly for seismic structure between 140 and 200 km of depth. This suggests that at least some of the low wave speeds have a thermal origin. Locally, pronounced positive wavespeed anomalies are detected to depths exceeding 200 km, as, for instance, beneath the Paleozoic basement of the New England foldbelt.

Farther to the west, beneath the Lachlan and Adelaide foldbelts, the seismic wave speeds in the upper mantle are significantly higher. The pronounced transition from the low wave speeds in the mantle beneath easternmost Australian to the moderately high wave speeds in the mantle farther to the west is relatively sharp and is well resolved by the data used.

A recent study by Debayle and Kennett [2000] shows a good general agreement with the previous results of Zielhuis and van der Hilst [1996] and van der Hilst et al. [1998]. The lateral variations in *SV* velocity corrected for azimuthal anisotropy are represented at 6 different depths, from 100 to 350 km in fig 3.2. Fig 3.2 was plotted based on the 3-D model developed by Debayle and Kennett [2000]. By comparing figures 3.2 and 3.1, a clear correlation cab be seen between seismic heterogeneities and surface tectonics in the uppermost 200 km of the mantle. Fig 3.2 suggests there is clear contrast in seismic wave speed between the eastern Phanerozoic margin of the continent and the central and western Precambrian cratons. At 100 km depth (fig. 3.2a), three regions with high velocities can be recognised within the Precambrian cratons [Debayle and Kennett, 2000]. In Western Australia, high seismic velocities are found beneath the Archaean Pilbara and Yilgarn cratons. In South Australia, the Archaean Gawler craton is associated with a positive wavespeed anomaly extending to the North-West beneath the Musgrave block. This structure vanishes to the north where the North-Australian craton extends from the Kimberley block in Western Australia to the east of Mt Isa. The transition between the Precambrian cratons and the eastern Phanerozoic margin is complex, and south of 25° S, a circular positive anomaly appears west of the Broken Hill Block, extending toward the Lachlan Fold Belt. These features are retrieved at 150 km depth (fig. 3.2b) but with a smoother pattern of heterogeneities. In South Australia, the amplitude of the high velocity anomaly beneath the Gawler block is slightly attenuated, but the Lachlan fold belt, the Musgrave block, the Mt Isa block and the Western Archaean cratons remain the four centres of high velocities anomalies [Debayle and Kennett, 2000].

At a depth of 200 km (fig. 3.2c), the magnitude of contrasts in seismic velocity decreases [Debayle and Kennett, 2000]. High velocities remains in northern Australia and around the four centres of high velocities observed at 150 km depth. At 250 km and 300 km (fig. 3.2d & e) depth, a broad region of low velocities is present in central Australia, west of 135° E. The high velocities beneath the western Yilgarn and Pilbara cratons are not well constrained of Debayle's model because of poor raypath coverage and may as well result from horizontal smearing along the dominant paths. On the eastern margin of the continent, where the path coverage is more dense, the New England Fold belt displays high seismic wave speed below 200 km depth, in agreement with Zielhuis and van der Hilst [1996]. However, at shallower

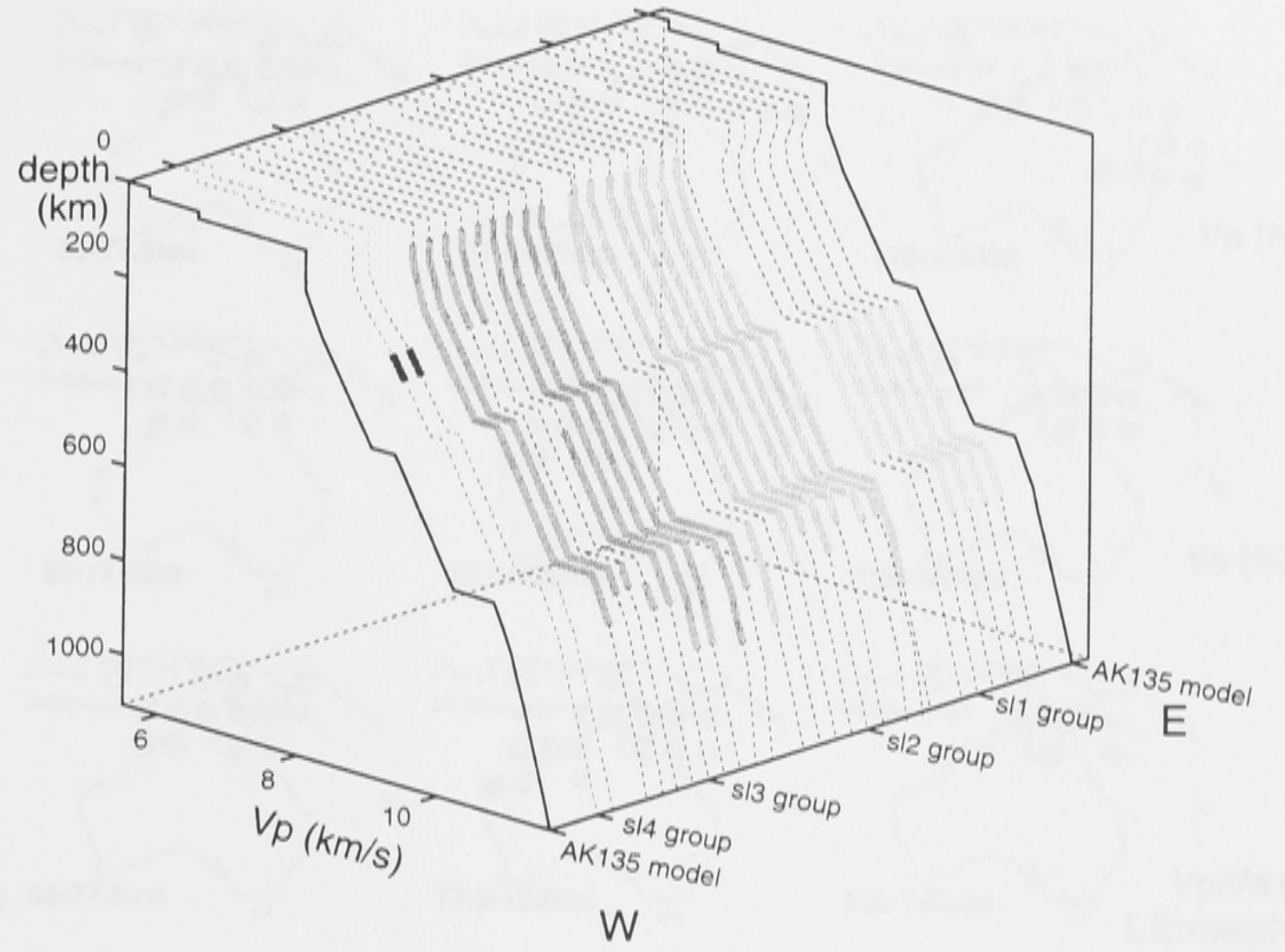

Figure 3.4: *P* (top) and *S* (bottom) wavespeed models for the azimuthal corridors. 15 different velocity models are determined from 26 sets of stacked data. The models associated with each group of azimuthal corridors are shown in the same grey tone. The segments in tone show those portions of the 1-D models which are well constrained by the available data; the remainder are indicated by dashed lines. The groups are ordered from west (sl4) to east (sl1) and within each group by azimuth progressing towards the east. Them *ak135* reference model is displayed for comparison. After Kaiho and Kennett [2000].

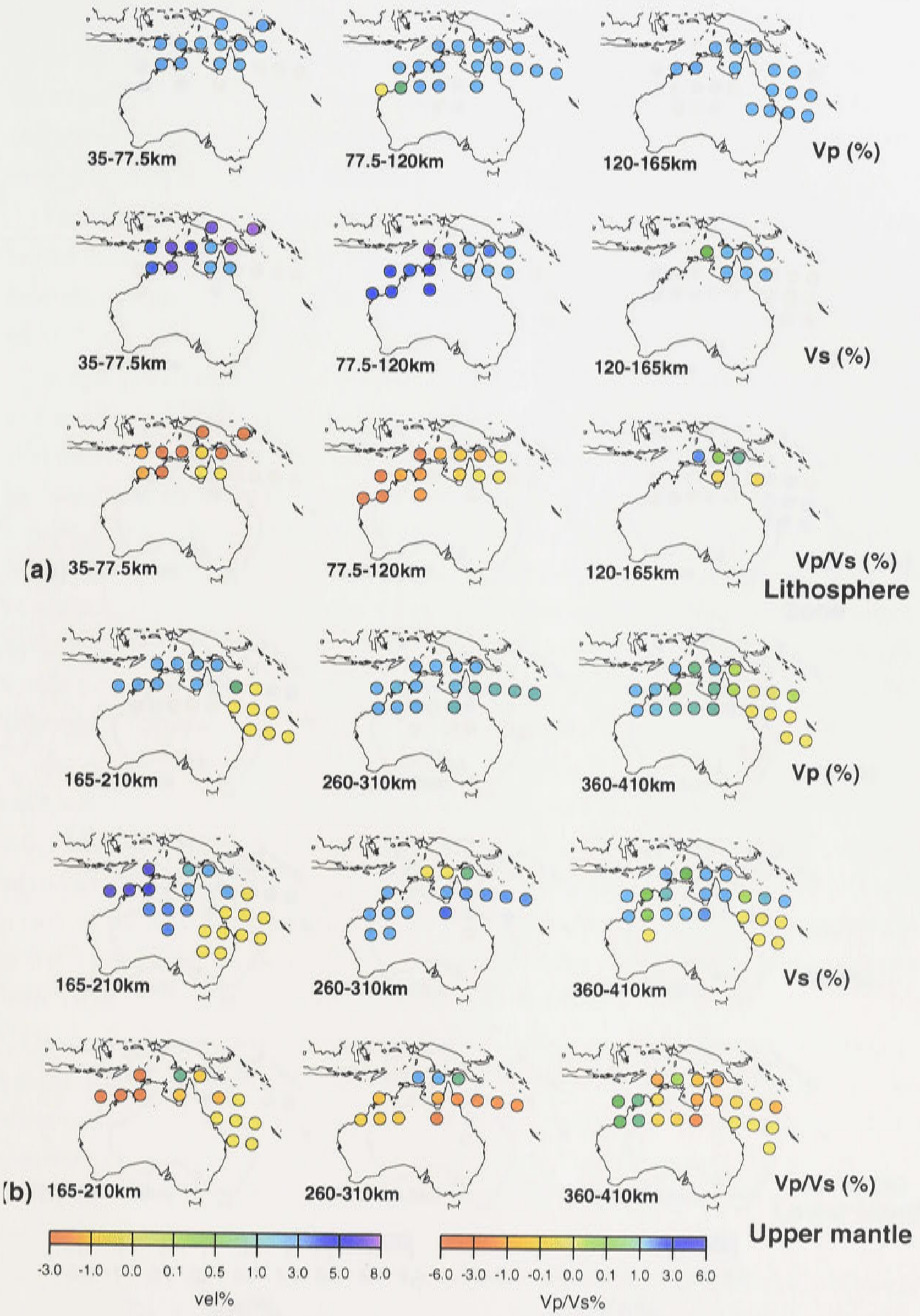

Figure 3.5: 3-D wavespeed variations constructed from the composition of the 1-D models for the different azimuthal corridors in the depth range down to 410 km. Only cells for which sampling is present are displayed, in each panel the P and S wavespeed distribution and Vp/Vs ratio are shown for each depth interval. (a) uppermost mantle down to 165 km. (b) upper mantle from 165-410 km. After Kaiho and Kennett [2000].

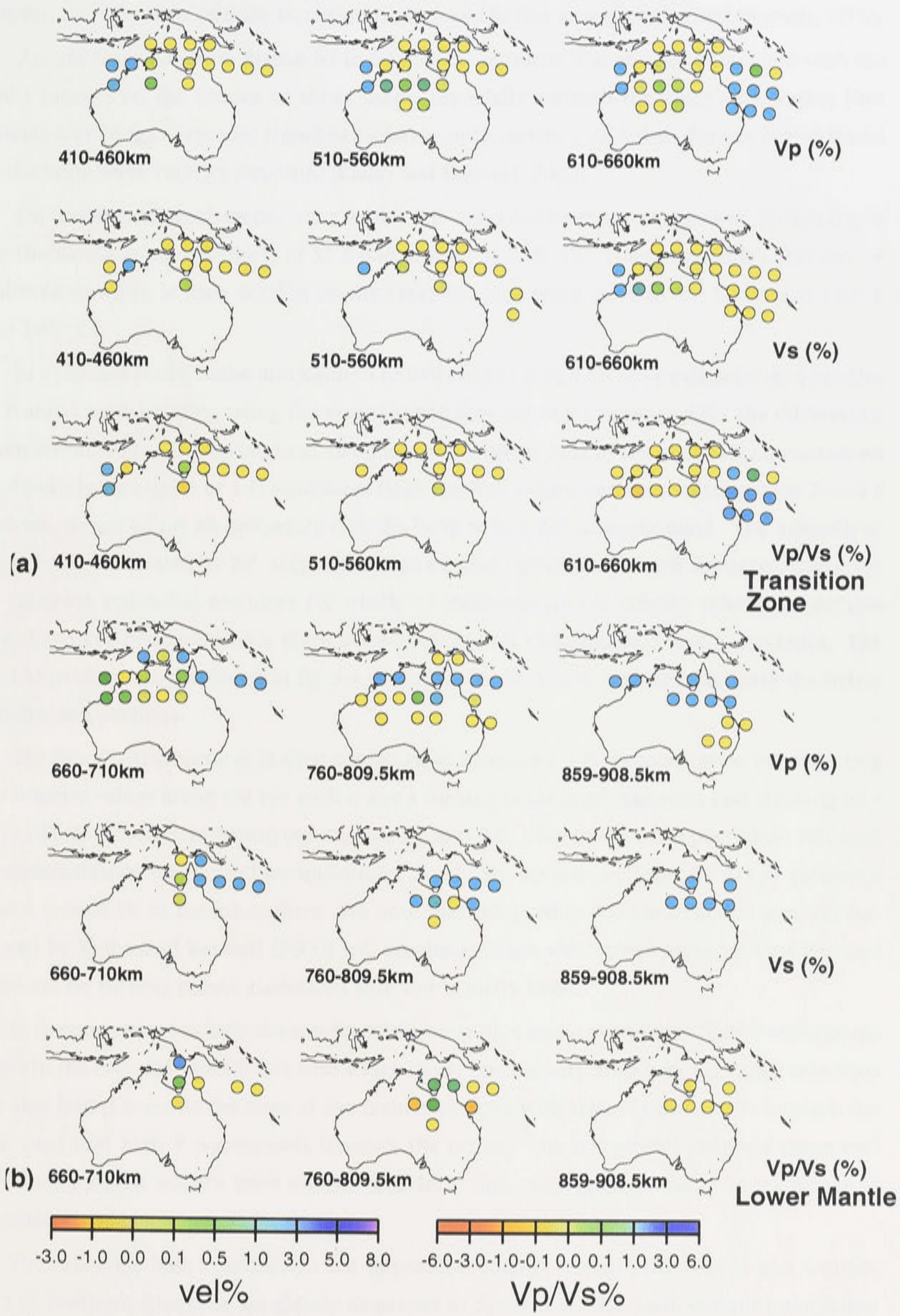

Figure 3.6: 3-D wavespeed variations constructed from the composition of the 1-D models for the different azimuthal corridors in the depth range below 410 km. Only cells for which sampling is present are displayed, in each panel the P and S wavespeed distribution and Vp/Vs ratio are shown for each depth interval. (a) transition zone (410-660 km). (b) lower mantle (660-900 km). After Kaiho and Kennett [2000].

depths, no clear high velocity signature is retrieved in this area [Debayle and Kennett, 2000].

An impressive feature displayed in fig 3.2, is the positive anomalies associated with the slabs located on the border of those maps, especially beneath the Philippine, Papua New Guinea and Tonga Kermadec trenches [Debayle and Kennett, 2000]. This feature is also found in the body wave velocity structure [Kaiho and Kennett, 2000].

On the vertical cross sections (fig 3.3(b)), the slabs can be followed down to 500 km depth for the Banda arc at a latitude of 5° S and around 128° E. The Tonga-Kermadec slab can be followed down to at least 400 km on the cross sections from 20° S to 35° S between 170° E and 180° E.

In a parallel study, Kaiho and Kennett [2000] constructed a set of one-dimensional profiles in *P* and *S* wave velocity, using the same SKIPPY data set that I have used for the differential attenuation study. The variation in structure in the upper part of the mantle is characterised by determining a suite of 1-D structures from stacked record sections utilising clear *P* and *S* arrivals, prepared for all propagation paths lying with a 20° azimuth band. The azimuth of these bands is rotated by 20° steps with four parallel corridors for each azimuth. This gives 26 separate azimuthal corridors for which 15 independent 1-D seismic velocity structures have been constructed, which show significant spatial variation in *P* and *S* structure. The 15 1-D profiles are displayed in fig 3.4 in which the thick line segments indicate the better constrained portions.

The set of 1-D structures is then combined to produce a 3-D representation by projecting the velocity values along the ray path using a turning point approximation and stacking into 3-D cells (5° by 50 km in depth) (see figures 3.5 and 3.6. Even though this procedure will tend to underestimate wavespeed perturbations, *S* velocity deviations from the *ak135* reference model exceed 6% in the lithosphere. We note that the pseudo 3-D construction method employed by Kaiho and Kennett [2000] will emphasise high wavespeed perturbations because there are no turning points associated with low velocity zones.

In the uppermost mantle the results display complex features and very high *S* wavespeeds beneath the Precambrian shields with a significant low velocity zone beneath. High velocities are also found towards the base of the transition zone with high *S* wavespeeds beneath the continent and high *P* wavespeeds beneath the ocean. The wavespeed patterns agree well with independent surface wave studies and delay time tomography studies in the zones of common coverage.

The relatively high velocities in the uppermost mantle beneath the central and western part of northern Australia are clearly displayed in figure 3.5. The small complex anomalies suggested by various 1-D models are suppressed to some extent in building the 3-D representation. In the east we note that *S* wavespeed drops back to close to the reference value for the depth range 120-165 km. In the next depth zone (fig 3.5) there is a shift to low velocities in the east in both *P* and *S*. This transition in depth is similar to that seen in surface wave models

but occurs at slightly greater depth. The differences may well arise from the influence of the binning procedures. At slightly greater depth the higher wavespeeds appear in the east, and in the west the velocities remain slightly higher than those for the *ak135* reference model. The depth interval 360-410 km displays a relatively complex pattern of variation across the continent particularly for V_p/V_s.

Structure in the transition zone and the upper part of the lower mantle is displayed in fig 3.6. Because more stations in southern Australia were used the coverage extends further to the south. Towards the base of the transition zone there is a prominent high velocity feature in P extending eastwards beneath the Tasman Sea which has the effect of raising the V_p/V_s ratio. In the lower mantle (fig 3.6) the trend is for higher wavespeeds in northeast Australia with lower velocities further south. The pattern appears to be common to both P and S and extends well into the lower mantle.

3.3 Discussion

In this chapter, I have reviewed the recent progress of the studies of the velocity structure beneath the Australian region. The velocity models are obtained by using various techniques based on different types of data, such as surface waveform and travel time residuals. The studies have also been made by various authors, but generally good agreement was achieved between the results using different approaches.

Part II

Spectral Theory and Numerical Simulation of δt^*_{sp}

Chapter 4

Numerical Simulation of Seismic Wavefield, Travel-time and t^*

4.1 Introduction

The target of this study is to construct the 3-D attenuation structure in the upper mantle beneath the Australian continent. The upper mantle has a relatively complex structure. Beneath continental areas the lithosphere commonly extends to 100 km and reaches 200 km in some cratonic areas. Beneath the lithosphere there is commonly a slight drop in seismic wave speeds to produce a 'low velocity zone' which was first revealed in surface wave dispersion studies [see e.g. Kennett, 1998]. The seismic velocities increase quite rapidly with depth below 250 km and near 410 km and 660 km there are noticeable jumps in seismic wavespeed, which are believed to be quite rapid (< 10 km in thickness) with details not readily resolved with seismic techniques.

For providing a background to understand and interpret the differential attenuation (δt^*_{sp}) estimation from SKIPPY data (see section 6.2). I need to understand the seismic wave field in regional scale up to 50°. For this purpose, I simulated the raypath distribution, travel-time curve, slowness variation and t^*.

To understand the complexity of ray presentation of regional propagation of seismic wave. In this chapter, I illustrate the influence of variation in wavespeed on the seismic ray, travel-time and slowness. Then I simulated the P and S travel-time from a global average model *ak135* which has been designed to provide a good representation of travel times of P and S for continental paths. I also used some representative regional models *sk14* and *pkq*.

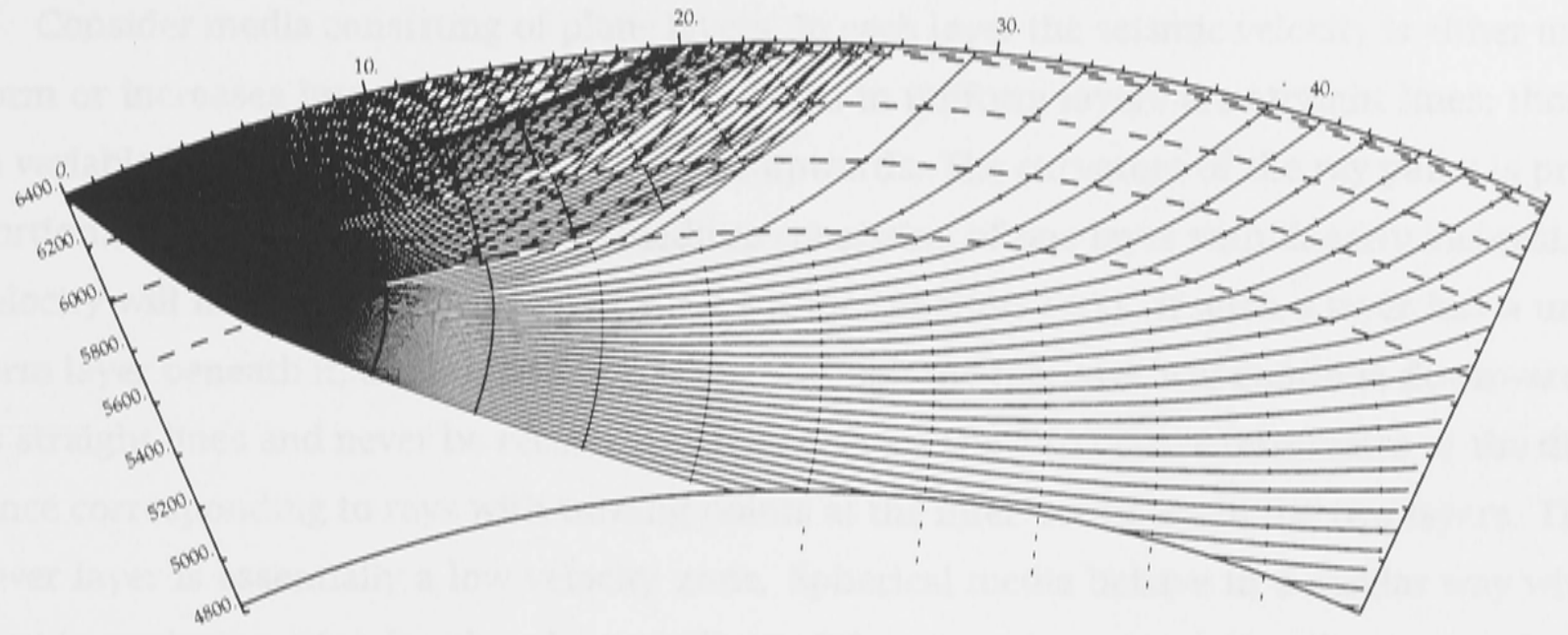

Figure 4.1: Rays and wavefronts for *S* waves in the mantle for the *ak135* model, the dashed lines mark the depths of 210 km, 410 km, and 660 km.

4.2 Ray Presentation of Regional Propagation

The presence of the major discontinuities in seismic wavespeed near 410 and 660 km depth has a major effect on the nature of the seismic wavefield at regional distances. The presence of the increase in velocity associated with each discontinuity has the effect of introducing triplications into the travel-time curves so that the arrivals at a single distance will contain both reflection from the discontinuity and refraction from below the interface. The situation is compounded by overlapping the triplication induced by the two discontinuities so that between 15° and 27° the pattern of expected arrivals become rather complex.

The raypath for reflected and refracted *S* waves in the *ak135* model is presented in figure 4.1 with wavefronts marked every 60 s up to a distance of 48°. The influence of the reflections from the discontinuities can be seen in the 'hooked' wavefronts, and the overlapping ray paths. The propagation characteristics are somewhat simpler for waves turned back by the velocity gradients in the lower mantle. I note in the true scale diagram in the figure 4.1 that the angles of propagation are relatively shallow so that the body waves will be sensitive to any horizontal variation in wavespeeds they encounter with largest influence occurring near the turning point.

The complications in the ray patterns are increased for the multiple reflections of the *S* rayfield. The surface reflections give rise to caustics associated with the main discontinuities.

4.3 Numerical Simulation of Travel-time

The common features of the travel-time - distance curve depend on the variation of seismic velocity with depth. The ray theory, the method to calculate travel-time and the properties of travel time through the influence of seismic wavefield variation on raypath is discussed in the appendix A.

Consider media consisting of plane layers. In each layer the seismic velocity is either uniform or increases linearly with depth. Ray paths in uniform layers are straight lines; those in variable layers are arcs of circles, concave upwards. The curvature of the ray paths is proportional to the velocity gradient. A medium consisting of one layer with linearly increasing velocity will have a monotonically increasing time function $T(\Delta)$. If such a layer has a uniform layer beneath it, then ray paths passing through the top layer will continue downwards as straight lines and never be recorded at the surface. The $T(\Delta)$ curve terminates at the distance corresponding to rays with turning points at the interface between the two layers. The lower layer is essentially a low velocity zone. Spherical media behave in a similar way with $V(r)/r$ replacing $v(z)$ for the plane medium. When a uniform layer lies above a medium with increased velocity multipathing can occur: there are two or more quite different arrivals which makes the interpretation difficult. For a two layer model, rays which have large take-off angles, do not penetrate the lower medium to any great depth and travel larger horizontal distances. Rays with small take-off angles, penetrate to a great depth in the lower medium and also travel larger horizontal distance. Rays with intermediate take-off angles travel shorter horizontal distances. In this case, the time-distance function is not a single valued function of distance. The two branches correspond to different sets of paths.

For a three layer model, if the velocity within each layer increases linearly with depth, but in the middle layer it increases at a more rapid rate than in the other two, this will produce a triplication in the travel-time distance curve. The branch, which corresponds to the rays traveling only in the top layer, increases monotonically with steep slope. Then the branch, which corresponds to the rays that travel in the middle layer, go down back. The lowest point of this branch corresponds to the rays that bottoms at the top of lowest layer. The branch, which corresponds to the rays traveling in the low layer, increase monotonically with distance in a less steep slope.

4.3.1 Velocity and Q Models for Calculating Travel-time and t^*

Three velocity models were used in this research to calculate travel time and t^*; they are *ak135*, *sk14* and *pkq*. The *ak135* is a global reference model; *sk14* is a modified model for regional use; and *pkq* is derived from earlier Australian studies. Those models are depicted graphically in figure 4.2.

The common features of these models is that they are all spherically symmetric models and there are P and S wave velocity discontinuities or a change in velocity gradient at depths of 35 km, 210 km, 410 km, and 660 km, which separate the internal Earth into the lithosphere (0-210km, crust (0-35km)), the asthenosphere zone (210-410km), the transition zone (410-660 km) and lower mantle (> 660 km).

The reference model *ak135* illustrated in figure 4.2 has been designed to provide a good

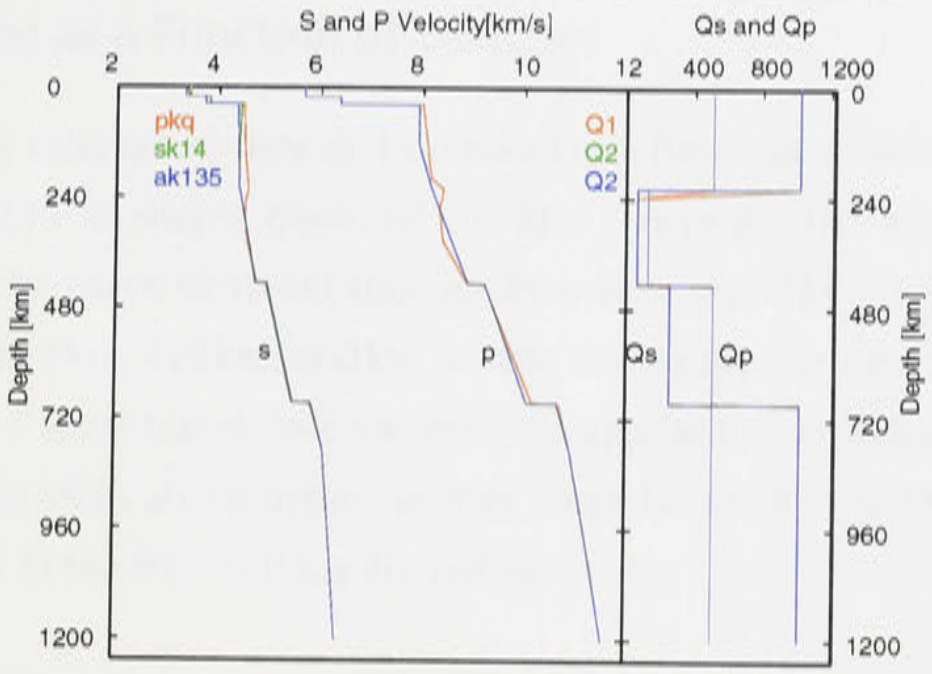

Figure 4.2: The velocity and attenuation models: *ak135* , *sk14* and *pkq* .

representation of the travel times of P and S for continental paths. By design there is no discontinuity at 210km, although there is a change in velocity gradient. Also, in order to achieve arrivals at all distance for arbitrary depth, no low velocity zone has been included. Whilst it is clear that a reduction in wavespeed is a common feature to most mantle velocity models, the geographic variability is considerable and so it is simpler to adopt a straightforward model.

The difference in velocity between *ak135*, *sk14* and *pkq* is generally quite small except in the shallow layers (less than 410km depth). The P wave velocity for *ak135* and *sk14* is almost identical, but there is a low S wave velocity zone between 35 km and 210 km for *sk14*. The *pkq* model seems more complex because from 35 km to 210 km, both P and S wave velocity in model *pkq* are larger than their values in model *ak135* and *sk14*, and there is a low velocity zone for both P and S below 210 km and above 320 km in model *pkq*.

The attenuation model ($Q2$) used with *ak135* and *sk14* are identical. They are listed in table 4.1 and depicted in figure 4.2.

Table 4.1: Attenuation model for *ak135* and *sk14*

Layer description	*Depth (km)*	Q_s	Q_p
Lithosphere	0-210	1000	2000
Upper mantle	210-410	125	250
Transition zone	410-660	500	1000
Lower mantle	660-2,890	1000	2000

It is assumed $Q_p = 2Q_s$.

The attenuation model ($Q1$) associated with *pkq* , which was developed by Gudmundsson et al. [1994] for northwestern Australia region, is slightly different from $Q2$ as illustrated in figure 4.2.

The attenuation model ($Q1$) for *pkq* is illustrated in table 4.2.

4.3.2 Travel-time as a Function of Distance

Figure 4.3 displays the travel-time and slowness as a function of distance calculated from reference model *ak135* at source depth of 100 km. There are three triplications for each phase produced in the curve of travel time against distance. The travel-time branches are associated with the 210 km, 410 km, 660 km mantle discontinuities and layers between those discontinuities. The *P* wave travel-time triplications appear in the distance range 10° to 30°, and *S* wave travel time triplications in the distance range 12° to 25°. But the different branches for the depth phases in the triplications are not distinct.

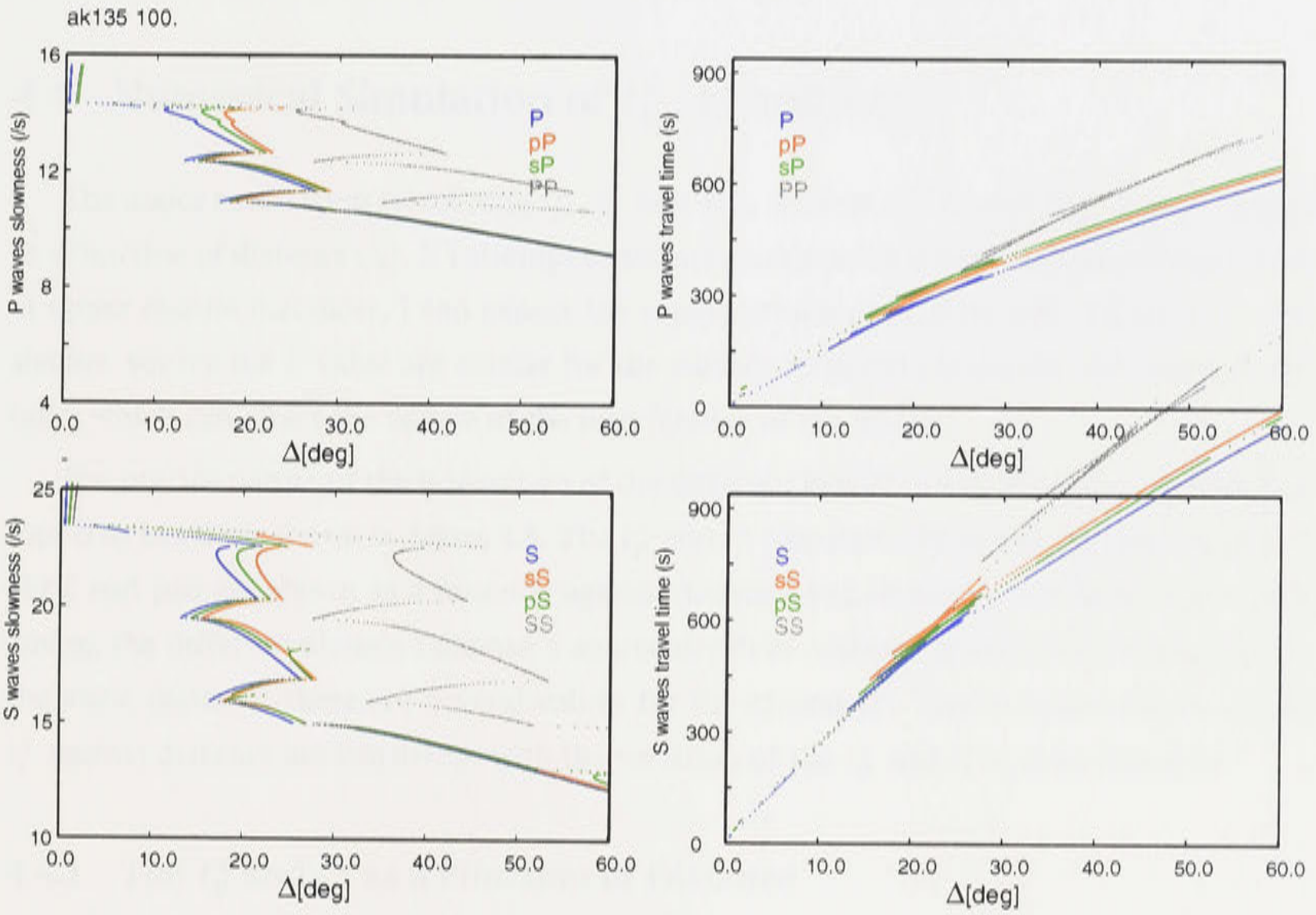

Figure 4.3: The *P* and *S* wave travel-time and slowness calculated from velocity model *ak135* as a function of distance, depth of source 100 km

Table 4.2: Attenuation model of *ak135* and *sk14*

Layer description	*Depth (km)*	Q_s	Q_p
Lithosphere	0-210	1400	2800
Upper mantle	227-407	100	200
Transition zone	412-657	600	1200
Lower mantle	662-2,890	1300	2600

It is assumed $Q_p = 2Q_s$.

4.3.3 Slowness as a Function of Distance

The diagrams in figure 4.3 of slowness against distance reveal the distribution of slowness along the various ray path. The slowness is single valued when the distance is less than 10°. From 10° to 30°, for the same distance, there are five slowness values for each phase. The multi-value of slowness reveals the spatial distribution of slowness in vertical and lateral variation. The branches of slowness are associated with the 210 km, 410 km and 660 km velocity discontinuities and the lithosphere (0-210 km), the asthenosphere zone (210-410 km), the transition zone (410-660 km) and the lower mantle (>660 km).

4.4 Numerical Simulation of t_p^* , t_s^* and δt_{sp}^*

The major result from calculating t_p^* , t_s^* and δt_{sp}^* are that t_p^* , t_s^* and δt_{sp}^* is multi-valued as a function of distance (Δ). If I attempt to extract an attenuation measurement from records at upper mantle distances, I can expect the superposition of arrivals with different t^*. For shallow source the t^*value are similar for the surface reflected phases but displaced in distance which can affect the nature of the interference of the phases.

The precise nature of the interaction of the different branches will depend on the velocity model as has been shown in figure 4.4. The t_p^* and t_s^* calculated from velocity models *ak135*, *sk14*, and *pkq* are shown as a function against distance and slowness. For better separation among the different phases, I choose a source depth at 100 km. From 10 to 40 degrees, for the same distance, there are several values for the t_p^* and t_s^*. The branches of the t_p^* and t_s^* against distance are consistent with the variation of the t_p^* and t_s^* against slowness.

4.4.1 The t_p^* and t_s^* as a Function of Distance

The multi-valued nature of t_p^* and t_s^* shown in figure 4.4 come from the mantle discontinuities and the high attenuation zones, which also cause the multiple-values of travel-time and slowness at same distance. The branches of the multiple t_p^* and t_s^* occur at the same distance as the branches of the multi-value travel-time. But the values of the t_p^* and t_s^* were mainly controlled by the Q. When the attenuation model was modified, so that Q_p and Q_s took same values of 500 and 1000 respectively for total depth (one Q layer). The different branches of the t_p^* and t_s^* could not be separated. When the model was changed to four Q layers (210, 410, 660 and 2900 km), the four t^*branches are distinct. For the same phase, the different branches of the t_p^* and t_s^* correspond to the specific paths which travel through different layers and refract or reflect from the different mantle discontinuities.

The t_p^* and t_s^* branches are associated with the 210 km, 410 km and 660 km mantle discontinuities and the lithosphere (0-210 km), the asthenosphere zone (210-410 km) which is highly attenuative, the transition zone (410-660 km) and the lower mantle (>660 km). There

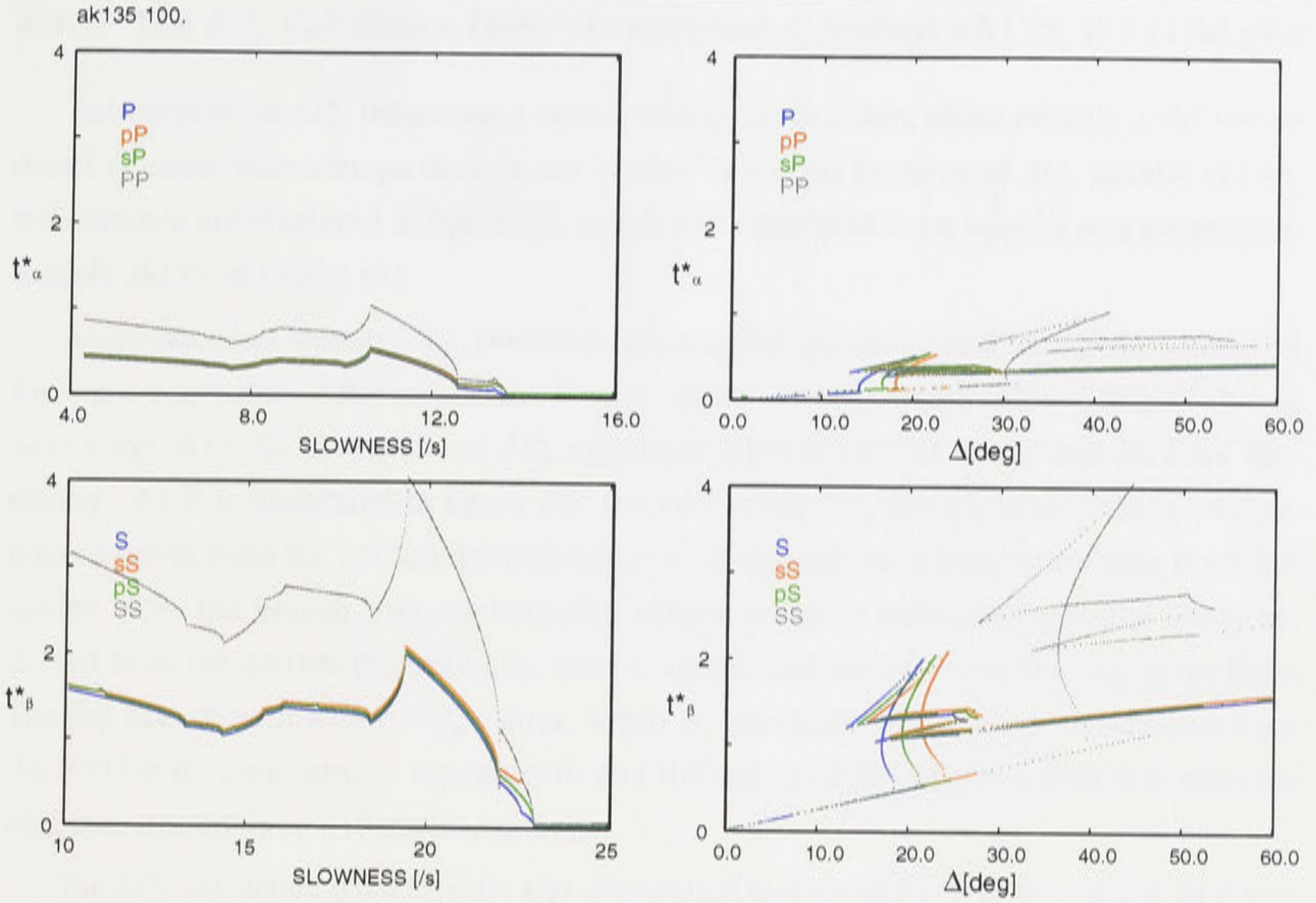

Figure 4.4: The t_p^* and t_s^* calculated from velocity model *ak135* as a function of slowness and distance

are three t_p^* and t_s^* branches that are very sensitive to the Q values at depths of 210 km, 410 km, and 660 km. A test was done to confirm the relationship between the t_p^* and t_s^* branches and the 210 km, 410 km, and 660 km mantle discontinuities.

The very steep t^*branch is associated with refracted waves from below the 210 km discontinuity, i.e. in the asthenosphere rather than the lithosphere. The flat branch with medium t^*values, which is associated with the waves reflected from the 410 km discontinuity, seems smooth and the values of the t_p^* and t_s^* are medium. The flat branch with lowest t^*values, which is associated with the waves reflected from 660 km discontinuity, is also smooth and the values of the t_p^* and t_s^* are a little less than the t_p^* and t_s^* corresponding to 410 km discontinuity.

4.4.2 The t_p^* and t_s^* as a Function of Slowness

The t_p^* and t_s^* vary monotonically with slowness, but all the curves appear in the several sections with different slopes as shown in figure 4.4. The t_p^* of *PP* and t_s^* of *SS* are clearly distinct from other three graphs. However, the t_p^* of *P*, *pP* and *sP* and the t_s^* of *S*, *sS* and *pS* are not separated. For the velocity model *ak135*, both the t_p^* and t_s^* slowness curves slight fluctuate at low slowness. There are dramatic variation in t_p^* and t_s^* in the medium range of slowness. The t_p^* and t_s^* drop to 0 at higher slowness,

4.4.3 The δt_{sp}^* Calculated from Velocity and Q Models *ak135*, *sk14* and *pkq*

To interpret the δt_{sp}^* behaviour, I choose source depth 25 km, which roughly is the source depth of most Warramunga data in our study. The main features of δt_{sp}^* against epicentral distance are displayed in figure 4.5, which was calculated from velocity and attenuation models *ak135*, *sk14* and *pkq*.

As described in section 4.3.1, the attenuation model for *ak135* and *sk14* is the same, and there are only subtle difference in the *S* wave velocities at the depth below 200 km between *ak135* and *sk14*. So the results of δt_{sp}^* calculated from models of *ak135* and *sk14* are very similar. As it is illustrated in figure 4.5, the very steep δt_{sp}^* branch is associated with refracted waves from the 210 km discontinuity, i.e. in the asthenosphere rather than the lithosphere. The flat branch with medium δt_{sp}^* values, which is associated with the waves reflected from the 410 km discontinuity, seems smooth and the values of the δt_{sp}^* is medium. The flat branch with lowest δt_{sp}^* values, which is associated with the waves reflected from the 660 km discontinuity, is also smooth and the values of the δt_{sp}^* is a little less than the δt_{sp}^* corresponding to 410 km discontinuity.

The δt_{sp}^* calculated from velocity and attenuation models *ak135* (curve A) and *sk14* (curve B) are almost identical, except the section near the largest values of the δt_{sp}^* in the range of distance between 14° -17°. The slope of this section in curve A is a little less than the slope of the curve B, and the highest value of δt_{sp}^* in curve A is less than the highest value of δt_{sp}^* in curve B. This is due to the result of the low velocity zone of the *S* wave in velocity model *sk14* in the depth range of 35 km - 210 km.

In principle, I can find that single branch in low δt_{sp}^* value slightly increase with increase of frequency in low frequency, multi-value branches, which steep increase then decrease in δt_{sp}^* with increase of frequency in the medium frequency band and multi-value branches in medium δt_{sp}^* value in high frequency.

The differential attenuation (δt_{sp}^*) against epicentral distance calculated from the velocity and attenuation model *pkq* (curve C) appears more complex due to the low velocity zone below the 210 km discontinuity. The differences displayed by the curve C in figure 4.5 from curve A and B are: (1) the consistently low value 0.6 in δt_{sp}^* out to distance of 14°; (2) followed by a discontinued branch jumping to very high value in δt_{sp}^* from 5.4 to 6.8 between distance of 10° and 17° ; (3) the sharp decreasing branch in curve A and B around 20° broke into two branches in curve C which are beyond 20°. The first one in those two branches sharply increase then followed by a branch gradually decrease in δt_{sp}^* with distance.

In conclusion, the δt_{sp}^* is in low value in short distance. Due to the existence of the low velocity zone and discontinuities in velocity in 210 km and 410 km depth, in medium distance from 14° to 22°, the δt_{sp}^* are multi-valued for certain distance. The δt_{sp}^* are very complex in the distance range from 14° to 22°. The δt_{sp}^* are also are multi-value in the distance beyond

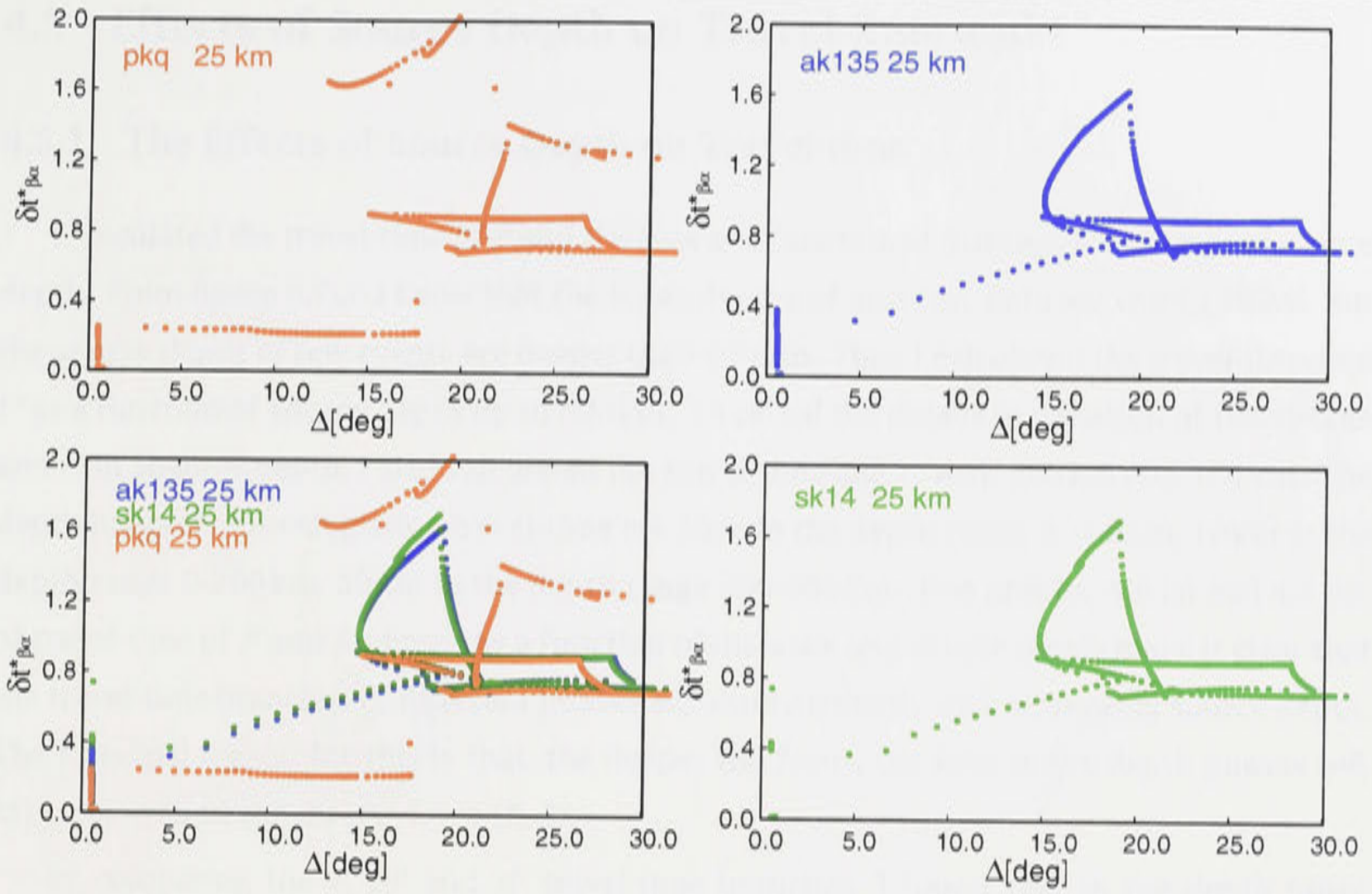

Figure 4.5: The δt_{sp}^* calculated from velocity and attenuation models *ak135*, *sk14*, and *pkq*.

the distance 22°. But they are less than complex than the δt_{sp}^* in the distance range from 14° to 22°.

4.4.4 δt_{sp}^* Behaviour Interpretation

The differential attenuation $\delta t_{sp}^* = t_s^* - t_p^*$ was calculated from the velocity and attenuation models *ak135*, *sk14*, *pkq*. The results vary depending on the velocity and attenuation models used. From the test was designed to confirm the relationship between the δt_{sp}^* branches and the 210 km, 410 km, and 660 km mantle discontinuities, I know the first two branches, which go up then down, are associated with the 210 km discontinuity and the high attenuation zone below 210 km. The flat branch with a medium value of δt_{sp}^* is associated with the 410 km discontinuity, and the flat branch with less δt_{sp}^* value is associated with the 660 km discontinuity.

When the results of theoretical δt_{sp}^* values are compared with the δt_{sp}^* measured from Warramunga data, it will be observed that the δt_{sp}^* calculated from *pkq* can interpret the behaviour of δt_{sp}^* measured from Warramunga data. The δt_{sp}^* calculated from *pkq* roughly shows the behaviour that relatively low constant value branch at short distance, steep increasing branch at the medium distance and gradual decreasing branch at larger distance. If I average those branches, the overall behaviour of δt_{sp}^* from *pkq* will be approximately agreed with the behaviour of the δt_{sp}^* measured from Warramunga data.

4.5 Effects of Source Depth on Travel-time and t^*

4.5.1 The Effects of Source Depth on Travel-time

I calculated the travel-time of P and S waves as a function of distance for a range of source depth. From figure 6.2(a) I know that the focus depths of most my data are within 50km. But the source depth of few events are deeper than 600km. Thus I calculated the travel-time and t^*as a function of source depth up to 600km. To reveal the details in variation of travel-time and t^*in shallow depth, I also calculated the travel-time and $t^*$with 200km and 100km. The depth intervals for calculating travel-time are 5km in the depth range 0-100km, 10km in the depth range 0-200km, 50km in the depth range 200-600km. Two graphs, 4.6 (a) and 4.6 (b), of travel-time of P and S phases as a function of distance and source depth make it clear that the travel-time branches of different phases separate distinctly with increasing source depth. The principal reason for this is that, the deeper the focus, the later is the depth phases (pP, sS) compared to the direct waves (P, S).

By comparing the P, pP and sP travel-time branches, I found that in the depth range between 40 km to 130 km, the first arrival of P wave triplication moves to shorter distance with increasing source depth. When focus is deeper than 130km, the outline of the first arrival of the P wave triplication basically parallel to the axis of source depth. Comparing with P and pP, the value of sP travel time become largest with increasing source depth, because the slow path of the S part, but no change on the outline of the first arrival of sP wave triplication. With increasing source depth, pP travel-time become larger than P, but smaller than sP, and the outline of the first arrive of pP wave triplication gradually moves to larger distance.

By comparing the S, pS and sS travel-time branches, I found that the first arrival of S wave triplication gradually moves to shorter distance with increasing source depth. The value of pS travel-time become larger than S, but smaller than sS, because the fast path of the p part, but no change on the of the first arrive of pS wave triplication. Comparing with S and pS, the sS travel-time becomes larger with increasing of source depth, the outline of the first arrive of sS wave triplication gradually moves to greater distance.

4.5.2 The Effect of Source Depth on t_p^* and t_s^*

The velocity and attenuation models and source depth range used for calculating t_p^* and t_s^* are same as for calculating travel time. For shallow source (0-30km), the different phases, such as P, pP, sP, S, sS and pS, etc can not be separated distinctly and the values of t_p^* and t_s^* are relatively small. The different branches of t_p^* and t_s^* which come from the 210km, 410 km and 660km upper mantle discontinuities are close. But as the source depth increases, the specific phases in the P and S wave groups begin to separate gradually as well as the different branches of t_p^* and t_s^*. The above behaviour of t_p^* and t_s^* as a function of distance and source

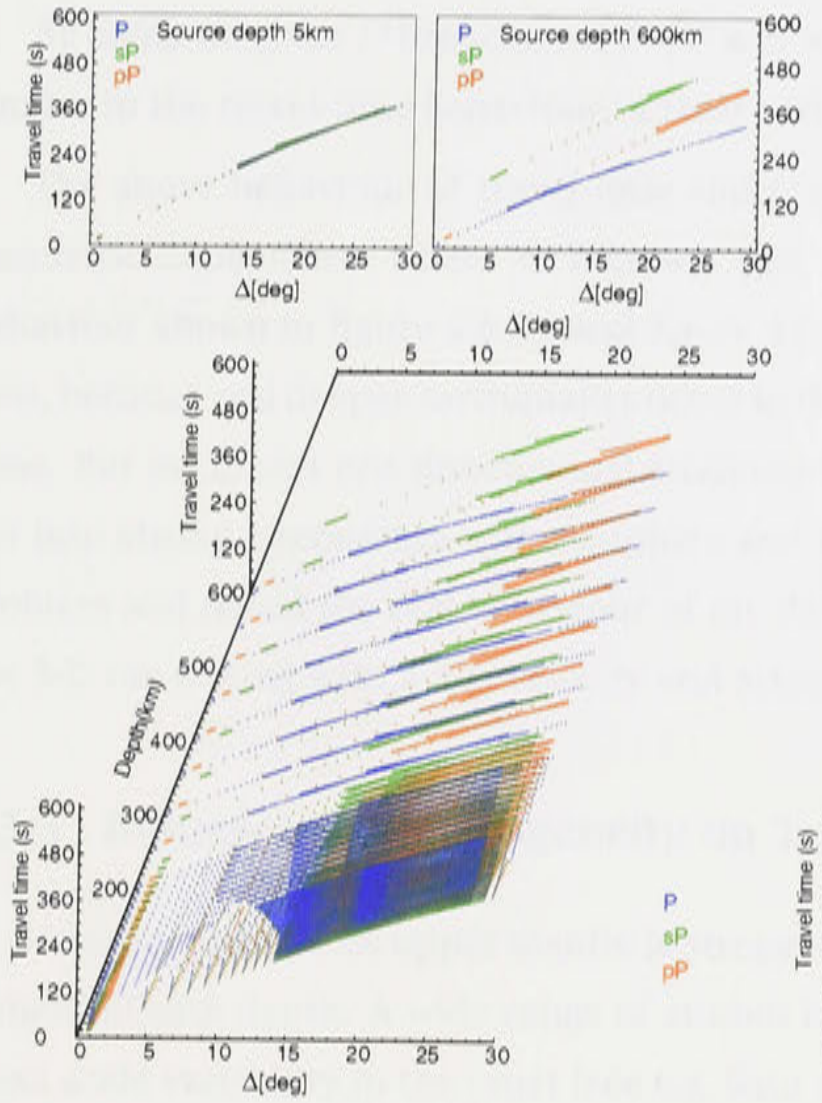

(a) P wave travel time

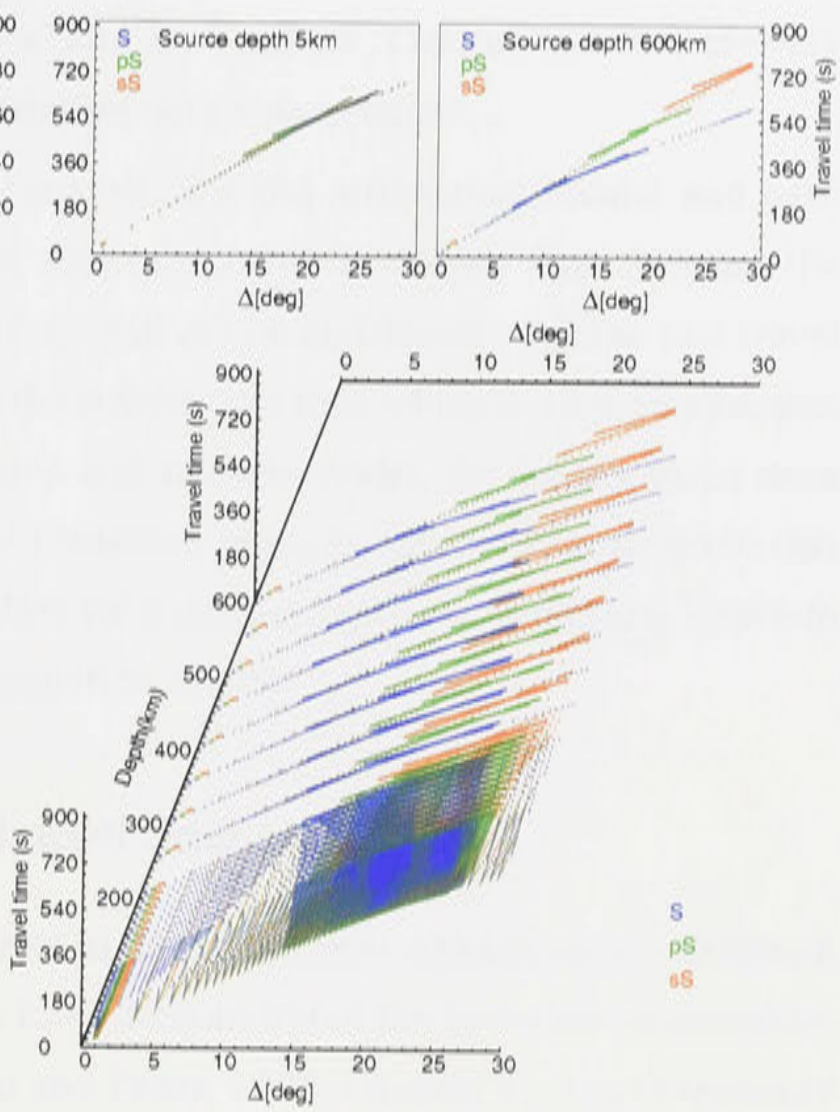

(b) S wave travel time

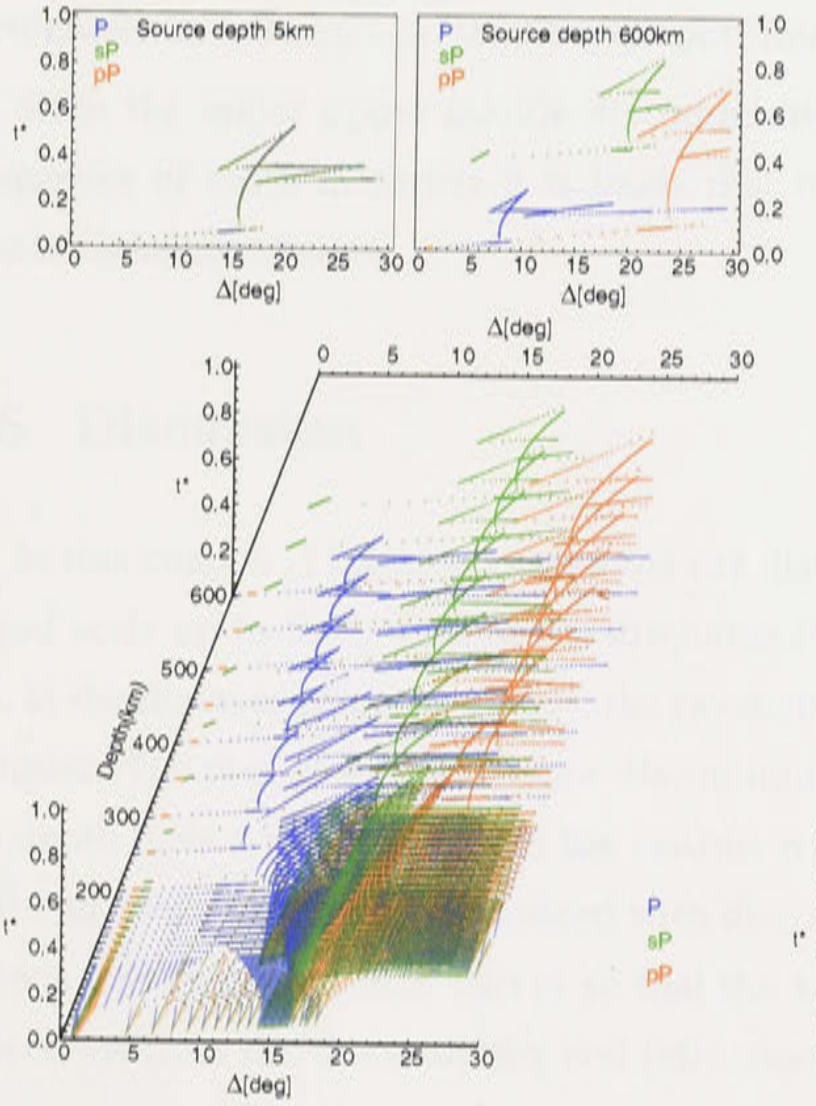

(c) P wave t^*

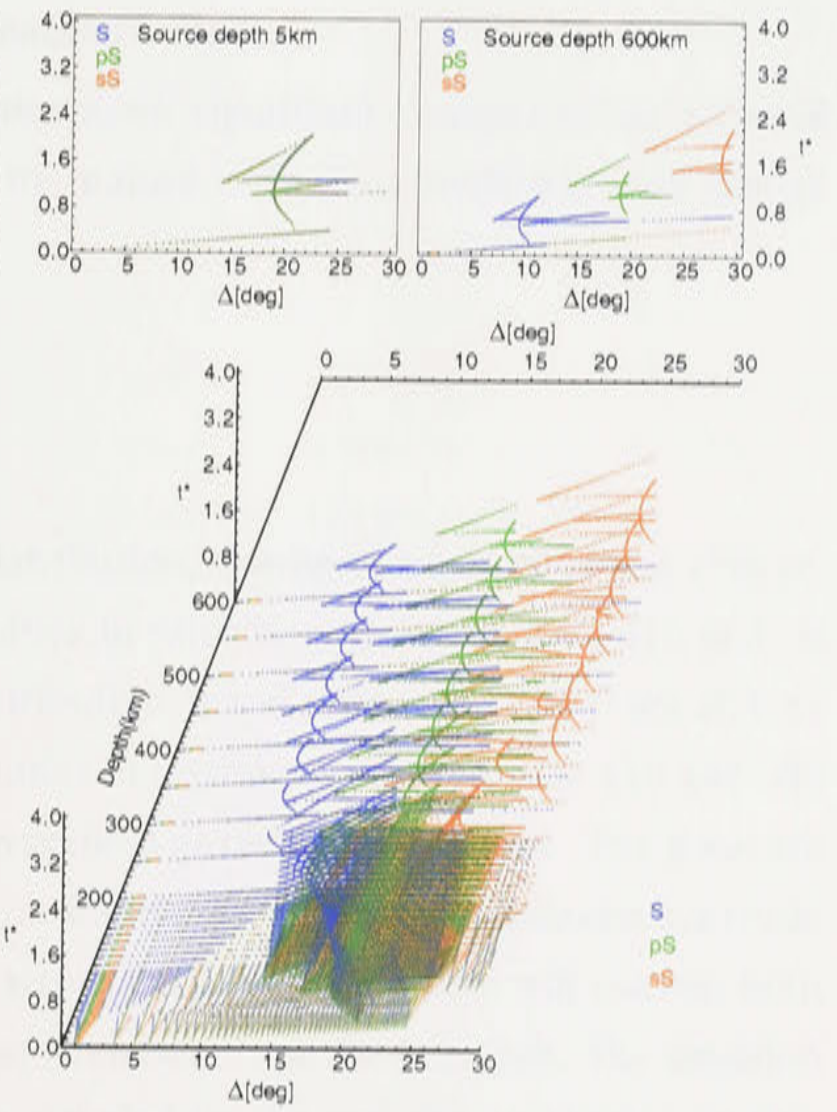

(d) S wave t^*

Figure 4.6: The P and S wave travel-time and t^* calculated from velocity model *ak135* as a function of distance and source, depth range 0-600 km.

depth is illustrated in the figures of 4.6 (c), and 4.6 (d).

By comparing the t^*branches of P, pP and sP and S, sS and pS , I found that they are very similar to the travel-time behaviour in their variation with source depth.

The above behaviour of travel-time and $t^*$are velocity and attenuation model and path geometric dependent. I have to mention that when the focus is deeper than 210 km, the behaviour shown in figure 4.6 (a) and figure 4.6 (c) will not be consistent with the real travel time, because real deeper earthquakes occur in the subduction zone which is a low attenuation zone. But in current one dimensional attenuation and velocity model, the deeper focus were put into strong attenuation asthenosphere and transition zone. In future work, to avoid this problem and reveal the real behaviour of my data with deeper depth up to 600 km, I have to use 3-D ray tracing with a 3-D velocity and attenuation model.

4.5.3 Influence of Heterogeneity on Travel-time and t^*

Heterogeneity in the upper mantle is strongest in the lithosphere and appears to diminish somewhat with depth. A wide range of studies have demonstrated the presence of pervasive small scale variability in the crust [see e.g. Sato and Feher, 1998, Chapter 1]. The complexity of lithosphere arrivals in cratonic regions also suggest the presence of heterogeneity on a variety is on a smaller scale than can be resolved by broad-scale tomographic methods, but fortunately its influence on the tomographic images is small.

Since the major upper mantle discontinuities mark significant changes in the physical properties of Earth materials it is likely that the nature of heterogeneity will also change across these boundaries.

4.6 Discussion

In this chapter, I have simulated the ray distribution, slowness, travel time and t^*in regional scale up to 50 °. Due to the discontinuities in velocity at depth of 210, 410 and 66 km, at the distance range up to 50°, the ray distribution, travel-time curve and $t^*$are all very complex. The presence of the major discontinuities in seismic wavespeed near 410 and 660 km depth have a major effect on the seismic wavefield at regional distances. The presence of the increase in velocity associated with discontinuity has the effect of introducing triplications into the travel-time curves so that the arrivals at a single distance will contain both reflections from the discontinuity and refraction from below the the interface. The situation is compounded by overlap of the triplications included by the two discontinuities so that between 15° and 27° the pattern of expected arrivals becomes rather complex.

Chapter 5

The Spectral Theory and the δt^* Measurement Techniques

5.1 Introduction

The main challenge in measuring and developing Earth models for attenuation structure is separating anelastic effects from both propagation and source effects. Spectral estimation techniques were introduced for attenuation measurement in the mid-1960s. The merit of these methods is that they can cancel the unpredictable, common, frequency-dependent factors by means of a spectral ratio and avoid geometrical effects on absolute amplitude by measuring the logarithmic frequency-derivative of the spectral ratio. However, every spectral estimation method is strictly speaking imperfect, and no fully exact method exists for determination of attenuation. All methods are more or less dependent on simplifying assumptions, which are necessary to reach numerical results. The two basic assumptions are that the normalised source spectrum is not a function of spatial coordinates and that the attenuation function can be expressed in terms of a frequency independent Q over the frequency band by

$$\exp(-\pi f \int_{Ray} dl/QV) \tag{5.1}$$

Here the intrinsic attenuation Q and body wave velocity V are functions of the radial variable $Q(r)\ V(r)$, and the integration is along the seismic ray. The logarithm of the spectral ratio of two body wave phases, i and j, will be a linear function of frequency, when instrumental and crustal effects are removed. Its slope, called differential attenuation, which can be measured by spectral analysis on the observed seismic waves, is expressed by

$$\pi(\int_j dl/Q_jV_j - \int_i dl/Q_iV_i) \tag{5.2}$$

This expression gives the difference in attenuation between the two body wave phases i and j. A plot of the differential attenuation data as a function of distance constitutes an experimental curve from which a Q depth relation can be derived [Teng, 1968].

Teng [1968] developed a method of spectral ratio measurement in the frequency domain, an approach which has been implemented and extended by a number of authors [Solomon and Töksoz, 1970; Ward and Young, 1980; Taylor et al., 1986], all using teleseismic data to measure the attenuation structure. Recently the method was modified by Evans [1993] by using the average spectrum for a particular source to calculate the spectral ratio, rather than using the spectrum of a single reference station, and combining the tomographic techniques to construct a three dimension attenuation image in volcanic regions or geothermal resource areas [Clawson et al., 1989; Evans, 1993; Sanders, 1993].

The spectral ratio techniques were grouped into three main types by Båth [1984] based on reviews of attenuation studies in the 1960s and 1970s depending on the way in which the estimation was made. (1) The frequency-ratio method [Takano, 1971]: Spectral ratio $A(f_i)/A(f_j)$ between wave i and wave j which have different frequency contents. Although the frequency-ratio method is mainly concerned with spectral slopes, the method could easily be enlarged to include spectral shapes on the whole; then, comparisons could be made between spectral shapes of a given wave at a given station. (2) The station-ratio (or Distance-ratio) method (see e.g. Teng, 1968): wave i and wave j are recorded at two stations; the benefit of the Station-ratio (or Distance-ratio) method is that it can give the Q distribution with depth and lateral heterogeneity. (3) The wave-ratio method (see e.g. Gudmundsson et al., 1994): Spectral ratio between wave i and wave j from one event recorded at the same station; the advantage is that with proper choice of waves for comparison, source and path effects are to a great extent eliminated.

In this study, I developed a method to estimate the δt^*_{sp} based on the spectral ratio between P and S. I have also investigated the effect of dispersion and attenuation dependence on frequency. Velocity and Q in equation (5.1) are both a function of frequency. But the effect of dispersion is very small (see also section 8.2.4) and the Q could also be treated as nearly frequency independent for the lower frequency band (< 1.0 Hz). In a broad frequency band up to 6 Hz, Q is a function of frequency and the frequency parameter of Q is also dependent on depth and lateral position.

5.2 Spectral theory and t^* definition

In the frequency domain, the amplitude for an isolated body wave phase $A(f)$, as a function of frequency f, can be expressed as a product of a source function $A_0(f;\theta,\phi)$, with a number of transfer functions representing different aspects of the propagation process [Teng,

1968].

$$A_i(f) = A^i_\phi(f;\theta,\phi)A^i_{INS}(f)A^i_{CR}(f)A^i_{MC}(f)A^i_{GS}(p_i,\xi_i)A^i_R(p_i,\xi_i) \tag{5.3}$$

where p stands for ray parameter, ξ represents azimuth, and i is the index for the particular observation. The various transfer functions can be characterised as:

$A_i(f)$ - recorded spectrum at distance r,

$A^i_\phi(f;\theta,\phi)$ - source spectrum,

$A^i_{INS}(f)$ - instrumental response,

$A^i_{CR}(f)$ - crustal response, including any other multipath effects,

$A^i_{MC}(f)$ - the influence of attenuation in the mantle ,

$A^i_{GS}(p_i,\xi_i)$ - geometrical spreading,

$A^i_R(p_i,\xi_i)$ - radiation pattern.

I will assume a power law relationship between Q and frequency f,

$$Q(f,r) = Q_0(r)f^{\alpha(r)}, \tag{5.4}$$

and define a frequency dependent $t^*(f)$ representing the integrated effect of attenuation along the path:

$$t^*(f) = \int_\Gamma \frac{dl}{Q(f,r)V(f,r)}. \tag{5.5}$$

In principal, when the seismic wave is attenuated, the velocity is also a function of frequency. This is so called the dispersion of velocity. I discuss this problem in sections 2.1.2 and 2.2.2 and simulate the effect of dispersion in section 8.2.4. I conclude that the dispersion is not an important factor in this study. Therefore, I ignore the dispersion in the following discussion. Based on the frequency dependent $Q(f,r)$ defined in (5.4), I can separate out the the dependence of t^* on frequency by writing

$$t^*(f) = t^*_0 f^{-\alpha(r)}, \tag{5.6}$$

where the frequency independent t^*_0 term is

$$t^*_0(f) = \int_\Gamma \frac{dl}{Q_0(r)V(r)}. \tag{5.7}$$

Based on equation 5.7 and the relation between amplitude and attenuation in equation 2.3, I could obtain the relationship between the amplitude and t^*.

$$\begin{aligned} dA &= A_0 \exp(-\frac{\pi f}{Q}\frac{dl}{\theta}) \\ &= A_0 \exp(-\pi f dt^*) \end{aligned} \tag{5.8}$$

With the dependence of Q on frequency in (5.4) and the relationship between amplitude and t^* in (5.8), the mantle transfer function $A^i_{MC}(f)$ takes the form

$$A^i_{MC}(f) = (A^i_{MC})_0 \exp(-\pi \cdot f^{(1-\alpha(r))} \cdot t^*_0). \tag{5.9}$$

If I now take the spectral ratio of the amplitudes for two body-wave phases i and j, from equation (5.3), the ratio can be expressed as:

$$A_{ij}(f) = c_1 c_2 \exp(\pi \cdot (f^{(1-\alpha_j(r))} t^*_{0j} - f^{(1-\alpha_i(r))} t^*_{oi})), \tag{5.10}$$

where c_2 represents the ratio of terms which do not depend on frequency

$$c_2 = \frac{A^i_{GS}(p_i, \xi_i) A^i_R(p_i, \xi_i)(A^i_{MC})_0}{A^j_{GS}(p_j, \xi_j) A^j_R(p_j, \xi_j)(A^j_{MC})_0} \tag{5.11}$$

and c_1 represents the ratio of terms which depend on frequency

$$c_1(f) = \frac{A^i_\phi(f; \theta, \phi) A^i_{INS}(f) A^i_{CR}(f)}{A^j_\phi(f; \theta, \phi) A^j_{INS}(f) A^j_{CR}(f)}. \tag{5.12}$$

The quantity A_{ij} is the observed spectral ratio. Combining the equations (5.7) and (5.10), I obtain

$$A_{ij}(f) = c_1 c_2 \exp(\pi \cdot (f^{(1-\alpha_j(r))}) \int_\Gamma \frac{dl}{Q^j_0(r) V_j(r)} - f^{(1-\alpha_i(r))} t^*_{oi}) \int_\Gamma \frac{dl}{Q^i_0(r) V_i(r)}). \tag{5.13}$$

Equation (5.13) is the relationship among the observed spectral ratio, reference velocity models, Q models and frequency dependent parameters. Based on this relationship, I could derive Q and frequency dependent parameters. But I have to work out how to deal with the constant c_1, c_2, and the relationship of Q and α between P and S. In the following section in this chapter, I will discuss how to solve Q and α from equation (5.13) and the assumptions involved.

5.2.1 Techniques for Measurement of Differential Attenuation δt^*_{sp}

In this application I choose the phases i and j to be the P and S arrivals from the same source. I assume that these phases share a common source spectrum $A^i_\phi(f; \theta, \phi)$ and instrumental response $A^i_{INS}(f)$. I also expect the crustal effects to be similar so that the frequency dependent factors in $c_1(f)$ cancel and $c_1 \approx 1$.

Now, taking the logarithm of both sides of equation 5.10, I find

$$\ln(A_{ij}(f) \quad = \quad \ln c_1(f) + \ln c_2 + \pi \cdot (f^{(1-\alpha_j(r))} t^*_{0j} - f^{(1-\alpha_i(r))} t^*_{0i}) \tag{5.14}$$

but $\ln c_1 \approx 0$, and so

$$\ln A_{ij}(f) \simeq \ln c_2 + \pi \cdot (f^{(1-\alpha_j(r))} t^*_{0j} - f^{(1-\alpha_i(r))} t^*_{0i}) \tag{5.15}$$

The spectral ratio method for P and S waves from one event recorded at a single station is employed. From equation (5.15) and (5.7) then I obtain

$$\frac{1}{\pi}\left(\frac{d(\ln c_1)}{df}+\frac{d(\ln A_{sp(r)})}{df}\right)=\delta t^*_{sp}=\int_p\frac{dl}{Q_p(r)\alpha(r)}-\int_s\frac{dl}{Q_sV_s}. \tag{5.16}$$

$A_{sp}=A_s(f)/A_p(f)$ which is the observed spectral ratio. The frequency factor

$$c_1=\frac{A^p_\phi(f;\theta,\phi)A^p_{INS}(f)A^p_{CR}(f)}{A^s_\phi(f;\theta,\phi)A^s_{INS}(f)A^s_{CR}(f)}. \tag{5.17}$$

Based on the following assumptions: (1) the crustal transfer function is the same for P and S waves, $A^s_{CR}(f)=A^p_{CR}(f)$; (2) source effects on spectrum are the same for both S and P waves, $A^p_0(f;\theta,\phi)=A^s_0(f;\theta,\phi)$; (3) the elastic responses of mantle on P and S $(M^p_{SC})_0$ and $(M^s_{SC})_0$ are same, then I obtained the $c_1=1,\ln c_1=0$,

$$\begin{aligned}\frac{1}{\pi}\left(\frac{d(\ln A_{sp})}{df}\right) &= \delta t^*_{sp},\\ &= \int_{path}\frac{dl}{Q_p\cdot V_p}-\int_{path}\frac{dl}{Q_s\cdot V_s}.\end{aligned} \tag{5.18}$$

Based on the relationship between Q_p and Q_s and the reference velocity model, this equation can be used to model the data in terms of a Q_s model in the upper mantle.

In the above discussion, I reviewed the spectrum theory briefly to state clearly the assumptions made. In the following section, I outline the method by which I measured the spectral ratio of S and P waves and their logarithmic slope on a single seismogram.

First, I isolate the P, SV, and SH phases and their noise and investigate how to treat the noise. Then spectra of the P, SV, and SH waves and their accompanying noise were estimated by using FFT of single real functions [Press et al., 1995]. Before undertaking FFT, I applied a sine-tapered rectangular window function to the data to reduce the spectrum distortion. I examined the factors which impact on spectrum, such as free surface correction, the choice of window length and window function and the choice of frequency band etc. After an optimum window length, window function, frequency band and spectrum estimator were chosen, the P, SV and SH phases were constructed and the FFT was undertaken. I then computed the power spectrum for P SV and SH waves, $P_p(f)$, $P_{sv}(f)$ and $P_{sh}(f)$, respectively.

A noise window of the same length as the signal window was taken from 6.4s before the onset of the P and S phases, for comparison with the signal spectrum. The window function applied to signal window was also applied to noise window. Noise power spectra for P, SV and SH waves, $\tilde{P}_{np}(f)$, $\tilde{P}_{nsv}(f)$ and $\tilde{P}_{nsh}(f)$, were calculated in the same way for signal power spectra. It was assumed that the noise characteristics of the signal window were similar to those for the noise window. After estimating the spectrum, the noise was smoothed and the smoothed noise spectrum which cover the outline of the noise spectrum was removed from signals. The difference operator in equation (5.19) removes the contributions of noise to spectra upon the assumption that the data and the noise are independent in phase.

$$\tilde{P}_p(f)=\tilde{P}_p(f)-\tilde{P}_{np}(f)$$

and

$$\tilde{P}_s(f) = \tilde{P}_{sv}(f) + \tilde{P}_{sh}(f) - \tilde{P}_{nsv}(f) - \tilde{P}_{nsh}(f) \tag{5.19}$$

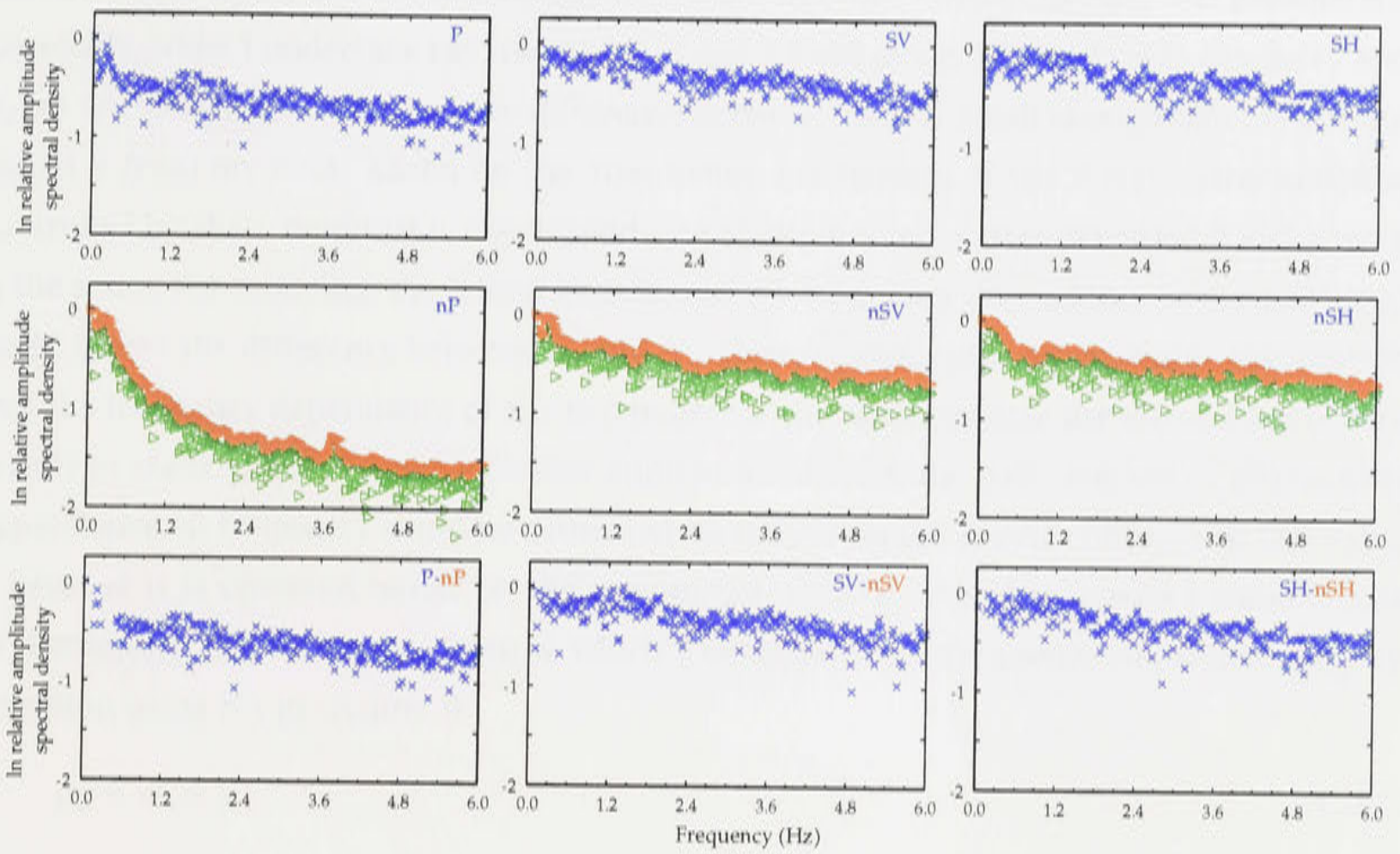

Figure 5.1: Illustration for smoothing and removing noise, the top three diagrams are signal spectra before removing noise, the middle three diagrams are noise spectra, the dark triangles represented the smoothed noise spectra and light and scattered triangles represented the original noise spectra, the bottom three diagrams are the signal spectra after removing noise.

Figure 5.1 illustrates the noise smoothing and removal. The sub-figures *P*, *SV* and *SH* are signal spectra which contain noise. The green graphs in *nP*, *nSV* and *nSH* are raw noise spectra, and the red graphs are smoothed noise spectra which are a good representation of the noise. The sub-figures *P -nP*, *SV -nSV* and *SH -nSH* are signal spectra after removing noise. On the other hand, the *SH* and *SV* waves are assumed to be completely coherent in time. In effect, the above removal of the noise contribution serves to identify ranges in frequency where the signal does not significantly exceed the noise, rendering the estimate of the power spectrum near zero or negative. This generally occurs at the lowest frequencies included in the analysis and beyond about 1 Hz for events beyond an epicentral distance of about 18°.

I defined the spectral ratio by

$$R_{sp}(f) = [P_s(f)/P_p(f)]^{1/2} \tag{5.20}$$

and measured the δt^*_{sp} which is equal to the logarithmic slope of the spectral ratio $\ln R_{sp}(f)$. I then fitted the $R_{sp}(f)$ as a function of frequency to a straight line in selected frequency bands by linear regression.

$$\delta t^*_{sp} = \frac{1}{\pi}\frac{d(\ln R_{sp})}{df} = \frac{1}{2\pi}\frac{d(\ln(P_s(f)/P_p(f)))}{df} = \frac{1}{2\pi}\left(\frac{d\ln P_s(f)}{df} - \frac{d\ln P_p(f)}{df}\right) \tag{5.21}$$

5.2.2 Path Average Properties of Frequency Dependence of Attenuation

The $\alpha_i(r)$ and $\alpha_j(r)$ are a function of depth. They are vary with horizontal position. Thus the $\alpha_i(r)$ and $\alpha_j(r)$ are not necessarily the same. In other words, they are 3-D parameters. Especially, when I undertake ray tracing for P and S wave along different path, the $\alpha_i(r)$ and $\alpha_j(r)$ are clearly different. But the difference between them is small enough that I could not model it from my data. Based on the attenuation mechanism, if the P wave attenuation is controlled by shear modulus μ, the dependence of attenuation on frequency for P and S wave is the same. For modeling the lateral variation of the frequency dependence of attenuation, I could ignore the difference between α_i and α_j. Here, I could make a reasonable assumption that the frequency dependence of the two phases is the same because the attenuation occurs mainly in shear waves. I make a further approximation that the path average of attenuation dependence on frequency could be estimated directly from the spectra ratio. I call this value γ because it is obtained based on the assumption $c_2 = 0$. Another reason I name it γ is to distinguish the difference from α which I obtained from frequency dependent δt^*_{sp} by inversion using NA in chapter 9

$$\alpha_j = \alpha_i = \gamma \tag{5.22}$$

then (5.15) reduces to

$$\ln A_{ij}(f) = \ln c_2 + \pi f^{(1-\gamma)} \cdot (t^*_{0j} - t^*_{0i}), \tag{5.23}$$

in terms of the differential t^* (δt^*_{0ij}) for the two phases. Note that if $\gamma = 0$, the logarithmic spectral ratio is a linear function of frequency with slope proportional to δt^*_{0ij}.

In principle, the c_2 is very close to 1. If I make an assumption that $c_2 = 1$ based on the geometrical spreading, the radiation pattern for P and S are same. Then $\ln c_2 = 0$, so that

$$\ln A_{ij}(f) = \pi f^{(1-\gamma)} \cdot (t^*_{0j} - t^*_{0i}), \tag{5.24}$$

Because $(t^*_{0j} - t^*_{0i})$ is the frequency independent part of differential attenuation, on taking the logarithm of (5.24), I obtained

$$\ln\ln A_{ij}(f) = (1-\gamma)\ln f + const. \tag{5.25}$$

Thus if $\ln\ln A_{ij}(f))$ is plotted as a function of $\ln f$, there will be a straight line relation with slope $1-\gamma$.

I have also tried to model the curve of equation (5.24) with non-linear least-square fitting. But this did not work well. One reason is that the single value of α could not represent the variation of α with depth. Another reason is that when I made the assumption of $c_2 = 1$, I lost information. I undertook an experiment with the synthetic data in figure 5.2. I calculated the synthetic curve of equation (5.24) from four layer α model and I tried to use single α to fit it. The results show that even the synthetic δt^*_{sp} calculated from multi-α could not be represented by a single α model.

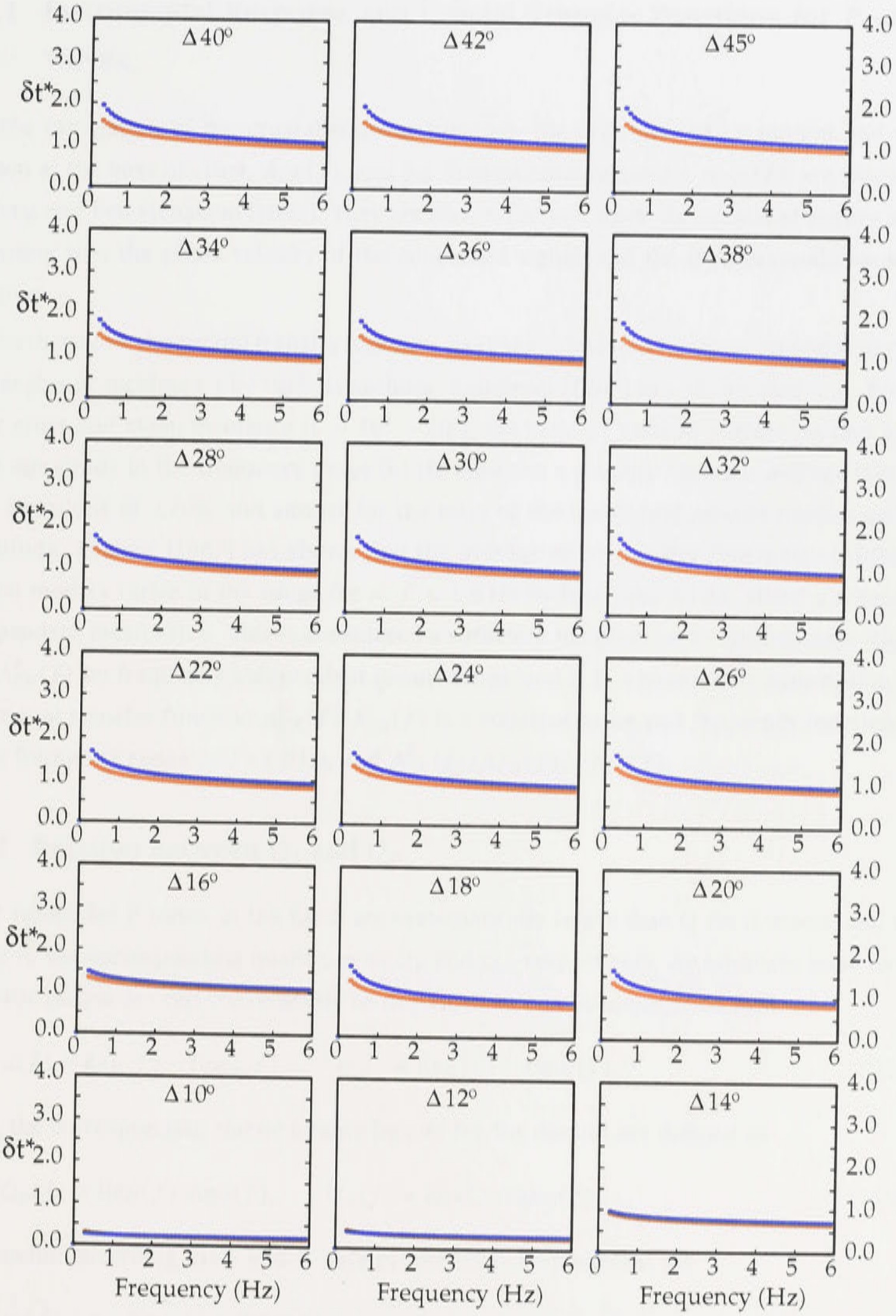

Figure 5.2: δt^*_{sp} (top line) calculated from velocity model for eastern Australia *a0sl1* and 4 layer α model ($\alpha = 0.1$ for lithosphere and $\alpha = 0.6,0.2,0.2$ for deeper part of mantle) based on $Q(f) = Q_0(f_0)(f/f_0)^\alpha$ with $f_0 = 1.0$ Hz then fitted by single value of alpha (bottom line).

5.3 Discussion on the assumptions involved

5.3.1 Instrumental Response and Crustal Transfer Functions for P and S Waves

The calculation of the crustal transfer function, the ratio of surface motion and wave motion at the base of crust, $A_{CR}(f)$, and the instrumental response, $A_{INS}(f)$, are discussed by Teng and Ben-Menahem [1965]. They are known factors, when the crustal structure at the recording site, the phase velocity of the concerned signal, and the instrumental characters are given.

Furthermore, the crustal transfer function, has been calculated for many crustal structures and angles of incidence i by various authors. Kanamori [1967] has shown that, e.g. for a 4-layer crust and steep incidence ($i = 10° - 20°$), the ratio of vertical surface motion and P wave amplitude in the frequency range 0-1 Hz assumes a roughly constant average level 2.5 with variations of ±20%, and similar for the ratio of the horizontal ground motion and SV amplitude. Leblanc [1967] has shown that the average of 20 transfer functions of different crustal models varies in the range $0.4 < f < 1.6$ Hz by less than $\pm 1dB$, about a frequency independent mean value. This is considered a sufficient justification to approximate $A^s_{CR}(f)$ and $A^p_{CR}(f)$ by frequency independent mean values, and it is a reasonable assumption that the crustal transfer function $A^p_{CR}(f)$ $A^s_{CR}(f)$ is a constant value and frequency independent in the frequency range 0.01 - 1.0 Hz, and $A^p_{CR}(f)/A^s_{CR}(f) = n(\approx 1)$.

5.3.2 Relation between Q_s and Q_p

Q values for P waves in the Earth are systematically larger than Q for S waves, and thus I refer to the corresponding quantities as Q_p and Q_s, respectively. An isotropic solid having anelastic properties can conveniently be described by complex elastic moduli

$$\mu(f) = \mathrm{Re}\mu(f) + i\mathrm{Im}\mu(f), \qquad \kappa(f) = \mathrm{Re}\kappa(f) + i\mathrm{Im}\kappa(f). \tag{5.26}$$

Then, the corresponding classic quality factors for the moduli are defined as

$$Q_\mu(f) = \mathrm{Re}\mu(f)/\mathrm{Im}\mu(f), \qquad Q_\kappa(f) = \mathrm{Re}\kappa(f)/\mathrm{Im}\kappa(f). \tag{5.27}$$

The moduli governing the S and P wave propagation, respectively, are

$$\begin{aligned} \mu_s(f) &= \mathrm{Re}\mu(f) + i\mathrm{Im}\mu(f) \\ \mu_p(f) &= \mathrm{Re}\kappa(f) + \frac{3}{4}\mathrm{Re}\mu(f) + i[\mathrm{Re}\kappa(f) + \frac{3}{4}\mathrm{Im}\mu(f)]. \end{aligned} \tag{5.28}$$

and the corresponding Q factors

$$Q_s(f) = \frac{\frac{1}{2}\mathrm{Re}\mu(f)}{\mathrm{Im}\mu(f)} \qquad Q_p(f) = \frac{\frac{1}{2}\mathrm{Re}\kappa(f) + \frac{3}{4}\mathrm{Re}\mu(f)}{\mathrm{Im}\kappa(f) + \frac{3}{4}\mathrm{Im}\mu(f)} \tag{5.29}$$

so that

$$\frac{Q_s(f)}{Q_p(f)} \approx \frac{V_s^2}{V_p^2}[\frac{3}{4} + \frac{\mathrm{Im}\kappa(f)}{\mathrm{Im}\mu(f)}] \tag{5.30}$$

where, for $Q \gg 1$,

$$V_s^2 \approx \frac{\mathrm{Re}\mu}{\rho} V_p^2 \approx \frac{\mathrm{Re}\kappa + \frac{4}{3}\mathrm{Re}\mu}{\rho} \tag{5.31}$$

If anelasticity is entirely due to energy loss in shear deformation $\mathrm{Im}\kappa = 0$, which is a widely adopted postulate and also used in this report, then the relation between Q_p and Q_s will be:

$$Q_p^{-1} = \frac{4}{3}\frac{V_s^2}{V_p^2} Q_s^{-1} \tag{5.32}$$

It is seen from Eq. 5.31 that the proportionality of Q_s and Q_p exists as long as the velocity dispersion remains negligible. Even if $\mathrm{Im}\kappa(f) \neq 0$ but is small relative to $\mathrm{Im}\mu$ or varying with frequency in a similar way, the proportionality of Q_s and Q_p may still be assumed to a good approximation.

5.3.3 Relation between V_s and V_p and ray divergence factor

Based on the assumption that the P/S velocity ratio is constant with depth, the ray divergence at a given epicentral distance is almost identical for P and S waves [e.g. Shimshoni, 1970; Gudmundsson et al., 1994]. However, the P/S velocity ratio is not necessarily a constant, but it is a function which varies with depth. There are very few results for the P/S ratios in the mantle, because in most cases the methods used for constructing estimates of P and S structures are very different.

The P/S velocity ratios as a function of depth beneath Australia are estimated directly by Kennett et al. [1994] from the P and S sections prepared from the same events. The results are depicted in figure 5.3. This ratio increases from 1.77 at the top of the mantle to 1.85 at the 410 km transition. Through the transition zone down to 660 km, the S wave gradients increase and the P/S velocity ratio is less than 1.81 below the 660 km transition. This result can be used to invert the Q^{-1} and I can calculate the ray path for P and S to investigate the influence of the ray divergence factor on P and S.

5.3.4 Source Spectra for P and S Waves

The assumption of the proportionality of source spectrum of P and S certainly needs careful and critical consideration, and the source spectrum is not necessarily the same for S and P waves. This issue received some attention in the 1970s.

If I consider the corner frequency $f_c(P)$ and $f_c(S)$ as representative quantities of the source spectra of P and S, it turns out that the information found in the literature is controversial. According to a critical review by Hanks [1981], it is found that $f_c(P)/f_c(S) > 1$, the

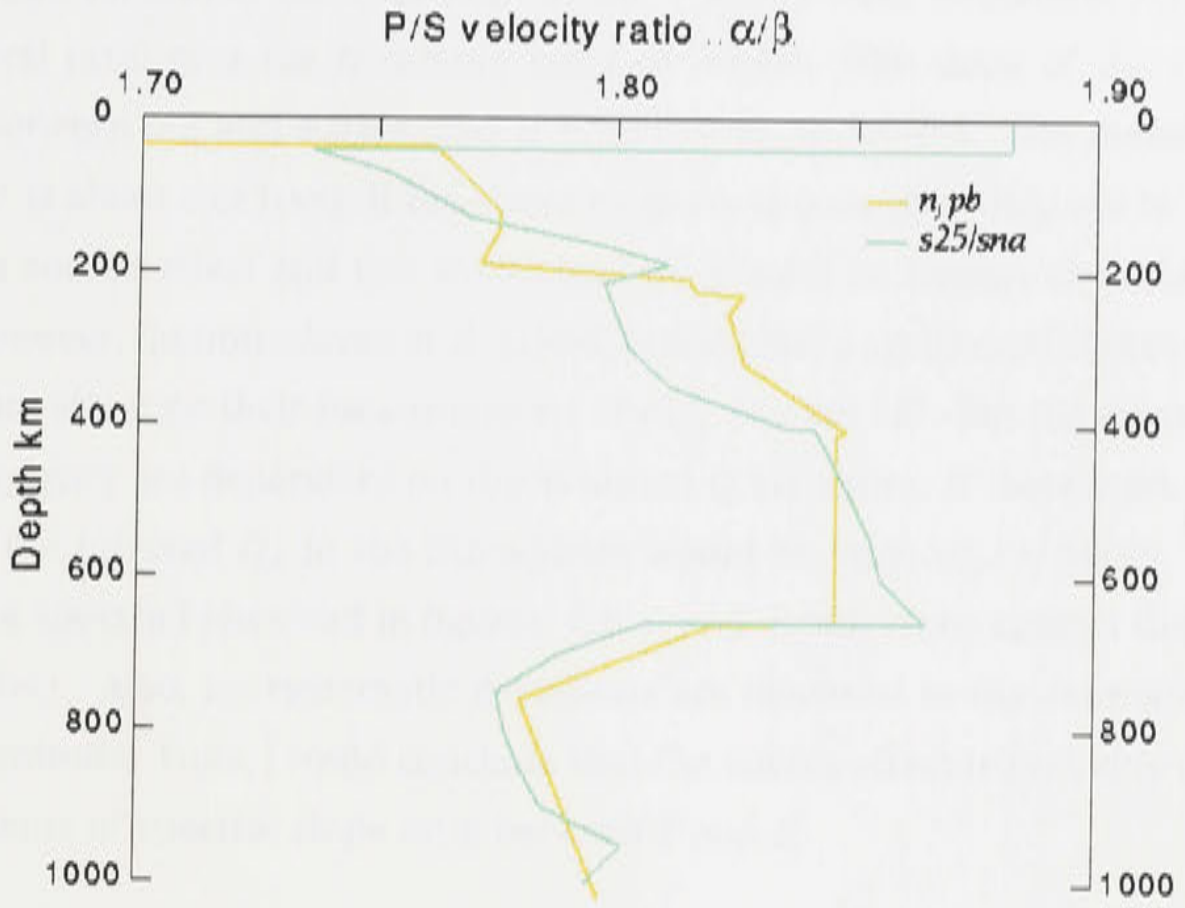

Figure 5.3: The velocity ratio between P and S wavespeeds as a function of depth, for model njpb representing the northern Australian region, and models for the North American Shield. After Kennett et al., 1994.

corner frequency for P is 20 – 70% higher than that for S, in the majority of observational cases. The dynamic crack model of Madariaga [1976] predicts a directional deviation of the P wave corner frequency from that for S waves within about 50%. However, some near-source observations in low-loss material show $f_c(P)/f_c(S) < 1$. Hanks concluded from numerical estimates that differential absorption of P and S waves may account for some of the difference of $f_c(P)$ and $f_c(S)$ but not for all. By applying two different types of source models, one-dimensional unilateral and bilateral dislocation models of Haskell type with rupture propagation along an elongated rectangular fault of L = 50 km and the Madariaga stress relaxation models with constant rupture velocity, to produce synthetic source spectra, Ulug and Berckhemer [1984] found that, despite the more or less pronounced oscillation, all spectral ratios follow a constant mean level through the frequency band (0.03-1.5 Hz) which may be taken as a justification for the assumption $A^s_\phi / A^p_\phi \approx$ constant (A^s_ϕ and A^p_ϕ are the source spectra of P and S respectively).

Gudmundsson et al. [1994] reviewed the dynamic crack model by Madariaga [1976] which predicts a directional deviation of the P-wave corner frequency from that for S waves within about 50%. Gudmundsson et al. 1994] concluded the source spectra for P waves and S waves may be different in more subtle ways than that characterised by the corner frequency. This is because the corner frequencies for P waves radiated from the earthquake source are perhaps expected to be higher than that for S waves [Hanks, 1981]. Thus, the source spectrum for P rises faster or decays more slowly than that for S waves. Gudmundsson et al. [1994] estimated the corner frequency for magnitude 5.0-5.5 as 0.18 Hz for shear waves according to Aki [1967] and added on 50% for P waves (0.27 Hz). Based on this assumption, Gudmundsson

et al. [1994] also measured the logarithm of the P and S wave amplitude-velocity spectra and the spectral ratio over the frequency band of 0-1 Hz. The slope of the spectral ratio is measured between 0.2 and 1.0 Hz, and is found to be about -0.5. The measured level of δt^*_{sp} out to 18° is about this level. If the above estimate is true, then δt^*_{sp} out to 18° could be attributed to a source effect and this would lead us to infer an infinite Q in the lid. This is unrealistic. However, Gudmundsson et al. [1994] argued that a systematic source effect would have a moderate effect on their measurements of δt^*_{sp} beyond 18°. But the measurements of the corner frequency are dependent on the assumed Q structure. If there were a significant source effect, the inferred Q_s in the lithosphere would be large ($Q_s > 5000$). This is also unrealistic. The spectra I observed in figures 6.8(a) and 6.8(b) argue against the importance of a source effect. Also, no systematic deviations are observed in the estimate of spectral slope with magnitude. Thus, I could conclude that the source effect is probably not affecting our measurements of spectral slope ratio between P and S.

5.4 Experiments on δt^* Measurement Procedure

5.4.1 Tests of δt^* measurement procedure on Warramunga data

Data selection and analysis

The earthquakes that occurred in the earthquake belt through Indonesia and New Guinea, and were recorded by the broadband seismometers at the Warramunga array in the Northern Territory of Australia, provide good coverage of propagation through the upper part of the mantle. The midpoints of the propagation paths lie along the northern margin of the Australian continent. Most of the observations come from the Güralp CMG3 seismometers at the Warramunga array, but these have been supplemented by field deployments using comparable instrumentation. These data have been analysed by Gudmundsson et al. [1994] and are reexamined here to set up a procedure which is also applied to data from the SKIPPY project. The location, origin time, magnitude, epicentral distance and measured δt^*_{sp} of the Warramunga data used in this study are listed in table 5.1.

For the epicentral distance out to 20°, the onsets of the SV and SH waveforms show high frequencies (greater than 1 Hz) associated with arrivals propagating within a thick lid extending to 210 km depth. At larger epicentral distance the onset of S, respecting waves refracted back from beneath the 410 or 660 km discontinuities, has a much lower-frequency content (0.25-0.3Hz). Such intermediate-period arrivals also characterise the S waves returned from the 410 and 660 km discontinuities at shorter distances.

Figures 5.4(a), 5.4(b), 5.4(c) and 5.4(d) show that the frequency contents of P and S wave vary with the epicentral distance. Beyond 18° there is a significant difference in the frequency content of P and S waves. The P waves remain high frequency, but the S waves returned

Table 5.1: Location, origin time, magnitude, epicentral distance and measured δt^*_{sp} of the Warramunga data used in this thesis

Event	*Date* dd.mm.yy	*Time* hh:mm:ss.ss	*Latitude* (deg)	*Longitude* (deg)	Depth (km)	Mag	Distance (deg)	δt^*_{sp} (s)
1	07.12.1990	20:31:03.21	-6.79	132.26	33.00	5.2	13.23	0.05
2	15.06.1990	15:04:50.91	-6.43	131.25	62.00	5.0	13.77	0.04
3	07.08.1991	04:54:49.80	-4.56	134.02	24.00	5.1	15.29	0.24
4	16.12.1990	20:19:48.10	-6.01	142.17	33.00	5.4	15.80	0.23
5	17.04.1990	14:56:49.60	-6.90	144.52	32.00	4.9	16.30	0.16
6	27.09.1991	23:01:25.61	-3.36	137.63	64.00	5.5	16.79	0.14
7	24.01.1992	12:09:24.11	-9.41	148.80	33.00	5.4	17.45	0.35
8	26.02.1990	18:13:59.80	-9.58	149.80	33.00	5.2	18.13	0.61
9	23.07.1990	10:57:28.21	-4.72	145.58	30.00	5.0	18.67	0.60
10	14.02.1992	12:02:03.00	-4.39	146.38	42.00	5.2	19.40	1.02
11	25.04.1990	15:32:21.71	-7.08	150.12	23.00	5.4	19.93	0.99
12	28.12.1991	11:05:20.30	-6.33	150.19	33.00	5.4	20.49	1.91
13	28.12.1991	03:40:31.40	-6.43	150.84	24.00	5.4	20.90	1.76
14	10.02.1990	13:12:14.20	-5.27	151.28	10.00	5.3	22.00	1.78
15	04.04.1990	19:51:48.96	-4.74	151.65	31.21	4.9	22.63	1.49
16	07.05.1990	14:52:51.60	-9.65	155.54	25.00	5.1	22.87	1.39
17	27.12.1991	17:14:30.71	-9.10	157.84	33.00	5.2	25.13	1.43
18	26.09.1991	09:14:50.41	-9.29	158.62	26.00	5.2	25.73	1.11
19	20.08.1990	14:11:43.00	-11.25	161.92	44.00	5.2	27.89	1.27

from the transition zone and below are of an intermediate period (0.1-0.5 Hz), which would be difficult to record without a broadband instrument and a quiet site. The latter branches associated with the 410 and 610km discontinuities are clearly seen in individual seismograms. The *S* waves recorded on the radial (*SV*) and tangential (*SH*) components are of comparable quality, because the hard-rock recording site minimises the influence of coupling to *P* on the radial component.

The change in the frequency character of *S* waves relative to *P* waves, which occurs between 16.9° and 19.5° epicentral distance, as is evident from many seismograms, may be explained by a layer of high shear attenuation at depth. The observation results can be described quantitatively by use of the spectral ratio of *S* and *P* waves. The logarithmic slope of this spectral ratio is related to the difference attenuation $\delta t^*_{sp} = t^*_p - t^*_s$.

Results of δt^*_{sp} Measurement Analysis

The common feature of the spectra of *P*, *SV* and *SH* waves and their noise measured from a seismogram recorded at the Warramunga seismic array are displayed in figures 5.4(a), 5.4(b), 5.4(c) and 5.4(d). The noise spectra were smoothed to a mean base line which quite clearly fitted the overall envelope of the noise spectrum, and then were removed from the signal spectrum. I did not smooth the signal spectra, so the signal spectra appear in great detail. Some data are very sparse, so they are far from the general trend of the spectrum. This led the slope of the spectral ratio to depart from the correct value. I have tried to skip the sparse data to obtain true value for spectral ratio.

Spectral ratios measured from Warramunga data were plotted as a function against the

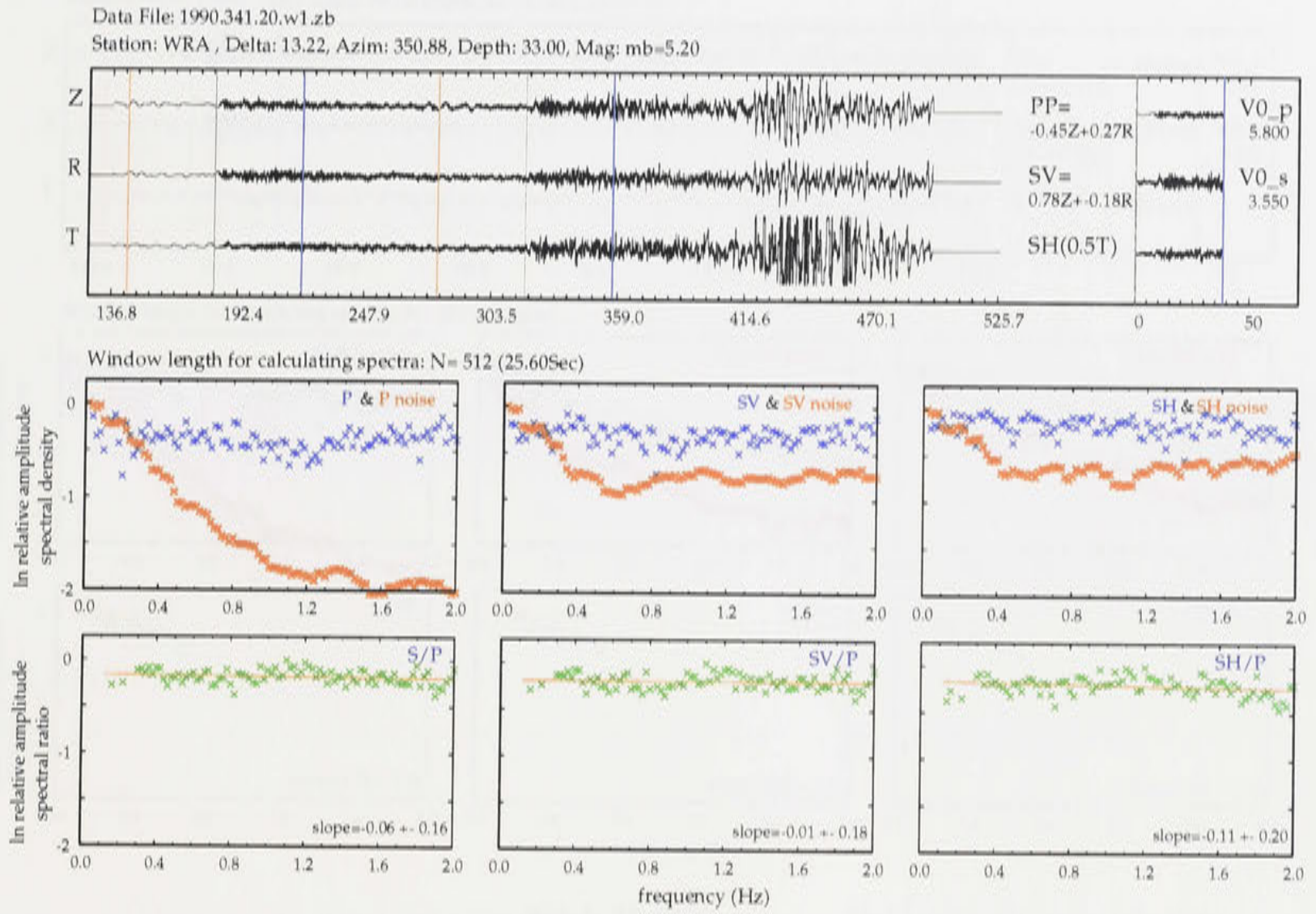

(a) Δ 13.22°

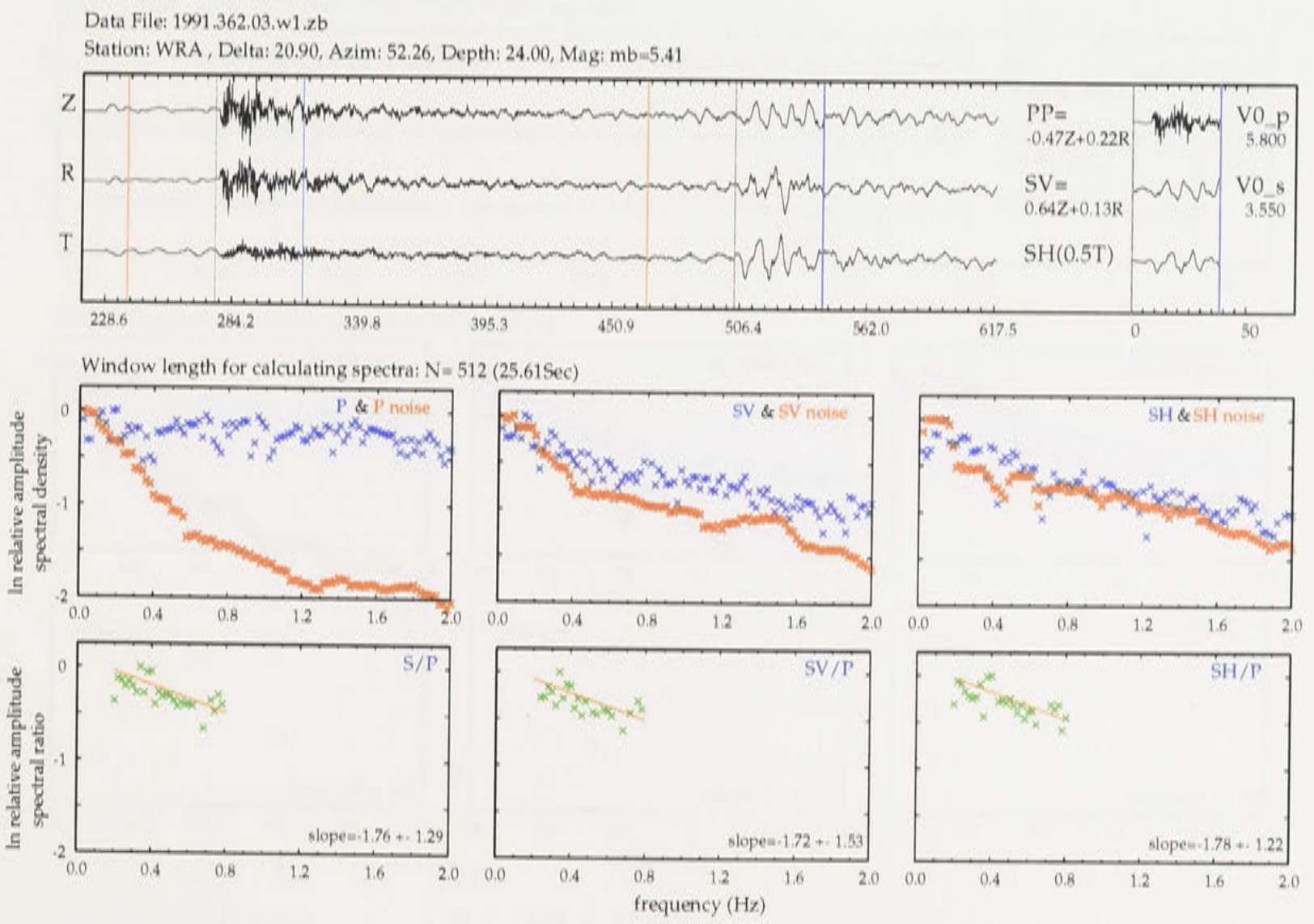

(b) Δ 20.90°

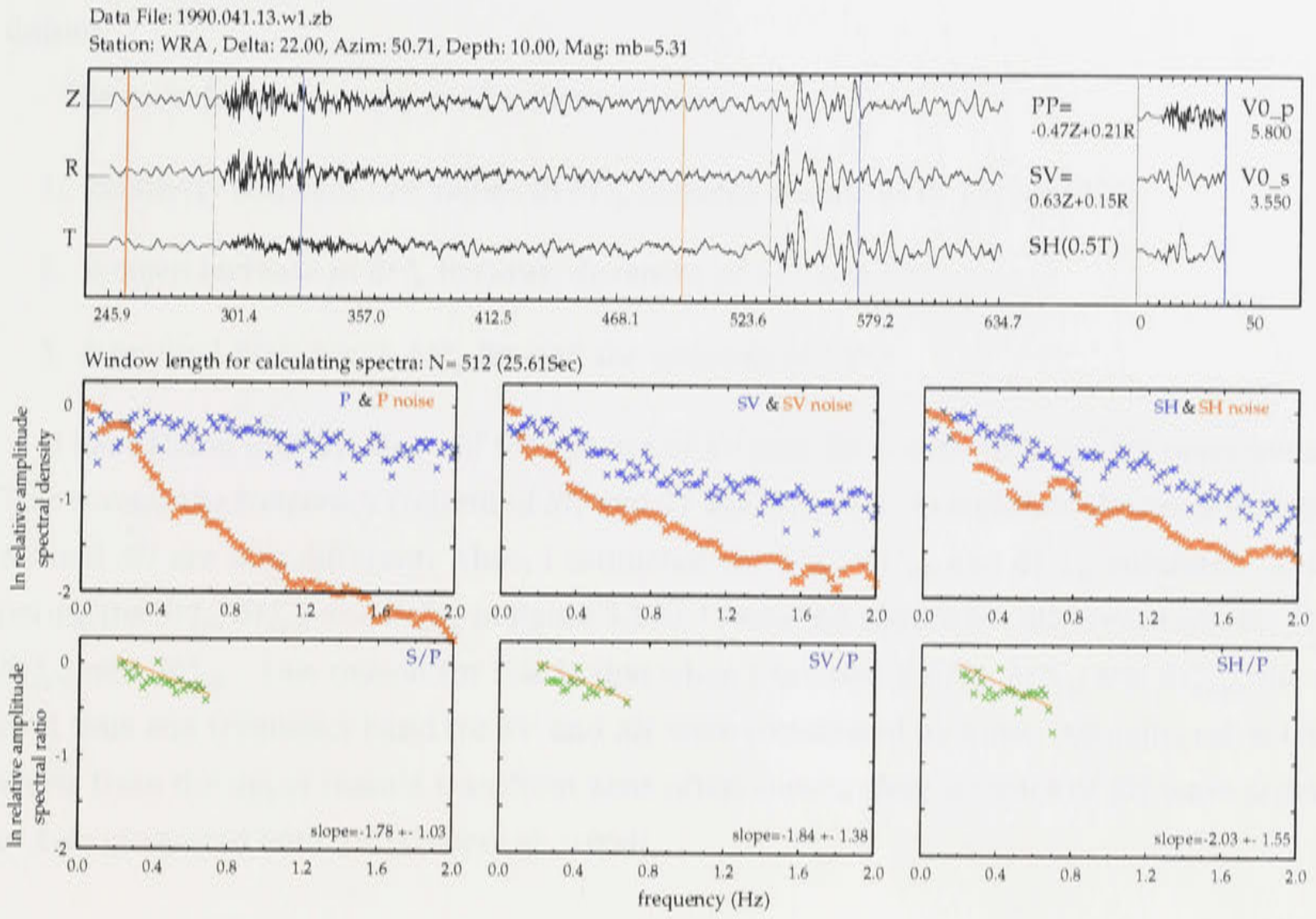

(c) Δ 22.00°

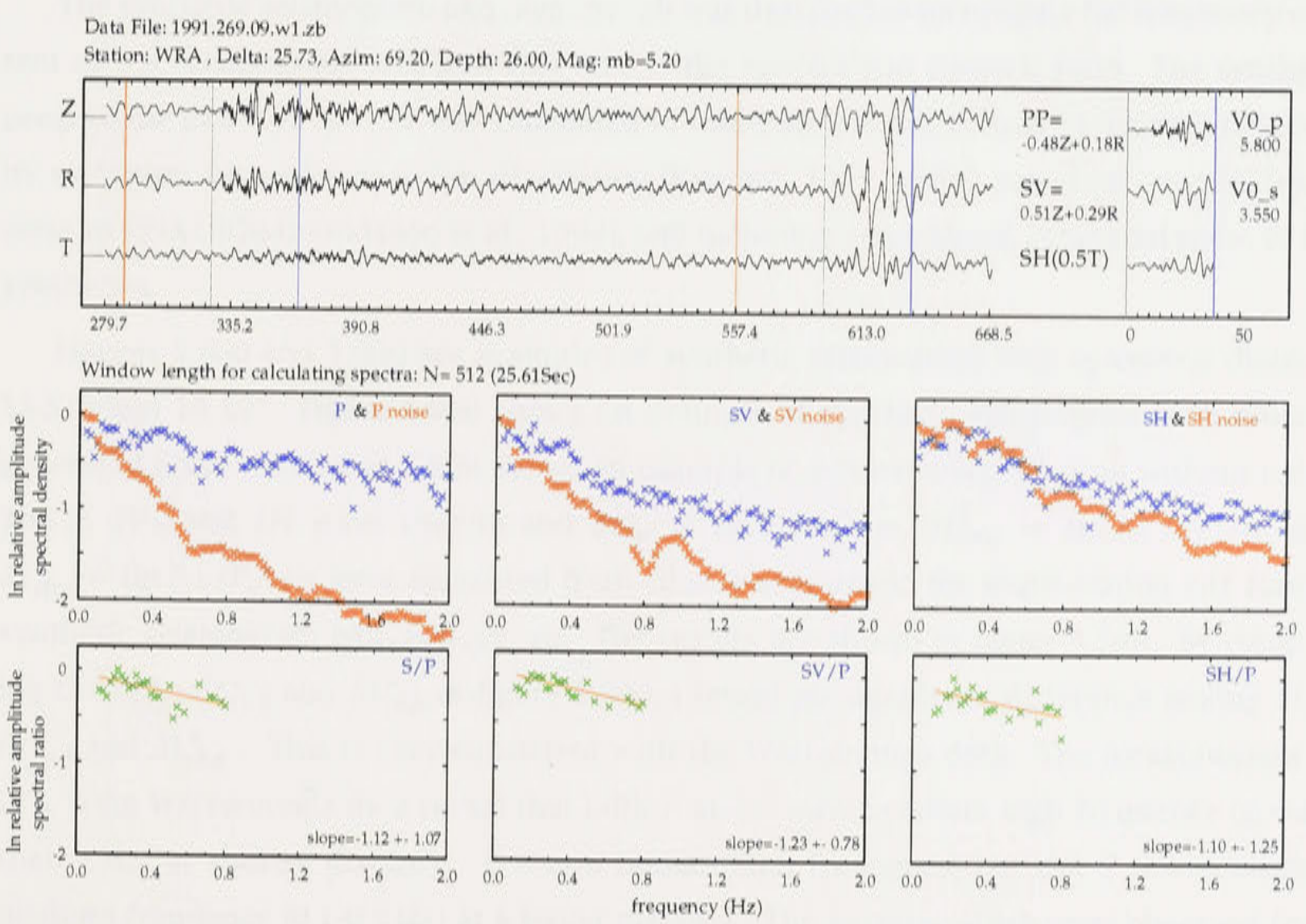

(d) Δ 25.73°

Figure 5.4: Examples of synthetic data and seismograms recorded at the Warramunga seismic array with different epicentral distances and the P, SV and SH wave spectra and S/P, SV/P and SH/P spectral ratio measured from those seismograms.

distance with one standard deviation error estimates. Each solid circle represents a single datum.

The main features displayed by these data are:

1. Relatively constant low values in δt^*_{sp} between distances of 13° and 17°.
2. A steep increase in δt^*_{sp} between distances of 17° and 20°.
3. A gradual decrease in δt^*_{sp} beyond the distance of 22°.

I have found that the slope of the spectra of *SV* and *SH* can be different for many events. This reveals the frequency content of *SH* and *SV* are different. In addition, the noise effecting *SV* and *SH* are also different. Thus, I estimated the δt^*_{sp}, δt^*_{svp} and δt^*_{shp} separately. Comparing the δt^*_{sp}, δt^*_{svp} and δt^*_{shp} in figure 5.5(a), I found no significant difference among δt^*_{sp}, δt^*_{svp} and δt^*_{shp} . One reason for this is that when I estimated δt^*_{sp}, δt^*_{svp} and δt^*_{shp}, the arrival time and frequency band for *SV* and *SH* were considered be same. Actually, refracted *S* waves from the upper mantle transition zone often show a clear advance of *SH* wave arrivals of 2-4s compared with *SV* [Tong et al., 1994].

5.4.2 Tests of δt^* Measurement Procedure on Synthetic Seismograms

The synthetic seismogram `pkq.syp.ps.zb` was designed to investigate the frequency content of the seismogram, and how this affects the spectra and spectral ratio. The synthetic programme `pkq.syp.ps.zb` was calculated in multi-station zdf format by using a reflectivity algorithm with allowance for attenuation [Kennett, 1975, 1994], based on a model (*pkq*) close to QNA1 [Gudmundsson et al., 1994], and including some signal generated noise in the synthetics.

Figures 5.6(a) and 5.6(b) are examples of synthetic seismogram with epicentral distance 15.51° and 16.19°. Figure 5.6(a) shows an example of synthetic seismogram with random generated noise and figure 5.6(b) shows an example of synthetic seismogram without noise. The *P*, *SV* , and *SH* wave spectra and $\delta t^*_{sp} = (\ln P_s/P_p)/\pi$, $\delta t^*_{svp} = (\ln P_{sv}/P_p)/\pi$, and $\delta t^*_{shp} = (\ln P_{sh}/P_p)/\pi$ were measured from all seismograms in the multi-station `zdf` format synthetic seismogram `pkq.syp.ps.zb`. The results are shown in figure 5.5(b). By comparing the δt^*_{sp}, δt^*_{svp} and δt^*_{shp} in figure 5.5(b), I found no significant difference among δt^*_{sp}, δt^*_{svp} and δt^*_{shp} . This is very consistent with the Warramunga data. The measurement of δt^*_{sp} from Warramunga data reveal that both *P* and *S* waves contain high frequency (greater than 1 Hz) at shorter distance. *P* waves remain high frequency, but the *S* waves become medium frequency (0.1-0.5 Hz) at a larger distance. The spectra, which were observed from synthetic seismograms, also reveal this characteristic of the frequency variation with different distances in the observed seismic data.

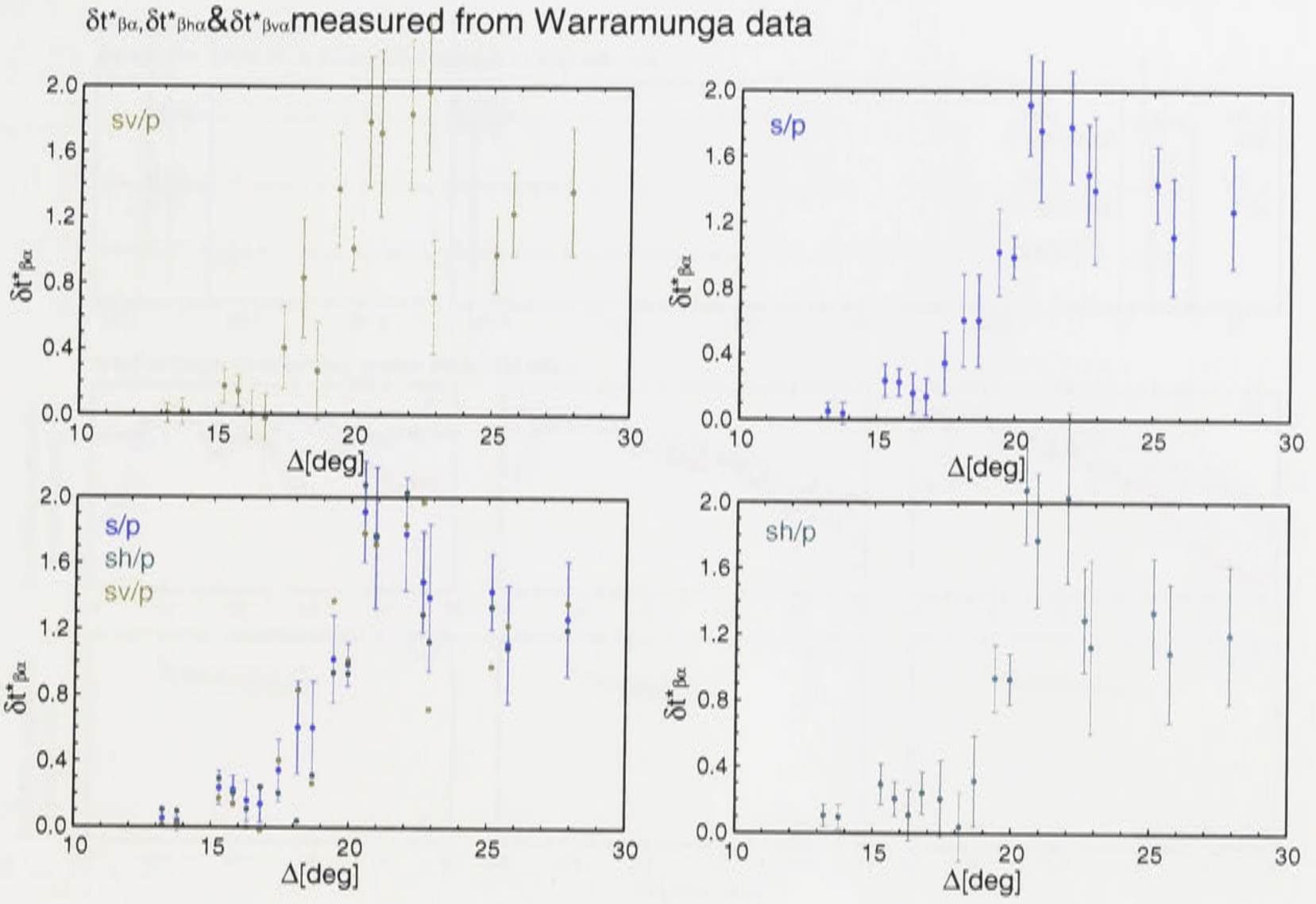

(a) Warramunga Data

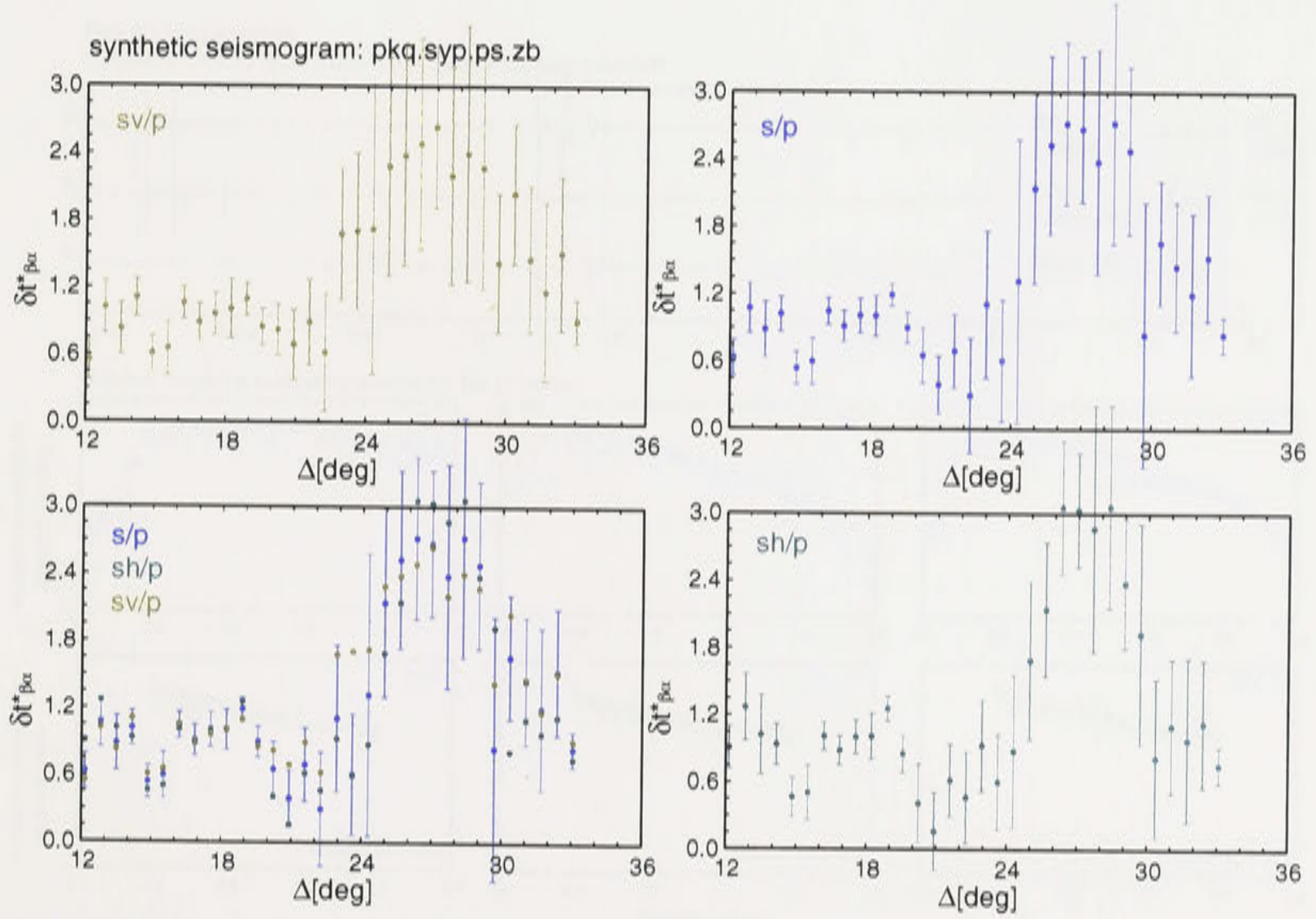

(b) Synthetic Data

Figure 5.5: The δt^*_{sp}, δt^*_{shp} and δt^*_{svp} against distance measured from Warramunga and synthetic seismograms

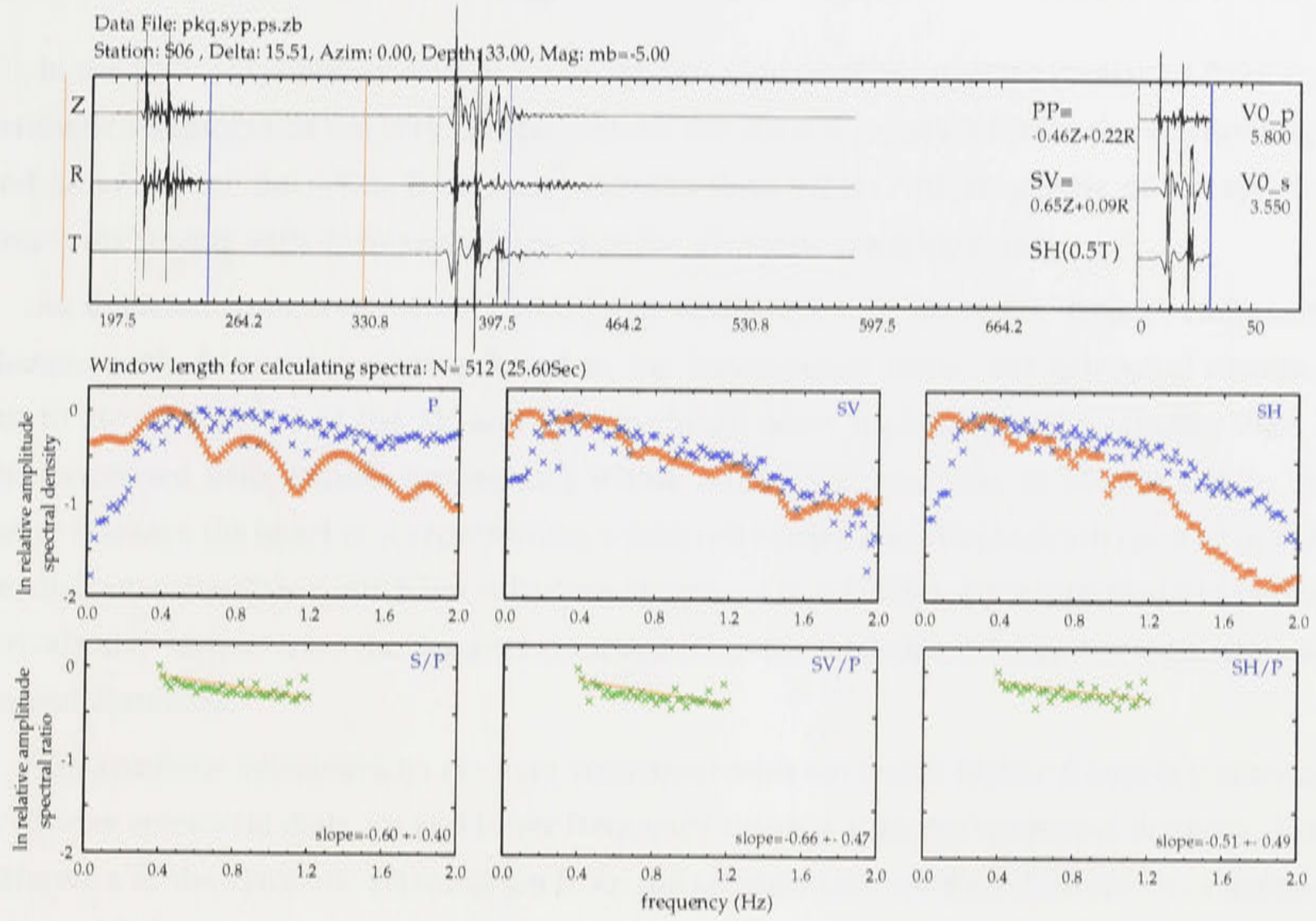

(a) Δ 15.51°, with noise

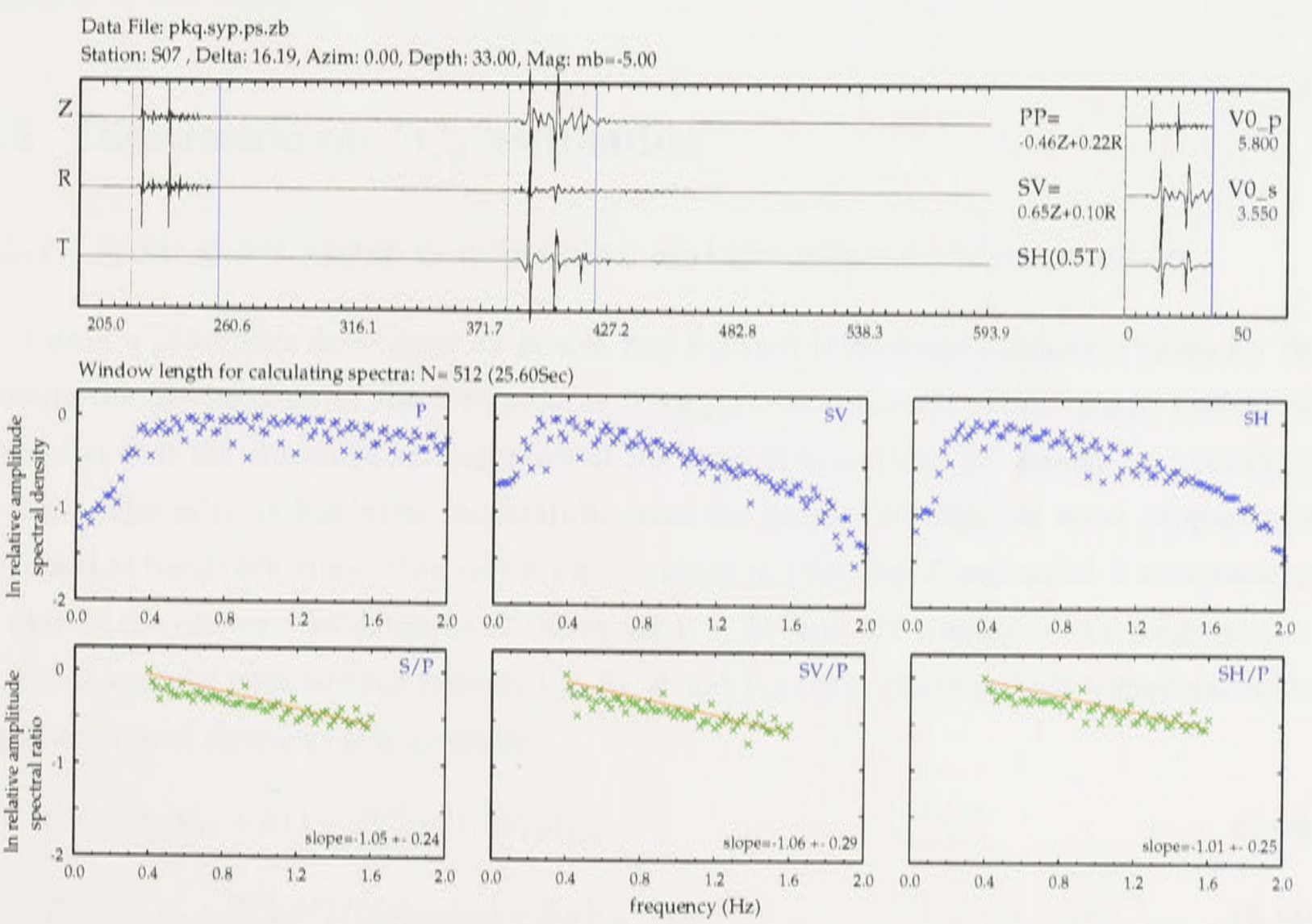

(b) Δ 16.19°, without noise

Figure 5.6: Examples of synthetic seismograms with different epicentral distances and the *P*, *SV* and *SH* wave spectra and S/P, SV/P and SH/P spectral ratio measured from those seismograms.

5.4.3 Comparison between δt^*_{sp} estimated from Seismic and Synthetic Data

In the narrow frequency band 0.2 - 2.0 Hz. the shapes of the spectra measured from the synthetic seismograms are very consistent with the spectra measured from the Warramunga and SKIPPY data. But when frequencies are less than 0.2 Hz, the amplitude of the spectra decreases steeply with decreasing frequency for synthetic seismograms.

As depicted in figures 5.4(a), 5.4(b), 5.4(c) and 5.4(d) etc., there are distinct frequency changes with different distances found in the Warramunga data. For epicentral distance out to 20°, the onsets of the *SV* and *SH* waveforms show high frequencies (greater than 1 Hz) associated with arrivals propagating within a thick lid extending to 210 km depth. At larger distance the onset of *S* representing waves refracted back from beneath the 410 or 660 km discontinuities has a much lower frequency content (0.5-0.3 Hz). Such intermediate-period arrivals also characterise the *S* waves returned from the 410 and 660 km discontinuities at shorter distances.

The synthetic seismograms are very consistent with data with higher frequency content at shorter epicentral distance and lower frequency content at larger epicentral distance. The difference of the synthetic seismogram from the seismic data are the relatively low constant values of δt^*_{sp} out to the distance of 23°, the steep increasing branch of δt^*_{sp} from 24° and the largest value of δt^*_{sp} at the distance of 27°. At a distance larger than 27°, the δt^*_{sp} gradually decrease to low value.

5.5 Discussion on δt^*_{sp} estimation

5.5.1 *P, SV* & *SH* phase construction and the effects of free surface

I used a procedure developed by Jepsen and Kennett [1990] and Kennett [1991b] for removing the interactions of the free surface from three component seismograms under the condition that the slowness and azimuth of the current wavefront are known as a function of time. The scheme has been successfully used for studies of regional wave propagation recorded at hard rock sites. This approach combines the vertical Z and radial R components of motion to construct an estimate of the incident *P*, *SV* and *SH* amplitude reaching the surface. For a model with surface velocity V_{p0} for *P* and V_{s0} for *S*, the *P* and *SV* contribution for a plane wave of slowness p is given by

$$SV = ZpV_{s0} + R(1 - 2V_{s0}^2 p^2)/2V_{s0}q_{V_{s0}} \tag{5.33}$$

$$P = -Z(1 - 2V_{s0}^2 p^2)/(2V_{p0}q_{p0}) + RpV_{s0}^2/V_{p0} \tag{5.34}$$

where

$$q_{p0} = (1/V_{p0}^2 - p^2)^{1/2}$$

$$q_{s0} = (1/V_{p0}^2 - p^2)^{1/2}$$

The slowness p was chosen based on the epicentral distance for each event from the IASPEI 1991 Seismological Tables by Kennett [1991a].

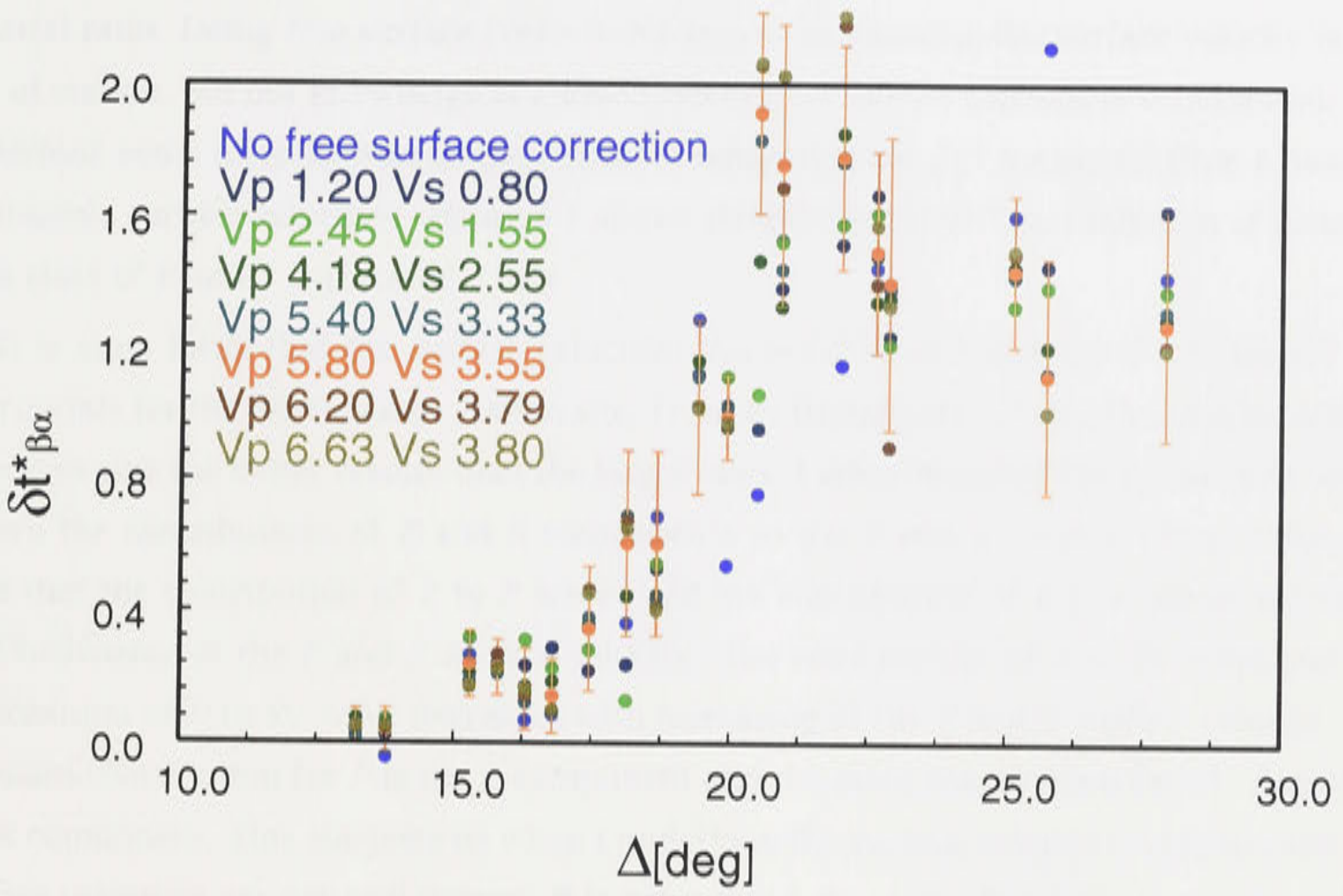

Figure 5.7: Comparison of δt^*_{sp} as a function of distance when constructing *P*, *SV* , and *SH* phases without free surface correction and with free surface correction from a number of classes possible free surface velocities.

Table 5.2: Comparison among constructions of *P* and SV with free surface correction from a number of classes possible free surface velocities

V_{p0}	V_{s0}	*P*	*SV*
1.20	0.80	-0.50Z + 0.06R	0.15Z + 0.49R
2.45	1.55	-0.50Z + 0.10R	0.28Z + 0.45R
4.18	2.55	-0.48Z + 0.16R	0.46Z + 0.33R
5.40	3.33	-0.47Z + 0.20R	0.60Z + 0.19R
5.80	3.55	-0.47Z + 0.22R	0.64Z + 0.13R
6.20	3.79	-0.46Z + 0.23R	0.68Z + 0.07R
6.63	4.05	-0.46Z + 0.25R	0.73Z + 0.05R

For *SH* waves, the equivalent transformation is a simple amplitude scaling of the transverse *T* component

$$SH = 0.5T \tag{5.35}$$

This transformation is simply a linear combination of the observed seismograms with real coefficient and it compensates for the amplification effects and phases distortion introduced by the free surface. The *P*, *SV*, and *SH* noise can be constructed in the same way as the signal. But this method requires us to know the exact surface velocities of *P* and *S* waves.

After comparing the spectrum results from constructing *P*, *SV* and *SH* phases with and without free surface correction, I found that the free surface correction had a slight effect on the shape of amplitude spectra, and it also slightly reduced the noise which is incoherent in time across components. But the free surface correction has a significant impact on the spectral ratio. Doing free surface correction requires us knowing the surface velocity at the site of station. But our knowledge of surface velocity for SKIPPY stations is very limited. So I undertook some tests on Warramunga data by comparing the δt^* measured from a number of possible surface velocities. Figure 5.7 shows the results for δt^* as a function of distance for a class of *P* and *S* surface velocities.

It is most likely that the surface velocities $V_{p0} = 5.8\,\mathrm{km.s^{-1}}$ and $V_{s0} = 3.55\,\mathrm{km.s^{-1}}$ are appropriate for the Warramunga station site. I can see from figure 5.7 that the smaller surface velocities give the better results than the larger ones. I also compared the parameters which govern the contributions of *Z* and *R* components to the *P* and *SV* waves. From table 5.2, I see that the contribution of *Z* to *P* waves and the contribution of *R* to *P* waves increases with increasing of the *P* and *S* surface velocity. The contribution of *Z* to *SV* wave and the contribution of *R* to *SV* wave decreases with increasing of the *P* and *S* surface velocity. But the main contribution for *P* is the *Z* component and the main contribution for *SV* should be the *R* component. This suggests us when I undertake the surface velocity correction and the surface velocities are not well known. It is safer that I chose smaller surface velocities than larger values.

At the same time, I see that from figure 5.7, even when I did not undertake the free surface correction, the δt^* are still within the error bar of the results with free surface correction and likely surface velocities. So, under the condition of surface velocity are uncertain for the plentiful SKIPPY data, even I undertake the δt^* measurement without free surface correction, I should obtain reasonable good results.

5.5.2 The choice of window length, window function and spectrum estimator

In choosing the window length for the spectral estimation, the window must be long enough that an accurate estimate of the spectrum can be made, but short enough that secondary phases do not move in or out of the window in different distance range. A longer window reveals the spectrum in greater detail. If the spectrum lacks detail, the spectral fall-off is difficult to identify accurately and is possibly undersampled in the case of very short windows, resulting in inaccurate estimates of the spectral decay.

In this study, an optimum window length was chosen to give the clearest amplitude spectra; the *P* and *S* waves together with a few seconds of their coda were used in the spectral analysis. The spectrum is close to stationary, matching the requirement for an FFT. In other

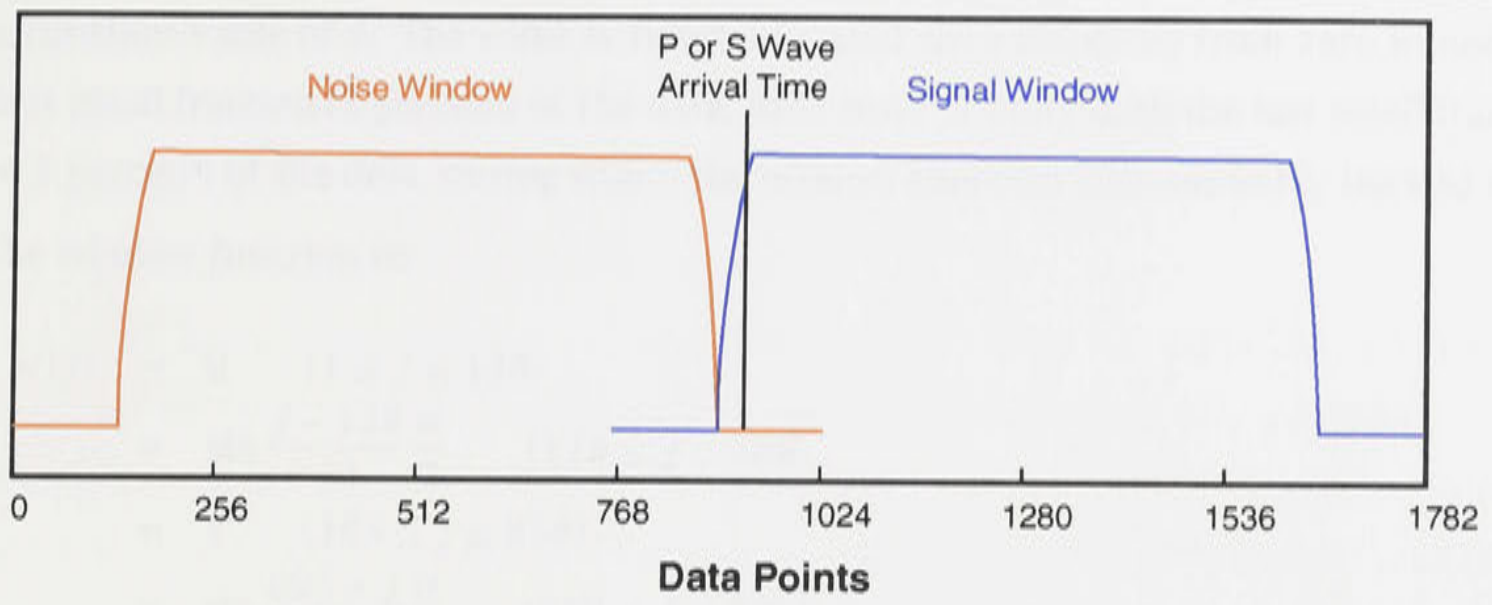

Figure 5.8: Graphical depiction of sin-taper window function.

words, the spectrum is very robust, but it is slightly influenced by the factors discussed in the following sections.

The application of window in spectrum analysis will lead to a distorted spectrum because of the limited window length. To keep the spectrum distortion close to minimum, the following properties from the spectral window will be required, which correspond to the applied window [Båth, 1984]:

1. A high concentration to the central (main) lobe which requires a broad time window;
2. A small or insignificant side-lobe which requires smooth time window without sharp corners.

In other words, the choice of window function lies in subtle trade-offs between making the central peak as narrow as possible versus making the tails of the distribution fall off as rapidly as possible.

A sine-tapered rectangular window was applied, which retains the merit of the broad time window, and avoids high-frequency oscillations and negative side-lobes caused by the sharp corners and vertical sides of the rectangular window.

I computed the discrete Fourier transform within time windows of 51.2s length (1024 samples at 20 sample s^{-1}) and the windows start 6.4s (128 samples at 20 samples) preceding the time for picking the earliest arrival of each wave type. The noise windows are also 51.2s in length and they start at 44.8s preceding the time for picking the earliest arrival of each wave type. To avoid tapering the signal, I put the signal window a few seconds before the P or S wave arrive time (see figure 5.8).

When I applied the data windowing to signal and noise windows containing 1024 samples, the first 128 and the last 128 samples were assigned to zero. After the first 128 samples and before the last 128 samples, a sine taper was applied to both sides of the signal and noise windows. The length of each taper was determined to be 2s of length (40 samples at 20 sample s^{-1}). In the middle part of the data window for 768 samples, the window function

has a constant value of 1. The window function I used rises smoothly from zero to unity in the first small fraction (5 percent) of the data, then stays at unity until the last small fraction (again 5 percent) of the data, during which the window function falls smoothly back to zero.

The window function is:

$$\begin{aligned} w(j) &= 0 \qquad (1 \le j \le 128) \\ &= \sin \frac{j-128}{40}\frac{\pi}{2} \qquad (128 \le j \le 168) \\ &= 1 \qquad (168 \le j \le 856) \\ &= \sin \frac{896-j}{40}\frac{\pi}{2} \qquad (856 \le j \le 896) \\ &= 0 \qquad (896 \le j \le 1024) \end{aligned} \tag{5.36}$$

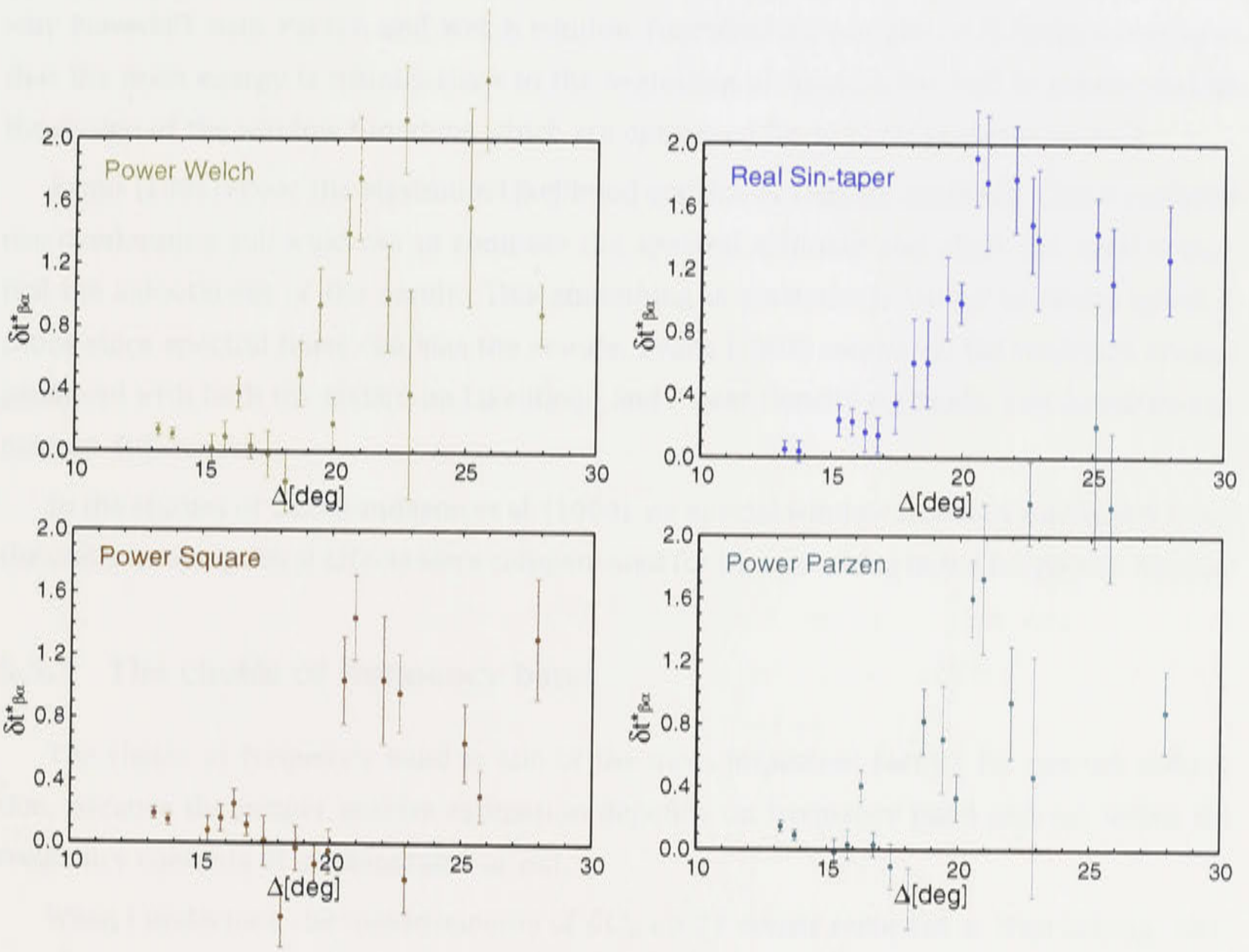

Figure 5.9: Spectral ratio as a function of distance calculated by RealFFT with sin-taper window function and calculated by PowerFFT with Parzen, Welch, Square window function.

By comparing the sine-taper window function used in this study with window functions like Square, Parzen, Welch etc, the effective window width and effective window rise/fall times of the Square, Parzen, Welch etc are both of the order of 50 percent of the data. Those window functions squeeze a little bit of extra narrowness out of the main lobe of the leakage function, but trade this off by widening the leakage tail by a significant factor [Press et al., 1995].

Another merit of the sine-taper window function I used here is that it is a flat-topped

window which throws away less of the data. An alternative way to deal with this problem is to use overlapping data segments.

The method of RealFFT used here gives 512 samples of the power spectrum up to the Nyquist frequency, 10 Hz, with a spectral resolution of 0.02 Hz.

I compared the spectrum results by using different FFT estimators and window functions. Although the overall envelope of the spectrum did not change much with different window functions, the window functions did have a great impact on the slope of the spectral ratio. Figure 5.9 shows the spectral ratio as a function of distance calculated by RealFFT with sine-taper window function and by PowerFFT with overlapping sub-windows and Parzen, Welch and Square etc window functions. I found the RealFFT with sine-taper window function gives the best results and PowerFFT with Square window function gives the worst results. One reason why PowerFFT with Parzen and Welch window functions do not give satisfactory results is that the main energy is usually close to the beginning of the window and is suppressed by the design of the window functions which are optimised for reducing spectra leakage.

Evans [1993] chose the Maximum Likelihood and Power Density methods. These methods use overlapping sub-windows to compute the spectral estimate and allow the user to control the smoothness of the result. This smoothing is particularly useful in taking spectral ratios since spectral holes can bias the results. Evans [1993] compared the resultant images produced with both the Maximum Likelihood and Power Density methods, and found no significant differences.

In the studies of Gudmundsson et al. [1994], no special window function was applied, but the undesirable spectral effects were compensated for by smoothing in the frequency domain.

5.5.3 The choice of frequency band

The choice of frequency band is one of the most important factors for spectra estimation, because the proper spectra estimation depends on frequency band pick-up fitting the frequency contents of seismograms or not.

When I undertook the measurements of δt^*_{sp} on 27 events recorded at Warramunga seismic array in the frequency band up to 2 Hz, I picked the frequency band by hand by looking at the spectrum of each specific event. The frequency band was chosen to be the part for which the slope of spectra is close to linear to minimise the dependence of attenuation on frequency. I undertook the measurements of δt^*_{sp} on Warramunga data. Generally, the frequency contents of seismograms are governed by epicentral distance.

In the low frequency band, the relationship between the spectral ratio and frequency is linear which indicates the weak attenuation dependence on frequency. In the frequency range higher than 1 Hz, the curve of spectral ratio against frequency is not linear, which reveals the frequency dependence in the broad frequency band.

In chapter 6, I use a narrow frequency band to obtain a robust δt^*_{sp} estimation at fixed frequency. In chapter 9, I will estimate δt^*_{sp} in a broad frequency band and construct a frequency dependent 3-D Q model.

5.6 Summary

In this chapter, I investigated the δt^*_{sp} estimation techniques. I discussed the choice of methods to calculate the FFT, the method to remove noise spectra and the assumptions involved. I have to make assumptions, such as the effect of source spectra is same for P and S, to obtain the δt^*_{sp} measurement. This is a good assumption for small events, but it is not necessarily same for the effect of source spectra for P and S for large events. However, I could not model this in this research, but the difference is reasonably small for my data. Therefore, the effect of source spectra is the same for P and S is a reasonably good assumption for my data.

I also investigated the effect of free surface on the spectra. I applied a method of free surface correction developed by Jepsen and Kennett [1990] and Kennett [1991b]. It works very well for the Warramunga data, because the surface velocity is very well controlled in the Warramunga site. But for most SKIPPY stations, I do not have enough information on the surface velocity. Thus I undertook experiments on Warramunga data with a range of surface velocities and without free surface correction. My experiments suggest the effect of free surface correction is reasonably small. Therefore, I will undertake spectra estimation on SKIPPY data without considering free surface correction.

Based on successful experiments of δt^*_{sp} estimation, I obtained a good estimation techniques of δt^*_{sp} which I could apply to the SKIPPY data set. In the following chapters, I will apply my techniques of δt^*_{sp} estimation to the SKIPPY data set.

Part III

Robust Measurement of δt^*_{sp} and 3-D Structure of Attenuation

Chapter 6

Measurement of the Path Average Properties of Velocity and Attenuation

6.1 Introduction

The deployment of 65 digital broadband portable seismic stations in the SKIPPY project which covers the whole Australian continent and the ideal configuration of earthquakes around Australia enables these natural events to be used as probes into the seismic structure of the upper mantle.

An attenuation estimation procedure has been developed based on the spectral estimation techniques in chapter 5. The slope of logarithm of the spectral ratio between P and S wave arrivals on the same record can be used to determine the differential attenuation between P and S because the frequency dependent factors common to the two wave types are canceled through the spectral ratio. The use of the logarithmic slope also minimises the influence of absolute amplitude variations. Tests on ways to treat noise show that the noise spectrum can be represented by a smoothed spectrum which fits the outline of the noise spectrum (see also section 5.2.1). The noise can be removed from the signal by subtracting the smoothed noised spectrum from the raw signal spectrum based on the assumption that the noise is stationary across the signal and noise windows. Tests using synthetic seismograms show that the differential attenuation between P and S can be recovered quite well but also that the influence of surface reflected phases within the P and S wave spectral windows can be important (see also section 5.4.2).

In the measurements of δt^*_{sp}, I found that in the low frequency band, there is a linear relation between the spectral ratio and frequency which indicate the weak attenuation depen-

dence on frequency. The curvature of the curve of spectral ratio against frequency occurs at frequencies higher than 1 Hz, which reveal the frequency dependence in the broad frequency band. The greater the curvature, the stronger frequency dependent of attenuation. In this chapter, I undertake the measurement of differential attenuation δt^*_{sp} and path average properties of dependence of attenuation on frequency γ at a fixed frequency around 1 Hz. The narrow frequency band and weak frequency dependence will reduce the error and enable robust estimation of δt^*_{sp}. This will also allow us to investigate the lateral variation of dependence of attenuation on frequency. In the chapter 9, I estimated the δt^*_{sp} over a broad frequency band. I could then invert Q and frequency dependent parameter as a function of depth at same time.

The estimation of differential attenuation between P and S using data from the Warramunga array shows relatively constant low values at shorter epicentral distances, a steep increase at medium distances, and a gradual decrease for larger distances. The differential attenuation variation with distance reveals the attenuation variation with depth. The systematic application of the spectral ratio approach to the estimation of the differential attenuation between P and S to the broadband data from SKIPPY stations provides measurements along nearly 2,000 refracted raypaths mostly sampling the northern and eastern part of the continent. The measurements also clearly delineate major variations in attenuation between the cratonic structures in the centre and west and the eastern part of Australia.

6.2 Broadband Data Selection and Analysis

6.2.1 Station Distribution and Path Coverage

I have used data from a set of portable broadband deployments across the Australian continent. Most of the data comes from the SKIPPY experiment [van der Hilst et al., 1994] during the period 1993-1996, in which a group of up to 12 instruments was used at a time. Each deployment had an interstation spacing of about 400 km, and a typical duration of 5 months which is sufficient to provide good coverage of paths from the strong regional seismicity to the North and east of Australia. The data is supplemented by a separate deployment, KIMBA in 1997-1998, with broadband instruments in the Kimberly region of Northwestern Australia. The earthquakes in the seismicity belt extending through Indonesia, New Guinea, Vanuatu, Fiji to the Tonga-Kermadec subduction zone recorded at the 65 SKIPPY and KIMBA stations provide nearly 2000 paths sampling the lithosphere and mantle under the Australian continent, Coral Sea and Tasman Sea.

The frequency content of the seismograms vary significantly with epicentral distance. For many paths beyond 20° the higher frequencies are reduced for P and almost suppressed for S.

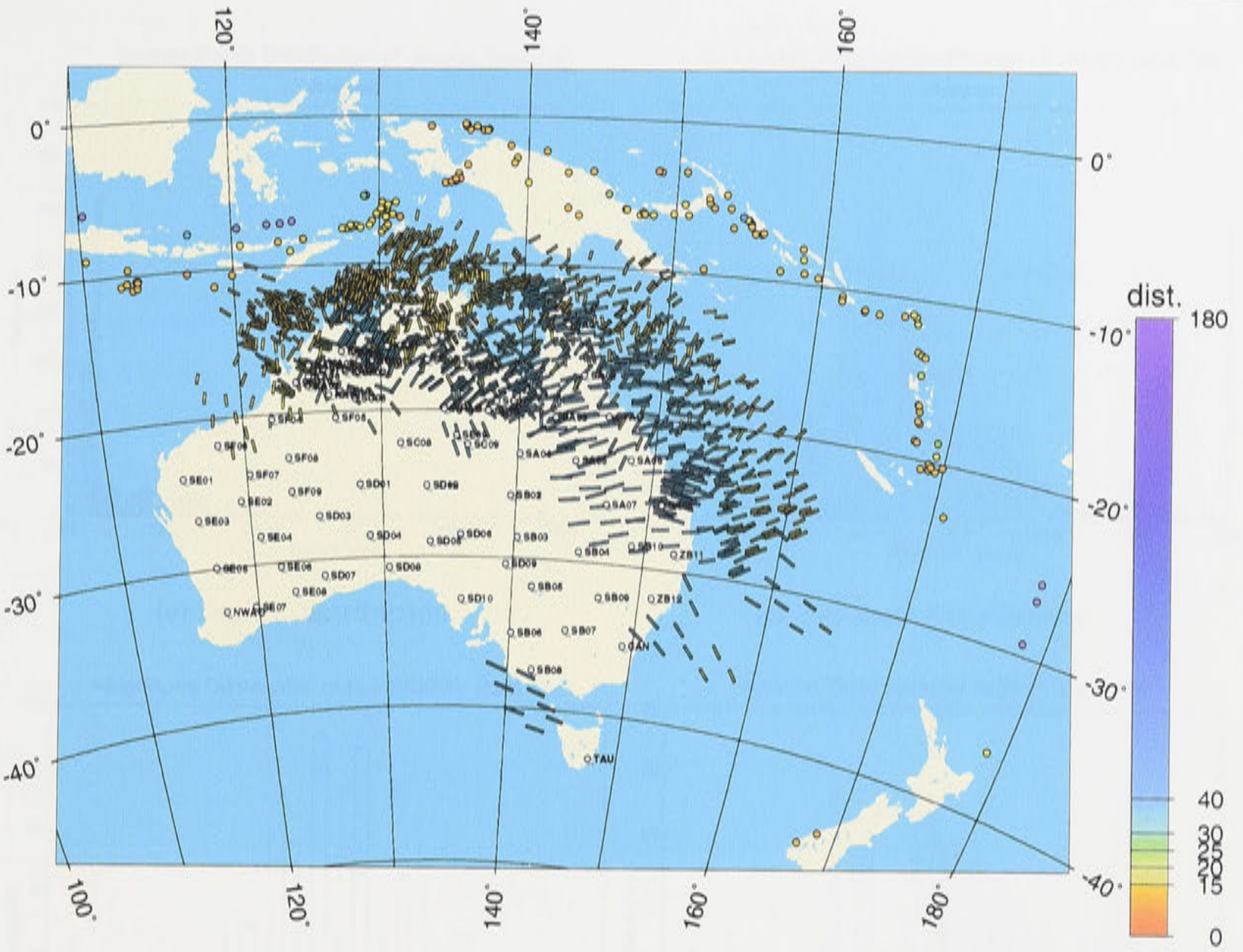

Figure 6.1: Illustration of SKIPPY data set with stations and midpoints of the raypaths colour scaled by epicentral distances. The location of each little bar represents the greatcircle projection of midpoint at Earth surface. The orientation of each little bar represents the direction of raypath.

6.2.2 Statistical Analysis on the SKIPPY Data Set

Depth Distribution of the SKIPPY Data Set

As illustrated in figures 1.1(a) and 6.2(a), most of earthquakes in my data set are shallow earthquakes. Over 56% of the earthquakes have source depths shallower than 40 km. There are around 30% earthquakes with source depths between 30-40 km and 20% earthquakes with source depths shallower than 20 km. Most of the shallow events occur in Indonesia, New Guinea, Vanuatu and Fiji.

However, there are a few groups of events which depth are deeper than 300 km, some of them up to 600 km. Those group of events are from Tonga-Kermadec subduction zone.

Epicentral Distance Distribution of the SKIPPY Data Set

Figure 6.2(b) shows the distribution of epicentral distances with SKIPPY data set. Most of epicentral distances in the SKIPPY data set are in the range between 20° to 30° with the largest number of ranges near 22°. This indicates that most of my ray paths will pass through the depth range of all upper mantle but the best ray path coverage will be in lithosphere and

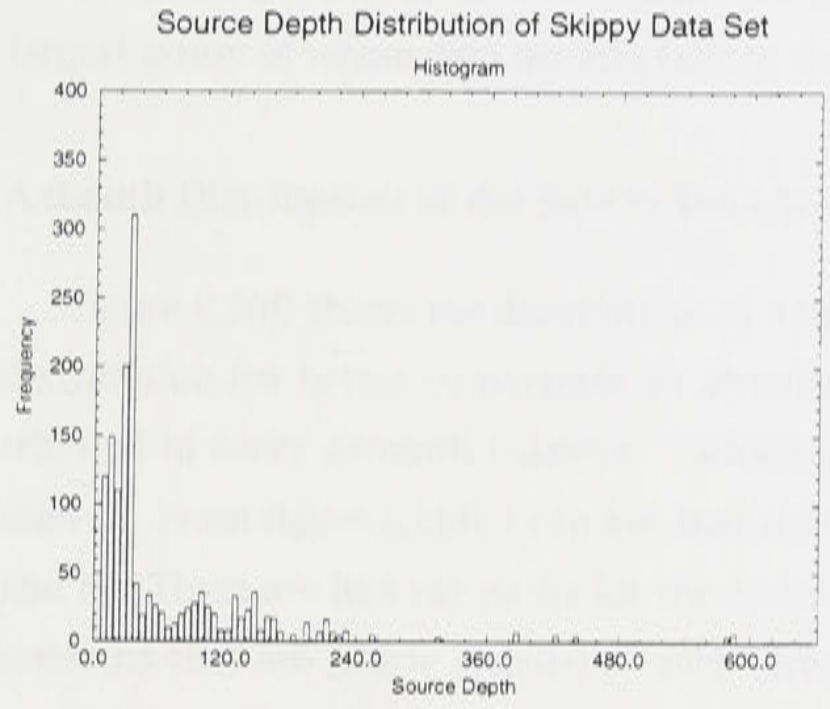

(a) Depth Distribution

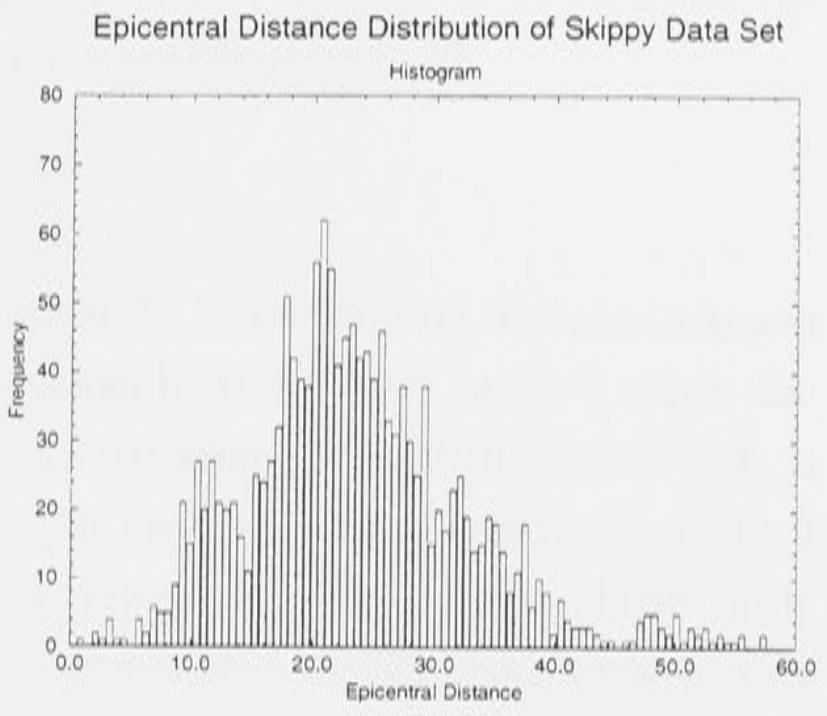

(b) Distance Distribution

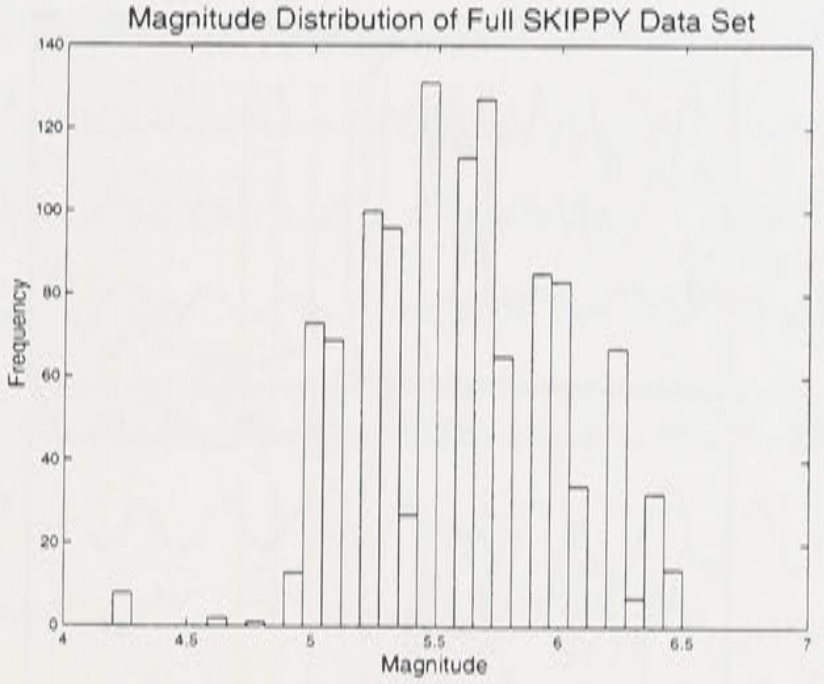

(c) Magnitude Distribution

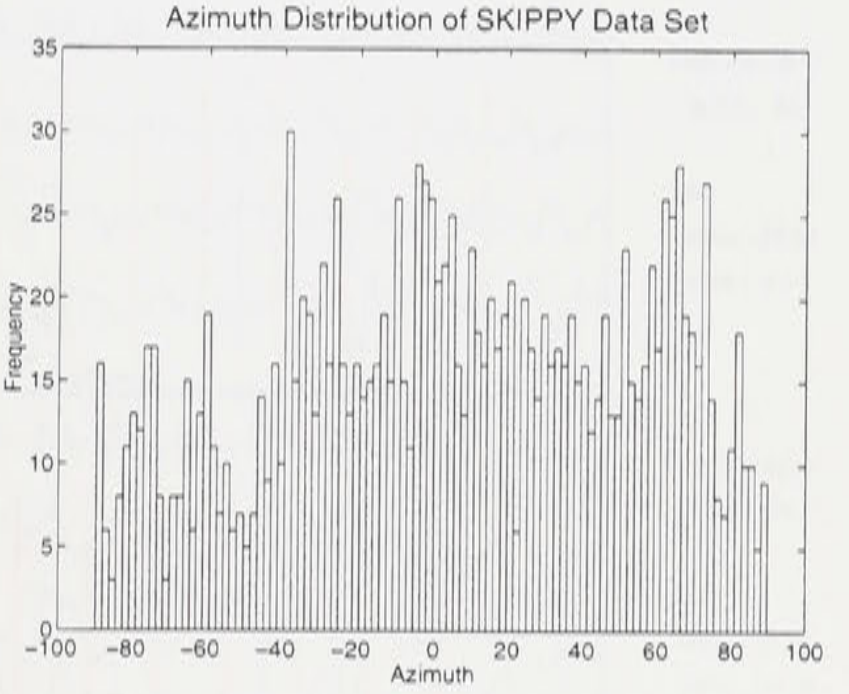

(d) Azimuth Distribution

Figure 6.2: Distribution of depth, distance magnitude and azimuth of the SKIPPY data set used in this study.

transition zone. Thus my data set will have limited resolution in the deeper part of the mantle.

The paths have been chosen to avoid the complex of subduction zone to the north where strong lateral variation in attenuation are to be expected.

Magnitude Distribution of the SKIPPY Data Set

Figure 6.2(c) displays the distribution of magnitude of the SKIPPY data set. The magnitude of most of the earthquakes recorded by SKIPPY stations are between 5 to 6. The magnitude distribution is very important for my δt^*_{sp} estimation. The assumption of source spectra of P and S are same I made when I estimated the δt^*_{sp} is only suitable for the small and medium events. Fortunately, most of my data are smaller than Mb 6. Therefore, the assumption that the source spectra of P and S are the same is reasonable for my data.

There are a group of data for which the magnitudes are not available in my database. The largest group of whole data set still falls in the the range between Mb 5-6.

Azimuth Distribution of the SKIPPY Data Set

Figure 6.2(d) shows the distribution of azimuth of the SKIPPY data set. The ideal azimuth distribution for better constraints on structure would be that the ray path are evenly distributed in every azimuth corridor. Unfortunately, the azimuth distribution of my data is uneven. From figure 6.2(d), I can see that there more ray paths for the azimuths near -40, 0 and 60. There are less ray paths for the azimuths near -80, -60, 80. This means I have many raypaths that are nearly parallel to each other. I do not have enough raypath which cross each other. This is the reason why I have to construct a set of 1-D model profile rather than to build a 3-D tomographic model.

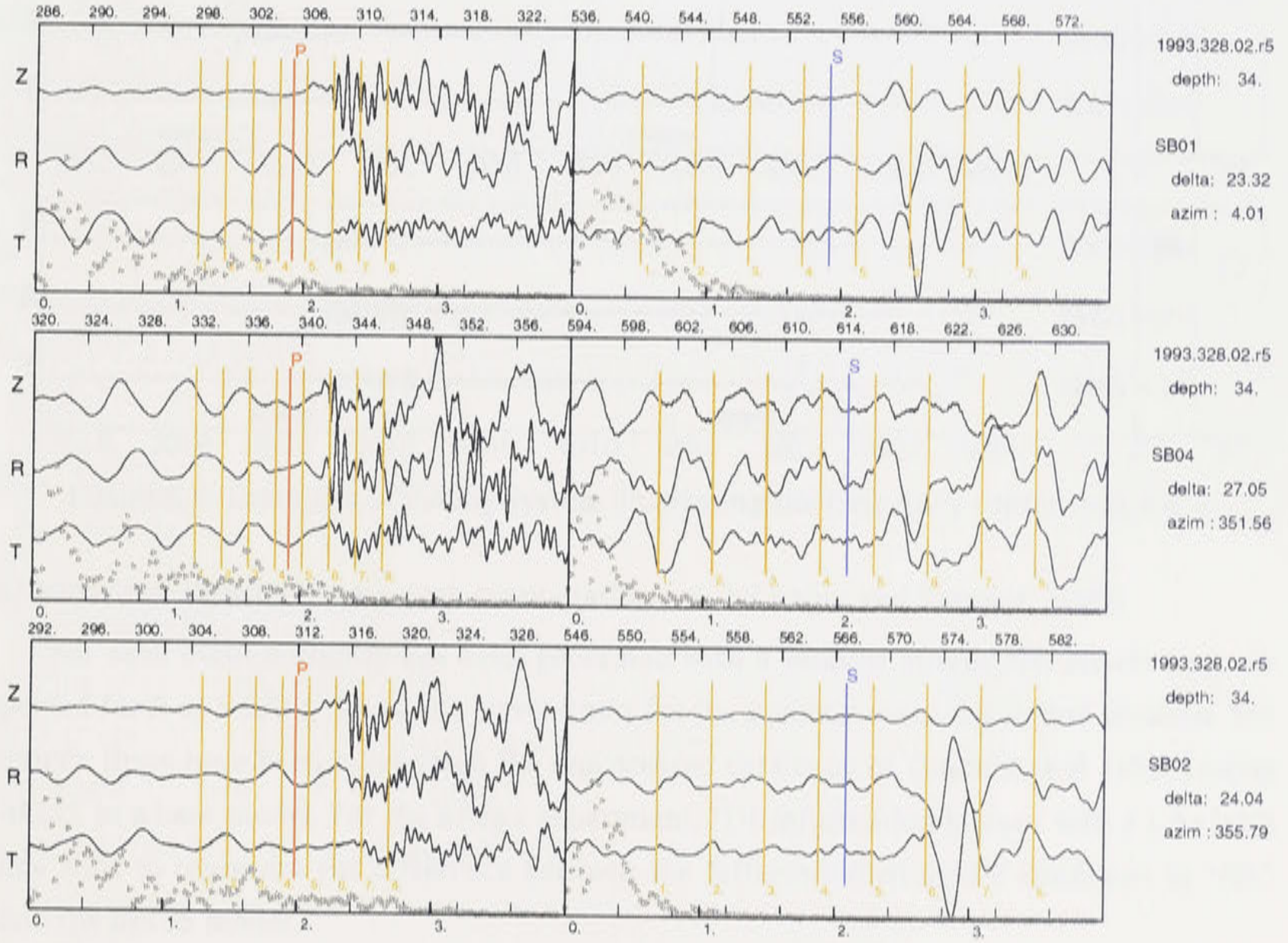

Figure 6.3: Examples of coding system for arrival time. The red line and the blue line indicate the *P* wave and *S* wave arrival time predicted by model *ak135* . The brown bars are used to locate the actural *P* wave and *S* wave arrival time. The grey triangles are *P* and *S* wave spectra.

6.2.3 Coding Scheme for Broad-band Data Set

In order to provide a convenient summary of the data set from the different stations I have used a simple coding scheme to provide an impression of the travel-time residual and

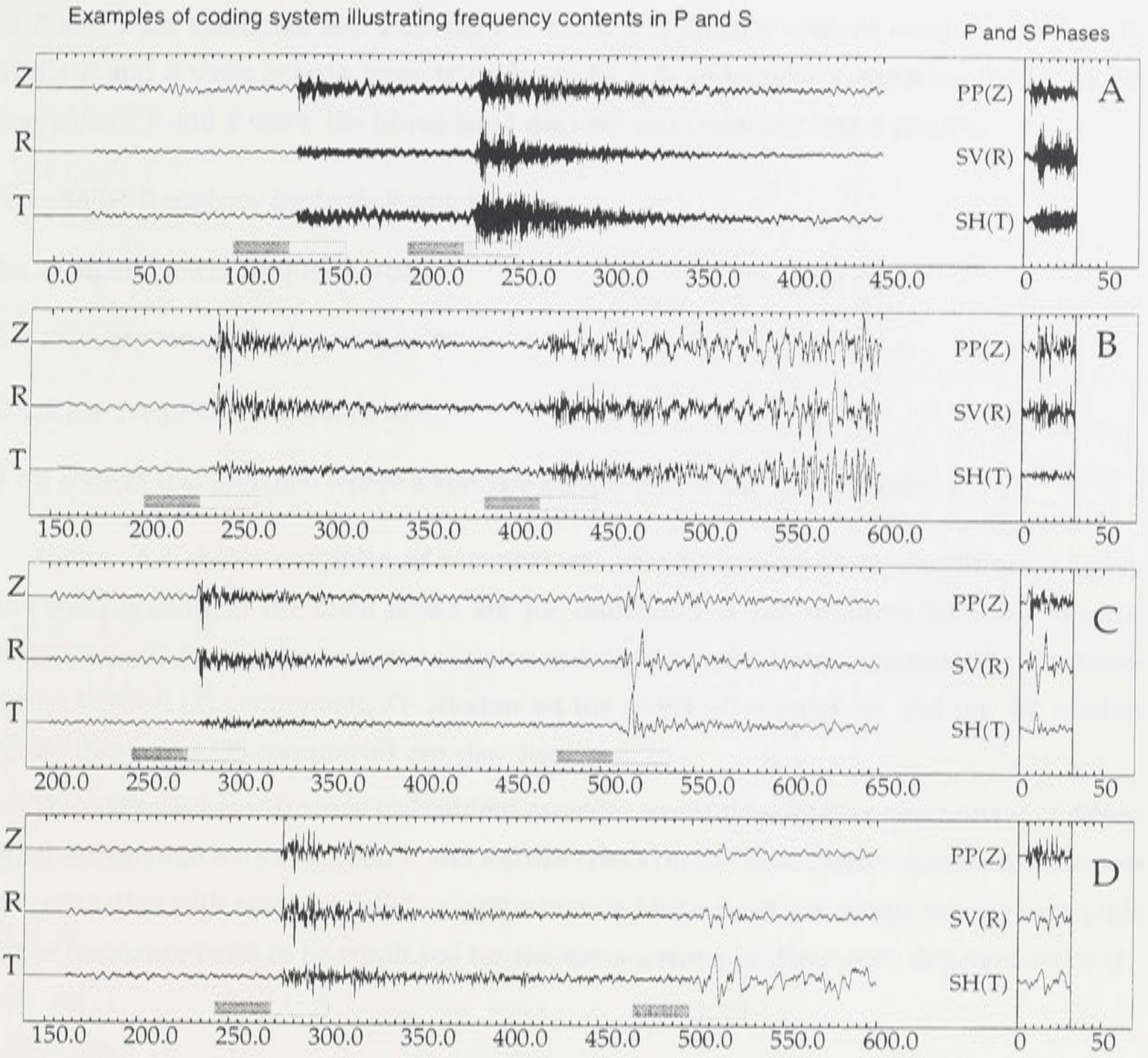

Figure 6.4: Examples of coding system illustrating the frequency contents in *P* & *S*

Q behaviour associated with each event-station pair [cf Kaiho and Kennett, 2000].

For each event a display has been generated with a window around the arrival time expected for *P* or *S* using the ak135 travel times for the nominal event depth and location. For SKIPPY these have been taken from the reprocessed catalogue of Engdahl et al. [1998] using *ak135* as a base model. For the KIMBA experiment, PDE information is used with a 1.8 s base line shift to represent the difference between the Jeffreys-Bullen model employed by NEIC and the *ak135* model.

The coding scheme is illustrated with an example in figure 6.3. The arrival is judged to lie in one of a set of time bins (2 s wide for *P*, 4 s wide for *S*) and assigned the code of the numbered bar to the right. Thus events which lie within ±1 s of the expected arrival time from the *ak135* model for *P* are assigned to bin 5 (±2 s for *S*). A code of 0 is assigned where the arrival time could not be adequately judged. The time bins for picking up the arrivals of *P* and *S* are illustrated in figure 6.3. The *P* and *S* wave spectra are also calculated and displayed in figure 6.3 as grey triangles.

This process allows rapid assessment of a large volume of data. In addition the spectra

of P and S are estimated and a measure of relative frequency content assigned. By looking at the P and S wave spectra (grey triangles in fig 6.3) and visibly comparing the frequency contents of P and S wave, the broad-band data set was classified into 4 groups:

A : similar frequency for both P and S

B : S slightly lower frequency than P

C : S clearly lower frequency than P

D : S low frequency compared to P

0 : a code of 0 is assigned where a spectral comparison could not be made.

Figure 6.4 shows examples of seismograms which correspond to the different codes. The solid boxes and the open boxes are the indication of the windows used for spectral measurements on precursory noise samples and signal for the P and S phases. The P window on the Vertical (Z) component, SV window on the radial (R) component and the SH window on the transverse (T) component are also displayed.

The coding scheme for spectral content provides a useful qualitative assessment of differential attenuation between S and P and a cross-check on the quantitative spectral techniques In conjunction with epicentral distance information I have used the coding system as a guide to the frequency band to be employed for the measurement of frequency dependence of Q.

6.3 Path Average Property of Velocity in the Upper Mantle

6.3.1 Introduction

The wavespeed patterns of body waves agree well with independent surface wave studies in the zones of common coverage. So I could ask the question 'Does the pattern of attenuation agree with the lateral velocity variation'.

The upper part of the mantle in the outer 700 km of the Earth contains some of the most important lateral heterogeneities in structure, such as those associated with subduction zones and major continental rifts. However, even in those regions away from the direct influence of active tectonics, there is a complex hierarchy of structural features in the mantle. Recently, it has become possible to construct high resolution 3 dimensional models of the seismic wavespeed distribution directly from observations of high frequency P and S waves, long-period S and surface waves.

Kennett [1993] has summarised much of the available information on the global seismic wavespeed distribution in the upper mantle. Most of the work on upper mantle structure has been directed towards the elucidation of radial structure. In general the radial gradients in

velocity are substantially larger than horizontal gradients [Kennett, 1991c]. But the deviation of seismic velocity structure from the purely radial are of particular significance because they can give a direct indication of processes operating in the mantle on a wide variety of scales. It is likely the small scale regional deviations from a radial base model have 1-2 per cent variability superimposed on the 5 per cent or so variation associated with the larger scale structures. Heterogeneity also exists on even smaller scales and this smaller scale 'speckle' is a major contributor to the complexity of body wave codes.

The high and low velocity features in the large scale structures determined by global tomography and the largest scale features in specific upper mantle models are likely to be thermal in origin. Smaller scale structures can be produced by the substructure of a conventional flow regime.

6.3.2 Estimation of Binned P and S Wave Travel Time Residuals δt_s and δt_p Based on Coding Scheme

For easy access to the SKIPPY data set, I have used a coding scheme described in 6.2.3 and illustrated in fig 6.3. By comparing the P and S wave arrivals to the expected arrival time from the *ak135*, the events were assigned to a set of time bins. Thus the P and S arrivals of each individual event are represented by the time codes assigned by the coding scheme. The SKIPPY data set could be easily processed by dealing with the time codes. By picking up the time codes assigned by the coding system, I have plotted the SKIPPY raypaths in fig 6.5 colour scaled by the P and S travel time residuals relative to the expected arrival time from the *ak135* model for the source depth. The raypaths in subfigures (a), (b) and (c) in the left column are colour scaled by the value of δt_p. The raypaths in subfigures (d), (e) and (f) in the right column are colour scaled by the values of δt_s.

The P and S travel time residuals represent the path average velocity of P and S wave. P and S travel time residuals are also the basic information to construct the fine velocity structure. In the following sections, I have analysed the lateral variation of δt_p and δt_s, and the correlation between δt_p, δt_s and δt_{sp}^*.

6.3.3 Lateral Variation of δt_s and δt_p

Figure 6.5 summaries the δt_p and δt_s estimated from the SKIPPY data set. Both δt_p and δt_s are plotted into three distance groups 8° -20°, 18° -30°, 28° -45°. There are strong lateral variation in δt_p and δt_s displayed in figure 6.5. The strongest contrast between northwestern Australia and Coral Sea area appears in the figure 6.5 (d) which is δt_s in the distance range 8° - 20°. There are a group of fast paths beneath the northwestern Australia and a group of slow paths beneath the Coral Sea area. This suggests that a shallow high velocity zone lie beneath the northwestern Australia and a shallow low velocity zone beneath Coral Sea area which

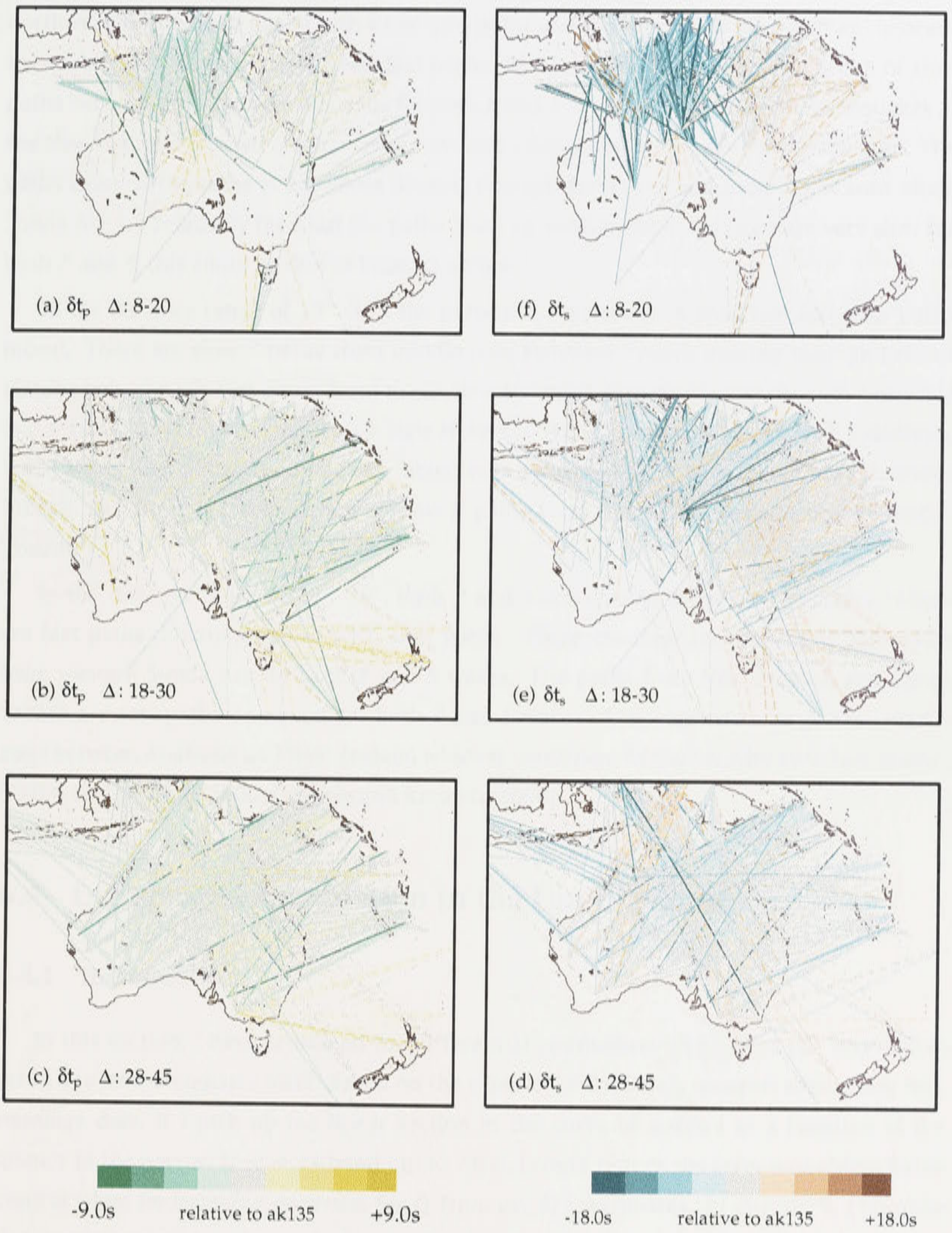

Figure 6.5: Summary of δt_p and δt_s estimated from the SKIPPY data set. The raypaths in subfigures (a), (b) and (c) lining along left column are colour scaled by the value of δt_p. The raypaths in subfigures (a), (b) and (c) lining along right column are colour scaled by the values of δt_s. The fast paths (negative δt_s and δt_p) are in solid lines and the slow paths (positive δt_s and δt_p) are in dash lines.

is confirmed by bodywave and surface wave studies [Kaiho and Kennett, 2000; Debayle and Kennett, 2000]. For *P* wave, in the depth range 8° -20°, the fast paths are dominant beneath the northwestern Australia mixed with a few slow paths and the slow paths are dominant beneath the Coral Sea Area mixed with a few fast paths. In this depth range, there is a group of slow paths beneath the middle of Australia for both *P* and *S* waves. The paths from earthquakes at the New Hebrides Trench are fast for *P* wave and slow mixed with a few fast paths for *S*. The paths from earthquakes at Indonesia passing through Banda Sea and subduction zone along Sunda Arc are relatively fast. But the paths from an earthquake at Sulawesi are very slow for both *P* and *S*, this could be due to location errors.

In the distance range of 18° -30°, the pattern is very complex with fast and slow paths mixed. There are slow *S* paths from middle New Hebrides Trench passing through Bellona Plateau between the fast paths from north New Hebrides Trench passing through Coral Sea and a group of fast path from South New Hebrides Trench passing through New Caledonia. For *P* wave, fast paths are dominant mixed with slow paths for paths from New Hebrides Trench. But there is a clear group of slow *P* paths from north New Zealand and Kermadec Trench.

In the distance range of 18° -30°, both *P* and *S* wave paths from New Hebrides Trench are fast paths dominant mixed with slow paths. There are clear two groups of fast paths from western Sunda Arc for both *P* and *S* waves. The paths from New Zealand and Tonga Trench are fast paths dominant for both *P* and *S* waves. This suggests a large low velocity zone between Australia and New Zealand which is confirmed by the velocity structure studies [Kaiho and Kennett, 2000; Debayle and Kennett, 2000].

6.4 Differential Attenuation in the Upper Mantle

6.4.1 Introduction

In this section, I have estimated the differential attenuation (δt^*_{sp}) from the SKIPPY data set at a narrow frequency band. Based on the experience from δt^*_{sp} measurement using Warramunga data, if I pick up the linear section in the curve of spectra as a function of frequency in the narrow frequency band (up to 2 Hz), I could reduce the error and obtain better control when undertaking inversion for Q from my δt^*_{sp} estimates. In chapter 9, I consider δt^*_{sp} measurement in a broad frequency band up to 6 Hz. Over the broad frequency band, I can obtain measurements of frequency dependence of attenuation, but the error bars are enlarged because in narrow frequency bands I have a limited number of data points. Thus, the δt^*_{sp} estimation in this section will provide us better constraints on the attenuation structure at fixed frequency around 1 Hz.

6.4.2 Estimation of the Differential Attenuation δt^*_{sp}

In the following, I investigate the dependence of attenuation on frequency based on the power-law relationship between frequency and attenuation $Q(f) = Q_0 f^{\alpha}$. For the SKIPPY data set, I find that the slope of the linear part of the curve of spectra as a function of frequency in a lower frequency band is controlled by Q but the shape of the curve controlled by α. The dependence of attenuation on frequency is weak in the relatively narrow frequency band which is lower than 2.0 Hz.

Over a narrow band in frequency Q can be treated as nearly frequency independent and then the slope of the logarithm of the spectral ratio is directly related to the difference in attenuation between P and S in the passage from source to receiver. The systematic application of this spectral ratio approach to the estimation of the differential attenuation between P and S δt^*_{sp} to the broadband data recorded at portable stations in Australia, provides measurements along nearly 2000 refracted raypaths mostly sampling the northern part of the continent for frequencies centred around 0.5 Hz. The measurements clearly delineate major variations in attenuation between the cratonic structures in the centre and west and the eastern part of Australia, with much stronger attenuation in the east.

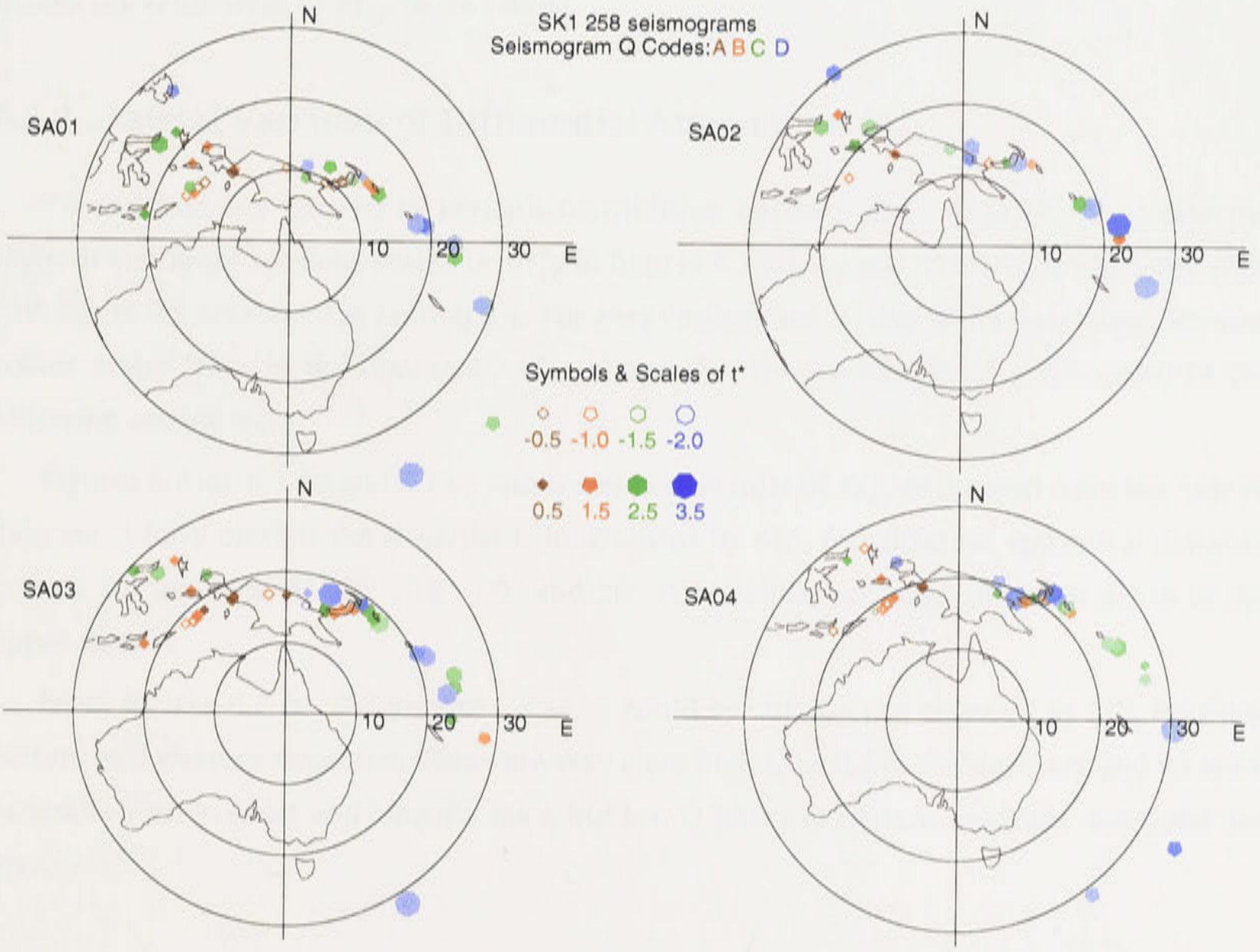

Figure 6.6: δt^*_{sp} estimated from the events recorded by SKIPPY stations SA01, SA02, SA03 and SA04. The different symbols represented the data group classified by the coding scheme and the size of the symbols are proportion to the value of δt^*_{sp}.

6.4.3 Tuning of δt_p, δt_s and δt^*_{sp} Estimation

To double check the δt_s and δt_p estimated by coding scheme and δt^*_{sp} estimated from spectral ratio. I have plotted the δt^*_{sp} station by station. Figure 6.6 is an example of δt^*_{sp} estimated from all the data recorded by stations SA01-SA04. The symbol and colour of the symbol represents the data group classified by coding scheme. The solid symbols represent the positive δt^*_{sp} and the open symbols represents the negative δt^*_{sp}. The size of the symbol is proportional to the value of the δt^*_{sp}. The position of the symbol is the location of the event from which the δt^*_{sp} was estimated.

If two close events are recorded by same station, they should belong to same data group. Because they travel along similar raypath, their attenuation should be similar. Thus if the colour of two close symbols is same, it suggests that the coding system works well. Otherwise, if the colour of two close symbols is different, this may suggest the coding scheme assigned wrong code for this event, e.g. the pick was close to a cell boundary. By undertaking this procedure and looking at the P and S wave arrivals and spectra illustrated in figures 5.4(a), 5.4(b), 5.4(c) and 5.4(d), I have checked all the events and corrected many errors generated by the coding scheme. This process is very time consuming but it reduces many errors and makes my estimation of δt^*_{sp} more robust.

6.4.4 Lateral Variation of Differential Attenuation δt^*_{sp}

To compare the pattern of raypath distribution between δt^*_{sp}, $\delta t_p$and δt_s. I plot the raypath distribution colour scaled by δt^*_{sp} in figures 6.7 (a), (b) and (c) which are in same style with figure 6.5 presented in section 6.4. For easy comparison, I have also plotted the raypaths colour scaled by γ in the figures 6.7 (d), (e) and (f). The estimation of γ discussed in the following section 6.5.

Figures 6.7 (a), 6.7 (b) and 6.7 (c) summarise my results of δt^*_{sp} estimated from the SKIPPY data set. I have plotted the raypaths colour scaled by δt^*_{sp} for different epicentral distance groups, for instance, 8° -20° , 18° -30° and 28° -45° , which sampling different depth in the upper mantle.

From figures 6.7 (a), 6.7 (b) and 6.7 (c), I could see distinctive contrast in δt^*_{sp} between eastern and western Australia. There are very clear high Q paths in the northern and western Australia both in short and long distance, but low Q paths in eastern Australia and Coral Sea area.

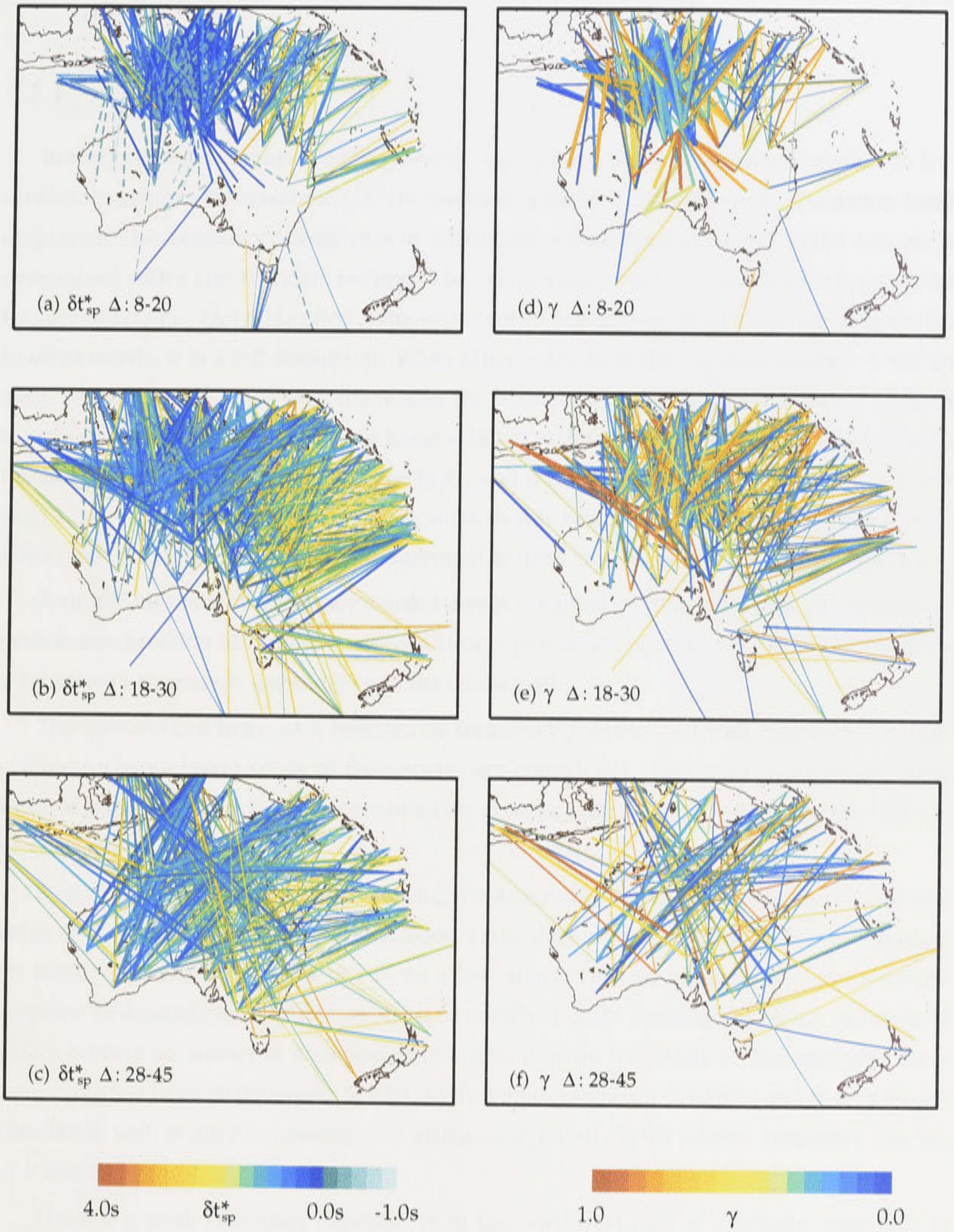

Figure 6.7: Summary of δt^*_{sp} and γ estimated from the SKIPPY data set. The raypaths in subfigures (a), (b) and (c) lining along left column are colour scaled by the value of δt^*_{sp} with line thickness inversely proportional to the inverse of the errors in the δt^*_{sp} estimation. The raypaths in subfigures (a), (b) and (c) lining along right column are colour scaled by the values of γ with line thickness inversely proportion to the inverse of the errors in the γ estimation.

6.5 Path Average Properties of Frequency Dependence of Attenuation γ

6.5.1 Introduction

In section 2.1.3, I summarised the previous research on dependence of attenuation on frequency. In general, the question 'is Q frequency dependent?' depends on the frequency band employed. The frequency dependence of differential attenuation between P and S arrivals is determined with a spectral ratio technique based on a power law relationship between Q and frequency $Q(f) = Q_0(f_0)(f/f_0)^{\alpha}$. The exponent α depends on depth and varies laterally. In other words, α is a 3-D parameter. When attenuation is frequency independent, α will be zero. The smaller the value of α, the weaker the frequency dependent of attenuation. When α is zero, the estimated δt^*_{sp} will have a linear relation with frequency. In my estimation of δt^*_{sp}, I found a nearly linear relation between $\ln R_{ij}$ and frequency f when the frequency is lower than 1 Hz. The frequency dependence is weak in this relatively narrow band of frequencies allows me to obtain a robust δt^*_{sp} measurement at fixed frequency around 1 Hz in section 6.4.

A simple measure of frequency dependence is obtained by fitting the spectral ratio information as a function of frequency using a simple power law relation $t^* = t^*_0(f/f_0)^{-\gamma}$ where γ represents an average dependence of the whole path.

The curvature of $\ln R_{ij}$ as a function of frequency f associated with non-zero γ is only apparent when a broad range of frequencies are considered. Therefore, a significant band width is required before the influence of a non-zero exponent γ in the power law relation can be determined.

By exploiting nearly 2000 paths crossing the Australian region, which provide a good coverage of the mantle, the geographic variation in the dependence of attenuation on frequency for body waves can be mapped in 3-D. As a first step, to obtain a general idea of the lateral variation of dependence of attenuation on frequency, I made some assumptions and defined a path average parameter of dependence of attenuation on frequency γ. The estimates for γ were extracted from observations in a broad frequency range (up to 6.0 Hz) and show a strong correlation with qualitative measures of attenuation based on the relative frequency content of P and S.

There is a weak frequency dependence in the northwest part of Australia, especially in the shallow part of the upper mantle where Q is very high. In the east part of the Australia, paths with high γ and low γ are mixed, which indicates a complex structure in attenuation.

6.5.2 γ Estimation Techniques and Assumptions Involved

I applied the γ estimation techniques I discussed in section 5.2.2 to the SKIPPY data set.

I illustrate the different classes of behaviour in figures 6.8(a) and 6.8(b). In each case I show the seismograms with indicators of the windows used for noise estimates (solid bars) and the *P*, *SV* and *SH* windows (open bars). The spectra for the *P*, *S*, *SH* signals are displayed as a function of frequency after subtraction of a noise estimate. In the lower panel I plot the variation of various logarithmic spectral ratios with frequency. The *S* spectrum is obtained by combining the *SV* and *SH* information.

For events with code A and B, I find that the spectral ratio as a function of frequency is close to linear for the frequency band up 6.0 Hz. For the data group A, both δt^*_{sp} and γ are small (figure 6.8(a)). For the data group B, the average δt^*_{sp} and γ are smaller than data groups C and D, but larger than the group A, and the dependence of the logarithmic spectral ratio on frequency is still close to a straight line, but there is a slight departure at higher frequencies. Not only the attenuation but also the dependence of attenuation on frequency is relatively weaker for groups A and B than groups C and D.

For events with codes C and D, the logarithmic spectral ratio shows clear upward curvature as a function of frequency indicating a clear frequency dependence, with γ typically greater than 0.3. For data group C, the dependence of the spectral ratio as a function of frequency could usually be approximated by two linear sections (figure 6.8(b)), with a break point between 1.2-2.5 Hz. The centre frequencies of the two sections lie around 0.6-1.2 Hz and 3.0-4.0 Hz. For data group D, most of the events have no high frequency content for *S* and observations are restricted to lower frequencies.

In the frequency band up to 1.0 Hz the logarithmic spectral ratio shows a nearly linear dependence on frequency for data from all four groups (A,B,C,D) and so I are able to obtain a reasonable estimate of δt^*_{sp} for frequencies around 0.5 Hz.

6.5.3 Geographical Variation of Path Average Properties of γ

Figures in 6.7 summarise the geographic behaviour of the exponent γ over the SKIPPY path coverage. I plot the raypaths colour scaled by γ for different epicentral distance groups, $8° - 20°$, $18° - 30°$ and $28° - 45°$, which sample different depths in the upper mantle. The lines are displayed with a thickness inversely proportional to the error in the estimation of γ. Thus thick lines represent paths for which γ has a small error and thin paths have large errors. Smaller values of γ are also normally associated with smaller errors. This suggest that measurements with weak frequency dependence are more robust than measurements with strong frequency dependence.

From fig 6.7, I could see clearly there is significant geographic variation in γ. Figure 6.7 (d) reveals the feature of geographic variation in γ for raypaths within relatively short epicentral range between $8° - 20°$. Therefore, this group of raypaths reflect the features of dependence of attenuation on frequency in the lithosphere and asthenosphere. Most of the sources of

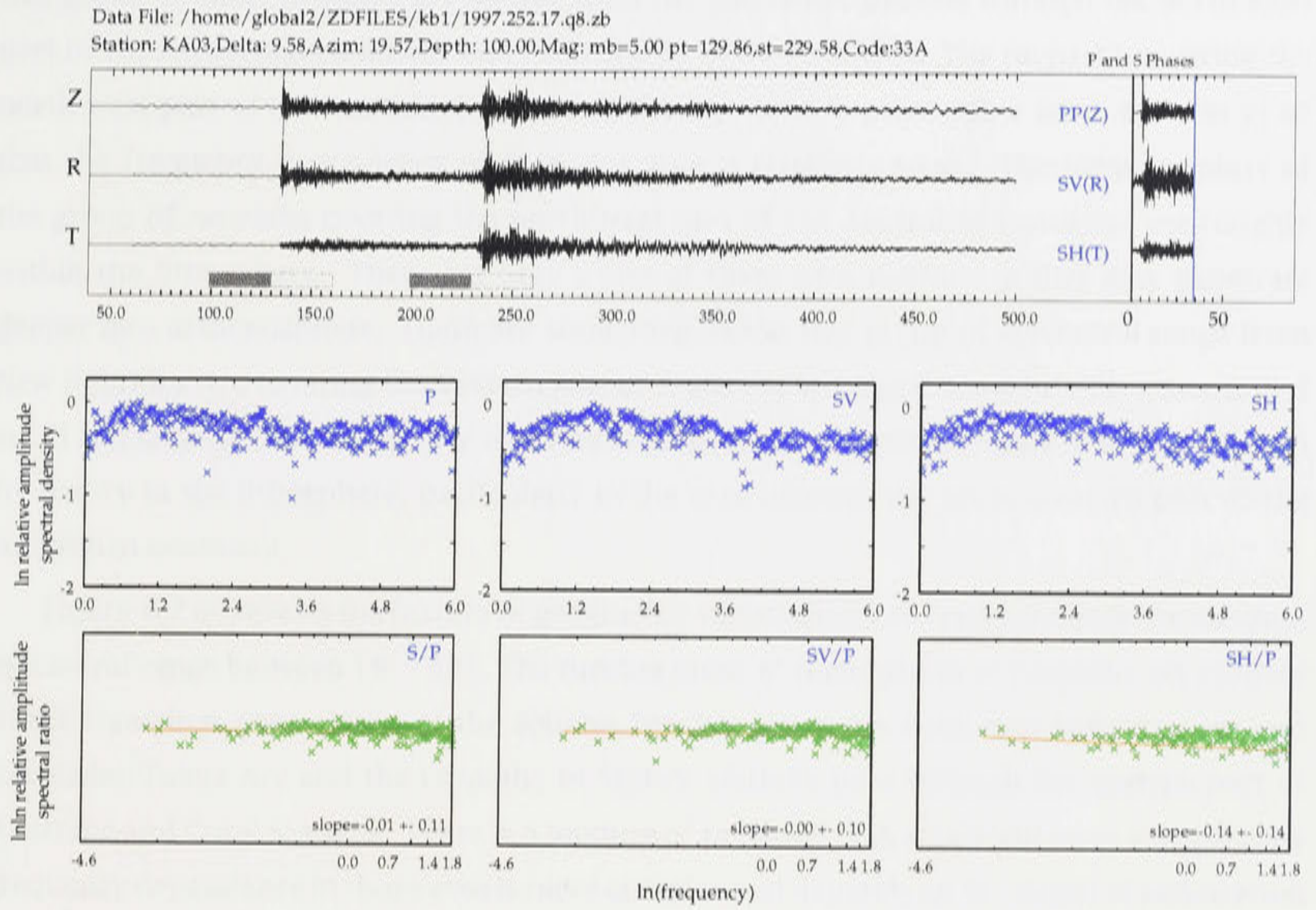

(a) Data Group A

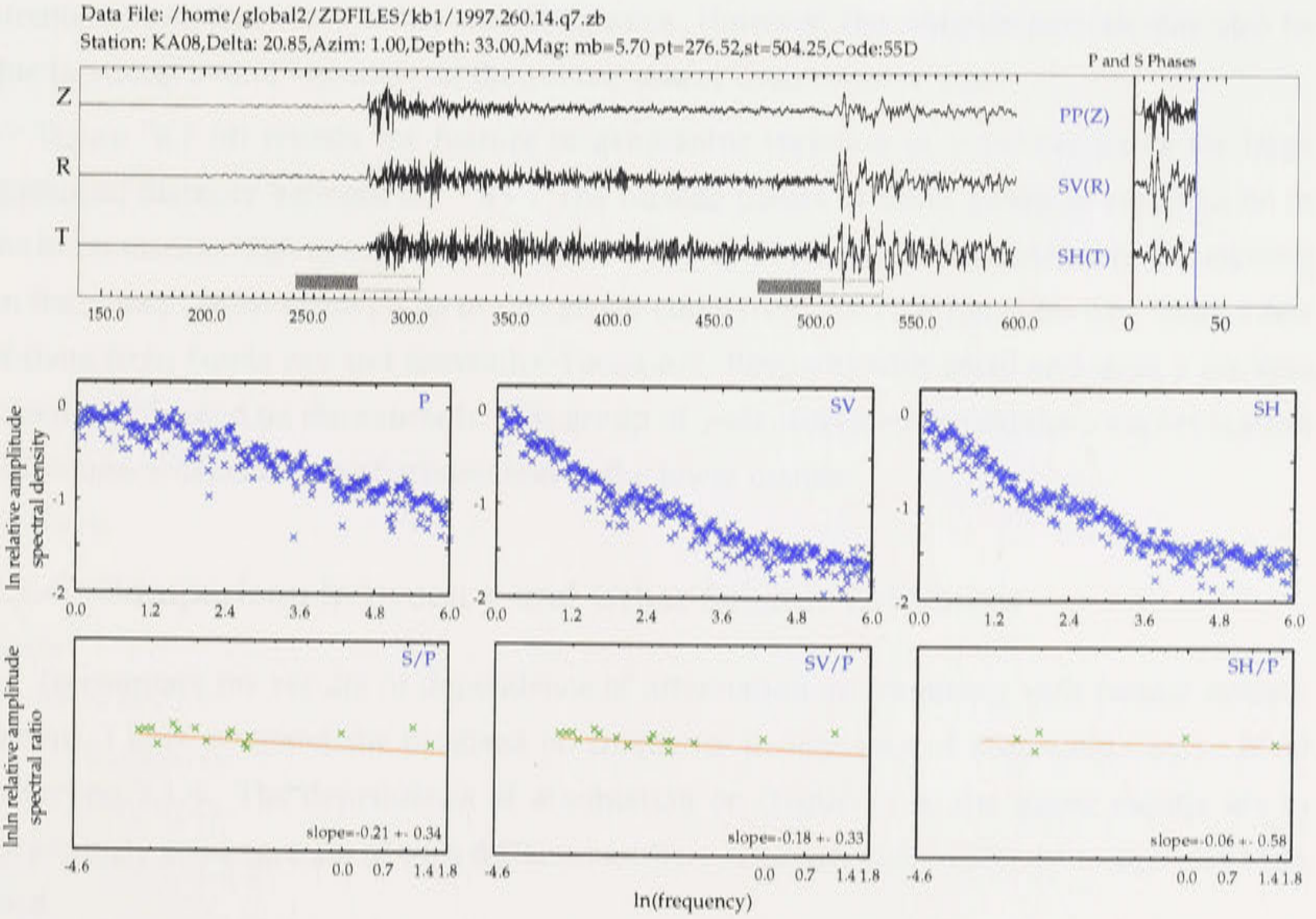

(b) Data Group C

Figure 6.8: Illustration of P and S phases, spectral ratio and log slope for different data groups

this group of short raypaths are mainly from the Sunda Arc passing through the north-west part of the Australian continent and recorded by SKIPPY stations. The raypaths covering the north-west part of the Australian continent show γ close to zero with a small error in γ; so that the frequency dependence of Q in this area is relatively weak. The turning points of the group of raypaths covering the north-west part of the Australian continent are roughly within the lithosphere. There are only a few of them with medium γ that may penetrate deeper into asthenosphere. There are some raypaths in this group of epicentral range from New Hebrides Arc covering the eastern part of Australia and Coral Sea area with a mixture of small and large γ. This group of γ measurement shows a weak dependence of attenuation on frequency in the lithosphere, particularly in the area beneath the north-western part of the Australian continent.

Figure 6.7 (e) reveals the feature of geographic variation in γ for raypaths with the medium epicentral range between 18° - 30°. The turning point of those group of raypaths are roughly in the transition zone. Many of the sources for this group are from New Hebrides Arc and Kermadec-Tonga Arc and the raypaths to SKIPPY stations pass through the eastern part of Australia and Coral Sea area. There is a mixture of raypaths with small and large γ so that the frequency dependence in those area is more complex and depends on the depth of penetration of the waves. The turning points of this group of raypaths are roughly within the transition zone. From this group of γ measurement, I could see complex feature of dependence of attenuation on frequency in the transition zone. However, the complex pattern may also be due to strong lateral variation on the source side or even receiver side.

Figure 6.7 (d) reveals the feature of geographic variation in γ for ray paths for large epicentral distance between 28° - 45°. The turning points of those group of raypaths lie in the lower mantle. This group of data also reveal complex feature of dependence of attenuation on frequency . Most of raypaths in this group come from the New Hebrides Arc, there a few of them from Sunda Arc and Kermadec-Tonga Arc. Raypaths with small and large γ are also mixed and depend on the azimuth. This group of γ measurement reveal the complex feature of frequency dependence of attenuation in the lower mantle.

6.5.4 Comparison between γ and Other Seismic Evidences

To compare my results of dependence of attenuation on frequency with former investigations, I have reviewed the progress on frequency dependence of attenuation up to 2000 in section 2.1.4. The dependence of attenuation on frequency in the upper mantle are in surprisingly good agreement with different authors although quite different techniques were used.

My measurement of frequency dependence of P and S waves in the upper mantle under Australia region are consistent with the results presented in the review above. The frequency

dependence of Q takes a power law form as defined in (5.4) and (5.22) with γ between 0.2-1.0 in the frequency range 0-6 Hz from near 2,000 paths. My results also indicated the depth and azimuth dependence of γ. The depth and azimuth dependence of the γ show that the frequency dependence of P and S waves in the upper mantle under Australia is complicated and three dimensional.

6.5.5 Comparison of γ with Mineral Physics Experiments

In section 2.2.2, I have reviewed the recent progress of laboratory measurement of attenuation and dispersion. The frequency dependence of Q^{-1} which is well documented in laboratory studies.

The values of γ obtained in this study are consistent with the results of frequency dependence of seismic wave attenuation in the upper mantle condition which have been done in the laboratory.

6.6 Correlation between the δt_p, δt_s, δt^*_{sp} and γ

6.6.1 Introduction

There is a range of evidence for lateral variations in seismic velocity in the lithosphere and the upper mantle transition zone. The lateral variation in velocity structure has been investigated by a number of techniques, including the analysis of travel-time residuals and waveform inversion, for both body and surface waves.

It has been observed that the Q variations generally correlate with the travel-time variations. There are many evidence show that fast travel-time paths are typically high Q and slow paths typically low Q [e.g., Der et al., 1986; Hashida and Shimazaki, 1987; Roult et al., 1990; Suda et al., 1991; Halderman and Davis, 1991; Roth et al., 2000]. In this thesis, an investigation has been conducted on the correlation of the lateral variation between velocity and attenuation.

I have used the broad-band information at frequencies up to 6.0 Hz to look for the frequency dependence of attenuation. With the assumption of a simple power law dependence of frequency (see equation 5.4) and the frequency dependence of attenuation for P and S waves is same, the spectral ratio information can again be used and γ can be extracted from the rate of change of the logarithmic slope of the spectral ratio with frequency. There turns out to be a strong correlation between γ and the differential attenuation δt^*_{sp}.

When the differential attenuation is low, the spectral content of P and S waves are similar, and the exponent γ is close to zero. The slope of the logarithmic spectral ratio departs further from linearity as the differential attenuation increases and γ departs from zero. For the

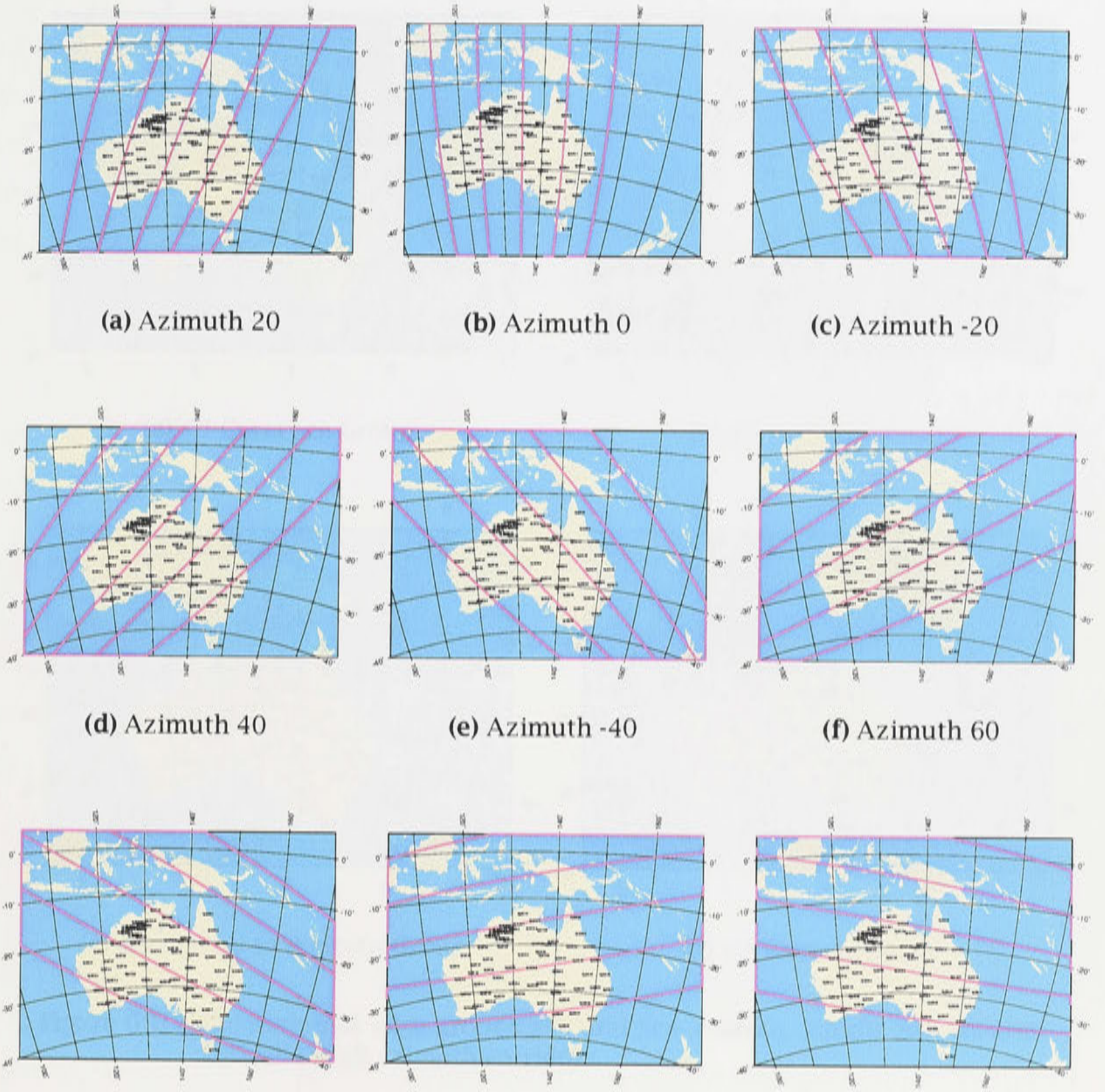

(a) Azimuth 20 **(b)** Azimuth 0 **(c)** Azimuth -20

(d) Azimuth 40 **(e)** Azimuth -40 **(f)** Azimuth 60

(g) Azimuth -60 **(h)** Azimuth 80 **(i)** Azimuth -80

Figure 6.9: Illustration of azimuth corridors and slices.

strongest differential attenuation where the frequency content of S is much lower than that for P, γ deviates noticeably from zero and the logarithmic spectral ratio shows distinct curvature over the frequency range from 0.25 to 2-3 Hz, although there is often little high frequency content. Normally γ is not too large and so a linear approximation to the logarithmic ratio is a good representation over the interval less than 1 Hz .

6.6.2 Sorting δt_p, δt_s, δt^*_{sp} and γ into Azimuth Corridors and Slices

To reveal the lateral variation of δt^*_{sp} in greater detail, I classified the raypaths into 9 azimuth corridors following Kaiho and Kennett [2000], The central corridor is the azimuth range from -10° to 10°with centre azimuth 0. Then I rotated the corridors by 20° step in

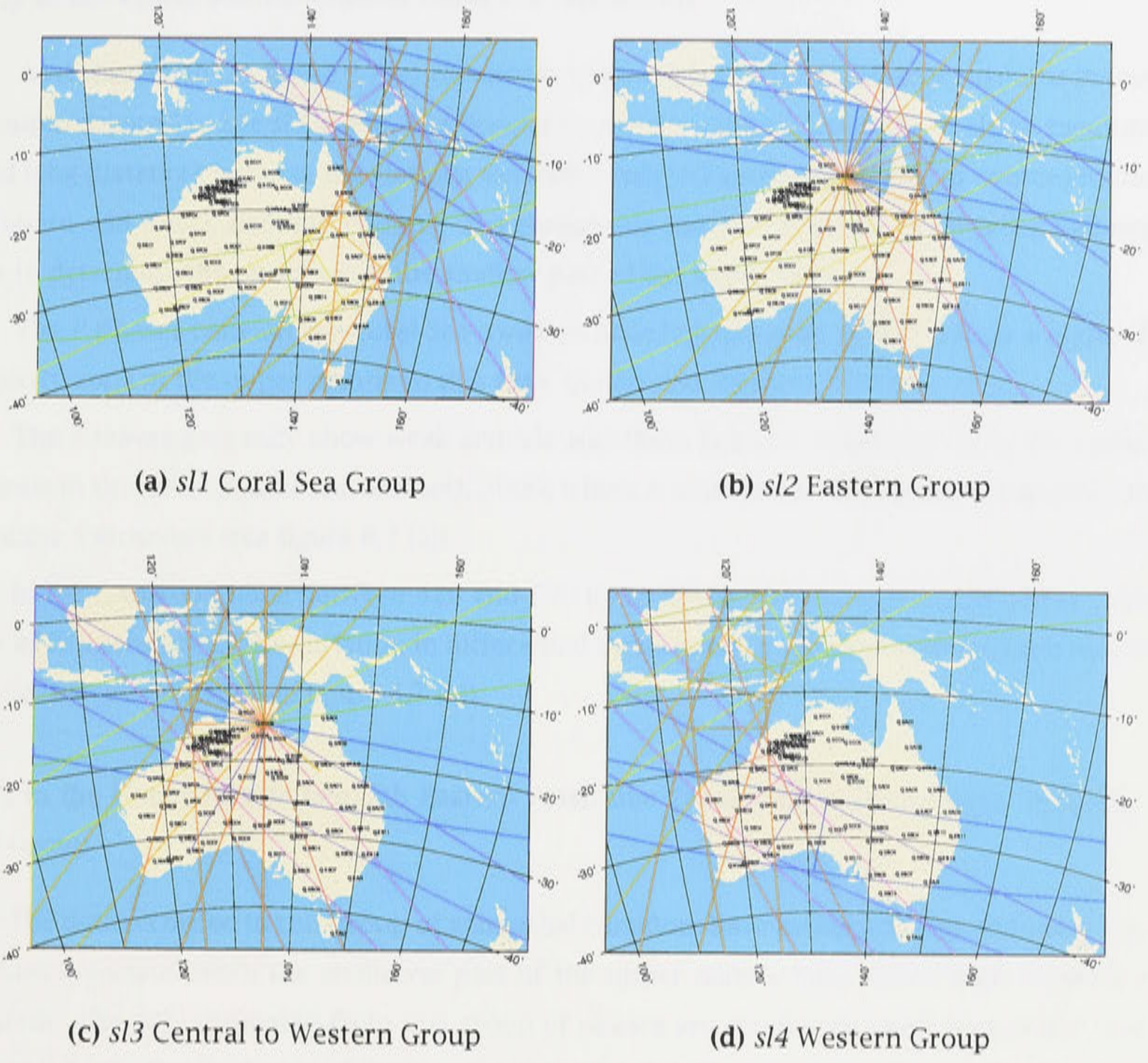

(a) *sl1* Coral Sea Group

(b) *sl2* Eastern Group

(c) *sl3* Central to Western Group

(d) *sl4* Western Group

Figure 6.10: Illustration of slice groups at Coral Sea, eastern, middle and western Australia in all azimuth corridors.

either clockwise and vise visa, and divided each corridor into 4 slices which are Coral Sea - *sl1*, Eastern Australia: from Gulf of Carpentaria to South - *sl2*, Central to Western Australia - *sl3* and Western Australia - *sl4*. In each corridor, I plotted the raypaths colour scaled by δt^*_{sp}. Then I divided each corridor into slices by looking the lateral variation in δt^*_{sp}.

6.6.3 Visual Path Average Correlation between δt_p, δt_s, δt^*_{sp} and γ

From figures 6.7 (a), 6.7 (b) and 6.7 (c) in section 6.4, I could see distinctive contrast in δt^*_{sp} between eastern and western Australian. There are very clear high Q paths in the northern and western Australia both in short and long distance, but low Q paths in eastern Australian and Coral Sea area.

δt^*_{sp} in the Upper Mantle beneath Coral Sea - *sl1* Group

As displayed in the figure 6.7 (a), (b) and (c), there are less shorter distance raypaths in this group compared to the *sl3* group. But there is reasonable raypath coverage at short, medium and long distances because the stations were deployed in Eastern Australia for sources in the Vanuatu and New Caledonia regions. The reasonable number of closer observations allows me to determine the structure in the shallow part of the upper mantle.

The *P* phases beneath the Coral Sea contains little high frequency, but there is a higher *P* velocity zone in the upper mantle in this area [Kaiho and Kennett, 2000].

The *S* waves generally show weak arrivals and there is a low velocity zone in the upper mantle in this area [Kaiho and Kennett, 2000] which is consistent with strong attenuation in shallow *S* structure (see figure 6.7 (a)).

In the transition zone between 410 and 660 im in depth, the wavespeed are higher than the *ak135* reference. The variation in differential attenuation is consistent to the variation in *P* and *S* wave velocity (see figure 6.7 (b)).

δt^*_{sp} in the Upper Mantle beneath Eastern Australia: from Gulf of Carpentaria to South - *sl2* Group

The data recorded in this group of azimuthal corridors have rather complex features. The phases associated with the shallower part of the upper mantle have rather high frequency content. The δt^*_{sp} estimated from this group of phases are small with weak attenuation (see figure 6.7 (a)). The thickness of the lithosphere varies significantly depending on the direction of propagation. For paths from the east, *P* wavespeeds in the uppermost mantle (above 120 km in depth) are slower; whereas from the north and west higher wavespeeds persist to greater depth. The phases returned from somewhat deeper in the upper mantle are clear for *P* with both low and high frequency content, but *S* is relatively weak [Kaiho and Kennett, 2000].

In shorter distance range from 8 to 20°, the δt^*_{sp} estimated from this group of phases are small with weak attenuation (see figure 6.7 (a)). In the medium distance range from 18 tp 30°, the δt^*_{sp} estimated from this group of data show mixed large and small values (see figure 6.7 (b)). The *P* waves returned from the top part of the lower mantle are also clear and the velocities in the transition zone are slightly faster than *ak135* [Kaiho and Kennett, 2000]. The *S* waves are characterised by strongly attenuated arrivals, and in some cases Vp/Vs ratio from *ak135* were retained by [Kaiho and Kennett, 2000] in order to construct models for azimuth bands in this group. The values of δt^*_{sp} estimated from this group of data are large with strong attenuation (see figure 6.7 (b)).

δt^*_{sp} in the Upper Mantle beneath Central to Western Australia - *sl3* Group

In this group of azimuthal corridors, in the upper part of the upper mantle P wavespeed is high and S wavespeed is very high [Kaiho and Kennett, 2000].

The S arrivals are faster than predictions of the *ak135* model by amounts varying from several seconds at epicentral distance around 10°, to nearly 20 seconds at 20° [Kaiho and Kennett, 2000].

The pattern of arrivals from the uppermost mantle is not very coherent suggesting complex local perturbations in shallow structure. The upper mantle phases are high frequency, which are consistent with the small δt^*_{sp} with weak attenuation (see figure 6.7 (a)). The phases returned from the uppermost part of the lower mantle have relatively low frequency and weak arrivals [Kaiho and Kennett, 2000], and are often later than expected from the *ak135* reference model which are consistent with large δt^*_{sp} with strong attenuation (see figure 6.7 (b)) and (see figure 6.7 (c)).

δt^*_{sp} in the Upper Mantle beneath Western Australia - *sl4* Group

The P wavespeed in the uppermost mantle is a little lower than for the other slices, but the S wavespeed in this zone is high but a little lower than for *sl3* [Kaiho and Kennett, 2000]. This is the reason that there are many negative δt^*_{sp} in this group than other groups. Because the raypaths of P and S wave are separated, the raypath of S wave stay in high Q region but the raypath of P wave penetrate into the low Q region. I have only a limited data coverage in this group, but as in *sl3* I see very high frequency arrivals to significant distance (17°).

In the following, I investigate the correlation between velocity, attenuation and the frequency dependence of attenuation.

The lateral variation of γ displayed in figure 6.7 was discussed in section 6.5.3. There is significant geographic variation in γ which is clearly displayed in figures 6.7. In the shorter distance 8° - 20°, the raypaths mainly sample the lithosphere and the sources for the raypaths are mainly from the Sunda Arc. The raypaths covering the upper most part of the mantle beneath north-west of the Australian continent show γ close to zero; so that the frequency dependence of Q in this area is relatively weak. In the lithosphere under north western Australian continent, δt^*_{sp} is small and the estimations robust with little error. Thus, the attenuation is low in this area.

There are some raypaths in this group of epicentral range from New Hebrides Arc covering the eastern part of Australia and Coral Sea area with the mixture of small and large γ. This group of γ estimation show relatively strong dependence of attenuation on frequency in the lithosphere, particularly in the area beneath the north-west part of the Australian continent. The δt^*_{sp} estimation show strong attenuation in this region.

Within the middle medium epicentral distance range from 18° - 30°, the raypaths are

roughly sampling in the asthenosphere and transition zone. Most of the sources for this group are from New Hebrides Arc and Kermadec-Tonga Arc and the raypaths to SKIPPY stations pass through the eastern part of Australia and Coral Sea area. There is a mixture of raypaths with medium and large γ so that the frequency dependence in those area is more complex and depends on the depth of penetration of the waves. From this group of γ estimates, I could see that even strong and complex feature of dependence of attenuation on frequency in the asthenosphere and transition zone. The δt^*_{sp} estimation show very strong attenuation in the asthenosphere and transition zone. It also show that the attenuation and its dependence on frequency are stronger in the asthenosphere and transition zone beneath eastern Australia then beneath western Australia.

Within large epicentral range between 28° - 45°, the turning points of raypaths are deep through lower mantle. This group of data also reveal complex feature of dependence of attenuation on frequency. Most of raypaths in this group come from the New Hebrides Arc, there a few of them from Sunda Arc and Kermadec-Tonga Arc. Raypaths with medium and large γ are also mixed and depend on the azimuth. This group of γ estimation reveal the complex feature of frequency dependence of attenuation in the lower mantle. The δt^*_{sp} estimation is also show complex feature in this distance group.

I could conclude that γ and δt^*_{sp} are reasonably well correlated. In the high attenuation area, such as in the lithosphere under eastern Australia, the attenuation dependence on frequency is also strong. In the low attenuation region, such as in the lithosphere under central Australia, the attenuation dependence on frequency is also weak. In the deeper part of the mantle, both δt^*_{sp} and γ estimates show complex feature. The SKIPPY data set does not sample the deeper mantle well.

6.6.4 Quantitative relationship between δt_p, δt_s and δt^*_{sp}

By comparing the raypath distribution colour scaled by δt^*_{sp}, δt_p, and δt_s, there is clear lateral variation and a visual correlation between attenuation and velocity as displayed in figures 6.7 (a), 6.7 (b), 6.7 (c) and 6.5. To reveal the quantity relationship between δt^*_{sp}, δt_p, and δt_s, I have plotted the δt^*_{sp} against the binned values of δt_p and δt_s in figures 6.11 and 6.12. The δt_s and δt_p were picked up by coding scheme described in section 6.2.3. The data within the epicentral distance range 8° - 20° were plotted in figure 6.11, and the data within epicentral distance 18° - 45° were plotted in figure 6.12. The circles are displayed with a size inversely proportional to the error in the estimation of δt^*_{sp}. This means that the small circle indicates a large error in the estimation of δt^*_{sp} and a large circle indicates a small error in the estimation of δt^*_{sp}. Figures 6.11 and 6.12 show that there is not much difference in the relation between δt^*_{sp}, δt_p and δt_s for the two epicentral distance groups. But the different data groups classified by coding scheme in section 6.2.3 show different features. The errors in δt^*_{sp} are small for data groups A and B, but large for data groups C and D. There is less

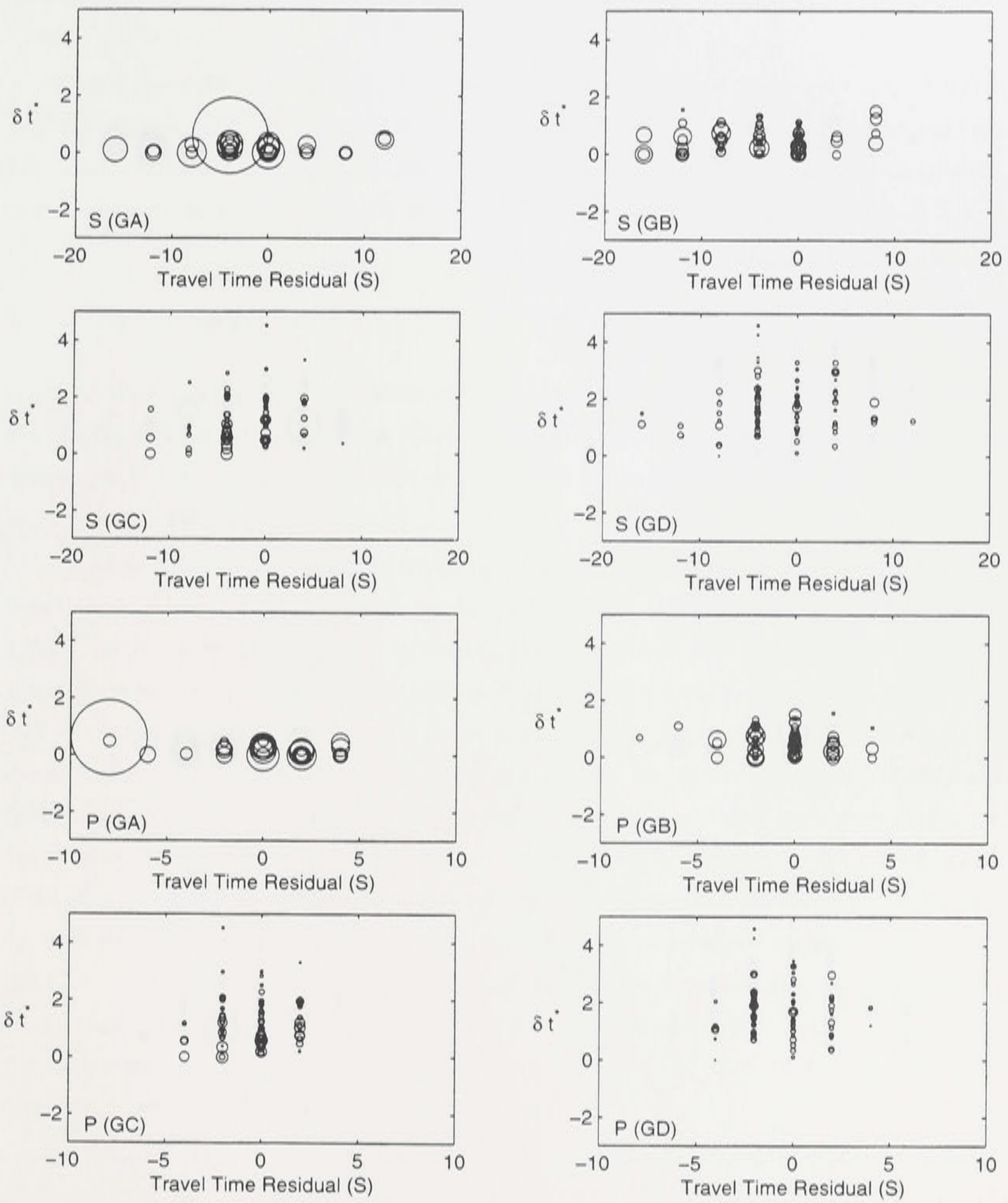

Figure 6.11: Correlation between δt^*_{sp}, δt_p, and δt_s for all arrivals at distance range 8-20° , the size of the circles are proportion to the inverse of the error of δt^*_{sp} measurement.

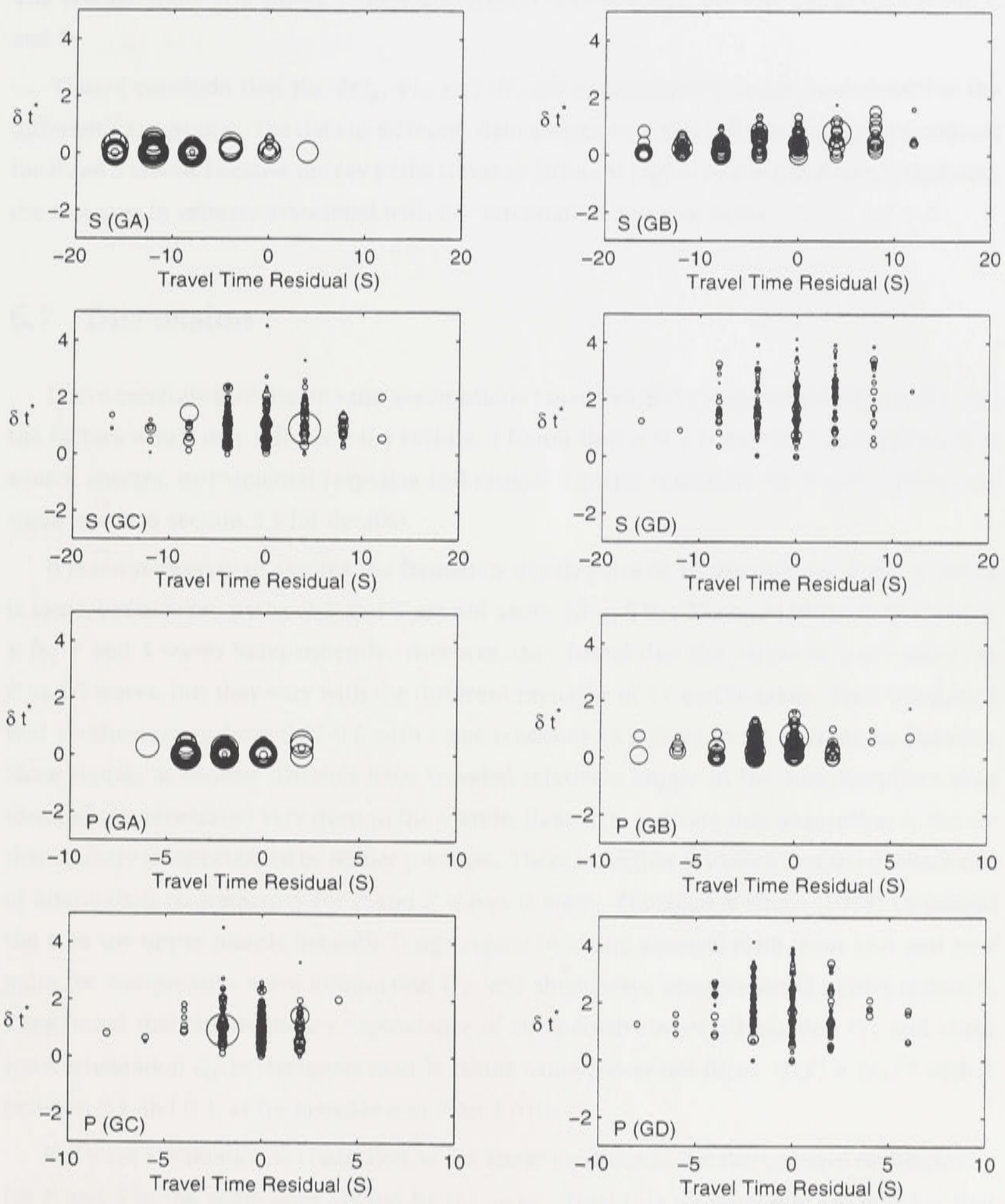

Figure 6.12: Correlation between δt^*_{sp}, δt_p, and δt_s for all arrivals at distance range 18-45° , the size of the circles are proportion to the inverse of the error of δt^*_{sp} measurement.

correlation between δt^*_{sp}, δt_p and δt_s in data group A. There is a good linear correlation between δt^*_{sp}, δt_p and δt_s in data group B and the δt^*_{sp} increase linearly with increase in δt_p and δt_s. The δt^*_{sp} observed from data C and D are more scattered with significant errors. The average trend still shows a linear correlation between δt^*_{sp}, δt_p and δt_s in data group C and D.

Thus, I conclude that the δt^*_{sp}, δt_p and δt_s are approximately linear correlated for the different data groups. The data in different data groups contains different frequency content for P and S waves, because the ray paths traverse different region and depth range. In general, the fast area in velocity associated with low attenuation and vice versa.

6.7 Discussion

I have carefully investigated the assumptions I made when I estimated the δt^*_{sp} and γ and the factors which may influence the results. I found that it is a reasonable assumption that source spectra, instrumental response and crustal transfer functions for P and S waves are same (see also section 5.3 for details).

It is not necessary to assume the frequency dependence of attenuation for P and S waves is same, because ray paths of P and S are not same. Ulug & Berckhemer [1984] estimated the γ for P and S waves independently. However, they found that the values of γ are same for P and S waves, but they vary with the different raypaths of 17 earthquakes. They concluded that γ-values range from 0.25-0.6 with some tendency to increase with decreasing distance. Since signals at shorter distance have traveled relatively longer in the asthenosphere than those which penetrated very deep in the mantle, their data indicate that absorption in the asthenosphere is represented by higher γ-values. There is further evidence that the dependence of attenuation on frequency for P and S waves is same. Flanagan & Wiens [1998] estimated the α in the upper mantle beneath Tonga region by using spectral-ratio from *sS-S* and *pP-P* pairs for compressive wave attenuation Q_α and shear wave attenuation Q_β independently. They found that the frequency dependence of compressive wave attenuation Q_α and shear wave attenuation Q_β in the upper mantle taking same power law form: $Q(f) = Q_0 f^\alpha$ with α between 0.1 and 0.3, at frequencies less than 1.0 Hz.

If P wave attenuation is controlled by the shear modulus μ, the dependence on frequency for P and S in the same layer should be the same. Thus it is a reasonable assumption that the dependence of attenuation on frequency for P and S is the same, provide the V_p/V_s ratio does not vary too much with depth.

From the above results, I have found that there is good agreement achieved in determining the velocity structure in the upper mantle beneath the Australian continent from various techniques in body and surface wave studies. My estimation of δt^*_{sp} show clearly lateral variation, which is very consistent with the velocity variation. In the areas of high S wavespeeds, the

attenuation is weak. Whereas, strong attenuation corresponds to zones of low wavespeed. In the upper mantle beneath western part of the Australian continent, fast velocity zone associated with high Q area. In the upper mantle beneath eastern part of the Australian continent and Coral Sea, low velocity zone associated with low Q area.

The correlation between velocity, differential attenuation δt^*_{sp} and path average frequency dependent parameter γ has been investigated. The relationship between velocity, differential attenuation δt^*_{sp} and path average frequency dependent parameter γ show strong spatial variation. In general, the high velocity zones are agreement with low attenuation and less dependence of attenuation on frequency, and the low velocity zones are the areas with high attenuation and strong dependence of attenuation on frequency.

Chapter 7

Attenuation Structure in the Upper Mantle

7.1 Introduction

Based on the robust estimation of differential attenuation δt^*_{sp} in the narrow frequency smaller than 1 Hz, I have constructed a 3-D attenuation model for the upper mantle beneath the Australian continent. First, I have done some statistical analysis on my estimation of δt^*_{sp} . I found the error of estimation is reasonably small, because I picked up the linear section of spectra which allow us to obtain δt^*_{sp} which represent the spectral ratio reasonably well. Then I have derived a average Q^{-1} model in the upper mantle beneath the whole Australian region. I found the 1-D average model did not fit my δt^*_{sp} estimates well; because my δt^*_{sp} have revealed strong lateral variation of attenuation in the upper mantle beneath eastern and western Australia. To model the lateral variation of attenuation, I sorted my raypaths into a set of azimuth corridors with a step of 20° from 0° to 80° clockwise and 0° to -80° anticlockwise. I have also divided every corridor into 4 slices. I then inverted the Q^{-1} from δt^*_{sp} by using the inversion with neighbourhood algorithm for each slice. Thus I constructed a set of 1-D profiles of Q^{-1} at fixed frequency around 1 Hz .

7.2 Statistical Analysis of δt^*_{sp} and its Errors

Figure 7.1(a) is the distribution of δt^*_{sp} observed from the SKIPPY data set. The figure 7.1(b) is the error distribution of δt^*_{sp} estimation. Figure 7.1(a) shows that most the values of δt^*_{sp} lie in the range from -0.5 to 3.0 seconds. The estimates with negative δt^*_{sp} can arise because the P wave penetrate to the high attenuation zone and S wave still in low attenuation area. Thus negative δt^*_{sp} values do not violate my assumption that the attenuation mainly

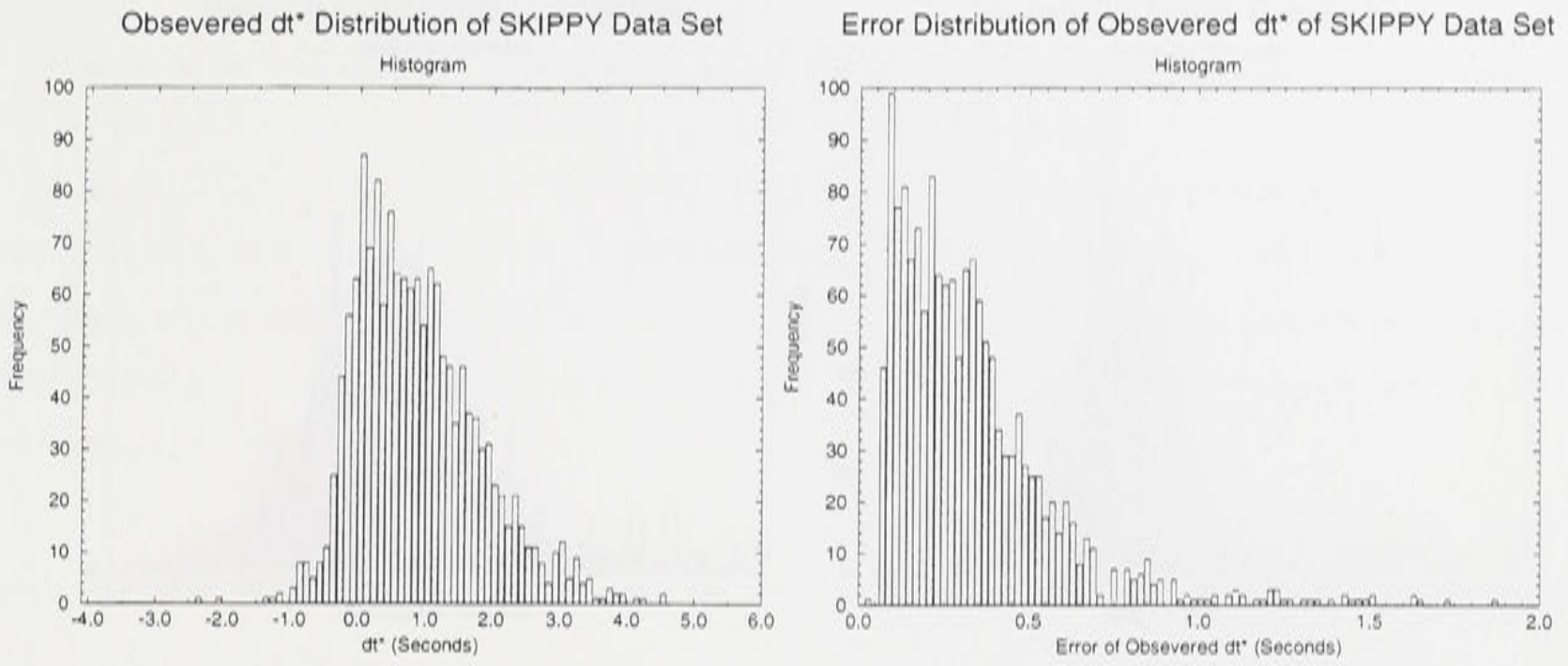

(a) δt^*_{sp} Distribution **(b)** Errors ofδt^*_{sp} Distribution

Figure 7.1: Distribution of δt^*_{sp} their errors observed from the SKIPPY data set

occur in the shear waves (see the detailed discussion on negative δt^*_{sp} in section 8.3.2).

7.3 Inversion for Q^{-1} from δt^*_{sp} Measurement

7.3.1 1-D Q^{-1} model inverted by nonlinear grid search

1-D average Q^{-1} model in the upper mantle beneath whole Australian continent

At the first step of inversion, I derived an average Q^{-1} model from the full set of my δt^*_{sp} estimation. I inverted the δt^*_{sp} data for a 1-D average Q^{-1} model (table 7.1) for the upper mantle beneath whole Australian continent by using a nonlinear grid search inversion method in order to search for a best fit attenuation model with smallest misfit. The difference between the observed and predicted δt^*_{sp} divided by the errors in the estimates of δt^*_{sp} with Gaussian distribution (L_2 norm $L = 2$ in (7.1)) is used here as a measurement of the misfit. The misfit is defined as chi square divided by the difference between number of data n and number of unknown parameters m. It is, therefore, a random variable with a χ^2 distribution with $n - m$ degree of freedom.

$$\chi = \left(\frac{\| \delta t^*_{obs} - \delta t^*_{pred} \|}{\sigma t^*_{obs}} \right)^L \tag{7.1}$$

$$\phi = \frac{\chi}{n - m} \tag{7.2}$$

where the L is the norm, the n is number of data, the m is the number of unknown parameters to be found and the σt^*_{obs} is the error in the estimates of δt^*_{obs}. I divided the Earth into four layers, thus there are four unknown Q^{-1} to be derived for the grid search method, thus

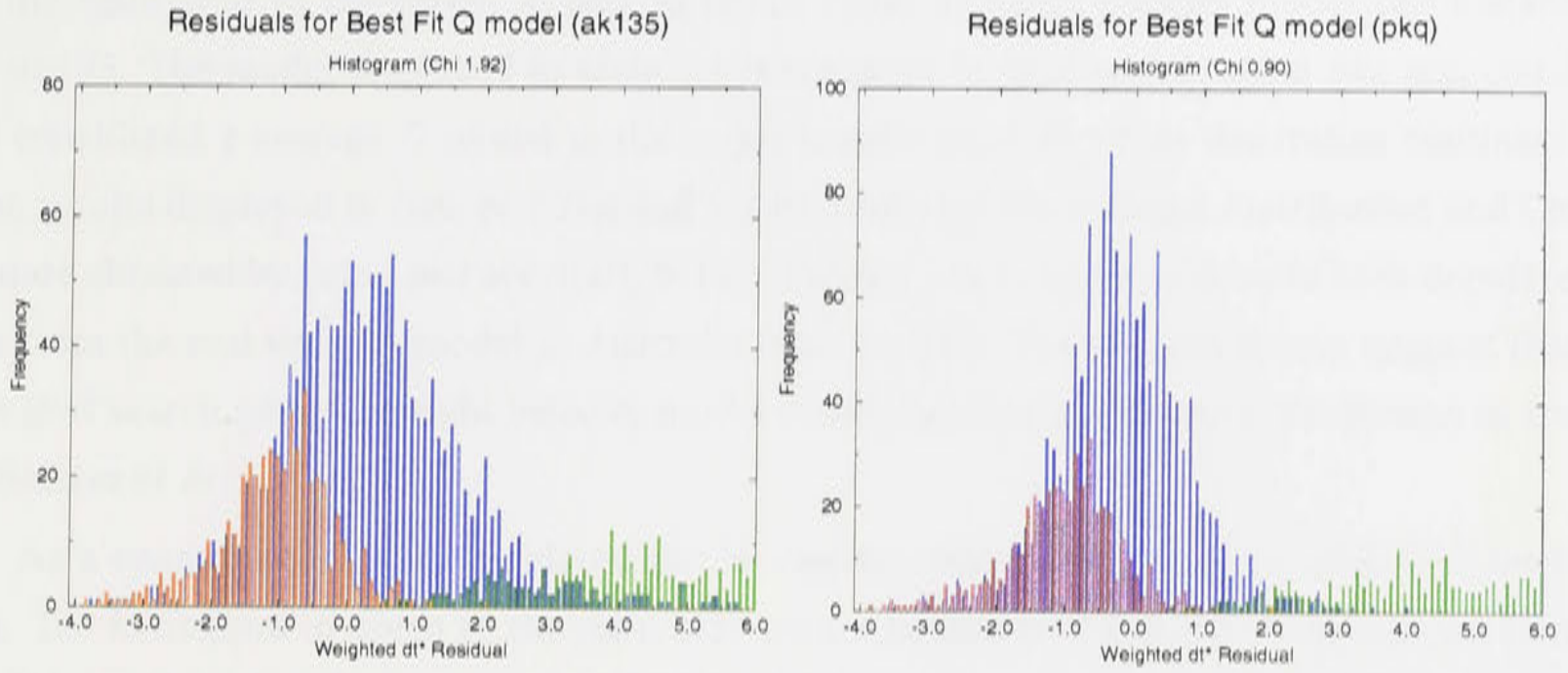

(a) Residual distribution *ak135* **(b)** Residual distribution *pkq*

Figure 7.2: Histogram of misfit to fit my estimation of δt^*_{sp} to a average Q^{-1} model by using velocity models *ak135* and *pkq*

in this case $\phi = \frac{\chi}{n-4}$. The grid search method of inversion involve the systematic search through each point in a predefined model space to locate the best fit models. For Q^{-1} models inversion, although there are only four unknown parameters, the model space is very large and the forward calculation is slow. The efficiency of grid search is highly dependent on the maximum and minimum Q^{-1} values and the size of increments. Here, I have conducted a 2-step grid search. At the first step, I used the broad range of minimum (0.0001) to maximum (0.02) of Q^{-1} with 50 large increments (0.0004) to locate a crude model. Then I reduce the range of minimum to maximum of Q^{-1} by allocate the value to focus around the crude model derived by the first step of grid search. The second step grid search was conducted with 50 fine increments (0.00001-0.00004) for different unknown parameters.

Table 7.1: Q model inverted by nonlinear grid search

Layer description	*Depth* (km)	Q_s	Q_p
Lithosphere	0-210	1300	2600
Upper mantle	210-410	160	320
Transition zone	410-660	650	1300
Lower mantle	660-2660	1300	2600

It is assumed $Q_p = 2Q_s$.

I have used global average velocity model *ak135* [Kennett et al., 1995] and a regional model *pkq* for north western Australia. The aim of experiments of inversion for Q using whole δt^*_{sp} estimates with different velocity is to look at the influence of velocity model on attenuation inversion.

Histogram in blue in figure 7.2(a) is the distribution of δt^*_{sp} residuals corresponding using a Q^{-1} model found using grid search. Here all of the whole set of estimates of δt^*_{sp} was used to invert the Q^{-1} model by using velocity model *ak135* . Histogram in blue in figure 7.2(b)

is the equivalent to histogram in blue in figure 7.2(a) by using velocity model *pkq* instead of *ak135*. The model displayed in table 7.1 is obtained by grid search using *pkq* and could be considered a average Q model in the upper mantle beneath whole Australian continent. The results displayed in figures 7.2(a) and 7.2(b) show that the residual distribution and Chi square obtained by using *pkq* are much better than the *ak135* because the *ak135* is departed far from the real velocity model in Australia than the *pkq*. These experiments suggest that the grid search using the right velocity model could significantly improve the fitness to the estimates of δt^*_{sp}.

As a comparison, I also calculated the histogram corresponds to some chosen Q models. The histogram in green in the right side corner in figures 7.2(a) and 7.2(b) are the part of δt^*_{sp} residual distribution generated using a one layer attenuation model with $Q_s = 100$ for the whole Earth. Note that the δt^*_{sp} residual values calculated from this Q model which represent a viscous Earth are out of the range in 7.2(a) and 7.2(b) because they are larger than 6.0. The histogram in red colour in the left side in figures 7.2(a) and 7.2(b) are the part of δt^*_{sp} residual distribution generated using a one layer attenuation model with $Q_s = 1000000$ for the whole Earth. The δt^*_{sp} residual values calculated from this Q model which represent a elastic Earth are also out of the range in 7.2(a) and 7.2(b) because they are smaller than -4.0. This experiments suggest using the one layer Q model could not fit the estimates of δt^*_{sp}. It is also proven that the grid search does extract the useful attenuation information from the the estimates of δt^*_{sp}. The histograms in blue suggest that the better attenuation models do significantly improve the fitness of the estimates of δt^*_{sp}.

1-D Q^{-1} model from δt^*_{sp} in corridor azimuth 0 inverted by nonlinear grid search

After I obtained the 1-D average Q^{-1} model from all the sets of measurement from SKIPPY data, I found the results of weighted δt^*_{sp} residual distribution (e.g. fig 7.2) are encouraging. But the average model mixes and smoothes the strong lateral variation of attenuation in the upper mantle. The information contained in the measurement of δt^*_{sp} are enough for me to construct a more detailed Q structure in the upper mantle. Thus I divided the whole set of measurement of δt^*_{sp} into 9 groups by spatial distribution of raypaths.

The best constrained of the set of 1-D velocity models developed by Kaiho and Kennett [2000] in the upper mantle beneath the Australian continent, are for both eastern and western Australia in the corridor with azimuth 0 ± 10. Therefore, I took my first step to construct the 1-D Q^{-1} model for eastern and western Australia by using the appropriate reference velocity models. The nonlinear grid search inversion method was used again to derive the the 1-D Q^{-1} model in the upper mantle beneath the eastern and western Australia from the measurement of δt^*_{sp} with azimuth 0 ± 10. As I discussed in previous section, 2-step grid search was here again to reduce the computation time.

The raypaths used in the inversion is illustrated in the figure 7.3(a) and the Q^{-1} model is

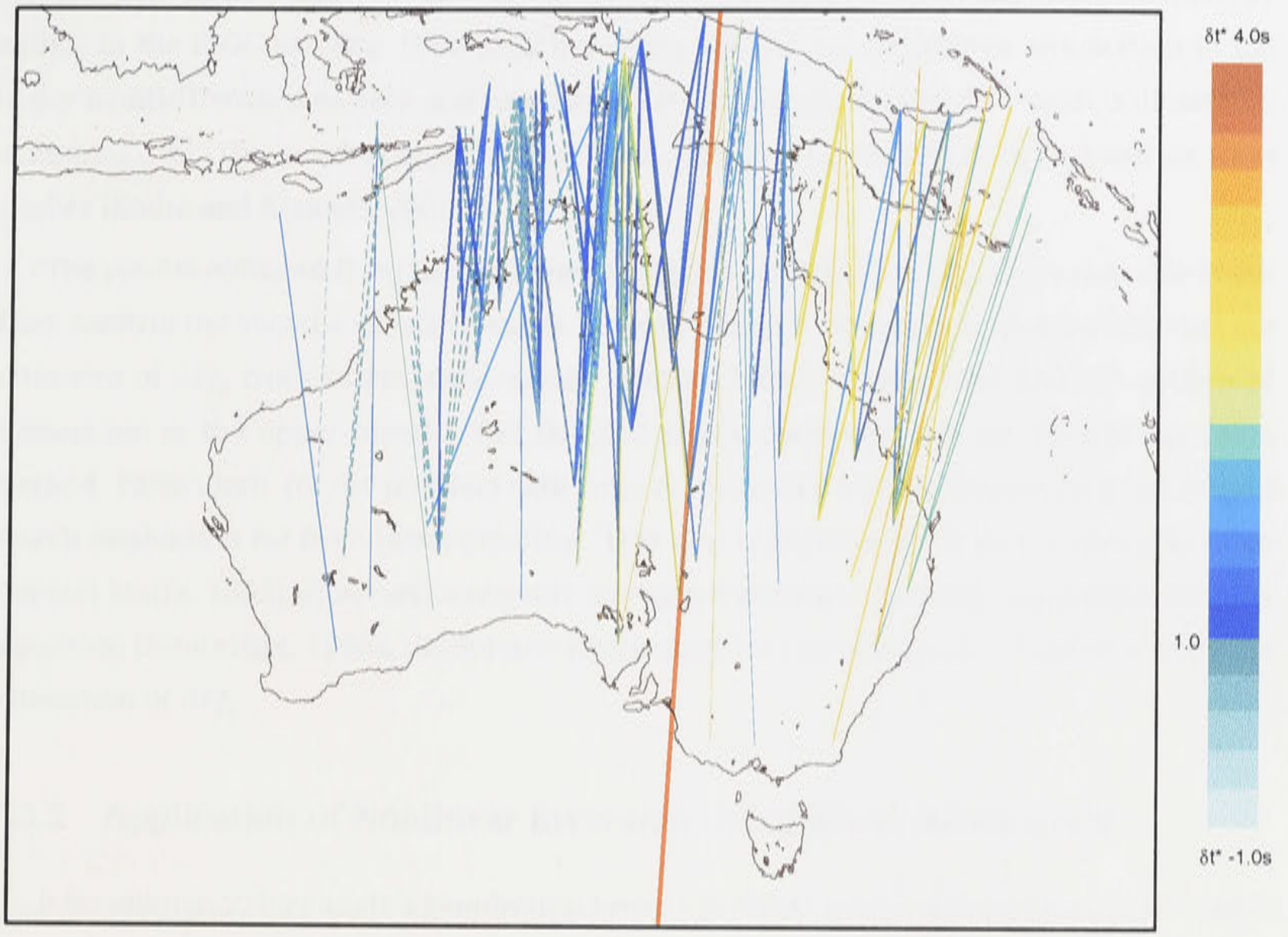

(a) Raypaths colour scaled by δt^*_{sp} in corridor with azimuth 0 ± 10

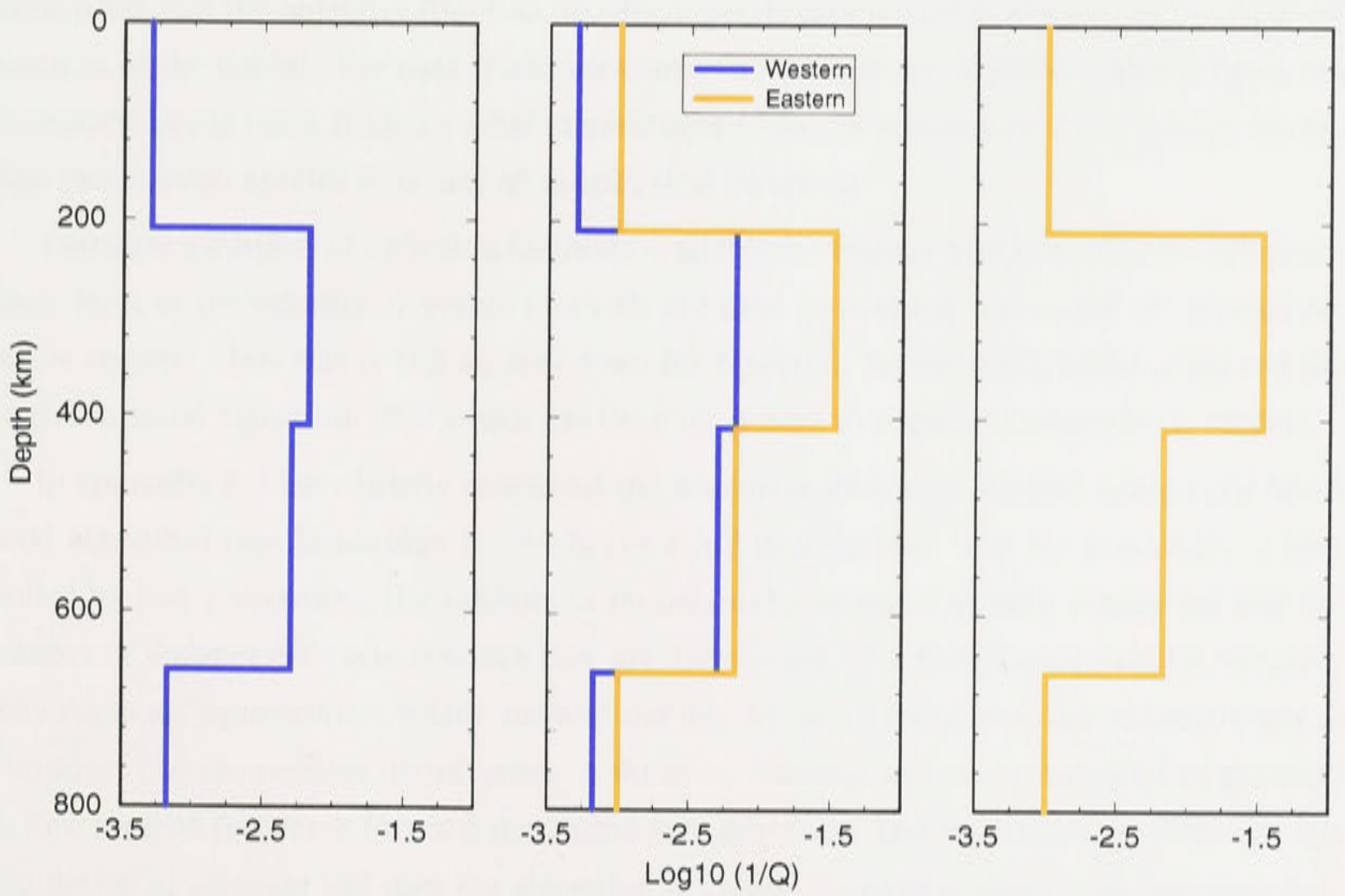

(b) 1-D Q in the upper mantle beneath eastern and western Australia

Figure 7.3: 1-D Q model in the upper mantle beneath eastern and western Australia derived from raypaths in corridor with azimuth 0 ± 10 by nonlinear grid search

displayed in figure 7.3(b). The Q^{-1} models displayed in figure 7.3(b) were also presented by author in the IUGG meeting 1999 at Birmingham, UK. Strong contrast in attenuation in the upper mantle between eastern and western Australia is confirmed by Q^{-1} models illustrated in figure 7.3(b). This result is expected by velocity structure from both body and surface wave studies [Kaiho and Kennett, 2000].

The results obtained from the grid search inversion method for δt^*_{sp} are reasonably good. They confirm the visual analysis from the raypath distribution colour scaled by δt^*_{sp} that my estimates of δt^*_{sp} from SKIPPY data contain detailed information on the spatial variation of attenuation in the upper mantle. But the grid search method is not an efficient inversion method. Particularly for my problem with large model space and fine increments, use of grid search methods is far from being practical. This idea is sheared by various authors [see also Sen and Stoffa, 1995]. However, a recently developed inversion method - the neighbourhood algorithm [Sambridge, 1999a,1999b] provides a good tool to construct Q^{-1} models from the estimation of δt^*_{sp} .

7.3.2 Application of Nonlinear Inversion Using NA to Attenuation

It is common to formulate a geophysical inverse problem as one of optimisation in a finite-dimensional parameter (model) space (possibly under constraints). Each point in model space represents a set of parameters describing some physical property of the earth, e.g. seismic wavespeed, and the objective function usually depends on a measure of data misfit and some function of the model. The data misfit measures the discrepancy between observations and theoretical predictions from a model (determined from the solution of a forward problem). This formulation applies to nearly all geophysical inversion.

There are a number of inversion methods available for various geophysical inversion problems. Most of the existing inversion methods are time consuming and could not provide accurate results. Thus this is still an area open for research. Sambridge [1999a] proposed the neighbourhood algorithm (NA) which has been used here to construct attenuation models.

In appendix B, I have briefly described the nonlinear inversion method using neighbourhood algorithm (see Sambridge [1999a,b] for a full description). The NA procedure is controlled by just 2 variables: the number of models to be sampled at each generation and the number of Voronoi cells across which they are distributed. The first step of each NA iteration constructs an 'approximate misfit surface' defined by previous model (the starting point is a uniform pseudo-random distribution. A set of n_r Voronoi cells are resampled to generate n_s new models for which forward modelling is undertaken. The n_s models are added to the population of samples and then the algorithm proceeds to the first step of the next iteration. The choice of n_s and n_r depends on the nature of the inversion problem and is critical to the NA algorithm.

7.3.3 Experiments on Model Parameterisation and Parameters Used by NA

Tests on Model Parameterisation

The first question raised when I undertook the inversion is how many layers should I choose for the Q^{-1} model. This depends on the nature of the seismic body wave attenuation in the upper mantle and the limitation of the depth resolution of the SKIPPY data. Because the lateral variation of lithosphere thickness across the Australian continent. The thickness of the lithosphere is much thinner beneath eastern than western Australia [Clitheroe et al., 2000]. I have tested the choice of the first layer at 35 km, 77.5 km, 120 km, and 210 km deep. The test results show that the SKIPPY data are not sensitive to as shallow a layer as 35 km. My investigation suggests that the depth of the first layer is suitable at 77.5 km for *sl1* groups in the Coral Sea area, 120 km for *sl2* groups in eastern Australia and 210 km for the *sl3* and *sl4* groups in the central and western Australia. For deeper mantle, I have tested choosing the depth step as 50 km and 100 km. But the results show that the SKIPPY data set does not have depth resolution as fine as 50 km or even 100 km. Thus, I chose to model the attenuation in lithosphere, asthenosphere, transition zone and deeper mantle (≥ 660 km). My final parameterisation is 5 layers beneath the Coral Sea and eastern Australia and 4 layers beneath the central and western Australia.

Tuning NA parameters n_s and n_r

The two control parameters for the NA , n_s and n_r, need to be tuned to find a balance between rapidly focusing to a solution and exploring the parameter space. Different effects can be achieved by varying n_r. For large value of n_r, the sampling encompasses more Voronoi cells and the algorithm will explore more of the parameter space, For smaller values of n_r, the algorithm samples only the best few Voronoi cells and the algorithm rapidly heads toward a minimum, exploiting the better values (Sambridge, 1999a). The effect of varying n_s is less clear. It is thought that as n_s increases (with n_r held fixed) more weight is given to the previous sample because the Voronoi cells are updated less frequently (Sambridge, 1999a). I have tested varying n_s and n_r from 10, 16, 20 to 30, as well as variation of the iterations used in the inversion. The results show that with larger values of n_r the algorithm requires more iterations to coverage. When n_r is low the algorithm rapidly converges, as n_r is increased there is more exploration of the parameter space. However, the misfit is still reduced as the number of forward modelling calculations is increased. Theoretically, the more iterations and the more sample sizes, the better results you could achieve. However, increasing iteration significantly increase the forward modelling. There is a tradeoff between better results and cost of computing time. My investigation suggests that 50 iterations, with NA parameter's combination of 10, 10, 2 gives reasonable results. However, larger n_r will allow thorough exploring in the parameter space thus will provide more robust inversion results. Therefore,

I have used 100 iterations, with NA parameter's combination of 20, 20, 4 for my standard inversion. After tuning n_r and n_s, I have also tested undertaking inversion with 280, 300, 500 and 1000 iterations, but there are no significant improvement to the final results. Finally, I stay with 100 iterations.

Misfit measurement selection

One of most the important problems in inversion is selecting which measure of misfit should be used to best deal with the effects of errors in the data. Although I have made big efforts in attempting to reduce the errors in δt^*_{sp} estimation, there are still a number of factors which contribute to the errors in estimating the δt^*_{sp}:

1. noise level in the signal; This is the main contribution to the δt^*_{sp} estimation. Although I have removed the smoothed noise spectrum from the signal spectrum as described in the section 5.2.1, the errors in δt^*_{sp} estimation are still associated with the noise level in the P and S signal.

2. effect of source spectra; The error associated with the source spectra has been reduced by the spectral ration between the P and S waves, based on the assumption that the source spectra for P and S are same. This is a good assumption for small earthquakes. However, the relationship between the corner frequencies of P and S waves are not consistent in the literature, particularly for large earthquakes. It is beyond the scope of this thesis to model the P and S source spectra.

3. effects of scattering; However, the effect of scattering is small in the lower frequency band (smaller than 2 Hz). At same time, the scattering coefficient is roughly one order smaller in the uppermost mantle than to crust [Yoshimoto and Wu, 2000]. The SKIPPY data set is not sensitive to the crust. Therefore, the error arising from the effects of scattering is small in this work.

4. errors in picking the P and S wave arrivals; I have looked at each individual seismogram and spectrum by picking up the P and S manually. Thus this error has been reduced to a minimum level but will be present for some seismograms with large noise when P and S arrivals are not clear.

Three norms were used in the NA programme with attenuation inversion - the L_1, $L_{1.5}$, and L_2 or Gaussian (L_2) norm. Experiments were conducted to investigate how these different norms cope with errors in the estimation of δt^*_{sp}. The NA programme was run for 100 iterations with 20 models generated at each iteration, the Voronoi cells containing the four best models re-sampled.

Of the three norms employed, the L_2 norm copes less well with dealing with errors because outliers are emphasised. The L_1 and $L_{1.5}$ are more robust and less effected by errors in the

estimation of δt^*_{sp}.

With the L_2 norm, the misfit after the first iteration is extremely large. But the misfits reduce very quickly with further iterations. The L_2 norm is more sensitive to the errors in the estimation of δt^*_{sp} than other two norms. The L_1 norm is often insensitive to the errors in the δt^*_{sp} estimates. With L_1 norm, the misfit is 20 times smaller than the L_2 norm after first iteration. This may be an indication that the L_1 norm is fitting noise as well as data. Thus the precise answers obtained with this norm may not always be accurate. In regard to this case, a $L_{1.5}$ norm might be favoured because it provides a balance between the extreme sensitivity of the L_2 norm and the insensitivity of the L_1 norm. In addition, in most cases the $L_{1.5}$ norm provides the smallest misfit. Therefore, I choose $L_{1.5}$ norm as standard when I conduct inversion for Q from whole set of δt^*_{sp} estimates.

7.3.4 Evaluating the solutions obtained by NA

Estimation of Misfit Cut-off

Because the nature of the inversion problem, there is often no unique solution and hence many solutions may satisfactorily fit the data. Rather than examine a single solution, it is more meaningful to attempt to extract information from all models that fit the data. The group of acceptable models will be useful for presenting the uncertainties in the solutions and in making inferences about the properties shared by all acceptable models. One of the advantage of using the NA is that information about all models found during inversion can be extracted for these purposes.

In searching a set of acceptable models using NA, a measure of the misfit between predicted and observed data and acceptable level of misfit should be made. This level of misfit that is considered acceptable is the misfit cut-off. Traditionally, the misfit cut-off is determined by calculating confidence regions. The misfit cut-off has been well documented in many other inversion problems [Parker, 1994], such as inversion for hypocentral location [Sambridge and Kennett, 1986; Sambridge, 1988; Sambridge and Gallagher, 1993; Farmer, 2000]. But the inversion for attenuation has been less studied because of the difficulty in extracting amplitude information from the seismic recordings.

A series of publications considered the estimation of confidence level or misfit cut-off [Bulland, 1989; Jordan and Sverdrup, 1981; Shearer, 1999; Sambridge and Kennett, 1986]. The common way to estimate the misfit cut-off is using the chi-squared statistic with some degrees of freedom. But the confidence regions are based on the assumption of a Gaussian distribution for residuals and the actual error distribution in the attenuation inversion problem is usually broader than Gaussian distribution. This is the situation for the attenuation inversion. Thus the region of confidence will always be overestimated by the assumption of a Gaussian distribution.

Confidence level for the inversion of attenuation parameter space can be deducted, by adapting the method of Bulland [1989] used for hypocentral location, by examining the spatial distribution of

$$\Gamma(q) = \phi(q) - \phi(\bar{q}) \tag{7.3}$$

where ϕ is the misfit criterion and $\bar{q}$ is the best estimate for the attenuation models. Confidence levels can be assigned to $\Gamma(q)$ using the chi-squared statistic (χ^2) with m degrees of freedom (m is the number of unknown attenuation parameters). The problem with this method is that chi-squared statistic assume a Gaussian probability distribution for residuals. However, as Gaussian statistic alone account only for picking errors the misfit is usually too small and solutions are underfit. For hypocentral location problem, this may result in chi-squared tests indicating the solution should be rejected because 'unmodelled velocity structure is dominating fit' [Shearer, 1999; Farmer, 2000]. Here, I have used the method of estimating the misfit region by Sambridge and Kennett [1986], which the misfit criterion $\phi(q)$ is rescaled to the expectation of a chi-squared distribution with (n-m) degrees of freedom (where n is the number of observation and m is the number of attenuation parameters to be found). The regions of parameter space then could be calculated by:

$$\frac{\phi(q) - \phi(\bar{q})}{\phi(\bar{q})} \leq \frac{\chi^2_m(0.95)}{n - m} \tag{7.4}$$

This method overcome the problem that solutions are underfit or be rejected because of the Gaussian statistic dealing with errors [Bulland, 1989; Shearer, 1999]. Another merit of the method for estimating misfit by Sambridge and Kennett [1986] is that it does not require a posteriori information which proposed by Jordan and Sverdrup [1981], hence it is easy to implement. These approximate results will overestimate the region of acceptable models.

Searching a Set of Attenuation Models by NA

The NA was adapted by Farmer [2000] so that it could take more thorough search over the region of acceptable models. In Farmer's adapted version of NA, to begin the process of mapping the region of acceptable solutions, the models with acceptable misfit values were extracted from the initial set of solutions. Random models are then added to the set of acceptable models, so that there is a reasonable initial sampling of the parameter space, and it is easy to initialise a search with this starting ensemble. Also, the NA was adjusted to accept input of the misfit cut-off as an additional parameter. The standard for acceptable models is defined as: A model is considered to be acceptable if $\phi - \phi_{acc} \leq 0$ where ϕ is the raw misfit of a model and ϕ_{acc} is the misfit cut-off. The raw misfit of all models which pass this test is transformed to 1.0. The raw misfit of models that are not acceptable is scaled to be greater than 1.0. The transformation of misfit forces the NA to treat all acceptable models equally when it is ranking models for resampling. When the adapted version of NA tested by Farmer

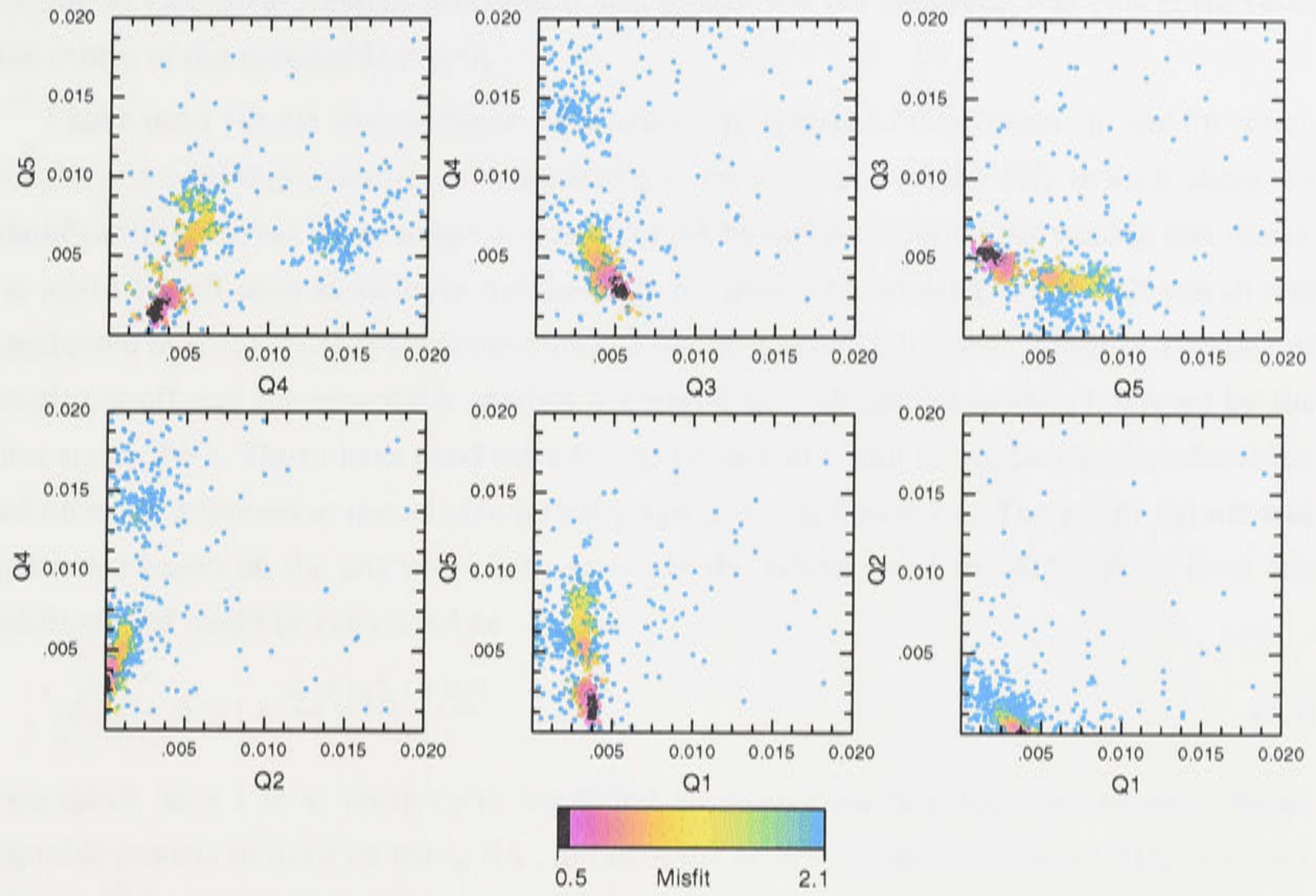

(a) Azimuth 40 Slice 1

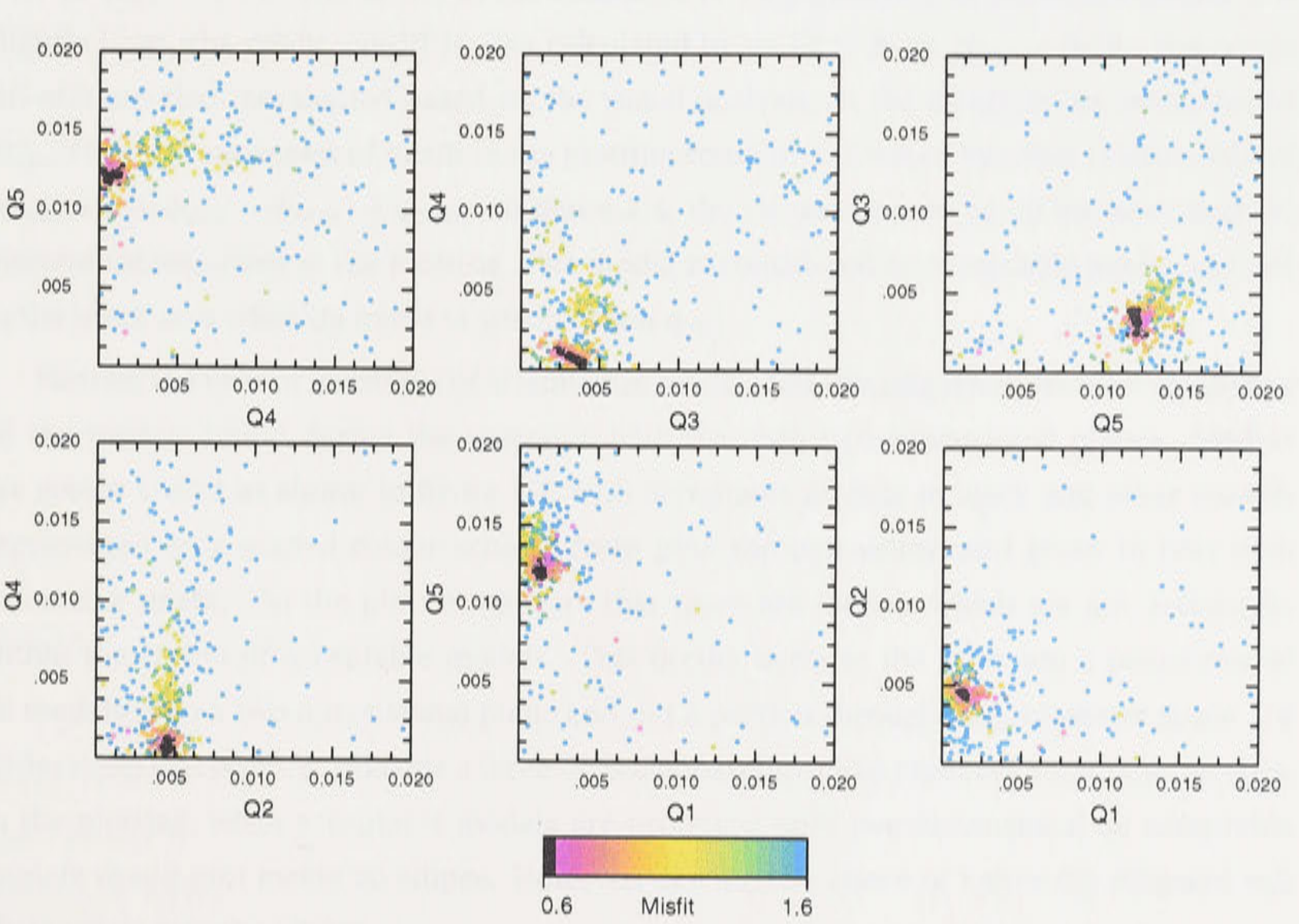

(b) Azimuth 0 Slice 1

Figure 7.4: Example of acceptable models obtained by using NA, colour scaled by misfit with acceptable models in black and other models represented on a graded colour scheme from pink through yellow and green to blue with increasing misfit.

[2000] on epicentral location problem, it was found that the sampling was concentrated in the centre of the acceptable region.

I have used NA for the inversion of attenuation models in this thesis. In my inversion for the attenuation parameter Q^{-1}, the errors in the estimates of the δt^*_{sp} in each slices are significantly different. Thus adapted version of NA by Farmer [2000] is not used in this thesis. No misfit cut-off used as an input parameter in my inversion. Instead a thorough search was conducted over the whole parameter space to obtain a set of solutions. However, the idea of misfit cut-off and the acceptable models are useful to evaluate the models I derived by the first stage of NA. Thus I have used the adapted version of S-plot to produce and evaluate my solutions of attenuation models from first stage of NA in figure 7.4. The misfit cut-off was estimated based on the analysis of the errors in the estimates of the δt^*_{sp}. From (7.4), the misfit cut-off could be calculated as

$$\phi_{acc} = \phi(\bar{q}) + \frac{\phi(\bar{q})\chi^2_m(0.95)}{n-m} \tag{7.5}$$

Two slices, slice 1 in azimuth corridors 0 and 40, were chosen to illustrate to map the acceptable models derived by using NA . Because the errors in the estimates of δt^*_{sp} in slice 1 in azimuth corridor 40 is very small, the misfit cut-off for this slice is calculated by using (7.5) as $\phi_{acc} = 0.58$. The errors in the estimates of δt^*_{sp} in slice 1 in azimuth corridor 0 is slightly large, the misfit cut-off is also calculated by using (7.5) as $\phi_{acc} = 0.65$. The misfit cut-offs are also reevaluated based on the visual analysis on the errors in the estimates of δt^*_{sp}. Then the maximum of misfit in the plotting could by estimated by using relationship of $\phi_{max} = cn(\phi_{acc} - \phi_{min}) + \phi_{min}$. In figure 7.4, the cn was chosen as 20 because there 20 discrete colours used in the plotting. The model is considered as acceptable model and lies in the black area when its misfit is smaller than ϕ_{acc}.

Plotting the view of ensemble of attenuation models found using NA is made by projecting all the models found during the inversion with NA onto two-dimensional planes. Models are colour scaled as shown in figure 7.4, with acceptable models in black and other models represented on a graded colour scheme from pink through yellow and green to blue with increasing misfit. On the plots it appears that there are models which are not acceptable within the region of acceptable models. This occurs because the plots are a projection of all models onto a two-dimensional plane and not a portion through the parameter space. To understand this plotting, imagine a three-dimensional ellipsoidal region of acceptable models. In the plotting, when acceptable models are projected onto two-dimensional all acceptable models would plot inside an ellipse. However, any models above or below the ellipsoid will also project into the ellipse.

Figure 7.4 is view of the ensemble of attenuation models found using NA. Here the set of attenuation models, inverted from the values of δt^*_{sp} estimated from the slice 1 in azimuth corridors 0 and 40, used to generate the figure 7.4. The δt^*_{sp} estimated from data in these

two slices are reasonably good with low level of errors. Thus the misfits in the region of acceptable models are fairly small. The figures 7.4(a) and 7.4(b) clearly reveal the process of NA searching over the whole parameter space. Initially is predominately generating models with high data misfit (show in blue). Then the searching process approaches the the models with medium misfit (show in green/yellow/pink) and finally focuses on the acceptable models with small misfit show in black.

In figure 7.4(a), the searching process is quickly focused and the black regions of acceptable models are quite small. The small region of acceptable models indicates better constraints on the Q^{-1} models, such as the subfigures of Q4 against Q2 and Q2 against Q1 in the figure 7.4(a). The long black bars in the subfigure of Q5 against Q4 and Q5 against Q1 indicate the Q^{-1} is better resolved in layer 4 than in the layers 1 and 5.

The error level in the estimates of δt^*_{sp} in the slice 1 in azimuth corridor 0 is slightly higher than in the azimuth corridor 40. At the beginning of the searching process, the misfit distribution in figure 7.4(b) is rather diffuse. But it gradually locate models with smaller misfit and finally focuses on the acceptable model region. The region of acceptable models are also reasonably small which is consistent to the error level in the estimates of δt^*_{sp}. This suggests the NA method be able to find the attenuation models which satisfactorily fit the estimates of δt^*_{sp}. This also confirms the robust estimates of δt^*_{sp} at fixed frequency around 1 Hz has effectively extracted the attenuation information from the seismograms.

In the following sections, the inversion methods with NA was systematically applied to the estimates of δt^*_{sp} from the SKIPPY data set. The δt^*_{sp} data set was first sorted into azimuth corridors and slices. Then a set of 1-D Q^{-1} profiles was constructed by using NA. The inversion results of Q^{-1} were plotted of a group of Q values with smaller misfits as a function of depth (see fig 7.6). The acceptable models are not distinct in the figure 7.6 because I only plot those models with reasonably small misfits. The range of misfits used in each case were chosen in order to give an impression of a spread of better fitting models.

7.3.5 Inversion by Using *NA* for a Set of 1-D Q^{-1} Profiles

Sorting δt^*_{sp} Data into Azimuth Corridor and Slice

The raypath coverage of SKIPPY data set is very dense, particularly in north western Australia. However, many raypath has similar azimuth and are nearly parallel to each other, thus I do not have enough crossing raypaths to construct a direct 3-D tomographic Q model. Meanwhile, a reference velocity model is required to construct a Q model. The best velocity model for the upper mantle beneath the Australian continent is a set of 1-D velocity profiles developed by Kaiho and Kennett [2000]. Thus I could not go beyond their 1-D profile to obtain a real tomographic 3-D Q structure. Under those limitations of the SKIPPY data set, I decide to construct a set of 1-D Q profiles instead of 3-D tomographic Q model. Figure 7.5

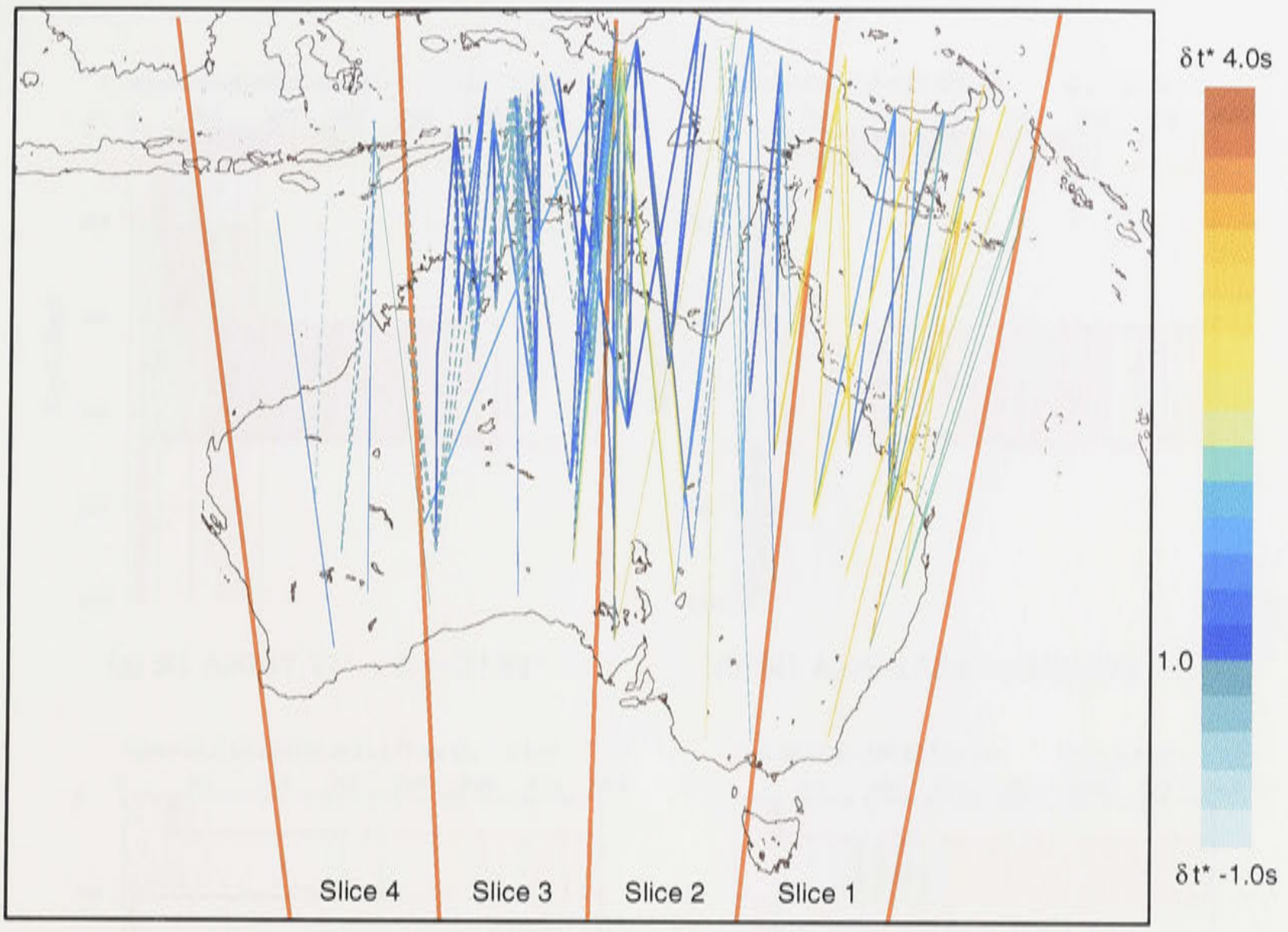

Figure 7.5: Example of sorting raypath into of slices in corridor with azimuth 0 ± 10. Raypaths are colour scaled by δt^*_{sp} . Line thickness is inversely proportional to the errors in the estimation of δt^*_{sp} . The dash lines indicate negative δt^*_{sp}.

is an example how I sort raypaths into slices for the corridor azimuth 0. I have sorted all the SKIPPY raypaths into azimuth corridors and slices, following the same parameterisation used by Kaiho and Kennett [2000], as discussed in section 6.6.2 and illustrated in figure 6.9.

I have also trimmed the raypaths displayed in figure 6.7 (a), 6.7 (b) and 6.7 (c) by removing some raypaths which pass through subduction zone between Indonesia and northern Australia. I have also removed some raypaths from Australian Antarctic ridge and some paths out of the area studied in thesis. The raypaths I have removed which pass through the subduction zones will allow me to construct the attenuation structure in the subduction area in the future.

1-D Q Profiles

I have undertaken inversion for Q^{-1} from the δt^*_{sp} estimates by using the NA method for each slice described in section 7.3.5. Figure 7.6 is a summary of inversion results which produces out a set of 1-D Q profiles for the upper mantle beneath the Australian continent. Q^{-1} was used in the inversion. To get a idea what the Q value is, the Q was used for plotting in figure 7.6. My main results are displayed in figures from 7.6(g) to 7.6(x), because the dense raypaths coverage and wide range of epicentral distances. Thus the inversion for Q is

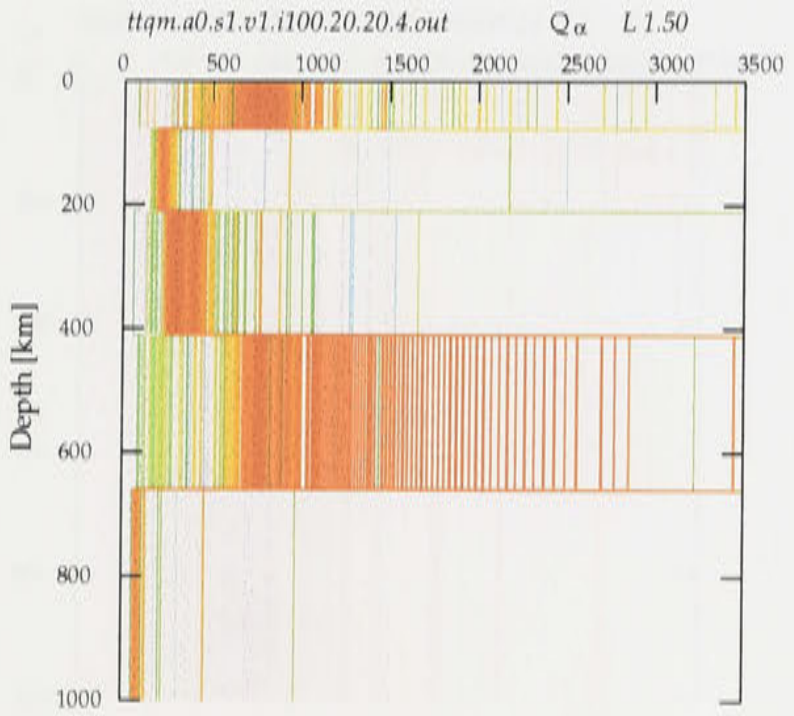

(a) Sl1 Az0 17.17° < Δ < 32.82°

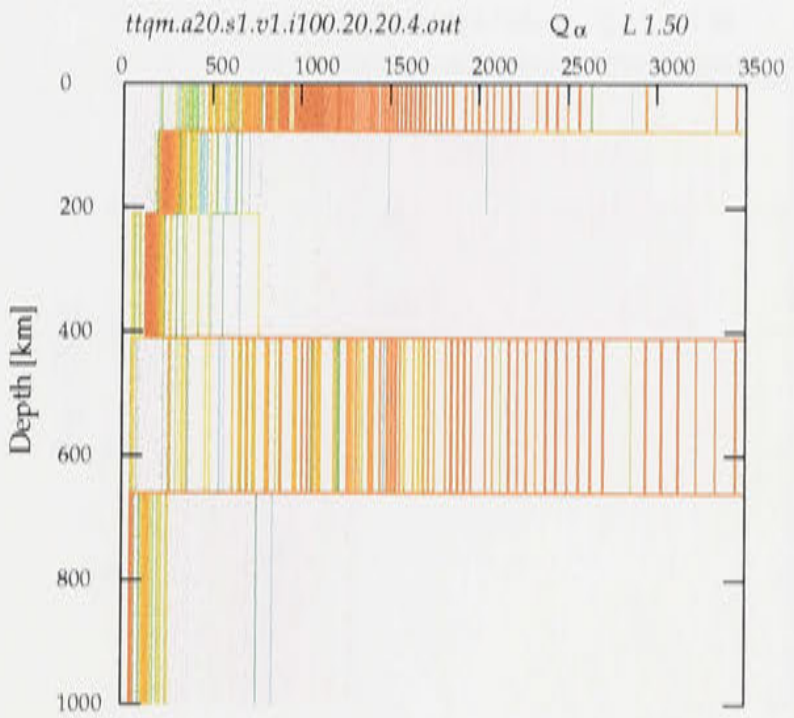

(b) Sl1 Az20 17.34° < Δ < 30.1°

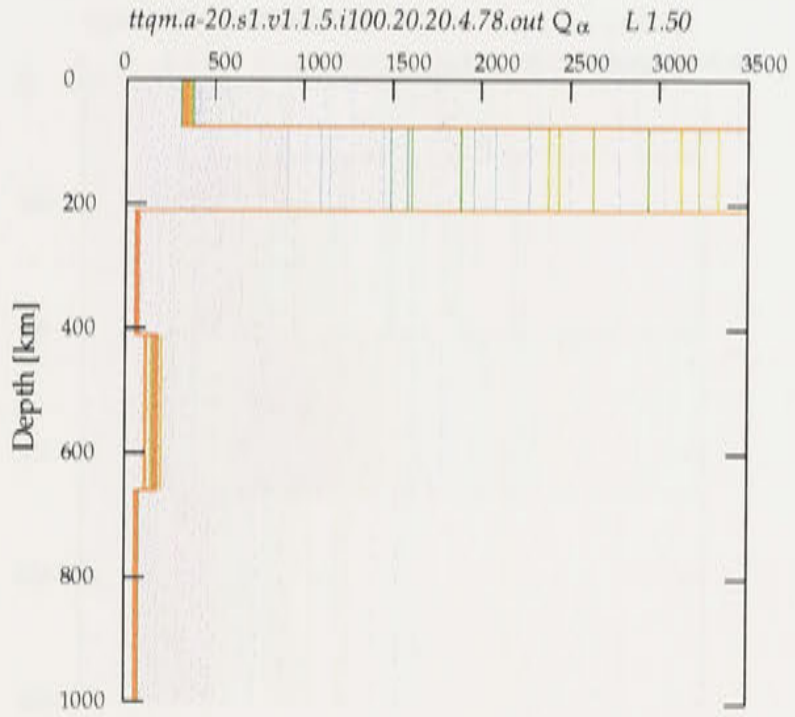

(c) Sl1 Az-20 21.03° < Δ < 26.82°

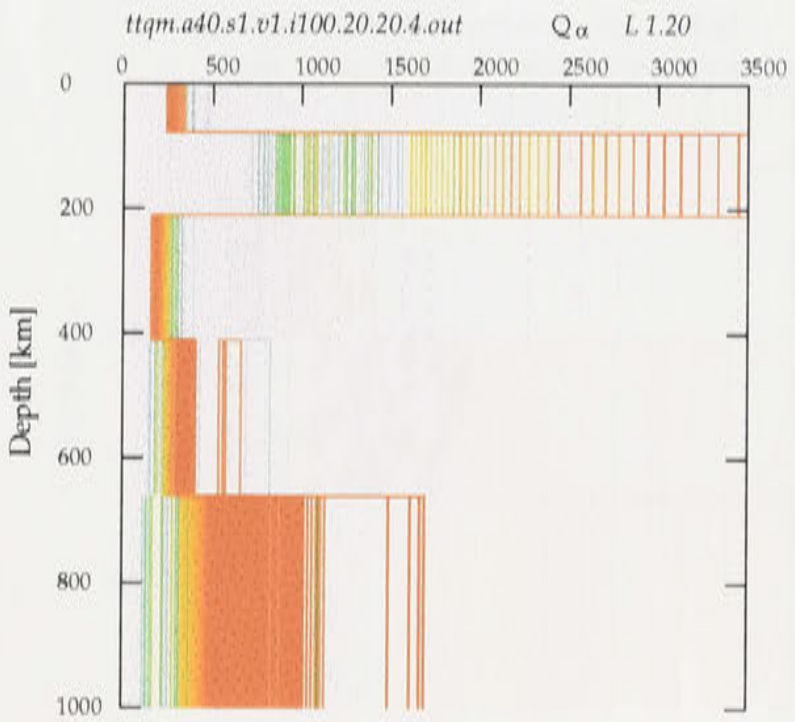

(d) Sl1 Az40 17.35° < Δ < 32.08°

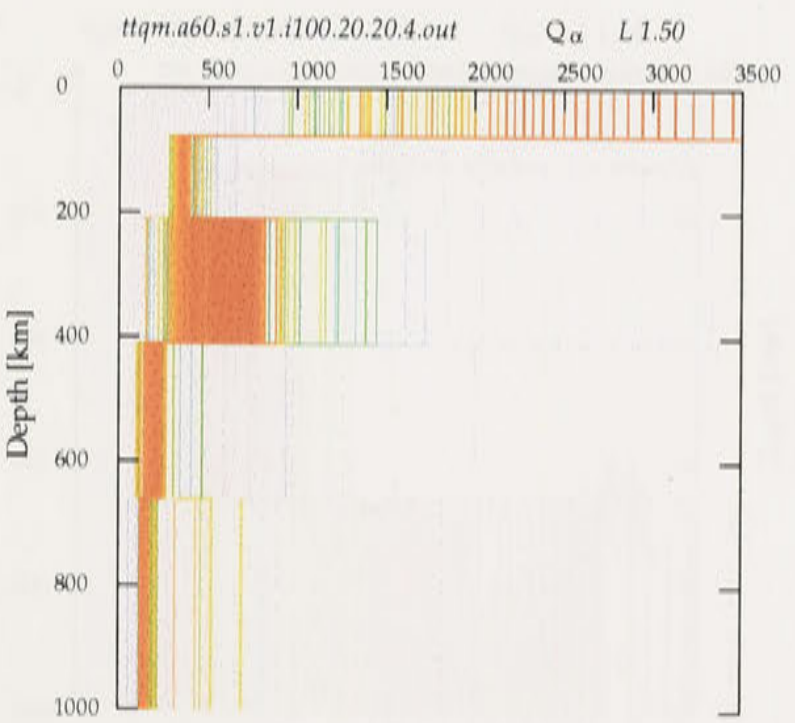

(e) Sl1 Az60 3.42° < Δ < 37.21°

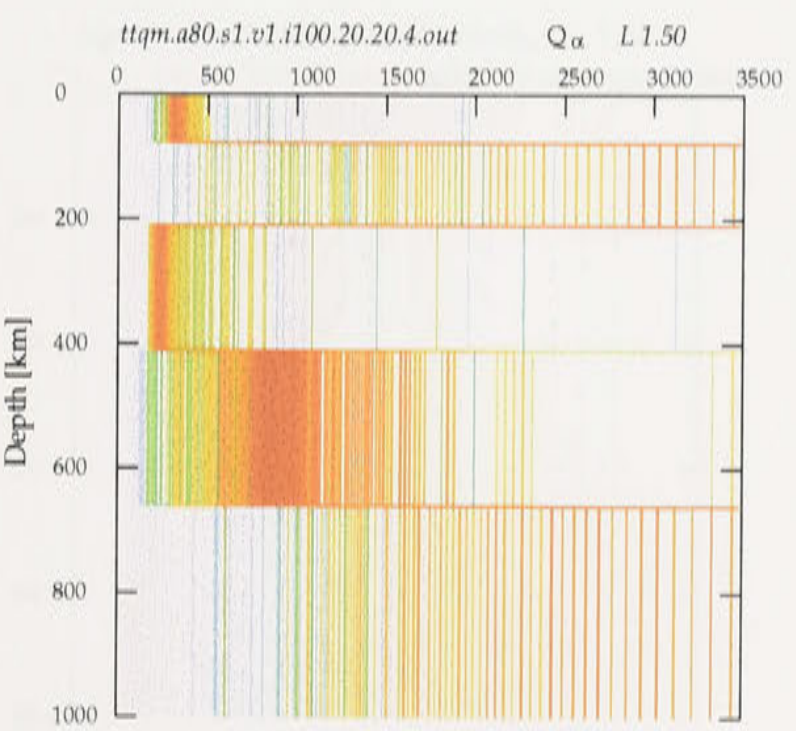

(f) Sl1 Az80 19.89° < Δ < 47.42°

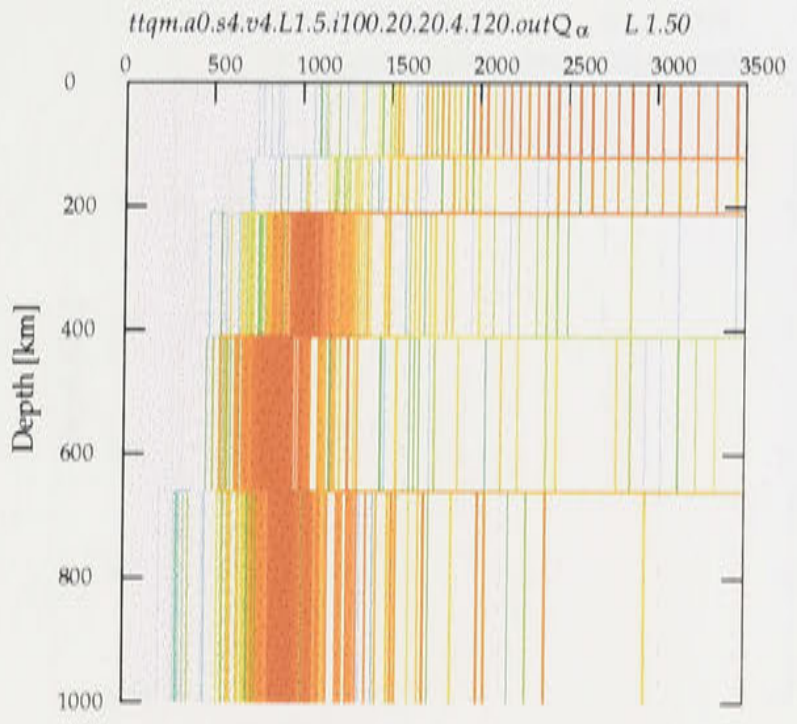

(g) Sl2 Az0 10.22° < Δ < 34.15°

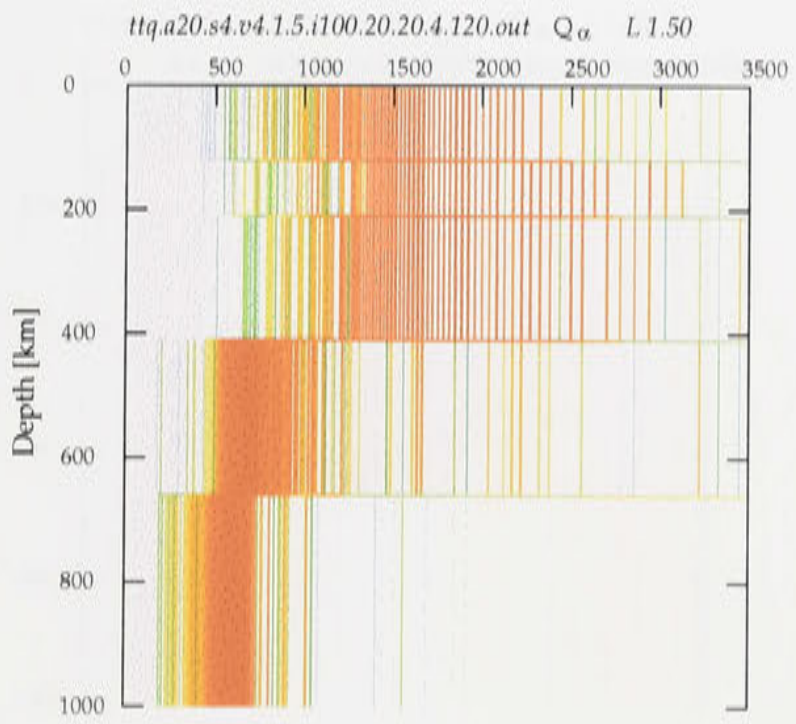

(h) Sl2 Az20 9.16° < Δ < 32.37°

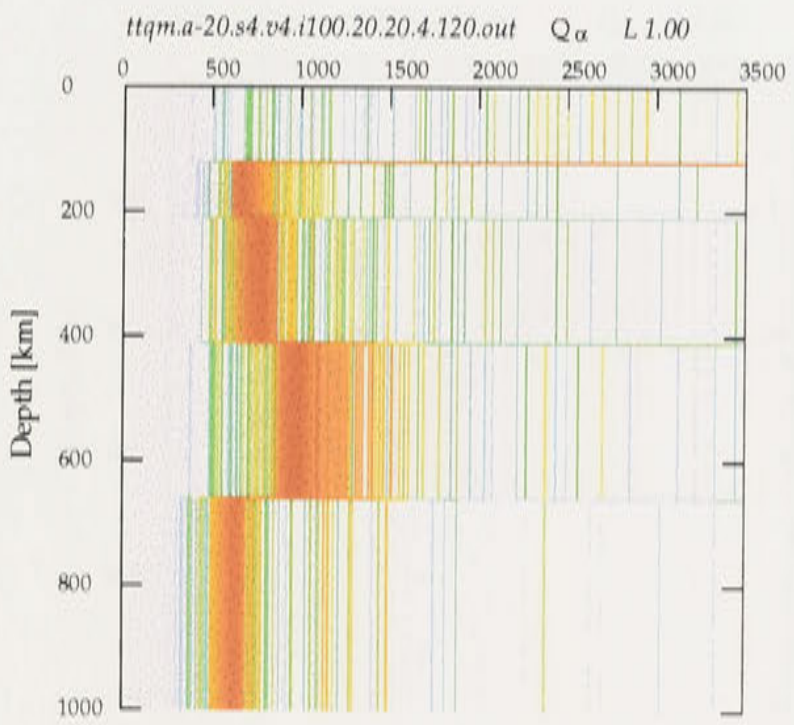

(i) Sl2 Az-20 17.46° < Δ < 34.76°

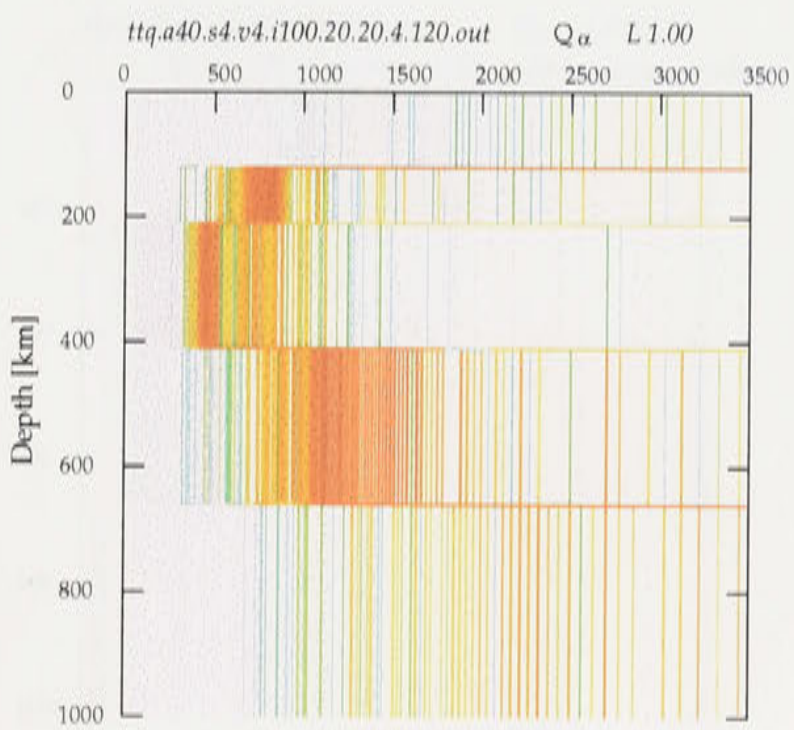

(j) Sl2 Az40 9.64° < Δ < 36.66°

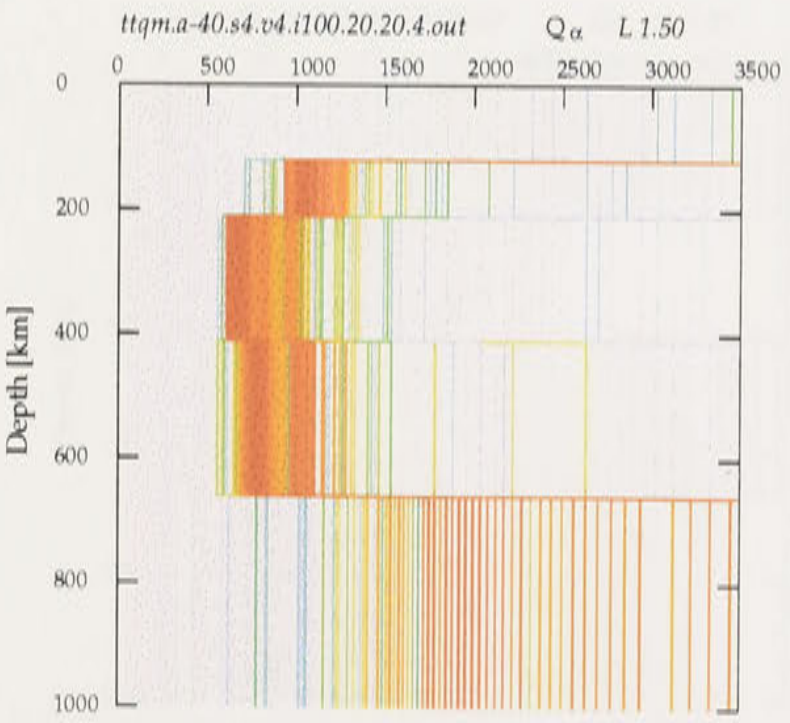

(k) Sl2 Az-40 12.37° < Δ < 32.19°

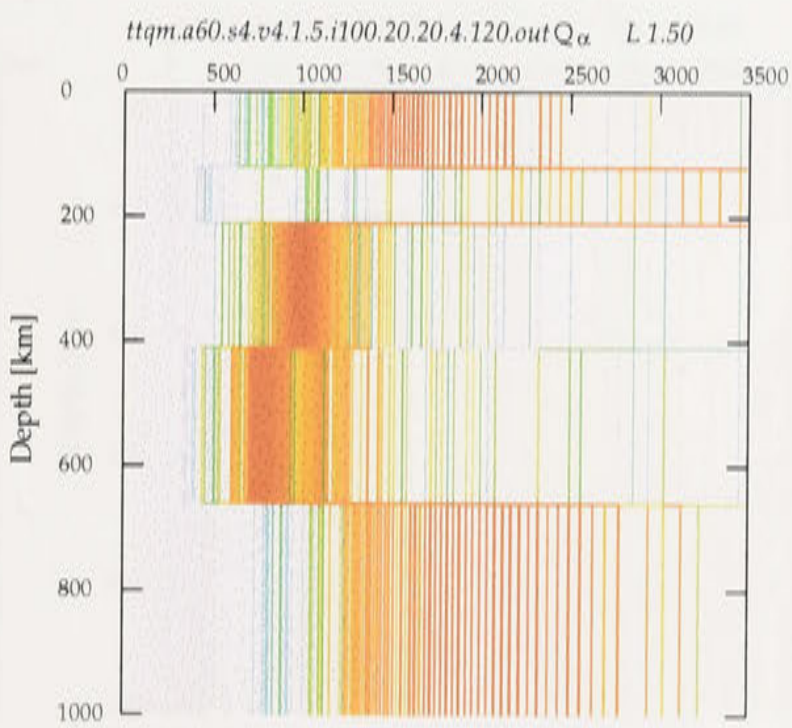

(l) Sl2 Az60 10.37° < Δ < 43.49°

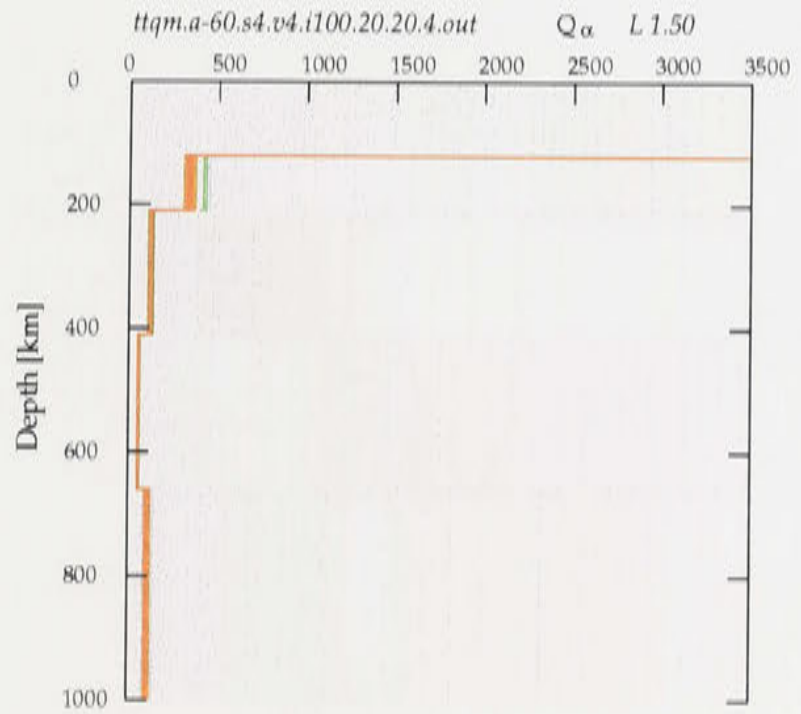

(m) Sl2 Az-60 14.44° < Δ < 18.49°

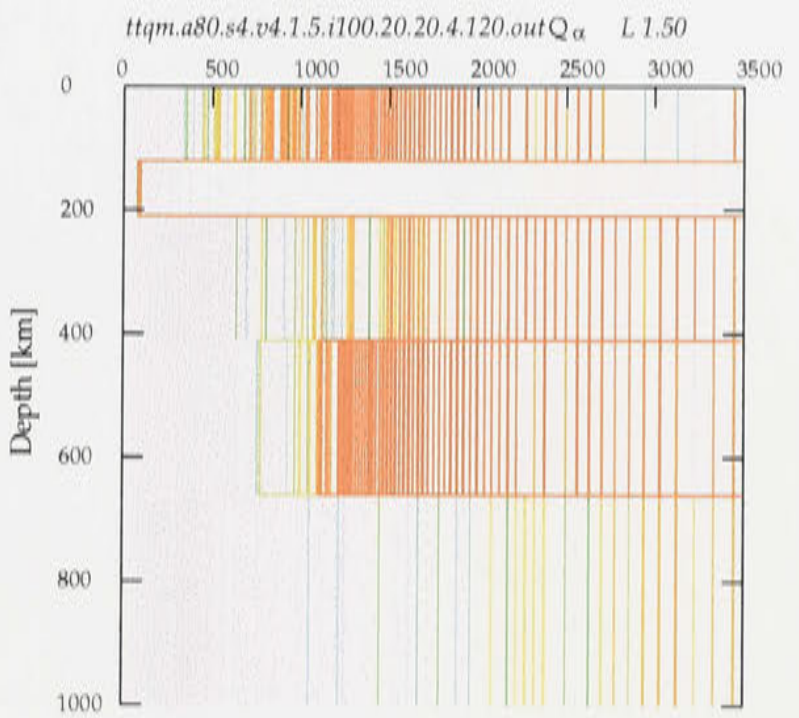

(n) Sl2 Az80 17.65° < Δ < 49.85°

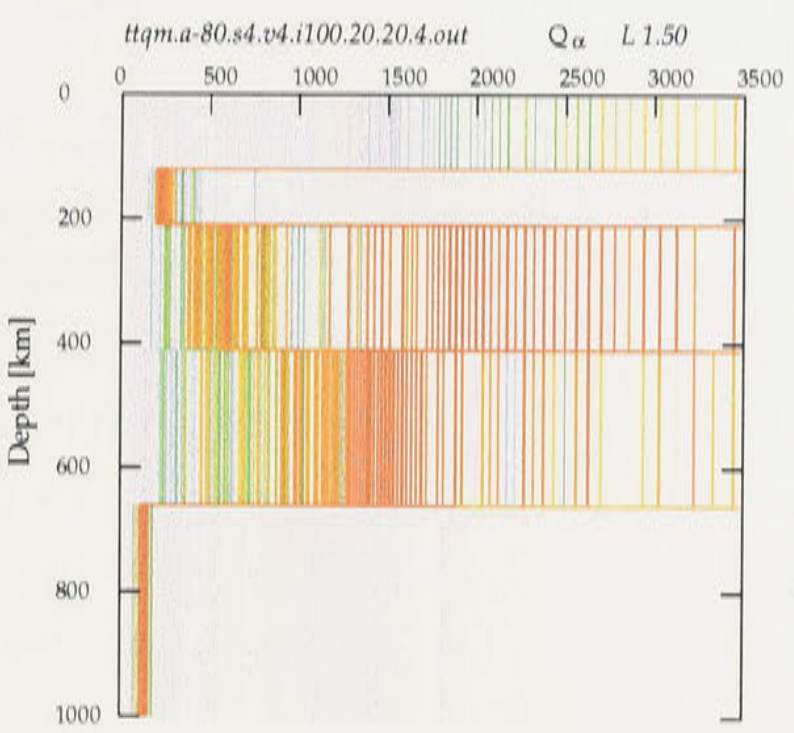

(o) Sl2Az-80 11.71° < Δ < 35.15°

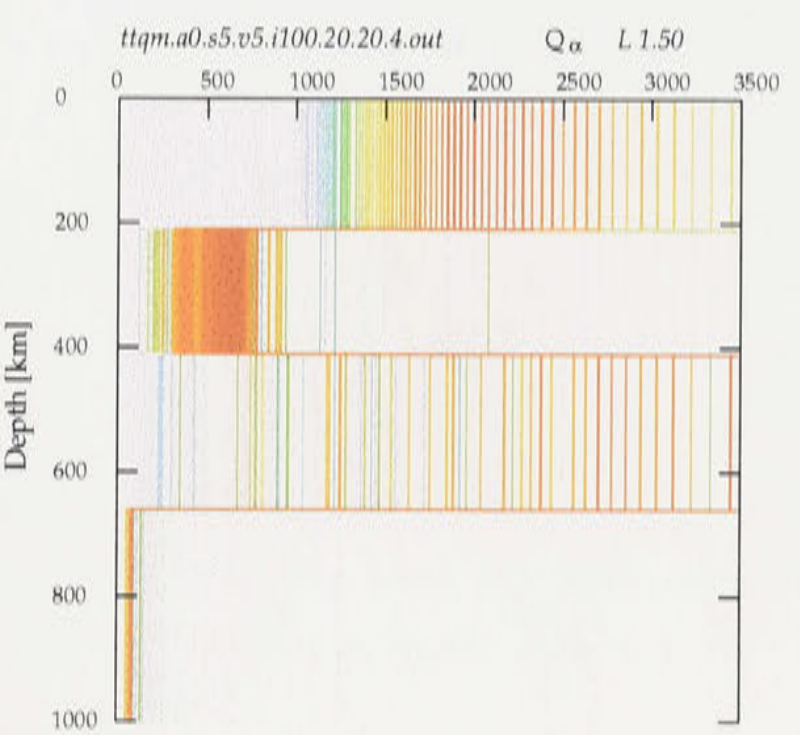

(p) Sl3 Az0 7.15° < Δ < 26.48°

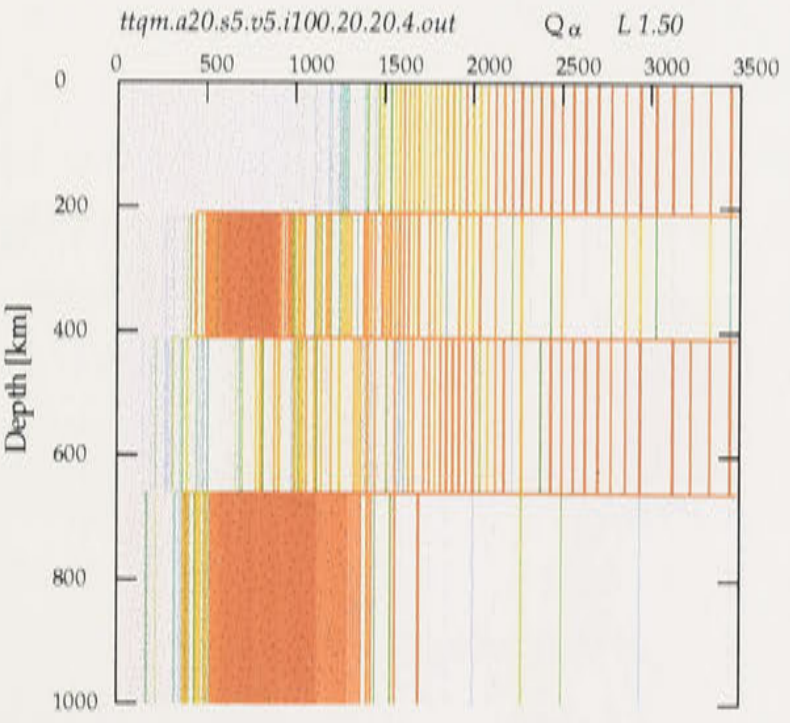

(q) Sl3 Az20 4.29° < Δ < 35.5°

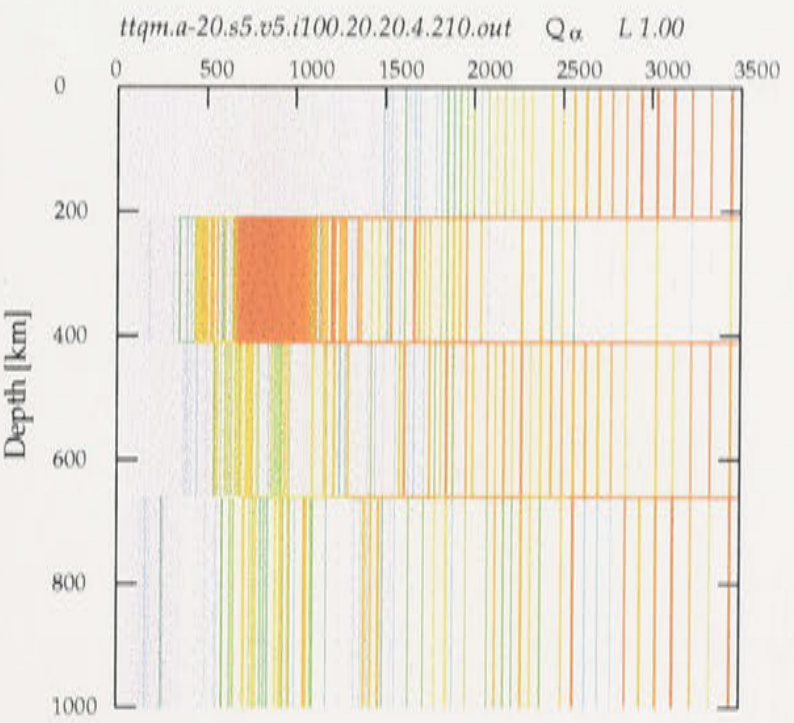

(r) Sl3 Az-20 2.2° < Δ < 37.89°

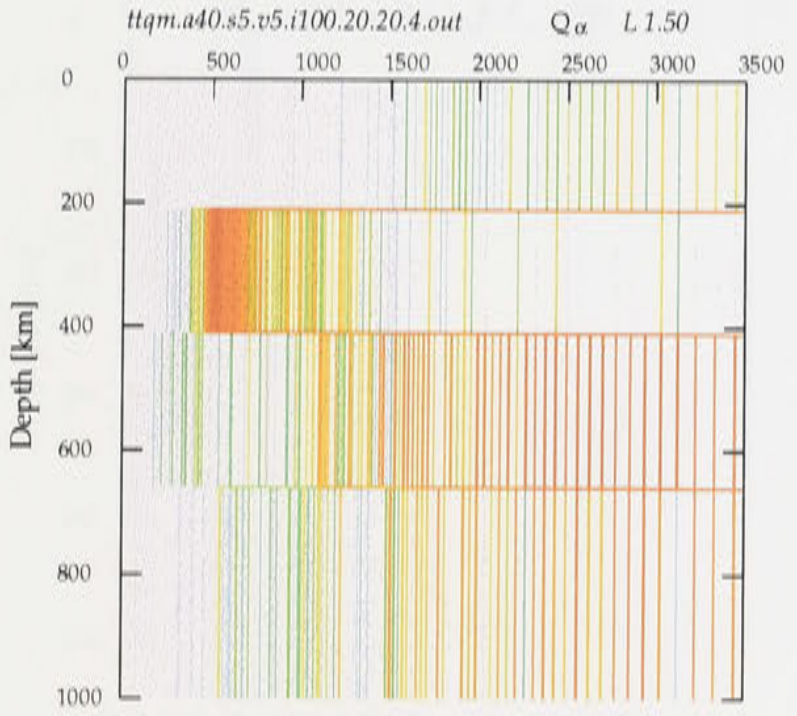

(s) Sl3 Az40 10.92° < Δ < 35.85°

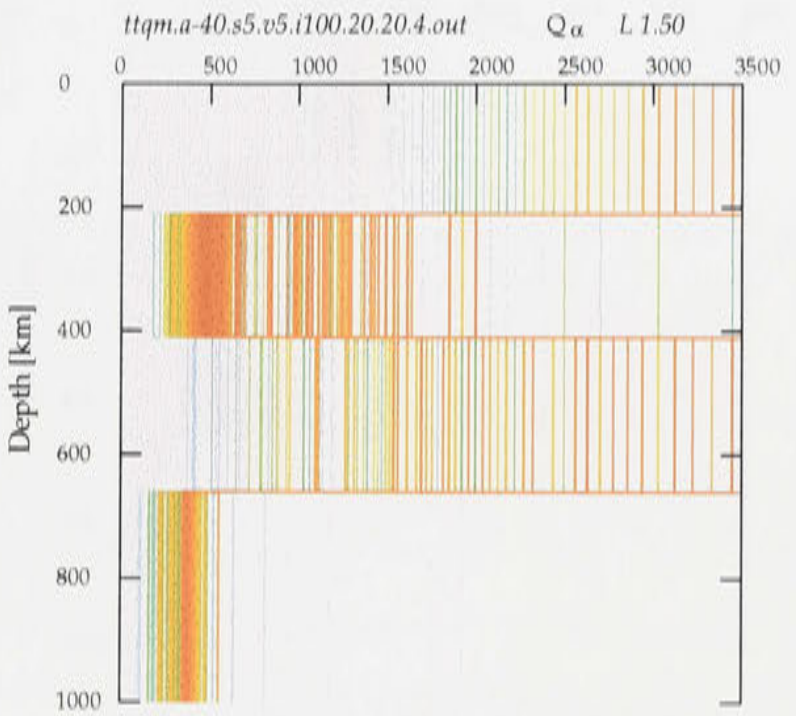

(t) Sl3 Az-40 0.98° < Δ < 30.89°

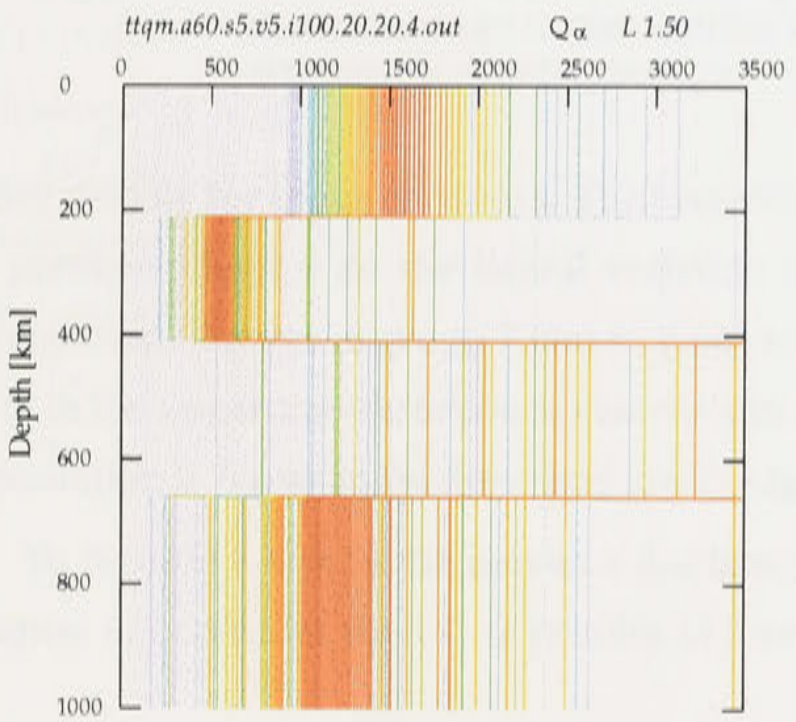

(u) Sl3 Az60 13.6° < Δ < 38.49°

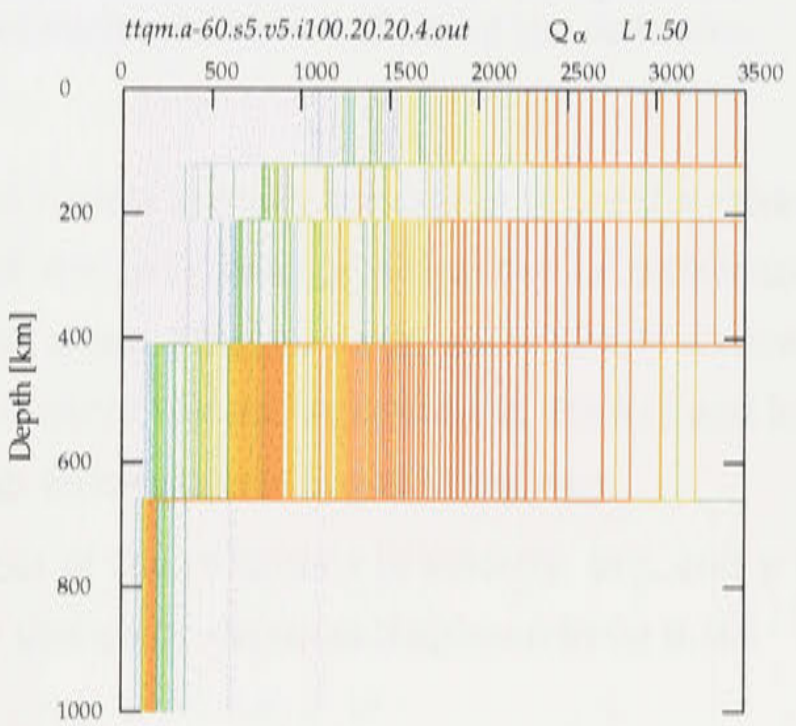

(v) Sl3 Az-60 3.26° < Δ < 31.35°

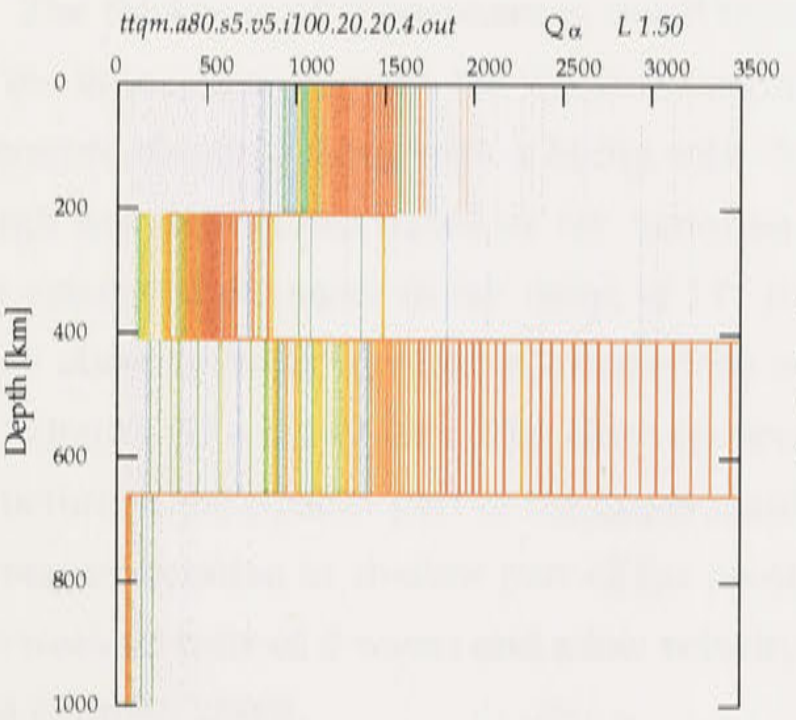

(w) Sl3 Az80 2.81° < Δ < 28.43°

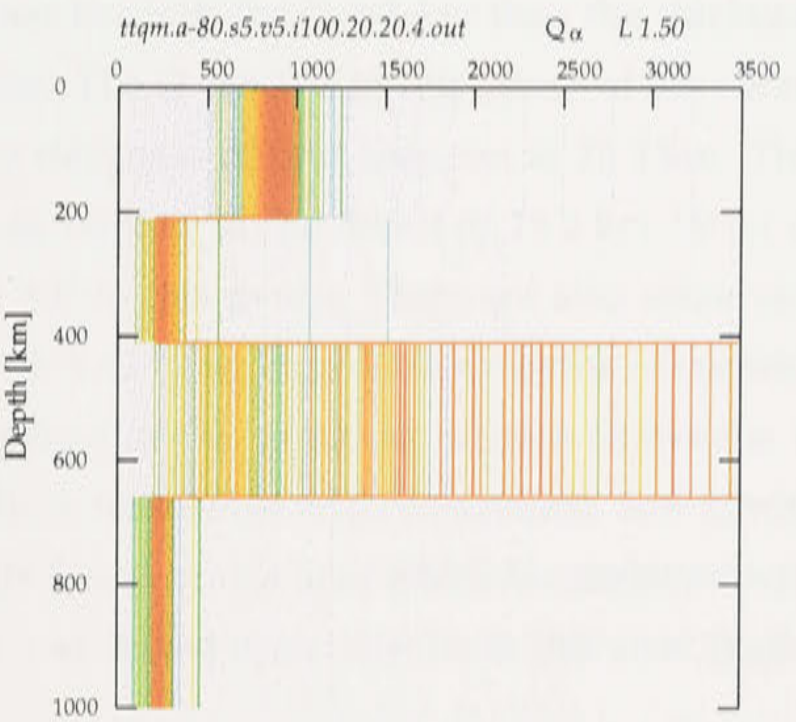

(x) Sl3 Az-80 4.03° < Δ < 41.17°

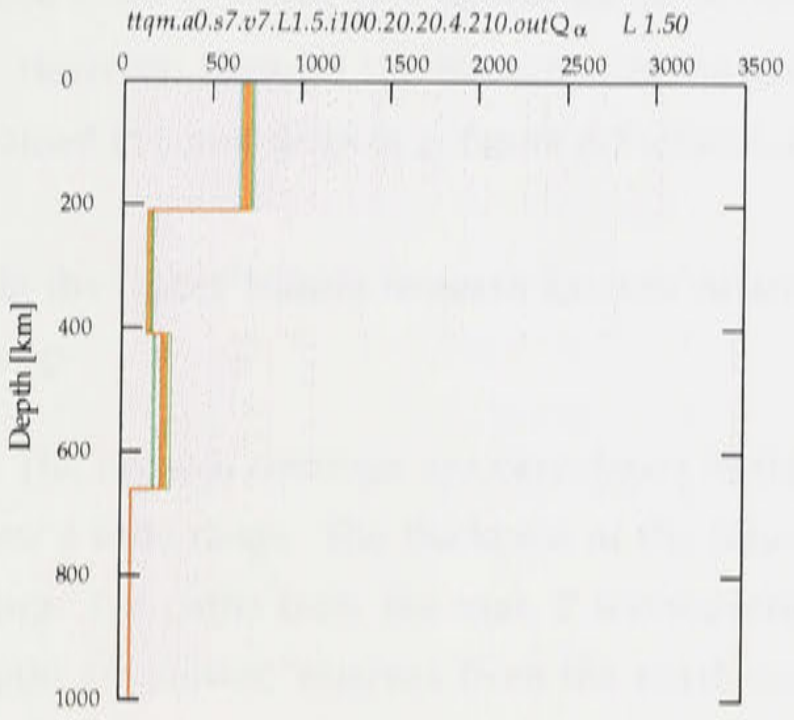

(y) Sl4 Az0 $14.86° < \Delta < 23.15°$

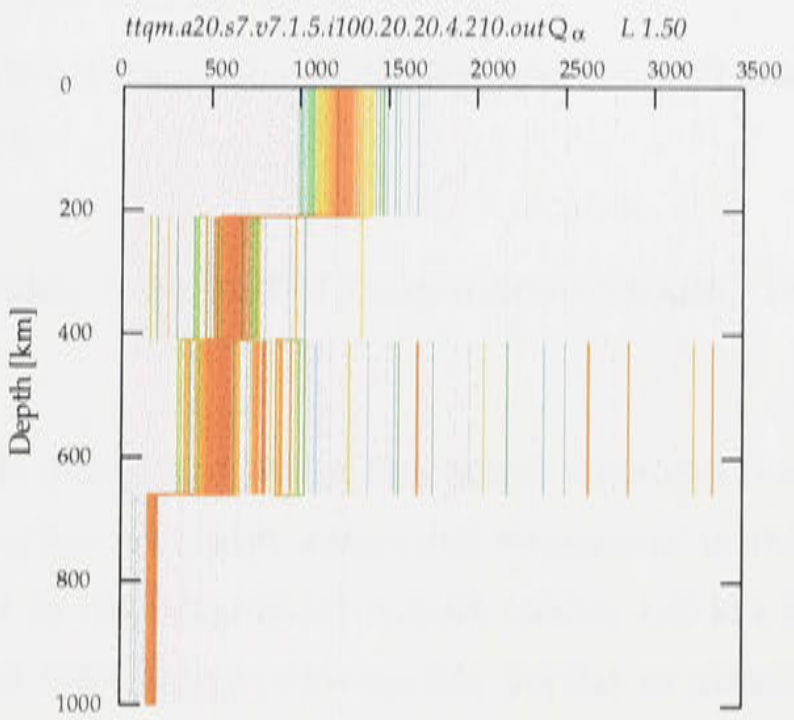

(z) Sl4 Az20 $14.14° < \Delta < 22.54°$

Figure 7.6: A set of 1-D Q profiles inverted from the SKIPPY data by NA. Epicentral distance range in the caption of each subfigure indicating the data constraints on depth coverage.

more reliable for those corridors. The inversion results are very consistent to the discussion in previous chapter on the lateral variation of the path average properties of differential attenuation. Figures in group 7.6(a) to 7.6(f) and group 7.6(p) to 7.6(x), show clearly contrast in Q in the upper mantle between eastern and western Australian continent. High Q and low attenuation is found in the west and low Q high attenuation is found in the east.

To provide a link to the previous discussions of the variations of velocity, δt^*_{sp} and γ in chapter 6. I consider the 1-D Q profiles in four groups of slices (as displayed in fig 6.10).

Q in the Upper Mantle beneath Coral Sea - *sl1* Group

The thickness of lithosphere is much thinner beneath the Coral Sea than the thickness of the lithosphere beneath the western Australia. The Q models in this group of slice were therefore obtained using with 5 layers with the thickness of first layer set at 75.5 km. This depth was determined based on the variation in velocity at the depth of 75.5 km. Most of the epicentral distances in the range of 17° to 30° in this group. There are also some very close observation in corridor of azimuth 60 with 3.42° and long distance paths in corridor of azimuth 80 with 47.42°. The close observations in this group of raypath allows the Q structure in the shallow part of the upper mantle is reasonably well constrained. Low Q with strong attenuation in shallow part of the mantle found in this area which is consistent with the weak arrivals of S waves and a low velocity zone in the upper mantle in this area [Kaiho and Kennett, 2000].

In the transition zone between 410 and 660 im in depth, the wavespeed are higher than the *ak135* reference. The variation in differential attenuation is consistent to the variation in

P and *S* wave velocity (see figures 6.7 (a) to (f)).

However, because the limitation of raypath coverage, the *Q* models are not well constrained in some slices (e.g. figure 6.7 (c) and (e)).

Q in the Upper Mantle beneath Eastern Australia: from Gulf of Carpentaria to South - *sl2* Group

The raypath coverage are very dense in this group and the of epicentral distances also cover a wide range. The thickness of the lithosphere is highly azimuthal dependent in this group. For paths from the east, *P* wavespeeds in the uppermost mantle (above 120 km in depth) are slower; whereas from the north and west higher wavespeeds persist to greater depth. In general, there are significant change in velocity at depth of 120km in this group of data. Thus the *Q* models are obtained in 5 layers with depth of first layer 120km . The common feature in this slice group is that the *Q* is higher than *sl1* but lower than *sl3*. However, the *Q* value in each layer varies across the different azimuths within the slice. Thus strong lateral variation in *Q* is revealed. This is consistent with the complex feature of variation in velocity and δt^*_{sp} in this group. As discussed in chapter 6, at shorter distances, the δt^*_{sp} estimated from this group of phases are small with weak attenuation (see figure 6.7 (a)). In the medium distance range, the δt^*_{sp} estimated from this group of data show mixed large and small values (see figure 6.7 (b)). The *P* waves velocities in the transition zone are slightly faster than *ak135* and the *S* waves are characterised by strongly attenuated arrivals.

δt^*_{sp} in the Upper Mantle beneath Central to Western Australia - *sl3* Group

In this group, the raypath coverage is most dense compared to other three groups and the epicentral distances also cover the widest ranges from 0.98° to 41.17°. The *Q* values obtained from this group of data is relatively high which is consistent with high *P* and *S* wavespeed [Kaiho and Kennett, 2000]. There are many short raypaths in this group, particularly the events recorded by KIMBA projects. The thickness of lithosphere beneath middle and western Australia are much thicker than eastern Australia. Hence, the *Q* models are developed using 4 layers for this group with first layer to a depth of 210km . The *Q* in the first layers are all very well constrained for most of slices in this group because the very good raypath coverage.

δt^*_{sp} in the Upper Mantle beneath Western Australia - *sl4* Group

The data in this group is very limited. There are only *Q* models obtained in the two slices with azimuths 0 and 20 in this group. The *Q* models were also constructed with relatively less number of raypaths. There are only 5 paths in the slice with azimuth 0 and 6 paths with azimuth 20. The *Q* model is based on 4 layers with the thickness of first layer set at 120km. This choice is based on the significant change in velocity at depth of 210km and the thickness

of lithosphere. The Q values obtained in this group at depth within 210 kmis very low which is consistent with the very low P wavespeed and slight low S wavespeed. The contrast in V_p/V_s ratio is also the reason of negative δt^*_{sp}. Hence, the negative value of δt^*_{sp} are helpful to recover the attenuation structure. It is not caused by the high noise in data. It is the nature of strong spatial variation in attenuation and strong spatial variation in V_p/V_s ratio. My forward modeling in chapter 8 has produced synthetic negative δt^*_{sp}. My experiments on inversion from synthetic δt^*_{sp} has confirmed the negative values of δt^*_{sp} are helpful to recover the attenuation models to generate the synthetic δt^*_{sp}.

7.4 Spatial Variation of Q in the Upper Mantle

7.4.1 Evaluation of Best 1-D Q^{-1} Model by Using NA

In the previous section a group of acceptable 1-D Q models was derived for each slice by using NA. One of the benefit of using NA is a set of acceptable models are derived rather than the single model. However, for constructing the 3-D attenuation models a best 1-D attenuation model is required for a particular 1-D profile. During the inversion by using NA , the misfit is reduced by increasing the number of iteration of the inversion procedure. However, the rate of reduction in misfit decreases with increasing iteration numbers. Hence, after certain number of iterations, the misfit level will have no significant change. Based on extensive experiments, as described in section 7.3.3, 100 iterations is chosen as standard for the inversion of attenuation models in this thesis. At the end of inversion, a model with smallest misfit is chosen as the final best model to be used for during the 3-D attenuation models.

7.4.2 Construction of 3-D Q^{-1} models

In the previous section a set of 1-D Q profiles have been constructed by NA inversion from δt^*_{sp} as a function of range. The 1-D profiles display the strong spatial variation of Q structure in the upper mantle beneath the Australian continent. It is also possible to construct a pseudo-3-D Q structure derived from the 1-D Q profiles. In order to construct the pseudo-3-D Q structure, I have first derived the vertical raypath density at each layer for each 1-D Q profile by undertaking raytracing for each raypath which contributes to the construction of this 1-D profile. The vertical raypath density has been derived with same depth resolution as the Q profiles.

The vertical relative raypath density of a particular slice at specified layer was calculated based on the length of total ray segments in this layer divided by the sum of ray segments at all layers of this slice. Then I have also constructed two sets of horizontal relative raypath density functions to represent the lateral variation of the ray distribution for each layer. One set of

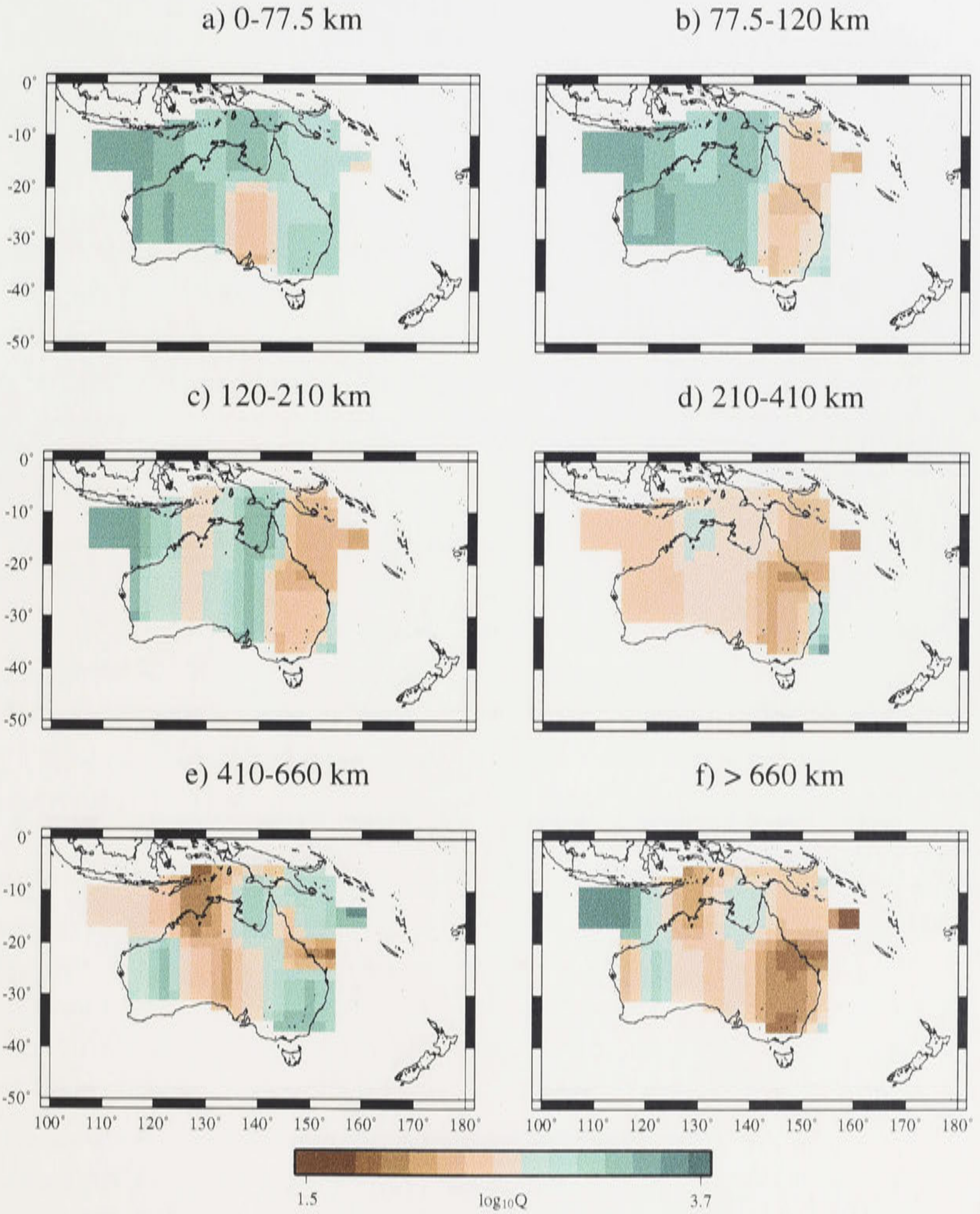

Figure 7.7: 3-D Q model in the upper mantle beneath the Australia region. The 3-D Q model was obtained by averaging the set of 1-D Q^{-1} profiles weighted by using three sets of ray density functions.

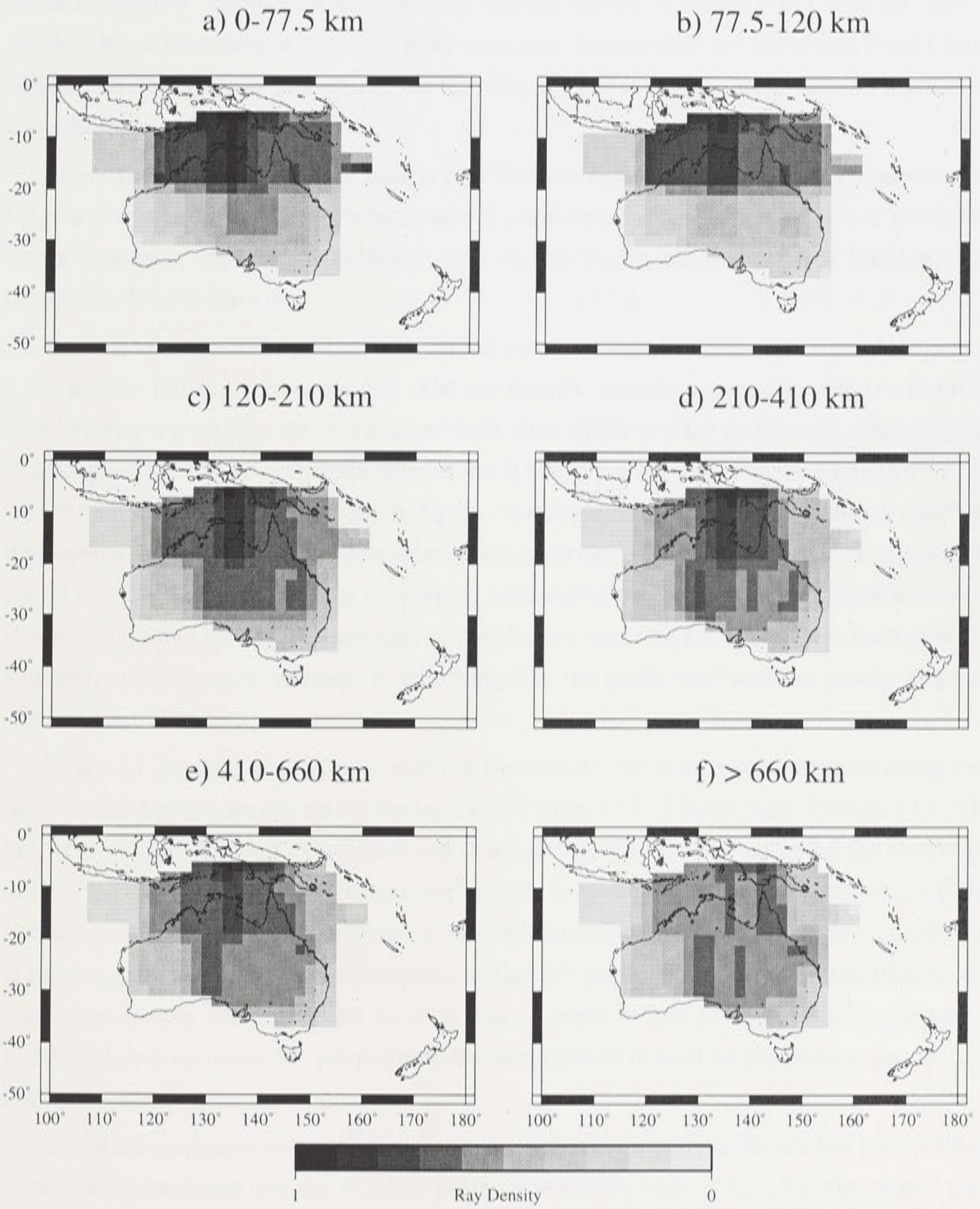

Figure 7.8: Ray density derived by averaging the ray density in each layer obtained by 1-D ray tracing for each slice. The dark areas indicate strong ray path coverage.

the horizontal raypath density functions represent the relative ray density of all available slices in one azimuth corridor. Thus, this density function is calculated from the length of total ray segments in one slice divided by the sum of ray segments of all available slices in this azimuth corridor. Another set of horizontal raypath density functions represents the relative ray density of slice groups 1, 2, 3, 4 in all corridors. Hence, they are calculated from length of total ray segments in one slice divided by the sum of ray segments of this slice group in all azimuth corridors.

I have then conducted a grid search over latitude from 0 tp -46° with increment 2° and longitude from 100 to 178° with increment 2°, and obtained a Q^{-1} estimate in a particular cell by averaging the 1-D Q^{-1} profiles, which overlap in this cell, weighted by the three sets of raypath density function.

I have also conducted a grid search over the same ranges in latitude and longitude to obtain a ray density pattern across the cell. The ray density value in a particular cell is produced by averaging the vertical ray densities of each slice which overlap in this cell. This raypath density gives a measure of the reliability of the Q image can band is displayed in figure 7.8. As we would hope, the raypath density in figure 7.8 does indeed correspond to the ray coverage displayed in figures 6.5 and 6.7. The densest ray coverage are in the northern part of Australia for all depths. Generally, the ray coverage is reasonably good for the upper mantle beneath the the Australian continent. However, in the shallow part, the ray coverage is limited in the southern area. The ray coverage is also limited in the north west and the corner of south eastern Australia.

Figure 7.7 displays a set of map views of the pseudo 3-D Q structure obtained using 2×2 degree cells. Images are shown for the layers 0-75.5km, 77.5 - 120km, 120 - 210km, 210 - 410 km, 410 - 660km, 660+km. As we have seen from the ray density maps in fig 7.8 the resolution of the available data set is limited and, particularly in the southern part of Australia, only the average properties in large blocks are at all well constrained. Nevertheless the pseudo 3-D Q images present the first representation of the 3-D spatial variation of attenuation in the Australian region. The dominant result is that Q tends to first to decrease with increasing depth and then increase; the attenuation of seismic waves is weak in the shallow part (< 120 km) of the Earth.

Low attenuation is dominant beneath the Australian continent in the shallow part of lithosphere with the depth less the 77.5 km. A low attenuation zone is found in the central part of south Australia. This is consistent to the cross sections B and C of velocity in figure 3.3(b). There is a low velocity zone found the in the shallow area of central south Australia (see cross sections B and C in figure 3.3(b). However, the raypath coverage is poor in this area in my data set, thus this zone need more investigation to confirm.

For the layers 77.5 - 120km and 120 - 210km, there are strong contrasts in the attenuation between western and eastern Australia where Q is about a few hundred to a few thousands

with strong lateral variation. The pattern of attenuation in layers 77.5 - 120 km is in good agreement to the surface wave velocity in the depth 150 km in figure 3.2. The exception is the low attenuation zone in the far north western area. This area is less reliable because of poor raypath coverage. There is a high attenuation narrow belt through north to south in the western part of Australia in the layer with depth 120 - 210 km . The pattern of attenuation in this layer is basically consistent to the surface wave velocity in the depth 200 km in figure 3.2 and the body wave velocity both in shear and dilation in the depth 165-210 km in figure 3.5.

The attenuation is most pronounced at depth of about 210-410 km in the upper mantle where a small low attenuation island in the north western area is surrounded by large area with strong attenuation. The strongest attenuation zone is found in eastern part of Australian. Another low attenuation zone is found in the south eastern Australia, but this is less reliable because of limited ray path density.

In the eastern part of the Australia, the low attenuation in the surface region (< 100 km) and high attenuation from 100 to 400 km displayed in figure is in very good agreement to the cross section F of velocity in the figure 3.3(b).

The attenuation in the layer at depth 410 - 660 km generally show strong contrast between eastern and western Australia; the strongest attenuation zone is in the north west of Australia and low attenuation zones lie in NE, SE and SW Australia. The P wave velocity show clear high velocity in the eastern Australia and low velocity in the western Australia in the depth 610-660 km in figure 3.6. The low shear body wavespeed is dominant in the eastern Australia in depth 610-660 km. There are strong contrast in V_p/V_s ratio in depth 610-660 km (see fig 3.6).

In the layer at depth greater than 660 km, the path coverage is limited. However, the attenuation is consistent with the layer 410 - 660 km in the western and central part of Australia. But the attenuation is very strong in this layer in the eastern part of Australia. The strongest attenuation zone in this layer is in the south eastern part of the Australia. The shear wavespeed obtained by Debayle and Kennett [2000] from surface waveform inversion is only upto 350 km because of the data limitation. The shear body wavespeed is only available in the north eastern Australia in the lower mantle (see fig 3.6). However, there are reasonable P wavespeed information extend to south and south eastern Australia in the lower mantle (see fig 3.6). The P wavespeed show clear high velocity in the north Australia and low velocity in the south and south eastern Australia. This is basically consistent to the attenuation pattern in the lower mantle in figure 7.7 with depth is greater than 660 km.

There are less velocity information in lower mantle compare to the upper mantle and lithosphere, but the attenuation is consistent to the frequency parameter α in the deep layers (see chapter 9 for details) although the reliability of α in the lower mantle need more investigation to confirm.

7.5 Discussion

A set of 1-D Q profiles as a function of depth has been constructed by successfully using NA inversion method applied to the robust δt^*_{sp} estimates at fixed frequency at around 1 Hz from quality digital broadband SKIPPY seismic data.

A series of acceptable models rather than a single model was obtained by using NA. These models were illustrated in two different ways: both as a function of depth (see figures 7.6), and by mapping the misfit variation of acceptable models (see figure 7.4). The acceptable models obtained by NA make it possible to investigate the behaviour of the inversion results and to evaluate the uncertainty in the solutions. The best model was chosen from the series of acceptable models as the final solution. I have done extensive experiments in finding satisfactory solutions for Q models from my δt^*_{sp} estimates.

One of most important factors affecting the Q models is how to set up the layer in depth of Q models. The parameterisation in depth for the Q models depends on the information contained in the δt^*_{sp}. Experiments on over 20 layers with thickness of 50 km and 100 km in depth show that the Q could not be resolved in thin layers. The Q values oscillate between layers because the information in the δt^*_{sp} could not reach the resolution of 20 layers in depth. My studies suggest that 4 layers in depth beneath western Australia and 5 layers beneath eastern Australia is a reasonable choice for the constraints provided by the δt^*_{sp}.

Experiments on the effects of the background velocity model suggest that choosing the right velocity model will help to improve the Q models. 1-D velocity models are not available for all slices of my δt^*_{sp} estimates. Hence, the Q model is affected by limited velocity information in some slices. This leaves some room to improve the results of the Q inversion by using more accurate velocity models in the future.

The Q models reveal strong lateral variation of body wave attenuation, and hence the set of 1-D Q profiles allows me to construct a 3-D Q model for the upper mantle. The 3-D Q model obtained in this chapter is different from the conventional cellular models. This 3-D Q model was obtained by averaging the set of 1-D Q^{-1} profiles and weighted by three functions of raypath density. The three raypath density functions reveal the depth and lateral dependence of raypath. The 3-D Q results are well correlated with the body wave and surface wave velocities obtained using very different techniques.

Experiments on constructing 3-D Q models by averaging 1-D Q values show that no significant contrast in Q in the shallow depth (< 120km) between the eastern and western. However, some 1-D Q profiles show strong lateral variation in attenuation in the upper mantle across the Australia. This is because in some slices the Q values are extremely large (> 3000) in the eastern region, and have a strong effect when averaging the 1-D Q profiles. Finally I solved the problem by averaging Q^{-1}. This effect has been significantly reduced by averaging Q^{-1}. However, Q values are used in the plotting as they have been used in the previous figures.

Part IV

Numerical Simulation and Estimation of Frequency Dependent Attenuation Model

Chapter 8

Numerical Simulation and Estimation of Frequency Dependent δt^*_{sp}

8.1 Introduction

The observation of δt^*_{sp} from the SKIPPY data set at a centre frequency of 1 Hz reveals the lateral variation of attenuation. The measurements of the path average property of the frequency dependence of attenuation γ also reveal lateral variations in the frequency dependence of attenuation. Both δt^*_{sp} and γ contains the depth dependent information on attenuation.

In this chapter, I examine the seismic body wave attenuation in 4 dimension space. I have estimated the frequency dependence of δt^*_{sp} which allows me undertake inversion for Q and frequency dependence at same time. I have undertaken forward modeling of δt^*_{sp} based on the frequency dependent attenuation model $Q(f) = Q_0(f_0)(f/f_0)^{\alpha}$ in each layer. I have discovered the effects of velocity, dispersion and α on δt^*_{sp}. I have found that the δt^*_{sp} is mainly controlled by Q, the effects of velocity on δt^*_{sp} are much smaller than the effects of Q, but sometimes small change in velocity values will change raypath of P or S and lead to significant variations in δt^*_{sp}. However, the effect of dispersion is very small. Thus I will ignore the effect of dispersion in the inversion for Q.

I have numerically simulated and estimated the surface of δt^*_{sp} as a function of frequency and distance, and I have fitted the estimated surface of δt^*_{sp} as a function of frequency and distance with synthetic one by NA inversion method.

8.2 Forward Modeling of Frequency Dependence δt^*_{sp}

For better understanding the estimation of δt^*_{sp}, I have calculated the δt^*_{sp} based on the formulation $\delta t^* = t^*_0 (f/f_0)^{-\alpha}$. I have also simulated the δt^*_{sp} from real velocity and attenu-

ation models based on $Q(f) = Q_0(f_0)(f/f_0)^\alpha$. The results suggest that the α are very small it the lithosphere, corresponding to distances less than 16° . There are dramatic changes in δt^*_{sp} and from 16° to 18° . The changes in δt^*_{sp} at this distance range are contributed by the big jump in velocity at 410km discontinuity. The changes in δt^*_{sp} at this distance range suggested a large difference of frequency dependence of attenuation in lithosphere and asthenosphere.

8.2.1 Calculation of δt^* Based on Formulation $\delta t^* = t^*_0(f/f_0)^{-\alpha}$

To get a feeling of how the α controls the behaviour of the function of power law relation between δt^* and frequency, I have calculated the δt^* from the formulation $\delta t^* = \delta t^*_0(f_0)(f/f_0)^{-\alpha}$ with α increasing from 0.05 to 0.95 at 0.05 step with $t^*_0 = 1.0$. The general features is the δt^* at frequency lower than 1 Hz increase dramatically with decreasing α but the δt^* at frequency higher than 3 Hz decrease slightly with increasing α.

The values of δt^* are controlled by both $\delta t^*_0(f_0)$ and α, but the curvature of the graph is controlled by α. Thus figure 8.1 suggest that the curvature of estimated δt^*_{sp} is controlled by the frequency dependence of attenuation. The above simulation provides us a background of the relationship between δt^*, frequency and α.

8.2.2 Effects of layered frequency dependence on δt^*_{sp}

I have also simulated the δt^*_{sp} as a function of frequency based on $Q(f) = Q_0(f_0)(f/f_0)^\alpha$ in each layer from various velocity models by undertaking ray tracing for P and S waves respectively, with different combination of α values in lithosphere, asthenosphere, transition zone and deep mantle.

Figure 8.2 is the results from three different combination of α. The graph with triangles is the δt^*_{sp} calculated from *ak135* with 0.1 in lithosphere, 0.6 in asthenosphere, 0.4 transition zone and deeper mantle. The graph with diamonds is the δt^*_{sp} calculated from *ak135* with 0.1 for all layers and the graph with crosses is the δt^*_{sp} calculated from *ak135* with 0.6 for all layers.

8.2.3 Effects of velocity model on δt^*_{sp}

There are strong lateral variations in attenuation and its frequency dependence between eastern and western Australia, as I have discussed in chapter 6. To reveal the influence of velocity on the δt^*_{sp}, I made the assumption that attenuation and its frequency dependence are same for the eastern and western Australia. I have chosen $\alpha = 0.1$ in lithosphere, 0.6 in asthenosphere, 0.4 in transition zone and deep mantle. I have also used an attenuation model which is close to *QNA1* for this calculation. Under those conditions, figure 8.3 suggests that the effect of velocity on the δt^*_{sp} is very small. This conclusion is important for inversion in

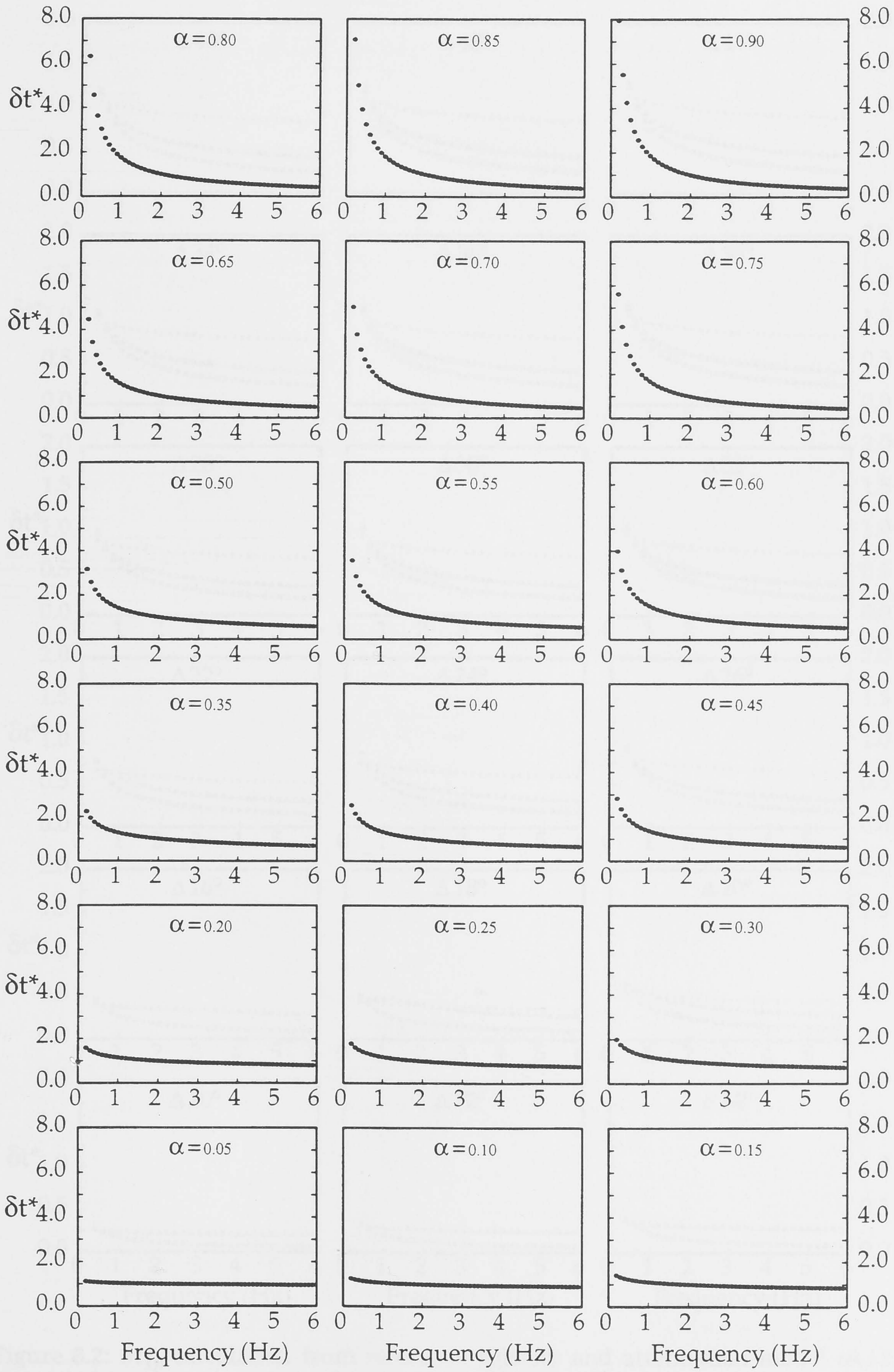

Figure 8.1: δt^* calculation based on formulation $\delta t^* = t_0^*(f/f_0)^{-\alpha}$

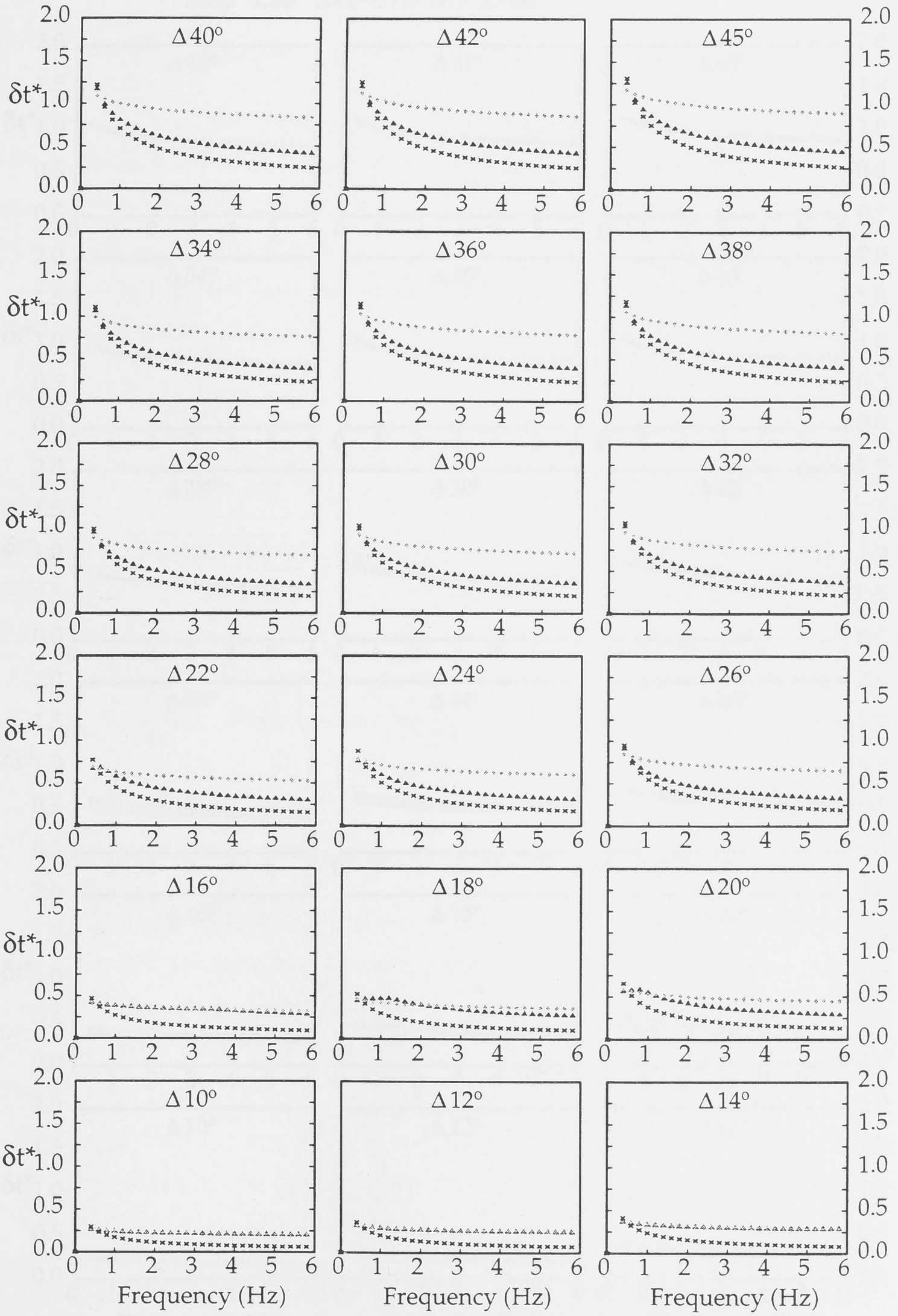

Figure 8.2: δt^*_{sp} calculation from reference velocity and attenuation model *ak135* based on $Q(f) = Q_0(f_0)(f/f_0)^\alpha$. The symbols of diamonds, triangles, and crosses represent the different combination of α in layers of lithosphere, asthenosphere, transition zone and deep mantle, see text for full description.

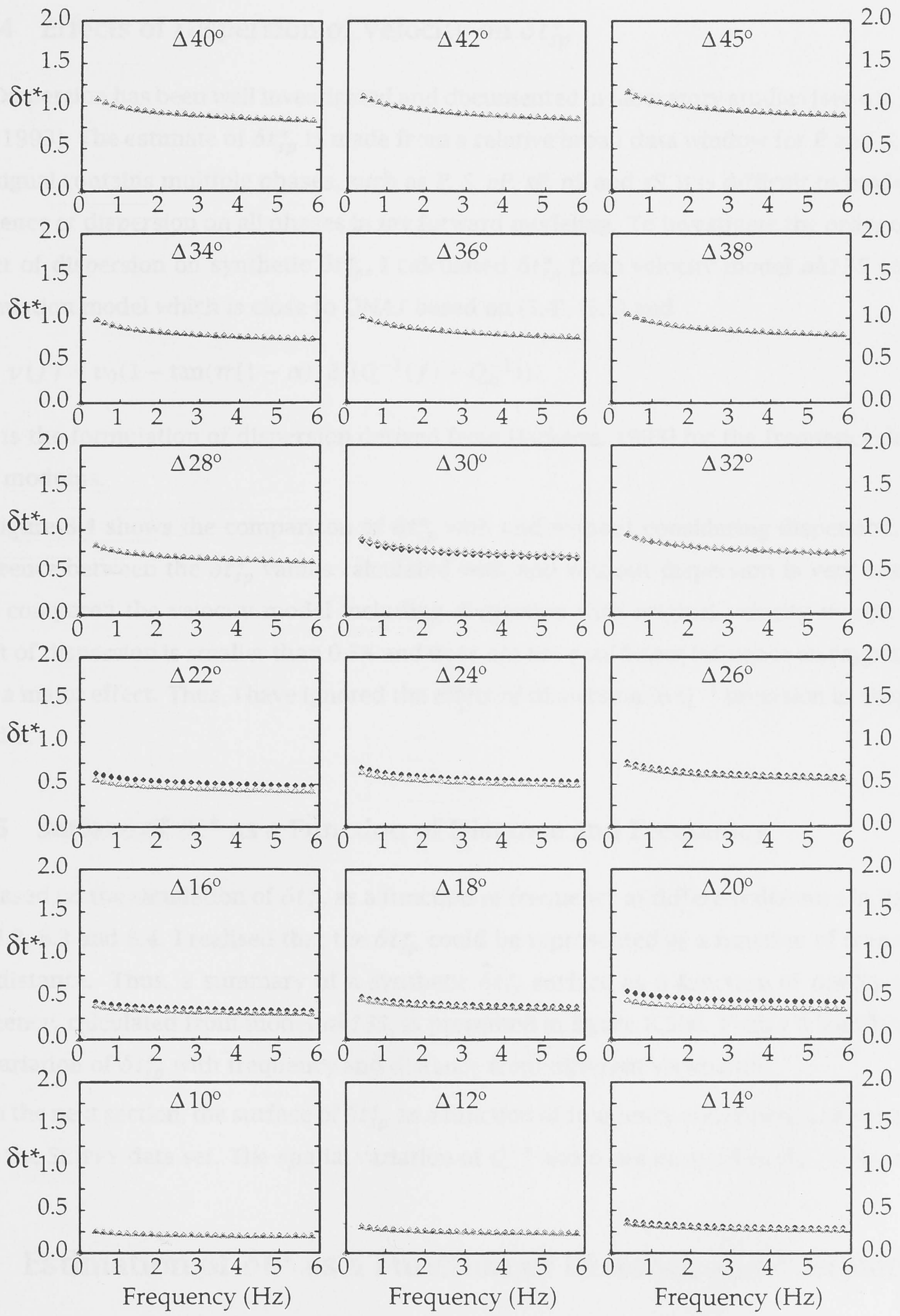

Figure 8.3: δt^*_{sp} calculation from velocity and attenuation models for eastern Australia *a0sl1* with diamonds and western Australia *a0sl3* with crosses based on $Q(f) = Q_0(f_0)(f/f_0)^\alpha$ with $f_0 = 1.0$ Hz.

chapters 7 and 9, because the 1-D velocity profiles are not available for all slices classified by δt^*_{sp}. Thus, for some slices, I have to use the velocity model from smae slice group from its close azimuth corridor to invert Q^{-1}.

8.2.4 Effects of Dispersion of Velocity on δt^*_{sp}

Dispersion has been well investigated and documented in laboratory studies [see e.g. Jackson, 1993]. The estimate of δt^*_{sp} is made from a relative broad data window for P and S, thus the signal contains multiple phases, such as P, S, pP, sP, pS and sS. It is difficult to model the influence of dispersion on all phases in my forward modeling. To investigate the order of the effect of dispersion on synthetic δt^*_{sp}, I calculated δt^*_{sp} from velocity model *ak135* and an attenuation model which is close to *QNA1* based on (5.4), (5.5) and

$$v(f) = v_0(1 - \tan(\pi(1-\alpha)/2)(Q^{-1}(f) - Q_0^{-1})). \tag{8.1}$$

(8.1) is the formulation of dispersion derived from [Jackson, 1993] for the frequency dependent modulus.

Figure 8.4 shows the comparison of δt^*_{sp} with and without considering dispersion. The difference between the δt^*_{sp} values calculated with and without dispersion is very small. I have compared the velocity model including dispersion with original velocity model. The effect of dispersion is smaller than 0.5% and does not have sufficient influence on raypaths to have a major effect. Thus, I have ignored the effect of dispersion in Q^{-1} inversion in chapters 7 and 9.

8.2.5 Surface of δt^* as a Function of Distance and Frequency

Based on the simulation of δt^*_{sp} as a function of frequency at different distance in figures 8.1, 8.2, 8.3 and 8.4. I realised that the δt^*_{sp} could be represented as a function of frequency and distance. Thus, a summary of a synthetic δt^*_{sp} surface as a function of distance and frequency, calculated from model *ak135*, is presented in figure 8.5(a). Figure 8.5(a) displays the variation of δt^*_{sp} with frequency and distance from different viewpoints.

In the next section, the surface of δt^*_{sp} as a function of frequency and distance is estimated from the SKIPPY data set. The spatial variation of Q^{-1} and α are inverted in the chapter 9.

8.3 Estimation of δt^* as a Function of Distance and Frequency

8.3.1 Frequency Band Setup Based on Golden Section

To estimate δt^*_{sp} as a function of frequency, I have divided the broad frequency band 0-6 Hz into a set of sub-frequency bands. Because of the dependence of attenuation on frequency,

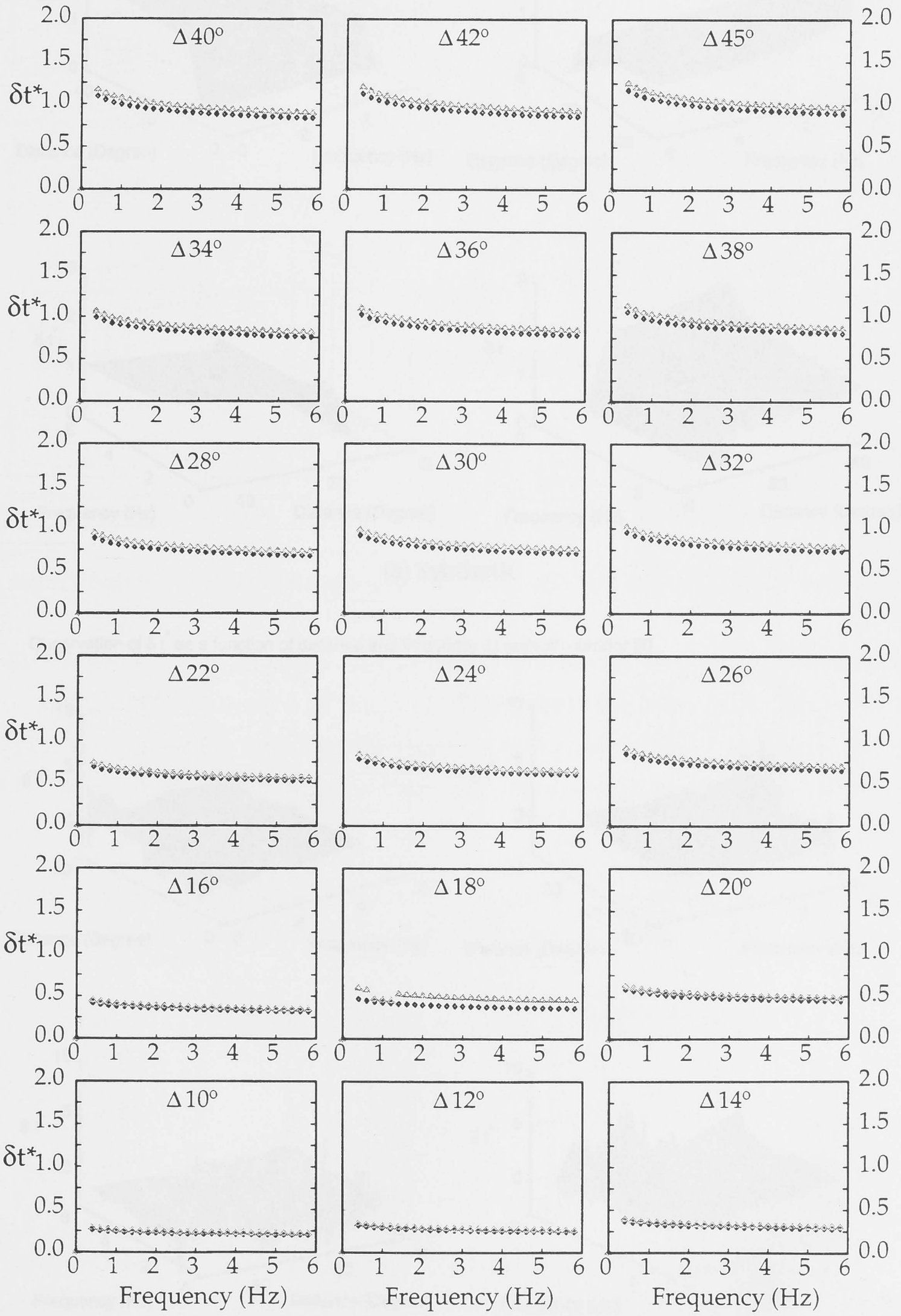

Figure 8.4: δt^*_{sp} calculation from velocity and attenuation model from *ak135* based on (5.4), (5.5) and (8.1), graph with triangle considering dispersion

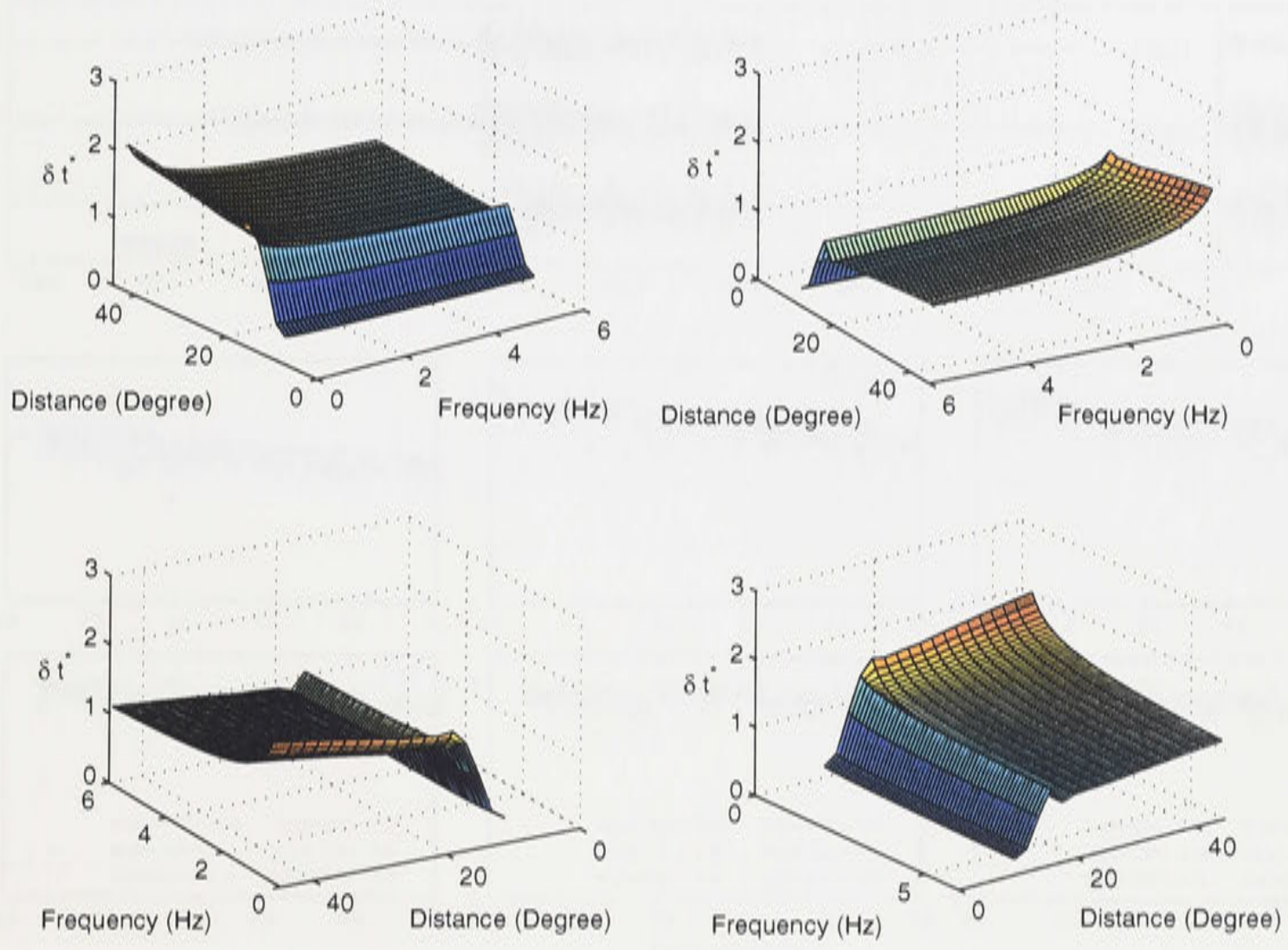

(a) Synthetic

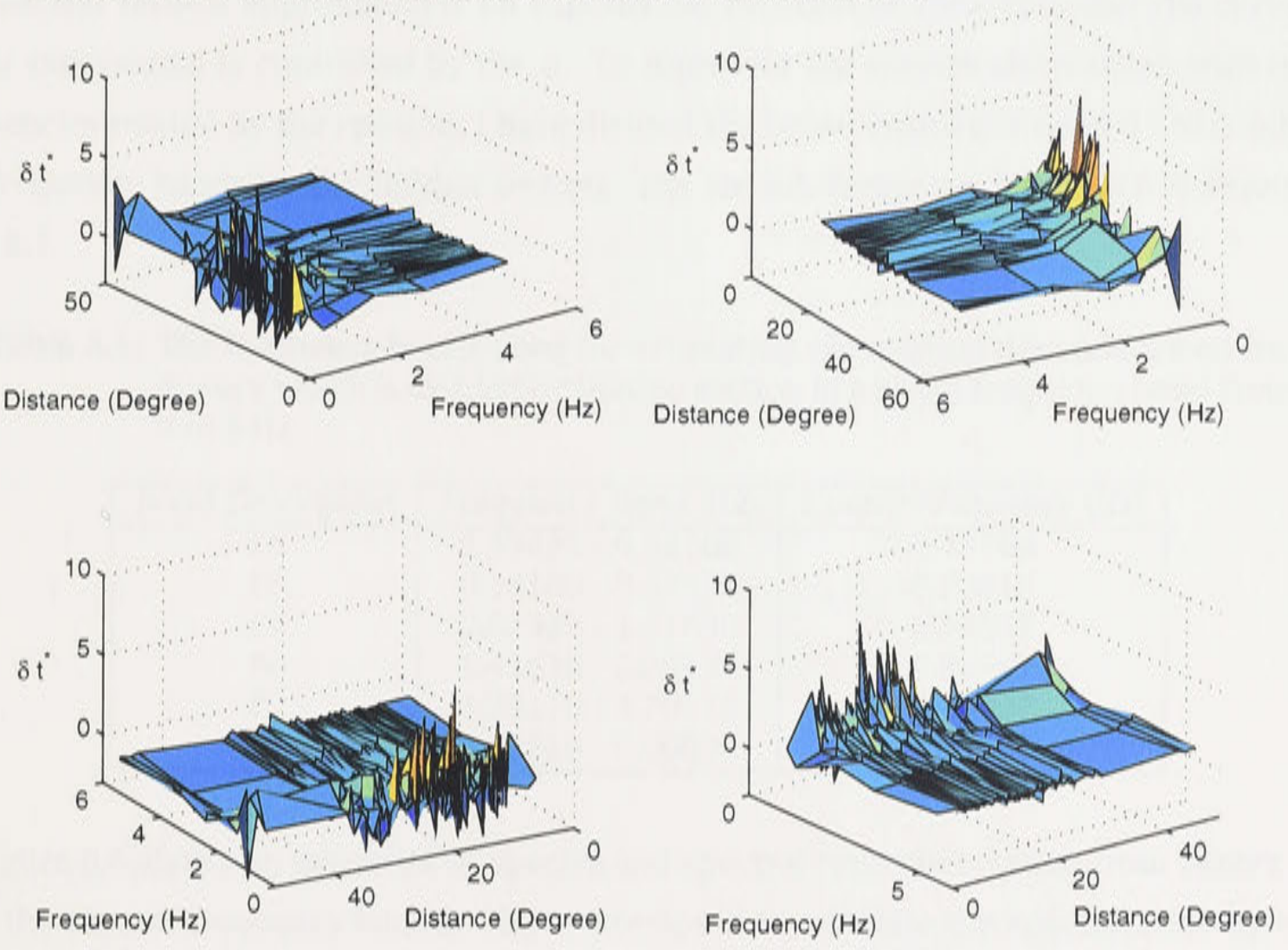

(b) Azimuth 20

Figure 8.5: Summary of synthetic δt^*_{sp} surface and an example of δt^*_{sp} surface estimated from raypaths in the azimuth corridor 20° , as a function of distance and frequency.

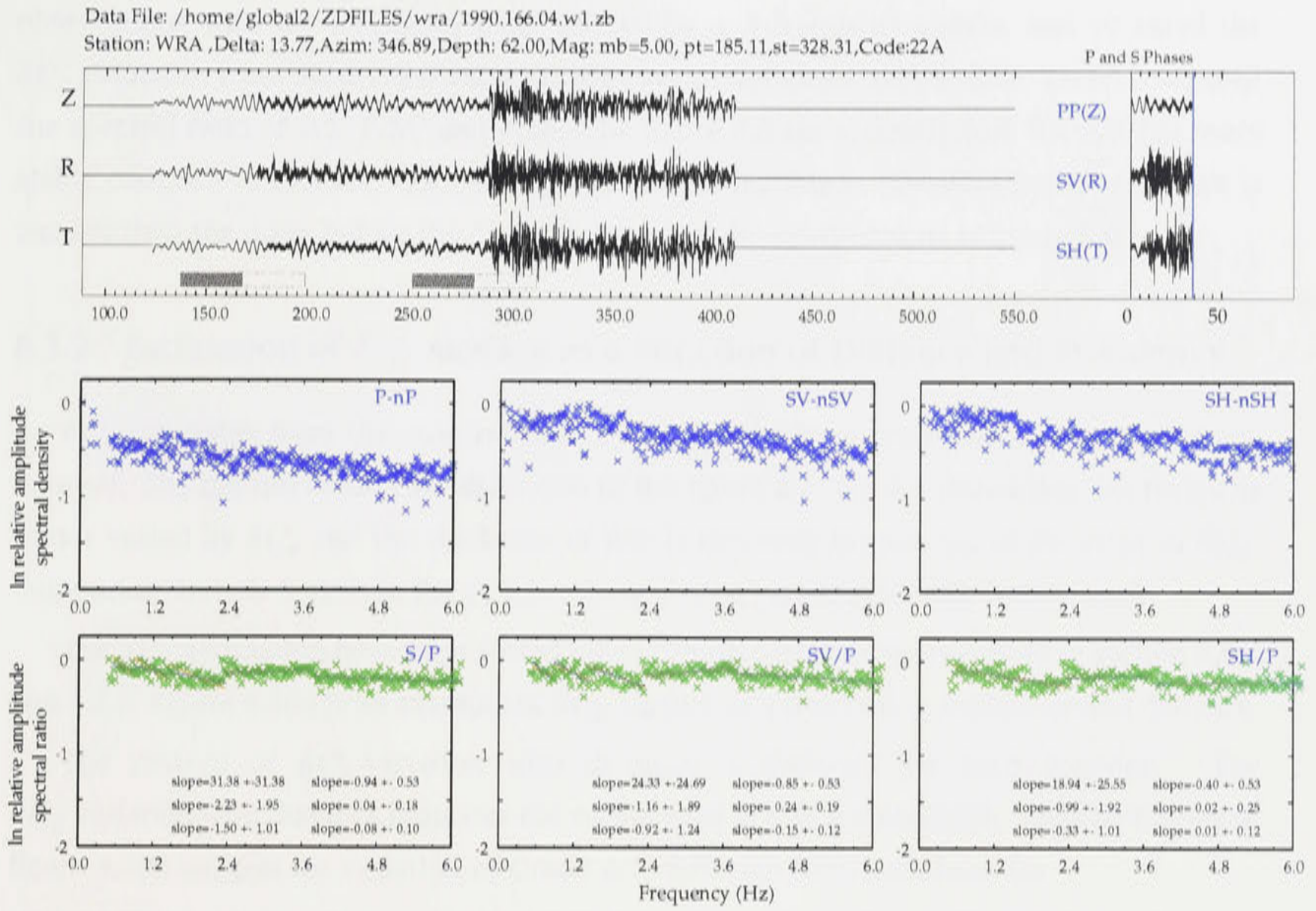

Figure 8.6: Example of estimation of δt^*_{sp} from spectral ratio *P/S*, *P/SV* and *P/SH*.

the spectral ratio is approximately an exponential function of frequency and the curvature of the exponential is controlled by the α. To represent the spectra observation with centre frequencies related by the relation, I have divided the broad frequency band 0 - 6 Hz into six sub-frequency bands by the Golden section. The six sub-frequency bands are illustrated in table 8.1.

Table 8.1: The frequency bands used for estimating attenuation dependence on frequency which is divided by Golden section in a broad frequency band from 0 to 6 Hz

Band Description	*Frequency Band* (Hz)	*Centre Frequency* (Hz)
f1	0.33435 - 0.54100	0.43768
f1	0.54100 - 0.87536	0.70818
f3	0.87536 - 1.41638	1.14587
f4	1.41638 - 2.29176	1.85407
f5	2.29176 - 3.70818	2.99997
f6	3.70818 - 6.00000	4.85409

Figure 8.6 shows an examples of spectra and spectral ratio observation from SKIPPY data from the six sub-frequency bands. I have attempted to estimate the spectral ratio by using *P/S*, *P/SV* and *P/SH* information. Because of the noise in the *P* and *S* waves, the residual *P* and *S* wave spectra are very scattered. Thus the sub-frequency bands also lead to instability in spectra observation. To reduce the the instability in the δt^*_{sp} estimation, I have combined

observations with the frequency band shifted by ± 3 frequency points, and obtained the δt^*_{sp} estimates from the average values to improve smoothness and stability. Then I compared the spectral ratio of *P/S*, *P/SV* and *P/SH*. The figure 8.6 show clearly that the *P/SH* is more stable compare to *P/S* and *P/SV*. One of the reason for this is the noise before *SH* wave is smaller than the noise before the *SV*, as is shown in the seismograms in figure 8.6.

8.3.2 Estimation of δt^*_{sp} surface as a Function of Distance and Frequency

δt^*_{sp} estimates from the spectral ratio of *P/SH* have been undertaken from the SKIPPY data set. The the full results are displayed in the figure 8.7. Fig 8.7 shows that the raypaths colour scaled by δt^*_{sp} and the thickness of line is inversely proportion to the error in δt^*_{sp}. Comparing the sub-figures in figure 8.7, strong spatial variation in δt^*_{sp} is displayed.

The δt^*_{sp} estimation have been sorted into azimuth corridors as described in section 6.6.2 and 7.3.5. Figure 8.5(b) is an example of δt^*_{sp} surface as a function of frequency and distance.

The pattern of δt^*_{sp} variation with distance is different for each corridor. The δt^*_{sp} variation with distance indicates the variation of Q and α with depth. The sub-figures in figure 8.5(b) suggest the variation of Q and α is different from each corridor.

Because the nature of exponent relation between δt^*_{sp} and frequency, for same distance, the δt^*_{sp} is more complex at the low frequency bands. At high frequency, the variation of δt^*_{sp} with frequency is less significant. This is consistent with the forward modeling in section 8.

Here I address one of important problems. The δt^*_{sp} estimation presented in figure 8.5(b) contain many negative δt^*_{sp}. The δt^*_{sp} calculated in this thesis is $\delta t^*_{sp} = t^*_s - t^*_p$. A negative value means the P wave is more attenuative than the S wave. Then a major question arises. Is it possible for P wave more attenuation than S wave? Does this violate the assumption that attenuation mainly occurs in shear waves? The answer is that the raypath of P and S differ and the P wave could be more attenuative than S when the raypath for the S wave still lie in a low attenuation zone but the P wave penetrate to high attenuation region. My simulation on synthetic δt^*_{sp} has shown that negative δt^*_{sp} occurred when I undertook raytracing for P wave and S separately, because the P and S wave gradients different as shown in figure 5.3. Including negative δt^*_{sp} in the inversion gives a better recovery of the Q model from the synthetic δt^*_{sp}.

8.4 Discussion

The δt^*_{sp} as a function of frequency and distance was simulated and estimated from the SKIPPY data set in this chapter. Thus the surface of the δt^*_{sp} as a function of frequency and distance obtained in this chapter which has not been done before. This set of surface of the

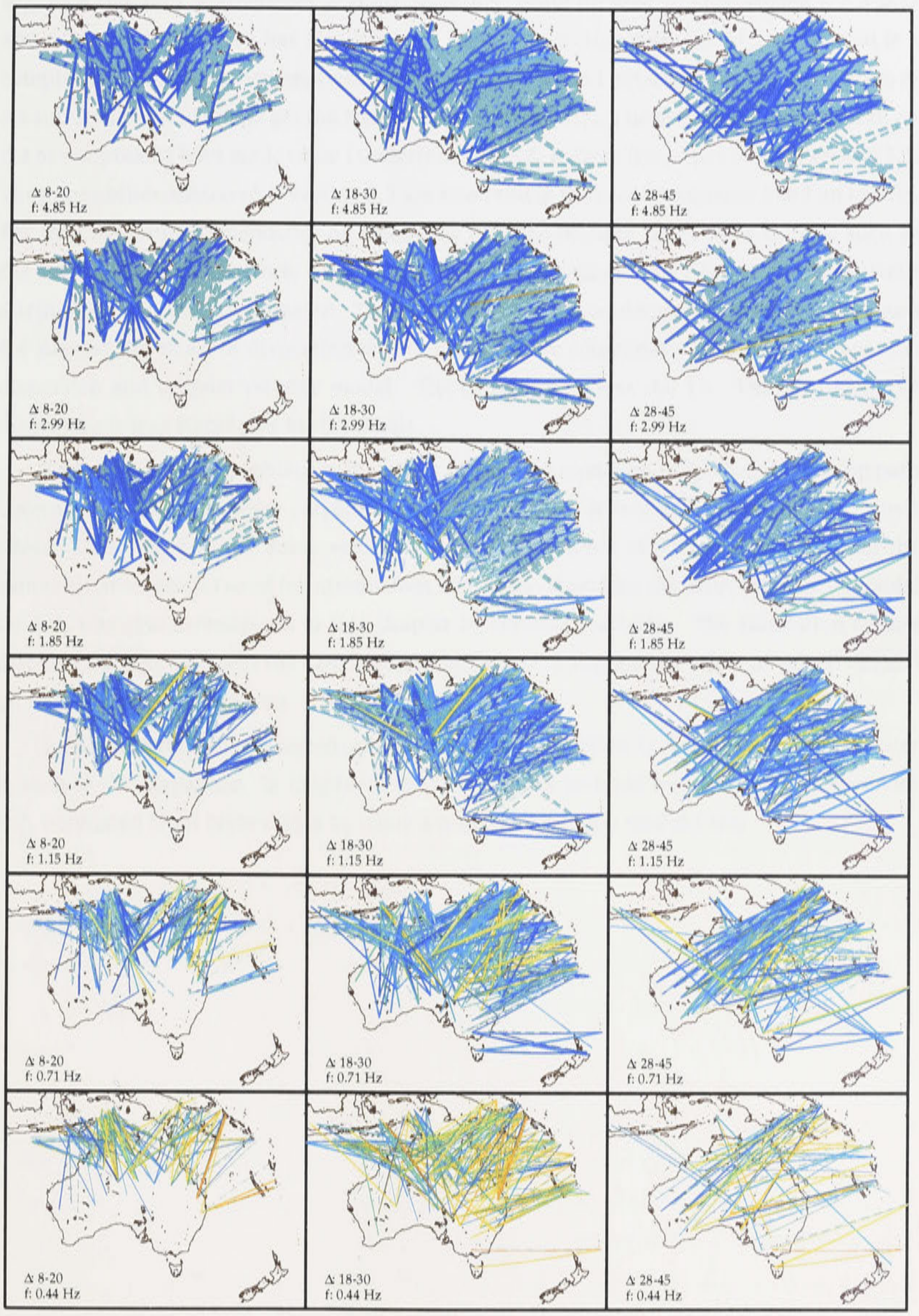

Figure 8.7: Summary of estimation of δt^*_{sp} from spectral ratio *P/SH*, colour scaled by δt^*_{sp} and the thickness of line is nonlinear proportion to the inverse of error of δt^*_{sp}.

δt^*_{sp} as a function of frequency and distance then could be used to constructed the 3-D Q and α in chapter 9 which has also not been done before. However, the δt^*_{sp} estimation is a complex process. Some assumptions have been made when I obtained the δt^*_{sp} estimation at six sub-frequency bands to get the frequency dependent δt^*_{sp}. I have thoroughly discussed on the assumptions I have made when I undertook the δt^*_{sp} in fixed frequency band in section 5.3. The assumption discussed in section 5.3 are also valid in the broad frequency band up to 6Hz. But the attenuation dependence on frequency has also brought some extra factors, such as the the dispersion. Therefore, the effect of velocity dispersion associated with seismic wave attenuation was also investigated. The simulation results on dispersion displayed in figure 8.4 suggest the effect of dispersion is very small. I have compared the velocity contains the dispersion and original velocity model. The difference is less the 1%. Thus the effect of dispersion is less significant in this thesis.

Another important problem is the effect of velocity model on δt^*_{sp}. Because the raypath coverage limitation, in some corridors there are only one or two velocity models for 3 to 4 slices. Thus I have to use some velocity models which is not exactly constructed from the same raypaths which I used for attenuation inversion. Therefore the effect of velocity model on δt^*_{sp} was also investigated in this chapter by forward modeling. The simulation results displayed in figure 8.3 and the discussion in section 8.2.3 suggest the effect of velocity model on δt^*_{sp} is less significant too.

I have ignored some less significant factors when I undertake Q and α inversion in chapter 9, such as the dispersion. In chapter 9, the Q and α are inverted from frequency dependent δt^*_{sp} estimated from SKIPPY data by using a nonliear inversion method NA.

Chapter 9

Frequency Dependent Attenuation Structure in the Upper Mantle

9.1 Introduction

Most of the previous studies on body wave attenuation structure in the upper mantle focus on modelling Q^{-1} in a relatively narrow frequency band over which the attenuation dependence on frequency is weak [Sipkin and Jordan, 1979; Gudmundsson et al., 1994; Sharrock, 1995; Sharrock et al., 1995]. For the frequency dependence of attenuation, I have found all the previous studies were based on modelling the frequency dependence of mean value of Q^{-1} along a raypath because of raypath coverage and/or data limitations [Sipkin and Jordan, 1979; Clements, 1982; Der et al., 1982; Ulug and Berckhemer, 1984; Flanagan and Wiens, 1998; Martynov et al., 1999]. In this thesis, I have made an attempt to construct a 3-D body wave frequency dependent attenuation structure in the upper mantle.

In a broad frequency band of 0 - 6 Hz, the spectral ratio as a function of frequency take a power form because of the attenuation dependence on frequency. The curvature of the spectral ratio depends on the attenuation dependence on frequency. The whole curve of the spectral ratio could be roughly divided into two linear sections. The turning frequencies lie in the range from 1 to 2 Hz. I have obtained the robust estimation of δt^*_{sp} with small errors from lower frequency bands at centre frequencies around 1 Hz in chapter 6 and this set of δt^*_{sp} estimates were used to construct a set of 1-D Q profiles and a 3-D Q model in chapter 7.

In this chapter, I have obtained a set of 1-D profiles of Q^{-1} and α inverted from the estimation of frequency dependent δt^*_{sp} by using NA inversion method. I have also constructed a pseudo 3-D Q^{-1} and α structure by combining the 1-D Q^{-1} and α profiles weighted by the raypath density.

9.2 Statistical Analysis on δt^*_{sp} and Errors in the Estimation of δt^*_{sp}

To reveal the attenuation dependence on frequency in detail, I have obtained a set of frequency dependent estimates of δt^*_{sp} from the six sub-frequency bands related by the Golden section in a broad frequency band 0 - 6 Hz in the section 8.3. Figure 9.1 displays that the frequency dependent δt^*_{sp} values distribution. The centre frequency of the six sub-frequency bands are 0.437675Hz, 0.70818Hz, 1.14587Hz, 1.85407Hz, 2.99997Hz and 4.85409Hz. The full description of the six sub-frequency band is in table 8.1.

The general trend is that in the lower sub-frequency bands, the absolute values of δt^*_{sp} are large with large errors (see figures 9.1(a), 9.1(b), 9.2(a), and 9.2(b)) and in the higher sub-frequency bands, the absolute values of δt^*_{sp} are small with small errors (see figures 9.1(e), 9.1(f), 9.2(e), and 9.2(c)). The large δt^*_{sp} values in the lower frequency bands reflect the rapid changes in spectral ratio over the lower frequency bands. One of the reason for the δt^*_{sp} estimates with large errors is that the frequency band centred at 0.437675Hz and 070818 Hz are too narrow. Thus there are not quite enough data points in those two frequency bands. However, the errors in those two frequency bands have been significant reduced by shifting the frequency band by ± 3 data points and averaging the spectra. At higher frequency, the variation of spectral ratio with frequency is more flat and the sub-frequency bands are more broader than the sub-frequency bands in the lower frequency. Thus the δt^*_{sp} observed at higher frequency bands are small with small errors. Also high frequency estimates are only possible for low Q^{-1}.

The average errors in the six sub-frequency bands are reasonably small. Thus this set of δt^*_{sp} measurement will allow me to invert Q^{-1} and α as a function of depth. In figure 9.2, it has been seen that a group of large errors around 10 occur in each of the subfigures. These are arbitrary errors which I used for marking those data where I could not obtain a δt^*_{sp} estimate. When the data quality is poor and I could not make an estimation of δt^*_{sp}, I mark the error as 9.99. The δt^*_{sp} with the assigned errors 9.99 are not used in the inversion. The number of events in this group reduce with the increase of the centre frequency of the subfrequency band.

9.3 Inversion for Q^{-1} and α from Frequency Dependent δt^*_{sp}

9.3.1 Experiments on Synthetic δt^*_{sp}

The model parameterisation and NA parameters have been tuned in the section 7.3.3 when I conducted inversion for Q from δt^*_{sp} estimated from fixed frequency around 1 Hz. However, the dimension of parameter space required in inversion for Q and α are doubled

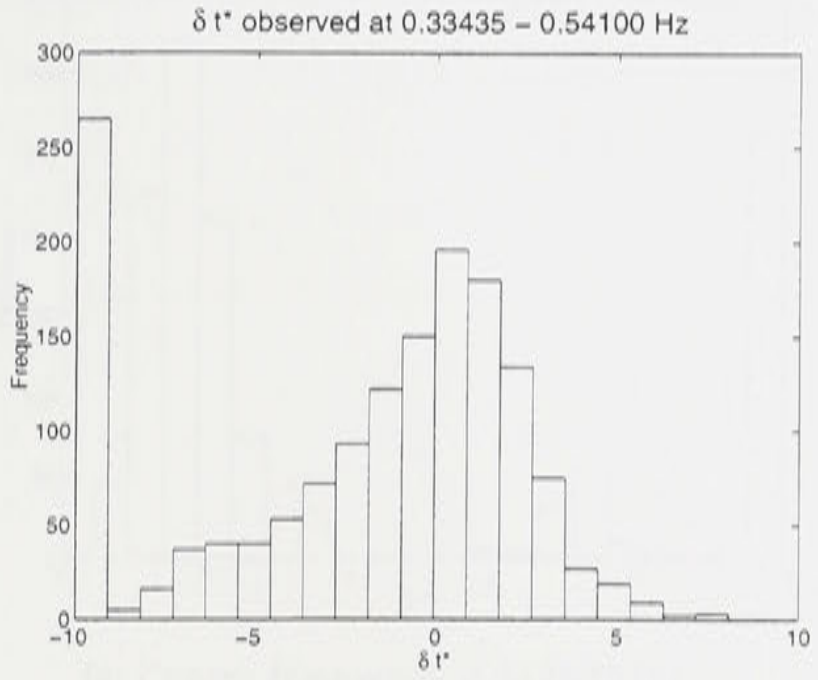

(a) Centre frequency 0.437675 Hz

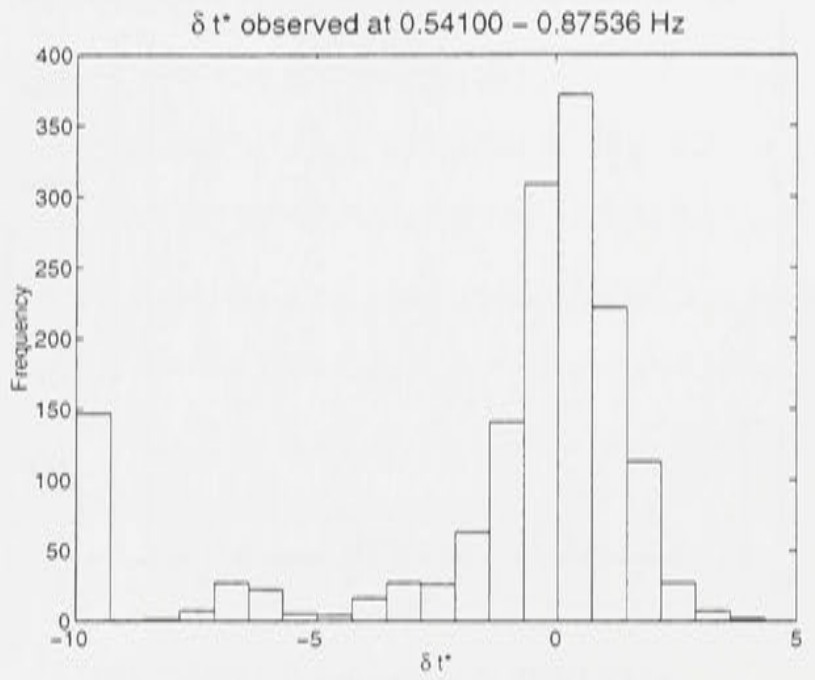

(b) Centre frequency 0.70818 Hz

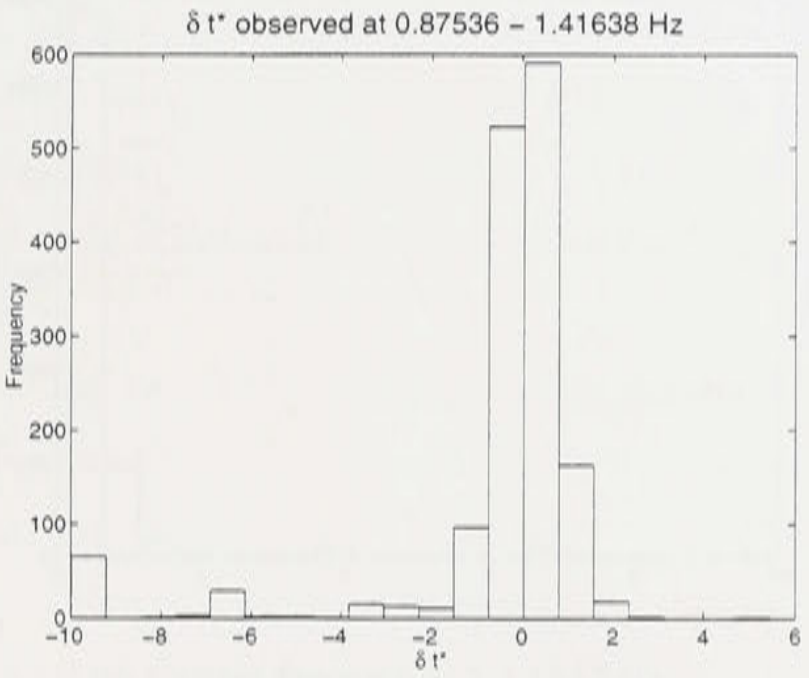

(c) Centre frequency 1.14587 Hz

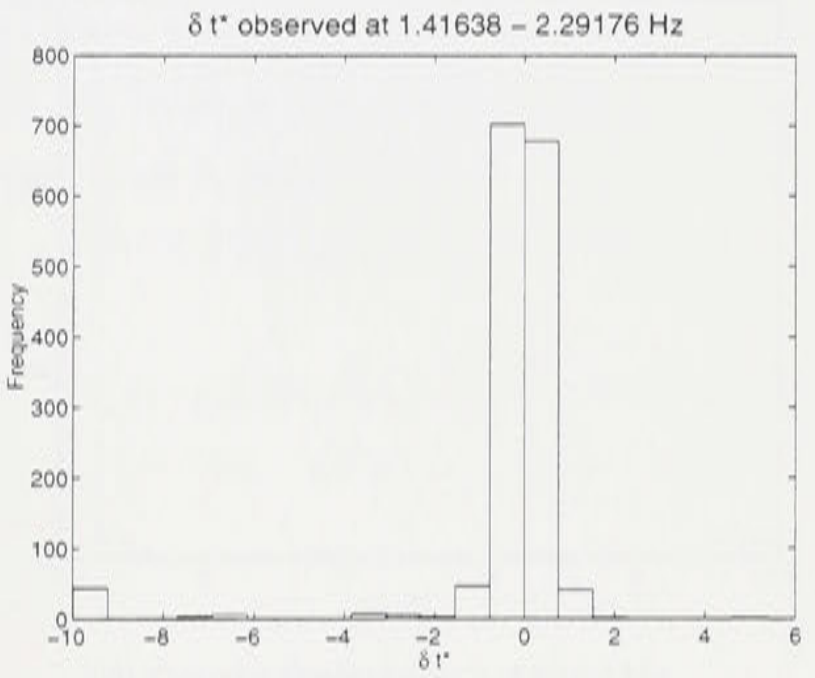

(d) Centre frequency 1.85407 Hz

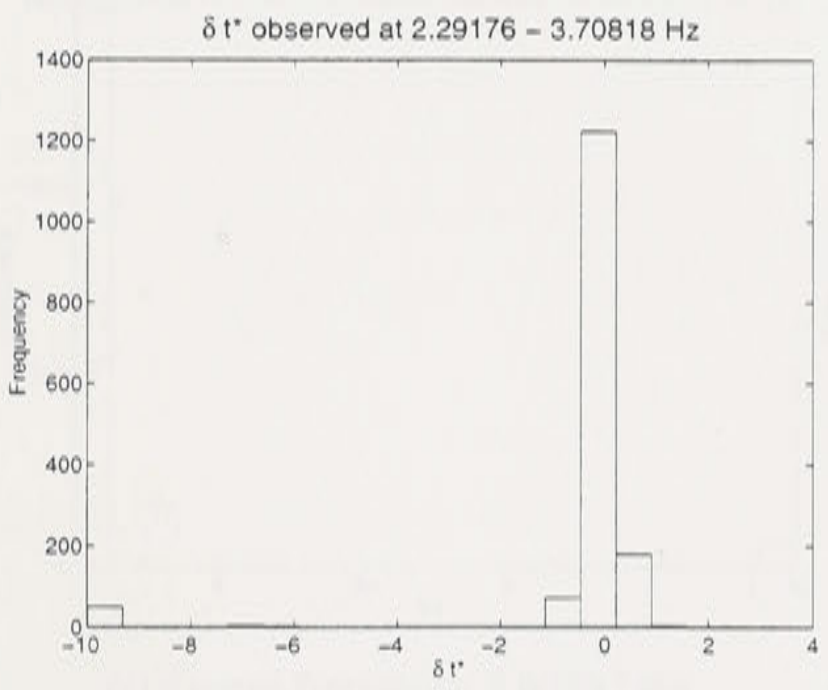

(e) Centre frequency 2.99997 Hz

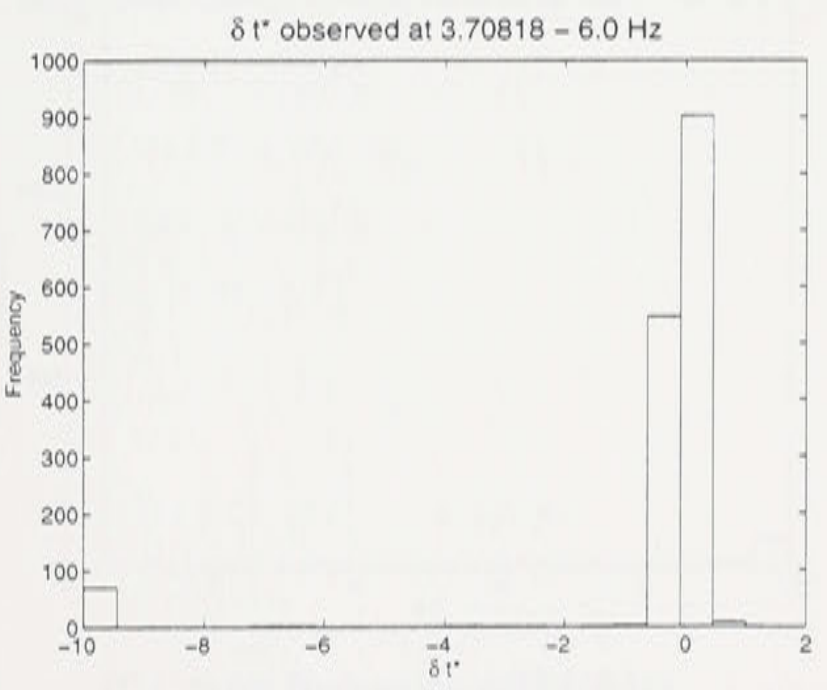

(f) Centre frequency 4.85409 Hz

Figure 9.1: Distribution of δt^*_{sp} measurement from the SKIPPY data set

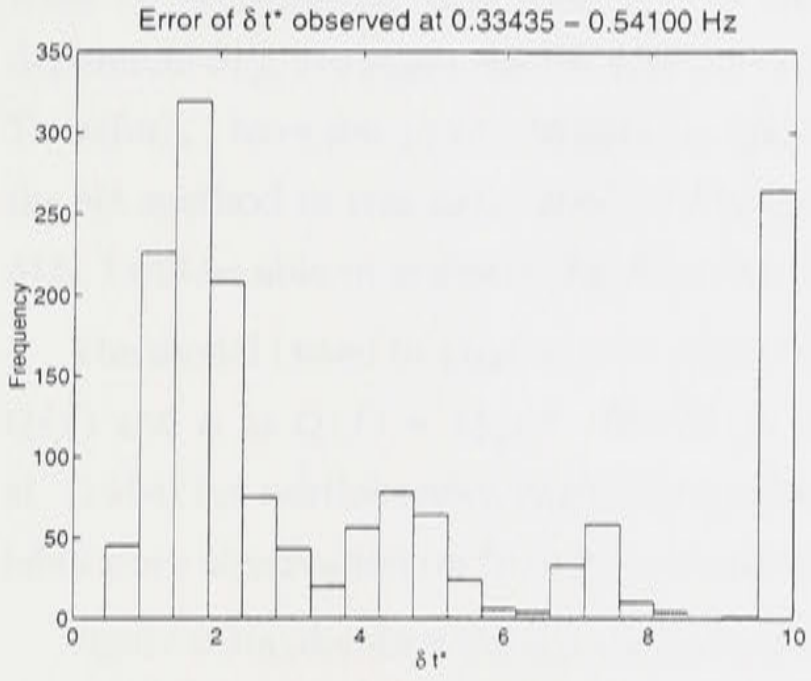

(a) Centre frequency 0.437675 Hz

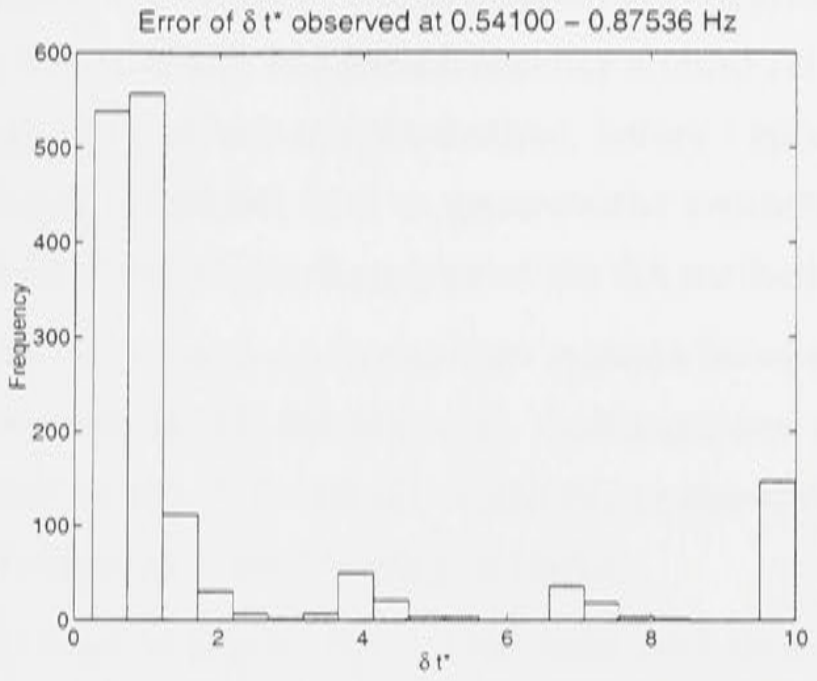

(b) Centre frequency 0.70818 Hz

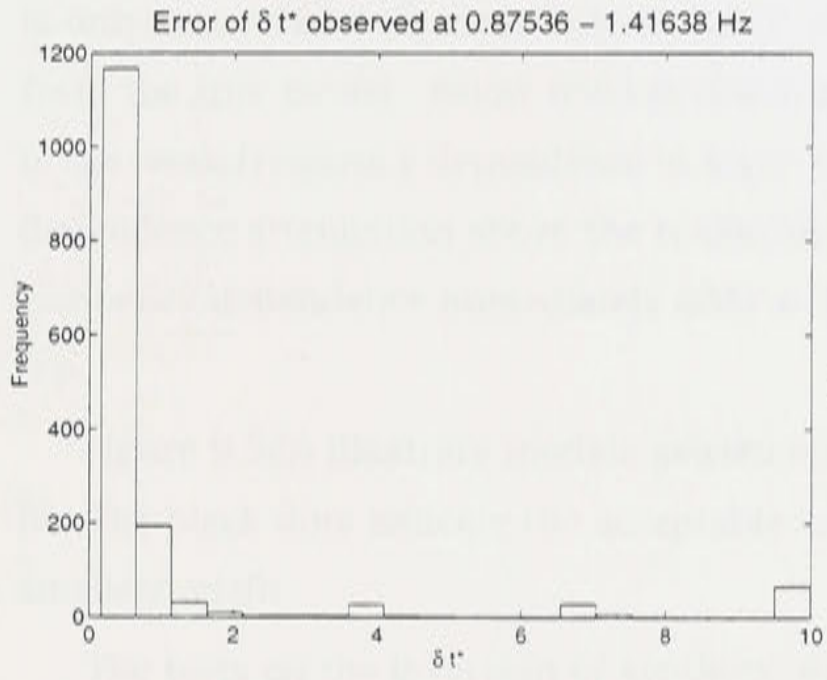

(c) Centre frequency 1.14587 Hz

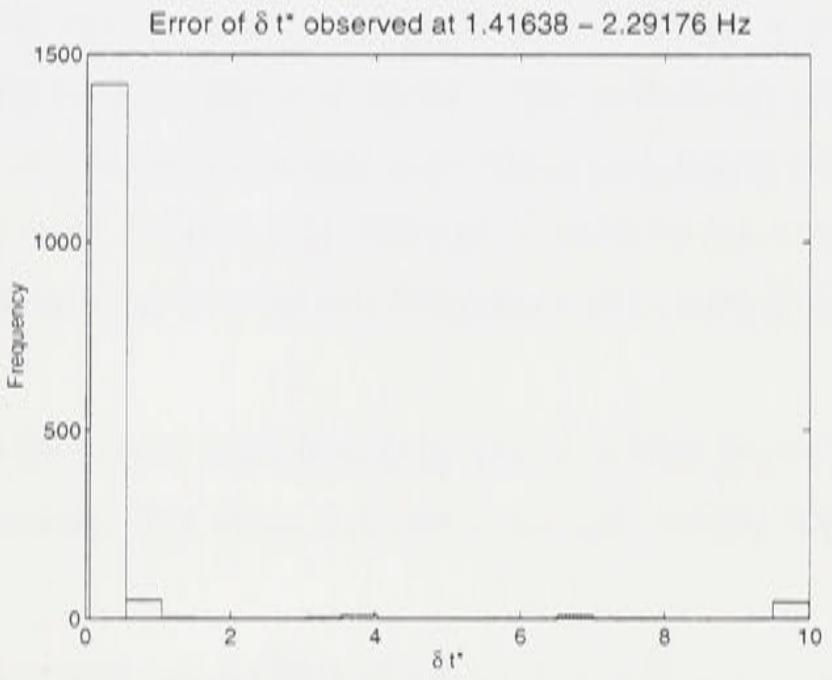

(d) Centre frequency 1.85407 Hz

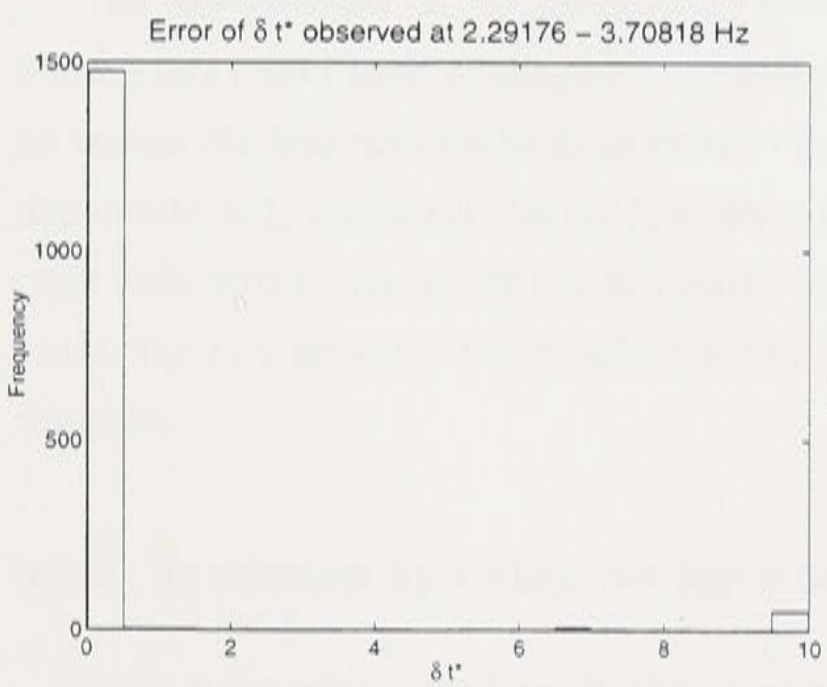

(e) Centre frequency 2.99997 Hz

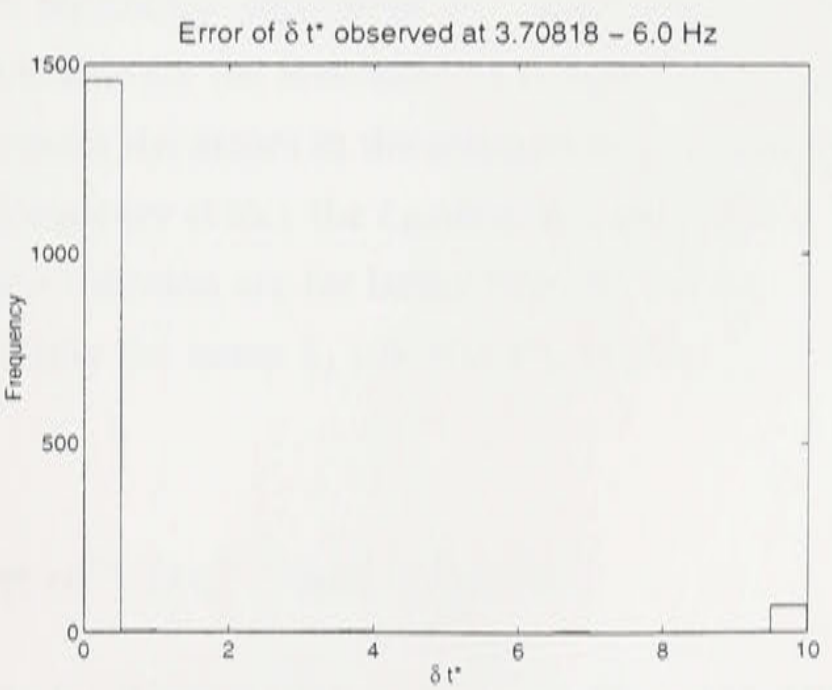

(f) Centre frequency 4.85409 Hz

Figure 9.2: Distribution of errors in δt^*_{sp} measurement from the SKIPPY data set. When the data quality is poor and I could not make an estimation of δt^*_{sp}, I mark the error as 9.99. The δt^*_{sp} with arbitrary errors 9.99 are not used in the inversion.

from the inversion for Q in chapter 7. In addition, the errors in the estimation of frequency dependent δt^*_{sp} are larger than the robust estimation of δt^*_{sp} in a fixed frequency around 1 Hz. Therefore, I have done experiments on synthetic δt^*_{sp} to test the NA method, before I apply the NA method to real data. Because I have know the model used to generate the synthetic δt^*_{sp}, I will be able to evaluate the inversion results and the performance of the NA method.

The model I used to generate the synthetic data is based on a power law relation between $Q(f)$ and α as $Q(f) = Q_0 f^\alpha$. The Q_0 is from the model developed by Gudmundsson et al. [1994] for northwestern Australia displayed in table 2.1, and the α values are based on laboratory observation on frequency dependent seismic wave attenuation (see 2).

Figure 9.3(a) displays the Q_0 and α inverted from synthetic δt^*_{sp} . It has been seen clearly that the Q_0 is recovered quite well in all layers. The black lines indicate the true models. The true models of Q are almost in the centre of best fitted model inverted from NA. But the α is only recovered well in shallow depth (< 410 km). The α in the layer 410 - 660 km is far from the true model. Below 660 km the α get back to the true model. The reason for this is the weak frequency dependence in layer 410 - 660 km is masked by the strong frequency dependence attenuation above the transition zone. Hence, it is difficult to recover the weak frequency dependence immediately after a layer with very strong frequency dependence on top.

Figure 9.3(b) illustrate models generated by NA in each iteration colour scaled by misfit. The black dots indicate the acceptable models. The cross indicates the best model with smallest misfit.

The tests on the inversion of synthetic data give me an idea of where I could get a good constraints and where I could not.

The experiments on NA parameters from frequency dependent δt^*_{sp} show that the NA parameters I have used in chapter 7 are still suitable for the inversion for Q and α. The tests on norms confirm my results in chapter 7. Because the errors in the estimation of frequency dependent δt^*_{sp} are larger than δt^*_{sp} at fixed frequency (1 Hz), the L_2 norm is again unable to cope with errors. The misfits with L_2 after first iteration are far larger than for L_1. In most cases, the $L_{1.5}$ provides the smallest misfit. Thus the norm $L_{1.5}$ is still my favoured misfit function.

9.3.2 Inversion by Using *NA* for a Set of 1-D Q^{-1} and α Profiles

After successful experiments of inversion on synthetic data, I undertook inversion with NA on the estimated frequency dependent δt^*_{sp} from SKIPPY data. Figure 9.4 is the summary of a set of 1-D Q and α profiles inverted from δt^*_{sp} measurement displayed in figure 8.5(b). Figure 9.5 is the same models plotted as a set of 1-D Q^{-1} and α profiles instead of Q. In agreement with the previous discussions on velocity, δt^*_{sp} and γ in chapter 6 and the 1-D Q

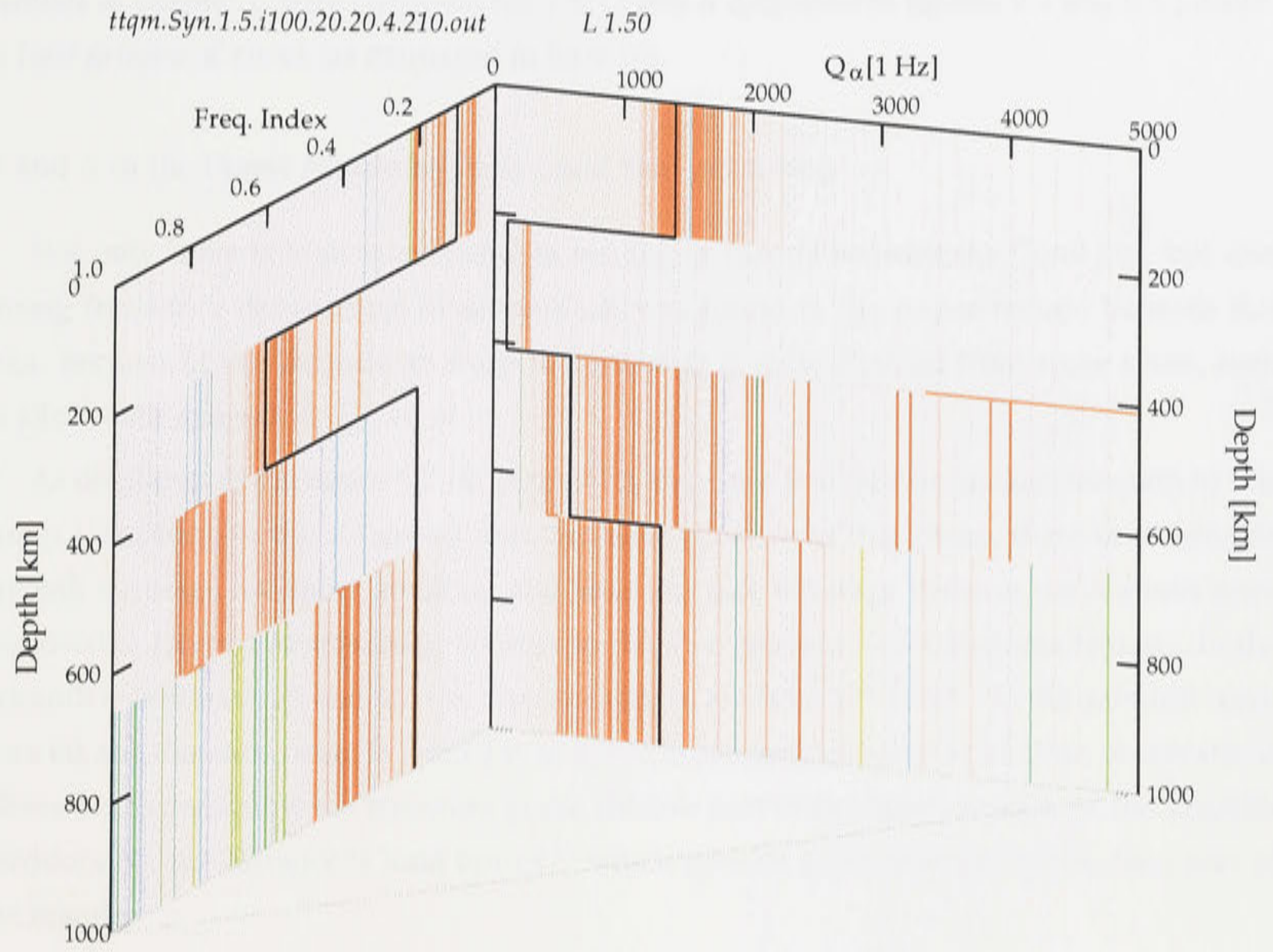

(a) Q and α inverted from synthetic δt^*_{sp}. The black lines indicate true models.

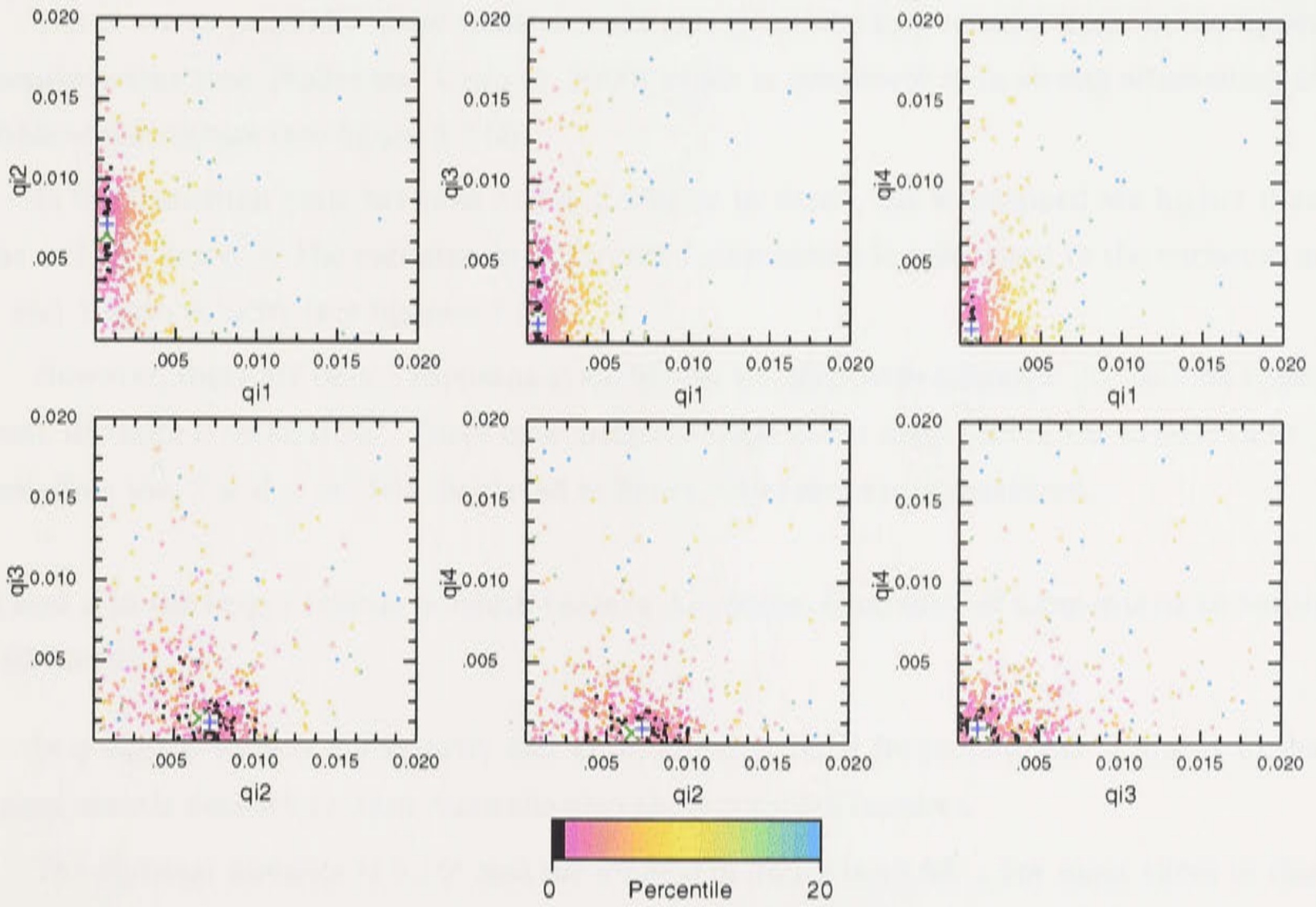

(b) The misfit correlation of Q models in different layers

Figure 9.3: (a) Q and α inverted from synthetic δt^*_{sp}; (b) Alternative plot of Q models found by NA from synthetic δt^*_{sp}. Acceptable models in black and other models represented on a graded colour scheme from pink through yellow and green to blue with increasing misfit.

profiles in chapter 7, here I analysis the 1-D Q and α displayed in figures 9.4 and 9.5 profiles in four groups of slices (as displayed in fig 6.10).

Q and α in the Upper Mantle beneath Coral Sea - *sl1* Group

Not only there is high attenuation in the upper mantle beneath the Coral Sea, but also strong frequency dependence of attenuation was found in the upper mantle beneath this area. Because of the raypath coverage limitation, Q is only obtained from some slices, such as slices with azimuth 0, 20, 40 etc.

As displayed in the figure 6.7 (a), (b) and (c), there are few shorter distance raypath in this group comparing to the *sl3* group. But, for most of slices in this group, there is reasonable raypath coverage for short, medium and long distance coverage because the stations were deployed in Eastern Australia for sources in the Vanuatu and New Caledonia regions. In the azimuth corridors 0, 20 and 40, the distance ranges are from 17° to 32°. In the azimuth corridors 60, the distance range is from 34° to 37°. The reasonable number of close observations allows me to determine the structure in the shallow part of the upper mantle. In the azimuth corridors 80, the distance is long upto 47° which provide good coverage in the deep part of the mantle.

The P phases beneath the Coral Sea contains little high frequency, but there is a higher P velocity zone in the upper mantle in this area [Kaiho and Kennett, 2000].

The S waves generally show weak arrivals and there is a low velocity zone in the upper mantle in this area [Kaiho and Kennett, 2000] which is consistent with strong attenuation in shallow S structure (see figure 6.7 (a)).

In the transition zone between 410 and 660 im in depth, the wavespeed are higher than the *ak135* reference. The variation in differential attenuation is consistent to the variation in P and S wave velocity (see figure 6.7 (b)).

However, there are only 5 raypaths available for the slice with azimuth -20, and the maximum distance is around 26°. There is no path coverage in the deep part of the mantle (≥ 660 km), thus the Q and α models displayed in figure 9.4(c) are less constrained.

Q and α in the Upper Mantle beneath Eastern Australia: from Gulf of Carpentaria to South - *sl2* Group

In a similar way to the velocity and Q obtained at fixed frequency, the Q and α in the upper mantle beneath eastern Australia also show complex features.

The shortest distance is 9.16° and the longest distance is 49.85° . For most slices in this group, the distance range lies in 10° to 35°, hence the data coverage is much better than *sl1* group. But the distance range lies in 14.44° to 18.49° for the corridor with azimuth -60, thus it is shown clearly in figure 9.4(v) there is no constraints on Q in deep layers.

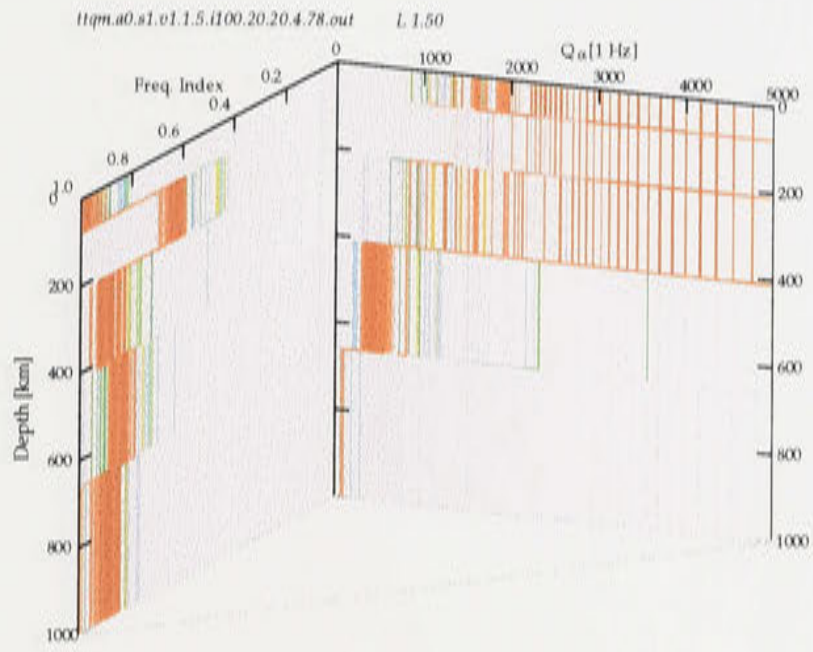

(a) Sl1 Az0 17.17° < Δ < 32.82°

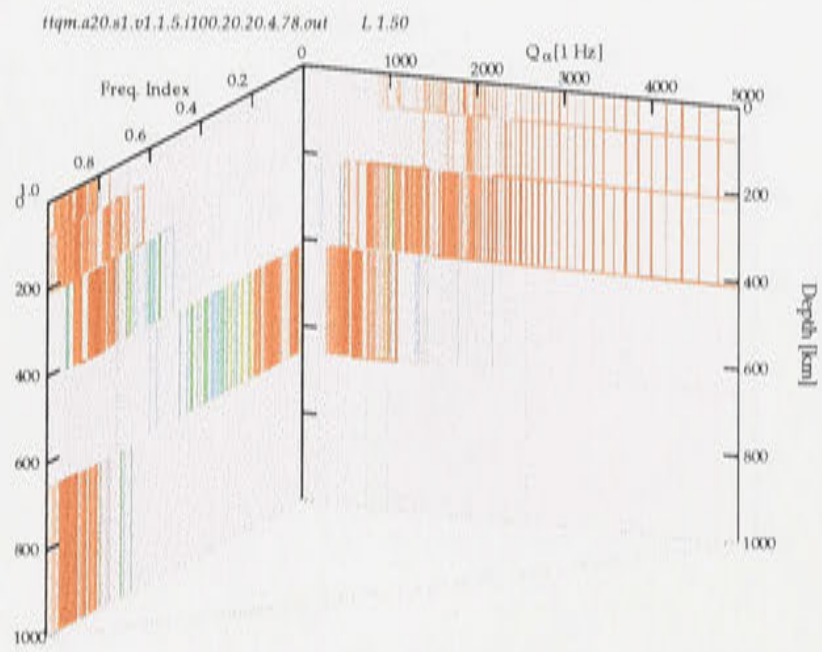

(b) Sl1 Az20 17.34° < Δ < 30.1°

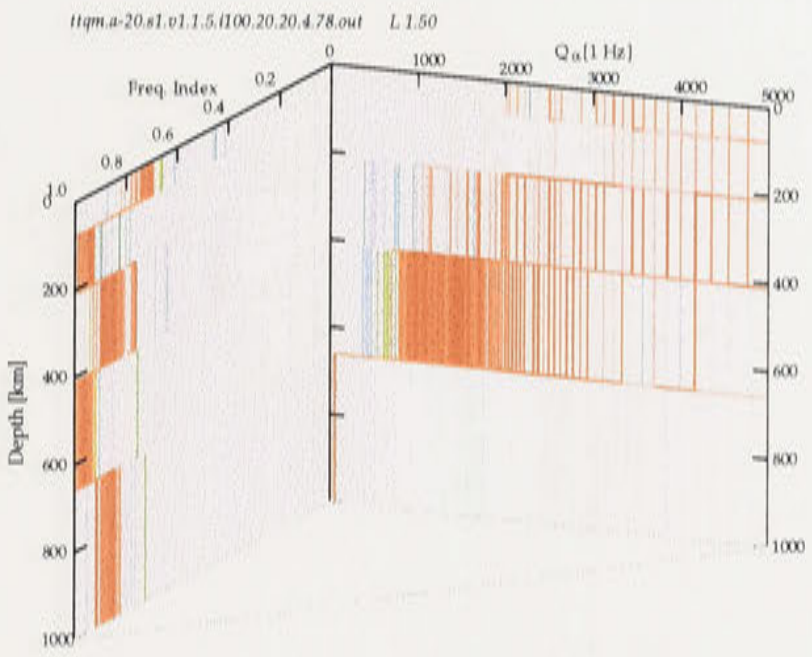

(c) Sl1 Az-20 21.03° < Δ < 26.82°

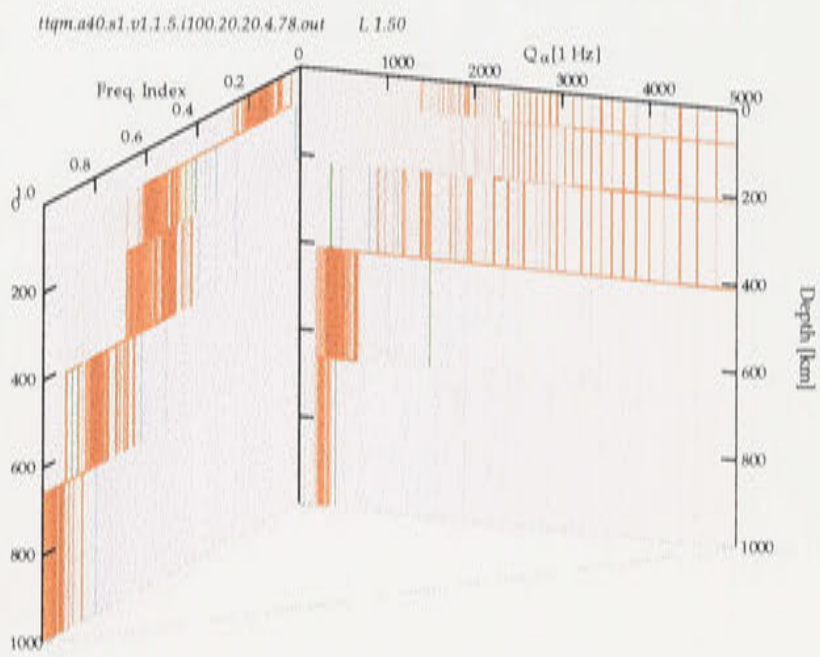

(d) Sl1 Az40 17.35° < Δ < 32.08°

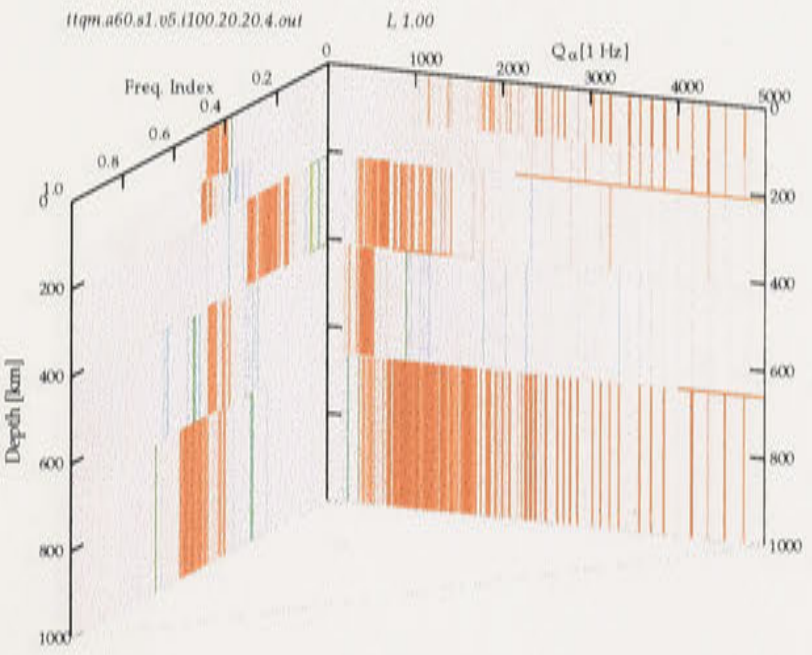

(e) Sl1 Az60 3.42° < Δ < 37.21°

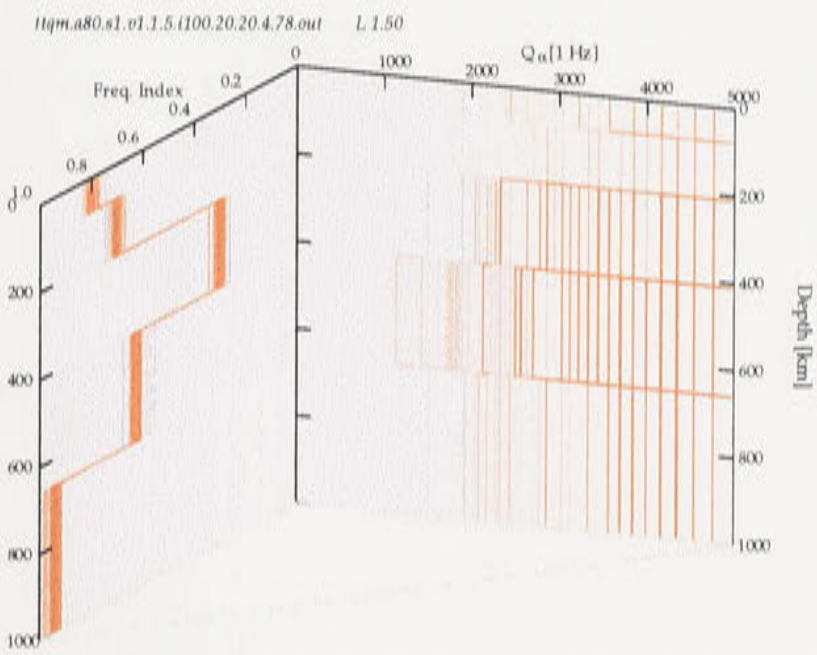

(f) Sl1 Az80 19.89° < Δ < 47.42°

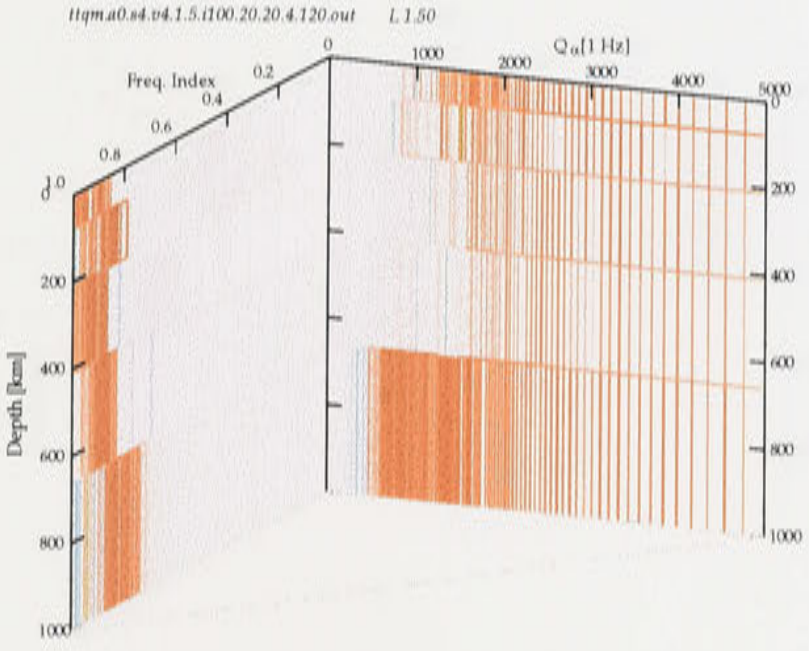

(g) Sl2 Az0 10.22° < Δ < 34.15°

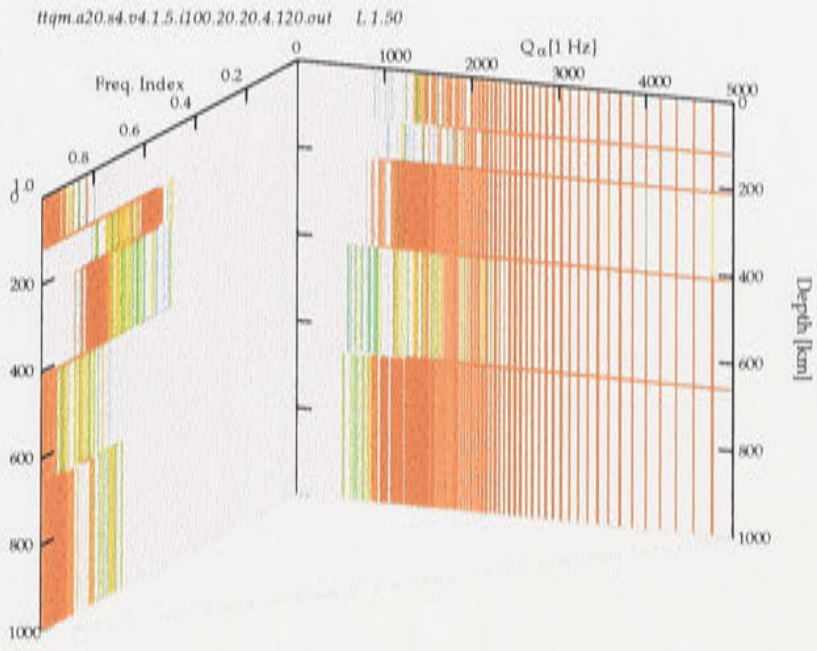

(h) Sl2 Az20 9.16° < Δ < 32.37°

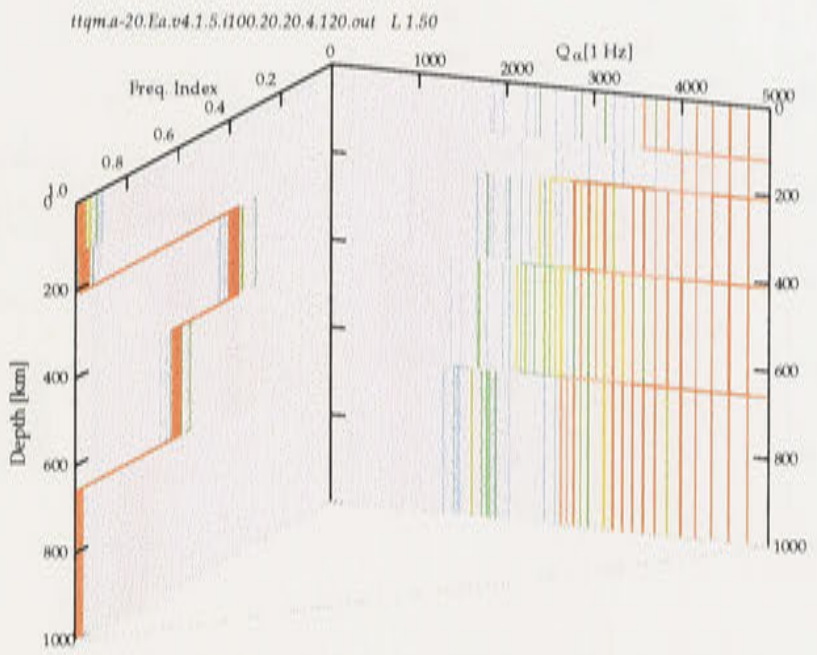

(i) Sl2 Az-20 17.46° < Δ < 34.76°

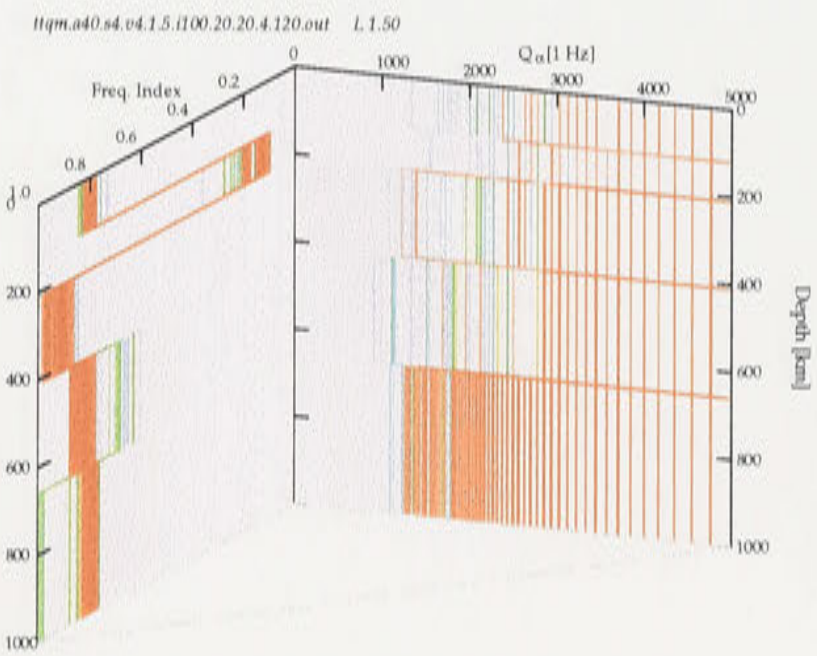

(j) Sl2 Az40 9.64° < Δ < 36.66°

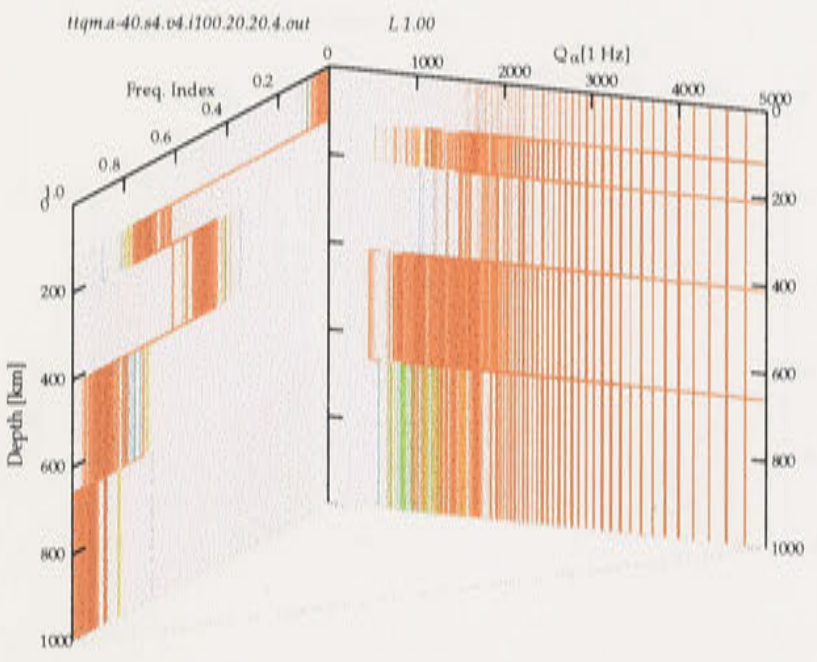

(k) Sl2 Az-40 12.37° < Δ < 32.19°

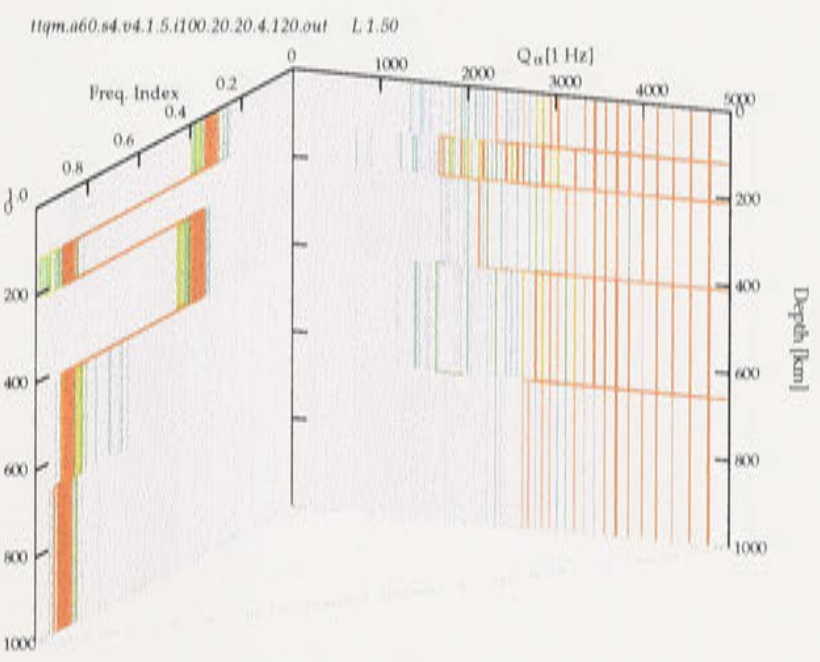

(l) Sl2 Az60 10.37° < Δ < 43.49°

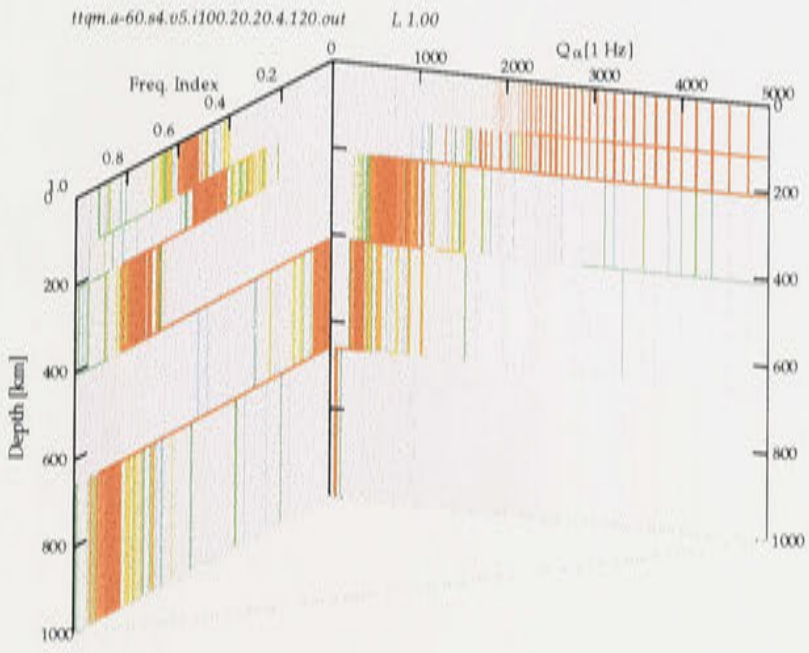

(m) Sl2 Az-60 14.44° < Δ < 18.49°

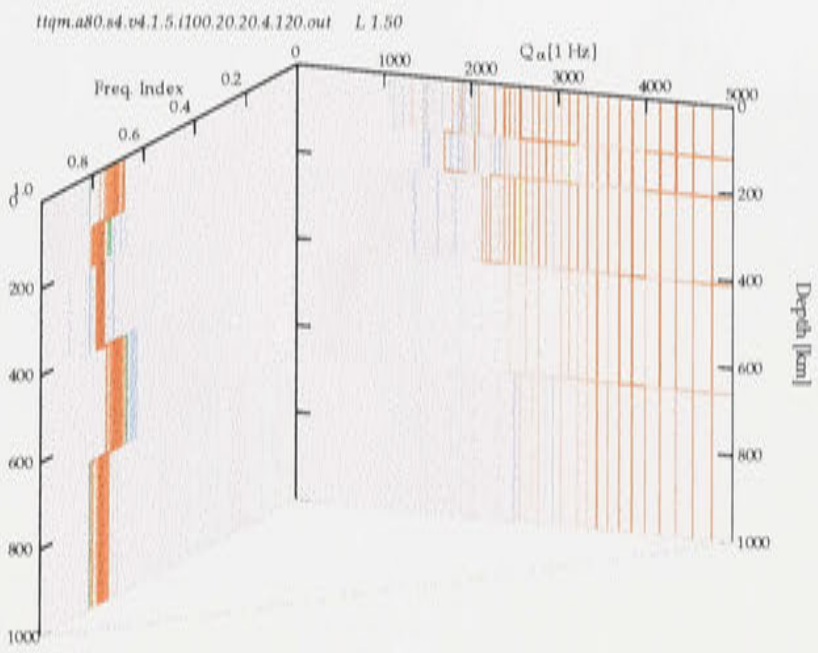

(n) Sl2 Az80 17.65° < Δ < 49.85°

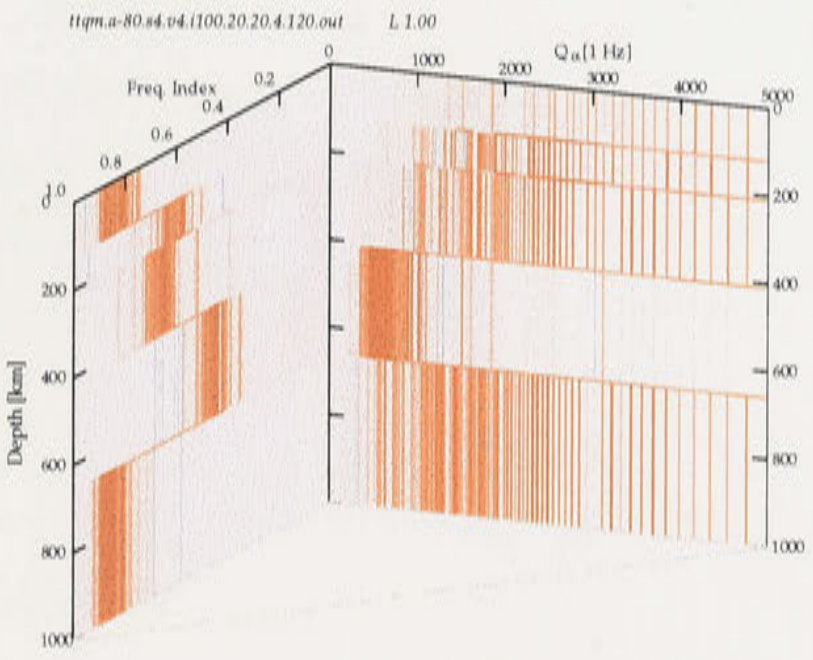

(o) Sl2 Az-80 11.71° < Δ < 35.15°

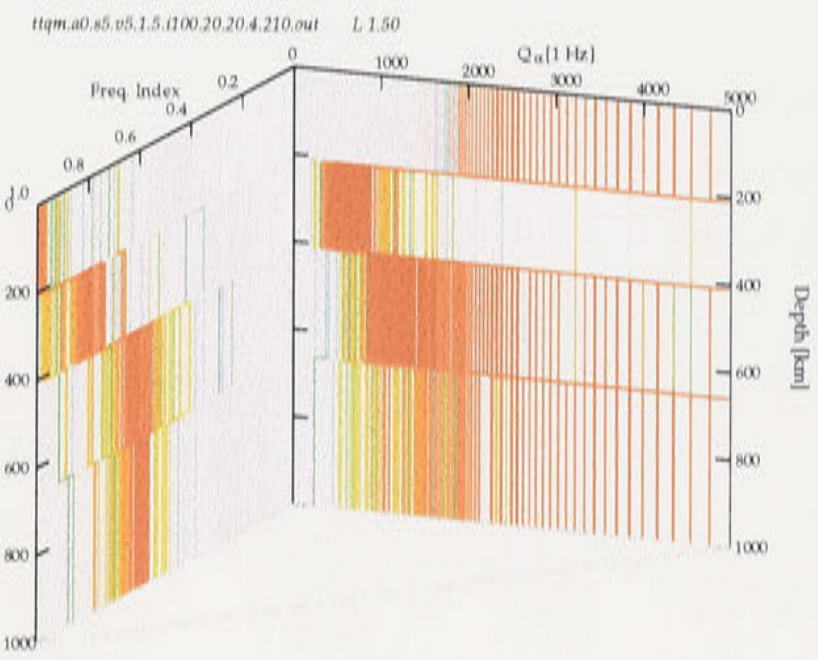

(p) Sl3 Az0 7.15° < Δ < 26.48°

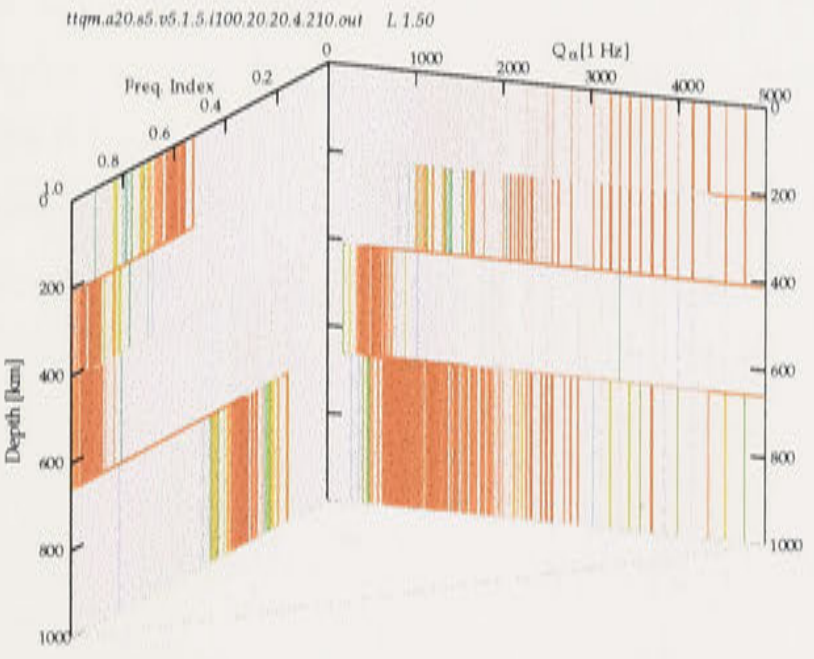

(q) Sl3 Az20 4.29° < Δ < 35.5°

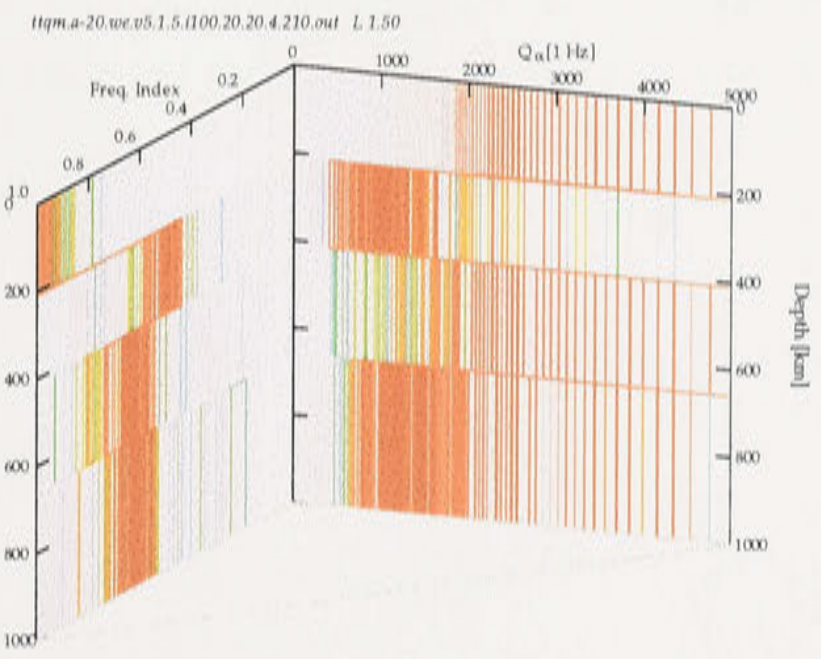

(r) Sl3 Az-20 2.2° < Δ < 37.89°

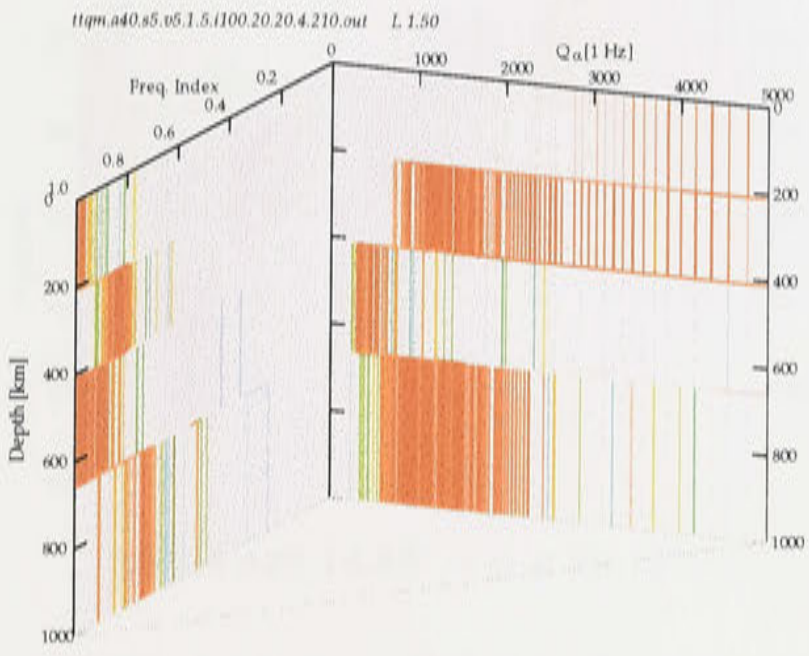

(s) Sl3 Az40 10.92° < Δ < 35.85°

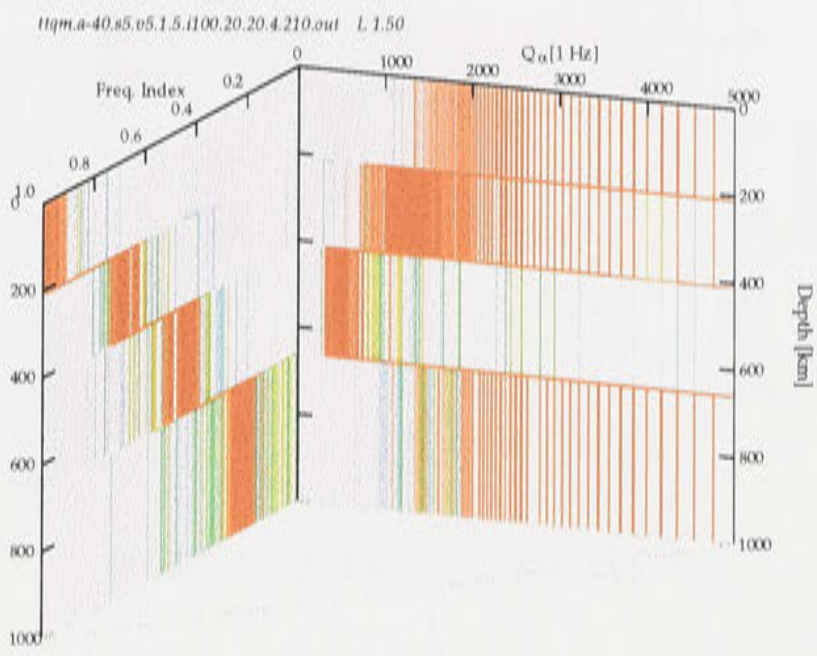

(t) Sl3 Az-40 0.98° < Δ < 30.89°

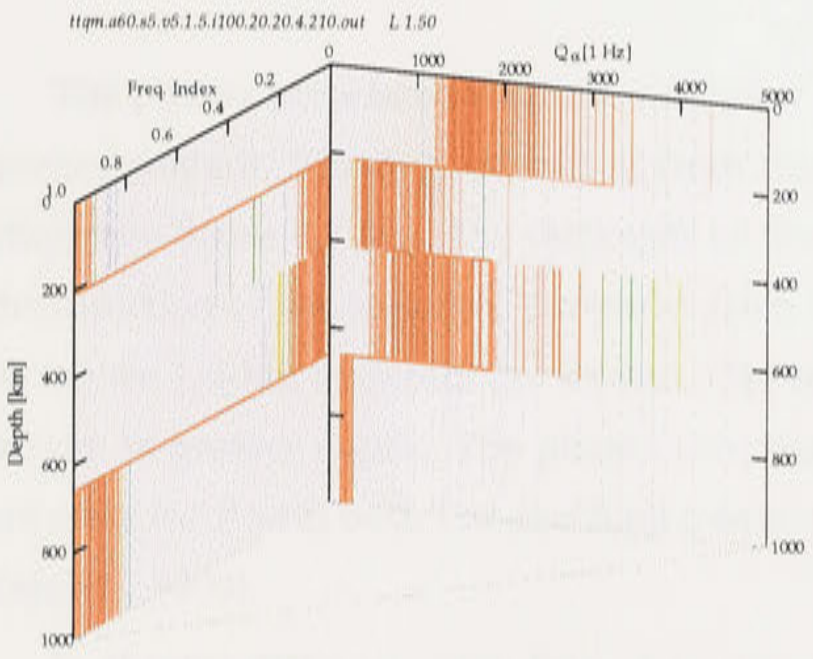

(u) Sl2 Az60 13.6° < Δ < 38.49°

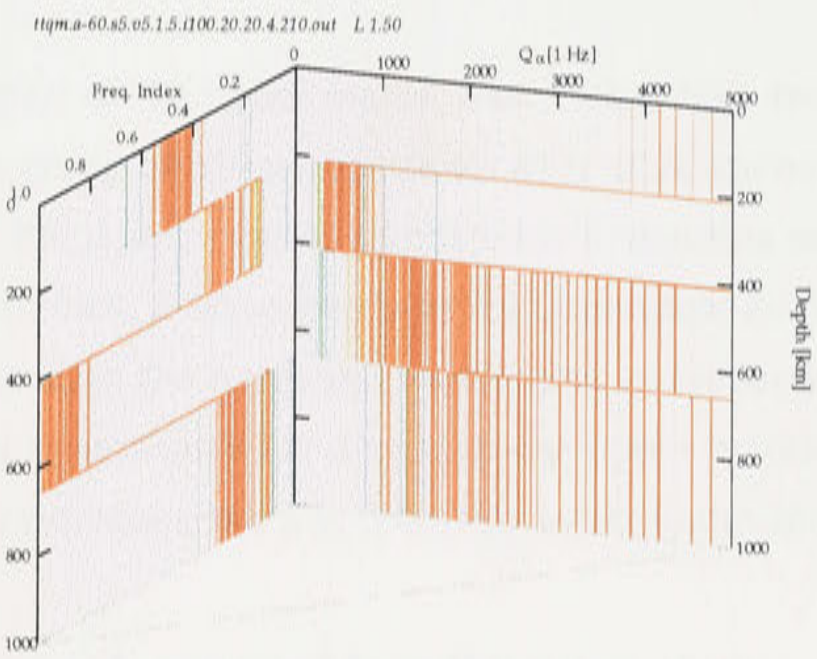

(v) Sl3 Az-60 3.26° < Δ < 31.35°

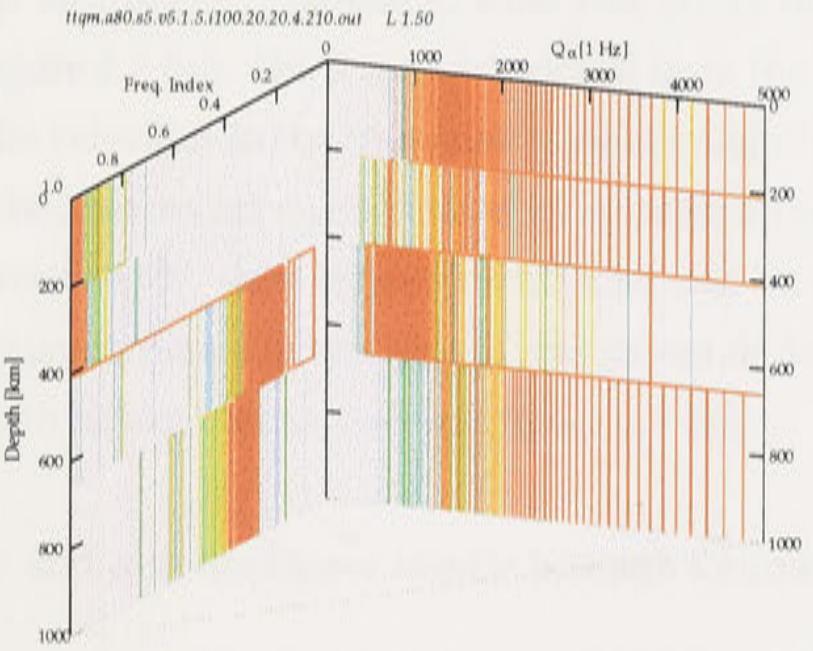

(w) Sl3 Az80 2.81° < Δ < 28.43°

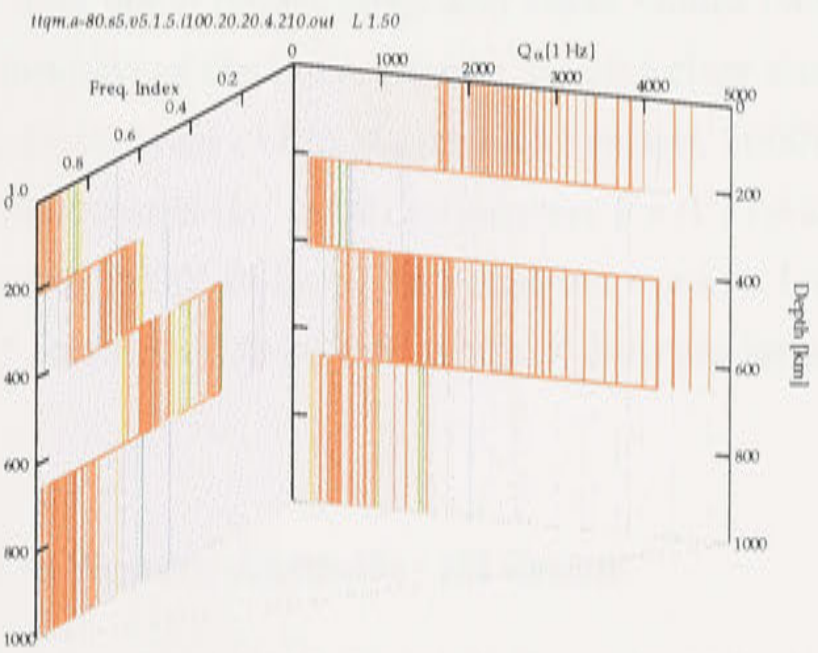

(x) Sl3 Az-80 4.03° < Δ < 41.17°

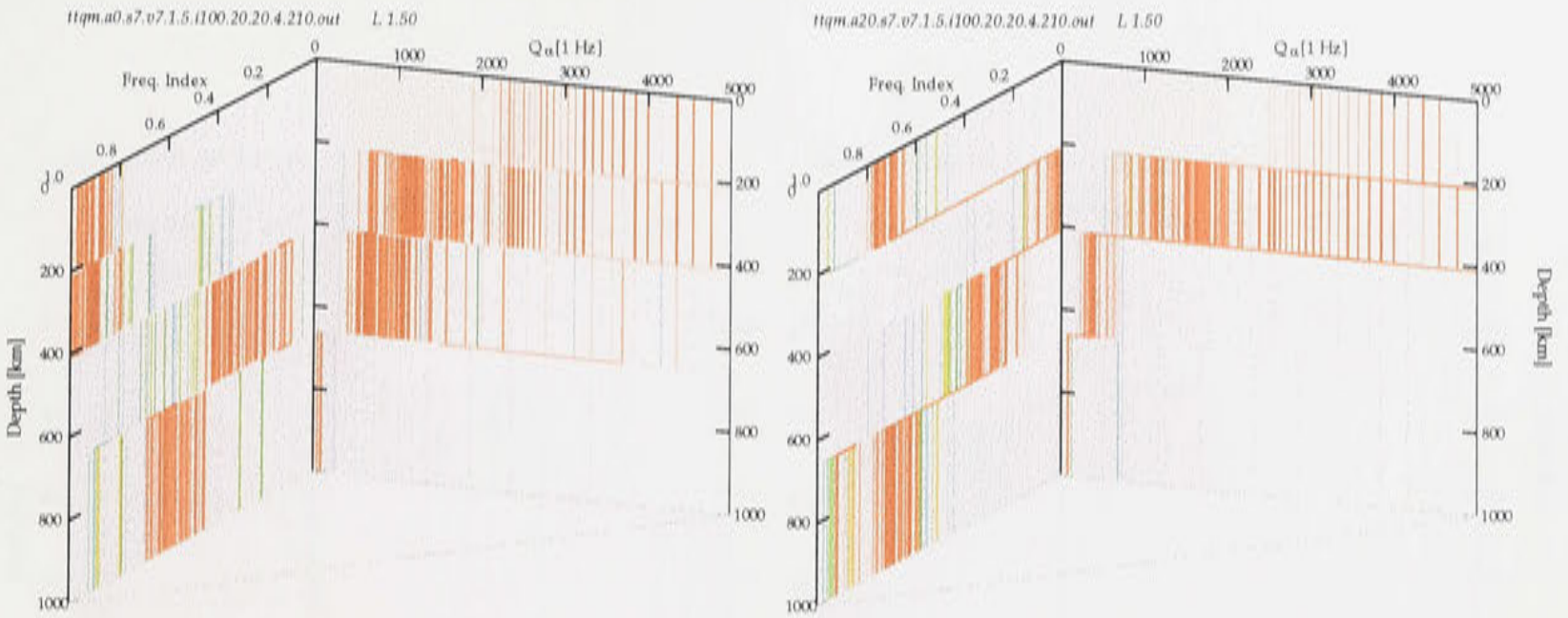

(y) Sl4 Az0 $14.86° < \Delta < 23.15°$ **(z)** Sl4 Az20 $14.14° < \Delta < 22.54°$

Figure 9.4: A set of 1-D Q and α profiles inverted from the SKIPPY data by NA. Epicentral distance range in the caption of each subfigure indicating the data constraints on depth coverage.

The phases associated with the shallower part of the upper mantle have rather high frequency content. The δt^*_{sp} estimated from this group of phases are small with weak attenuation (see figure 6.7 (a)). The thickness of the lithosphere varies significantly depending on the direction of propagation. For paths from the east, P wavespeeds in the uppermost mantle (above 120 km in depth) are slower; whereas from the north and west higher wavespeeds persist to greater depth. The phases returned from somewhat deeper in the upper mantle are clear for P with both low and high frequency content, but S is relatively weak [Kaiho and Kennett, 2000].

In shorter distance range from 8 to 20°, the δt^*_{sp} estimated from this group of phases are small with weak attenuation (see figure 6.7 (a)). In the medium distance range from 18 tp 30°, the δt^*_{sp} estimated from this group of data show mixed large and small values (see figure 6.7 (b)). The P waves returned from the top part of the lower mantle are also clear and the velocities in the transition zone are slightly faster than *ak135* [Kaiho and Kennett, 2000]. The S waves are characterised by strongly attenuated arrivals, and in some cases Vp/Vs ratio from *ak135* were retained by [Kaiho and Kennett, 2000] in order to construct models for azimuth bands in this group. The values of δt^*_{sp} estimated from this group of data are large with strong attenuation (see figure 6.7 (b)).

Q and α in the Upper Mantle beneath Central to Western Australia - *sl3* Group

The thickness of lithosphere beneath this group of slices is relatively thick, I chose the thickness of first layer for Q and α model at the depth of 210 km in accordance with the significant variation in velocity at the depth of 210 km. In general, the attenuation and its frequency dependence is weak in the upper mantle beneath this group of slices.

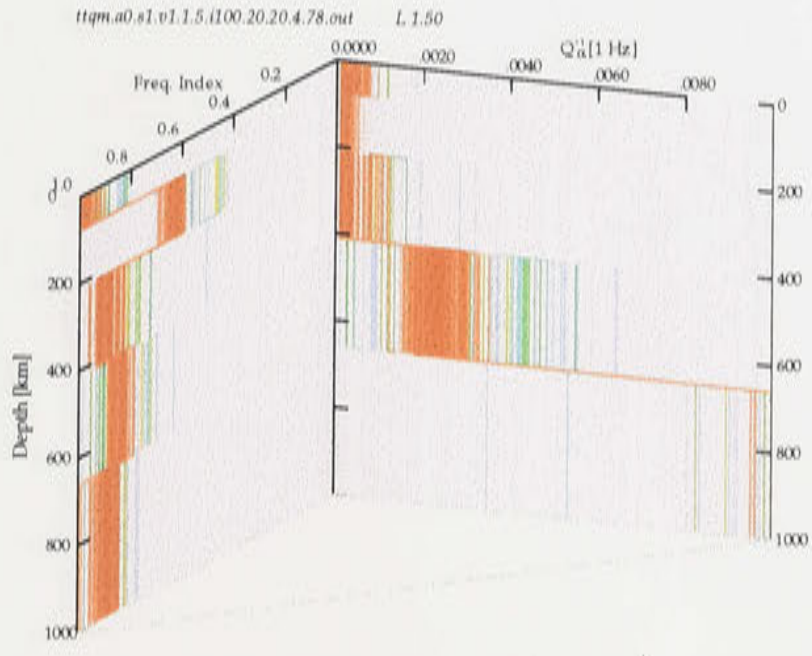

(a) Sl1 Az0 17.17° < Δ < 32.82°

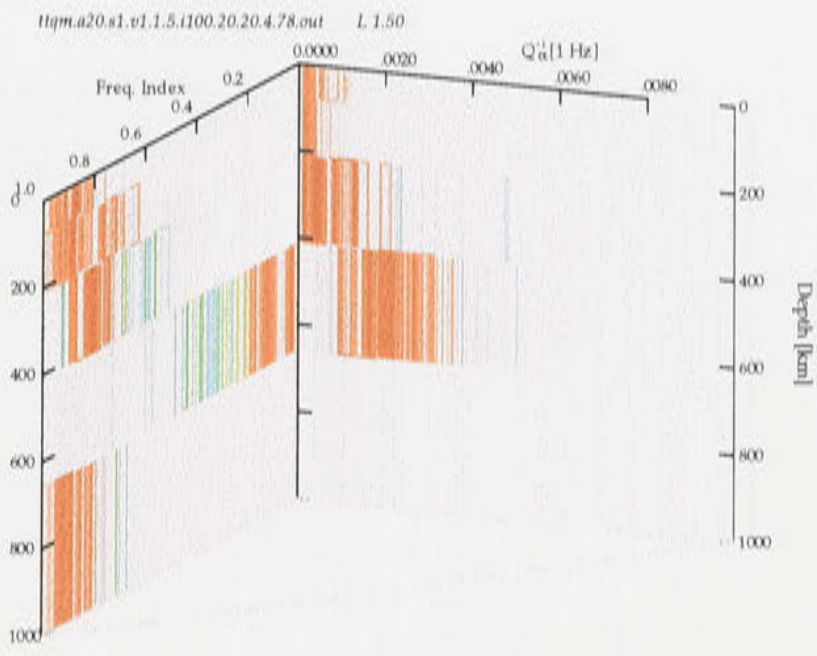

(b) Sl1 Az20 17.34° < Δ < 30.1°

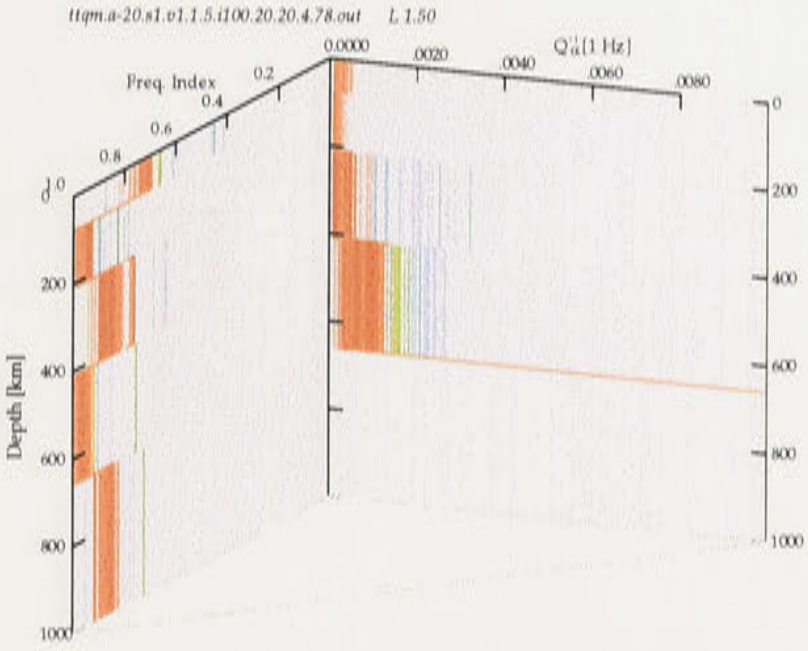

(c) Sl1 Az-20 21.03° < Δ < 26.82°

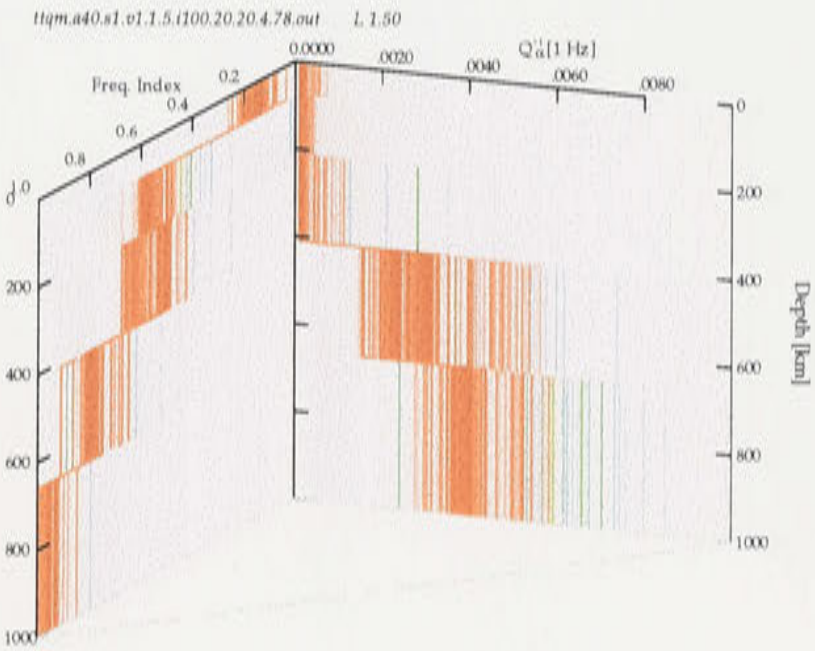

(d) Sl1 Az40 17.35° < Δ < 32.08°

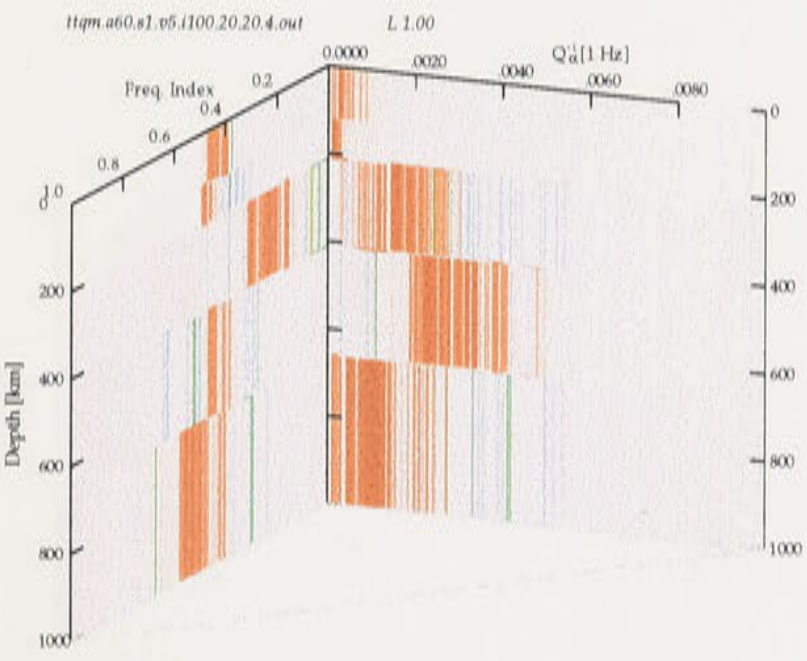

(e) Sl1 Az60 3.42° < Δ < 37.21°

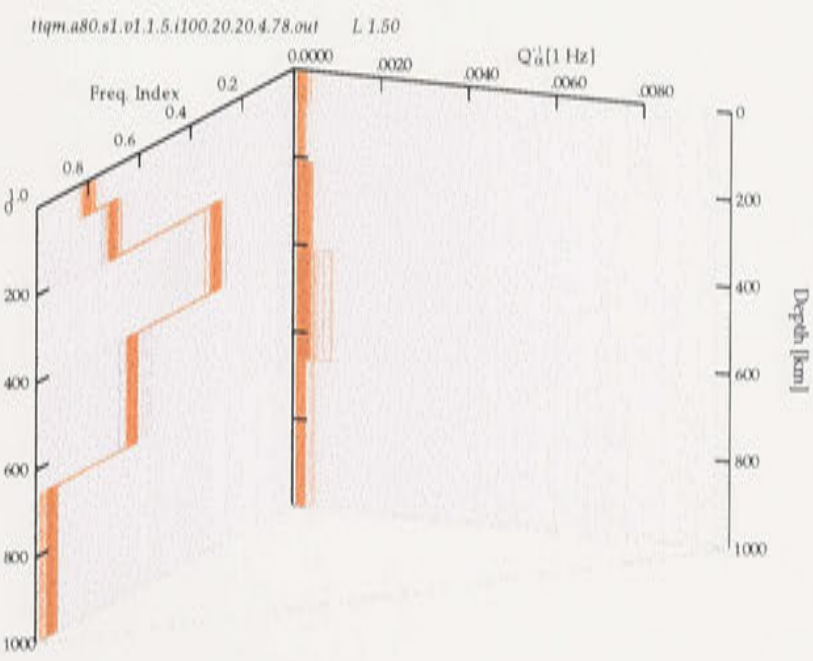

(f) Sl1 Az80 19.89° < Δ < 47.42°

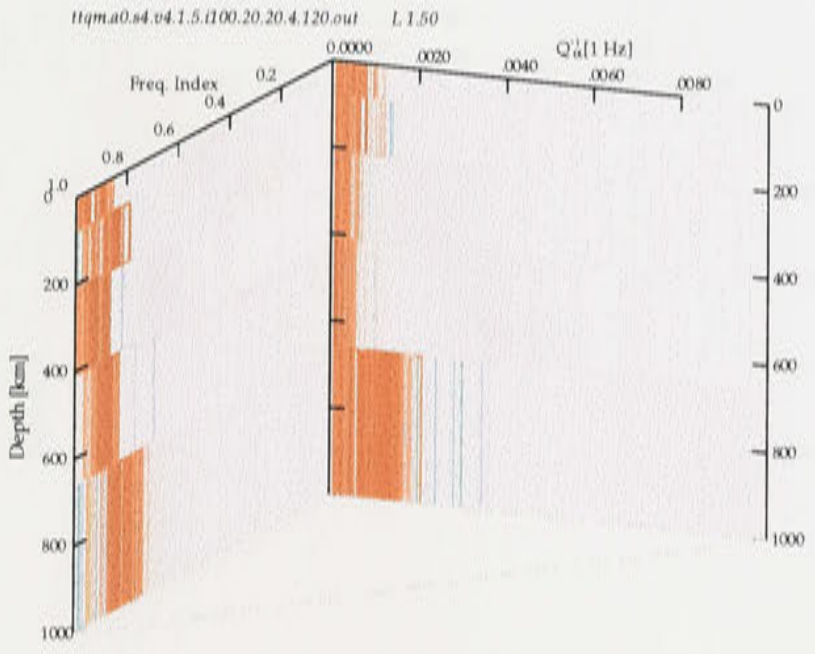

(g) Sl2 Az0 10.22° < Δ < 34.15°

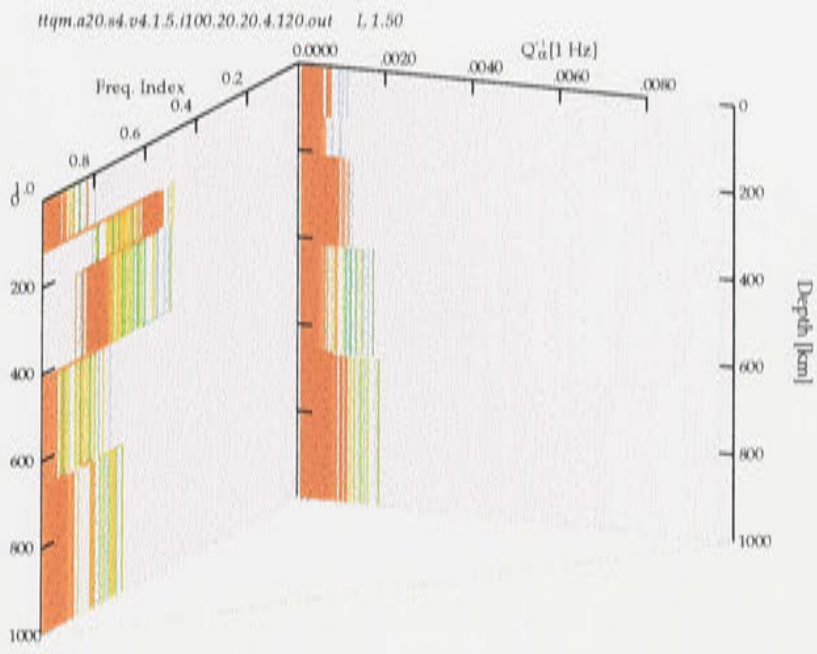

(h) Sl2 Az20 9.16° < Δ < 32.37°

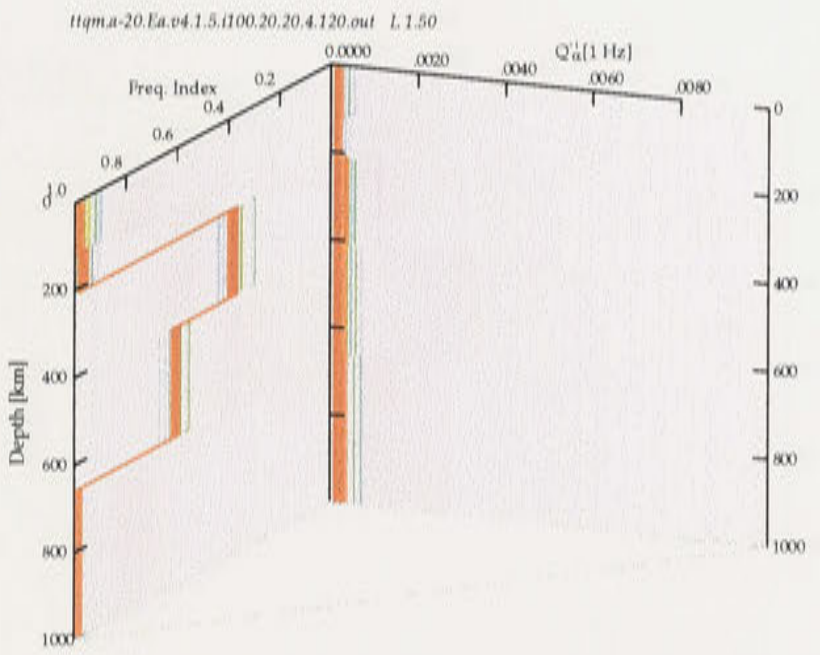

(i) Sl2 Az-20 17.46° < Δ < 34.76°

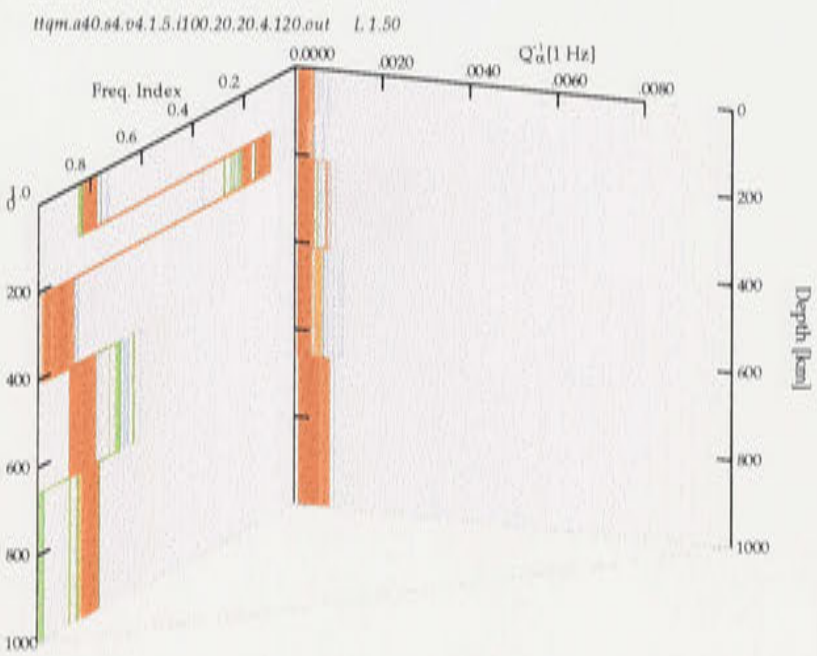

(j) Sl2 Az40 9.64° < Δ < 36.66°

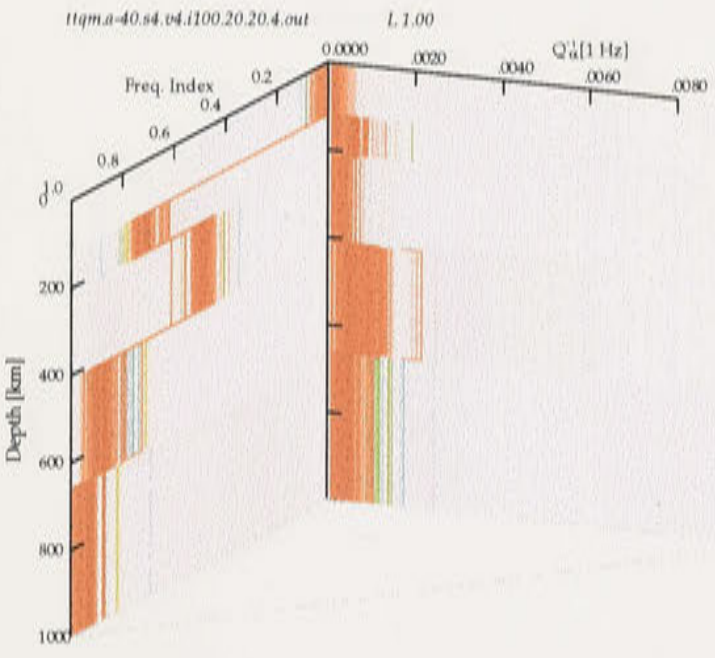

(k) Sl2 Az-40 12.37° < Δ < 32.19°

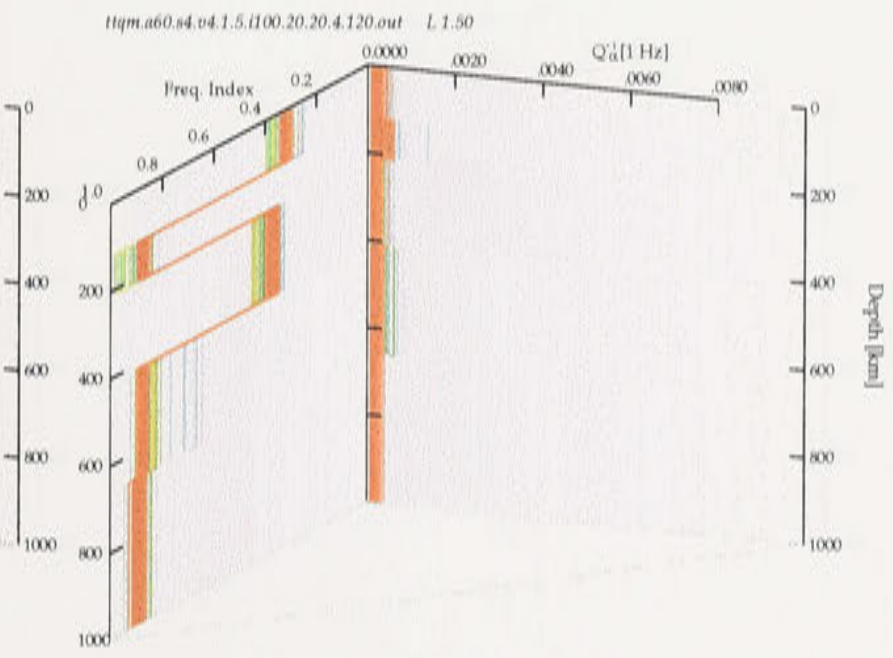

(l) Sl2 Az60 10.37° < Δ < 43.49°

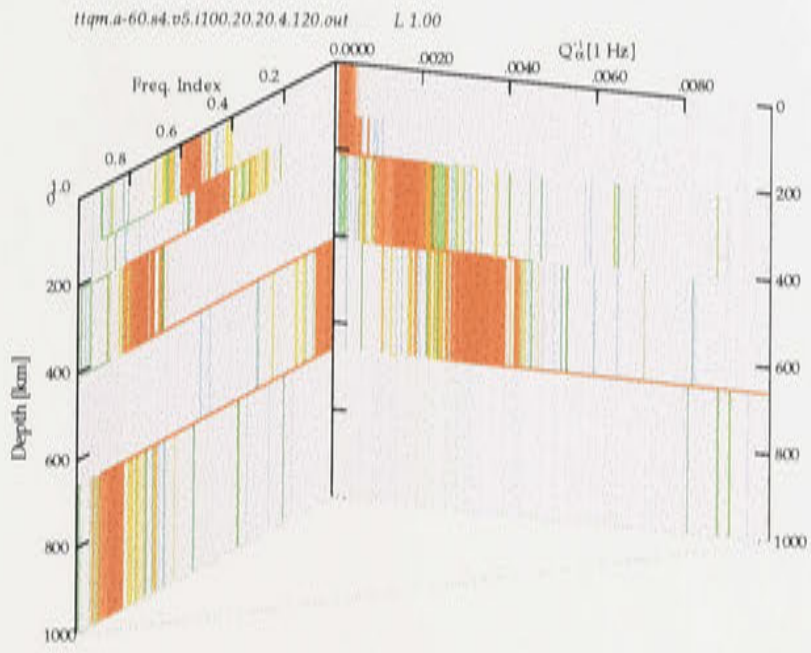

(m) Sl2 Az-60 14.44° < Δ < 18.49°

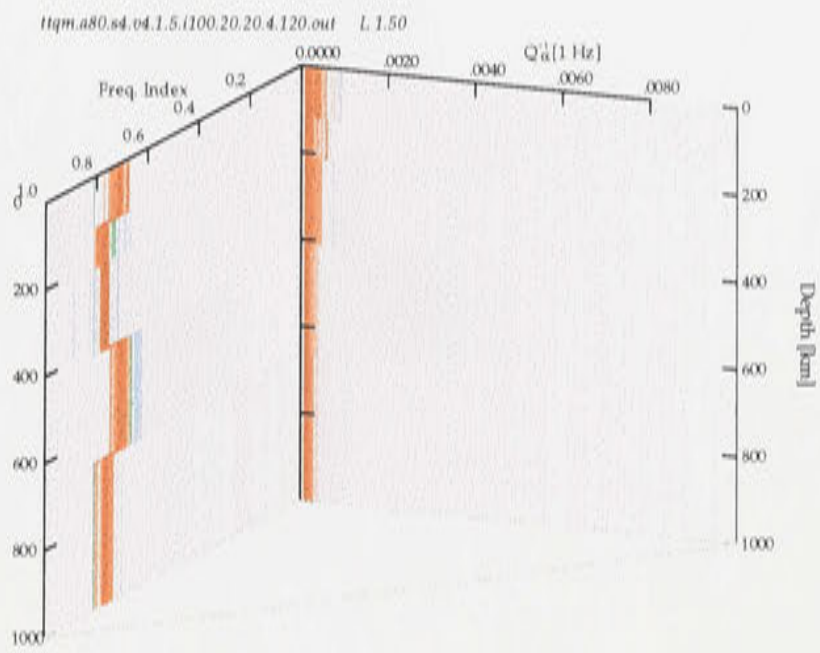

(n) Sl2 Az80 17.65° < Δ < 49.85°

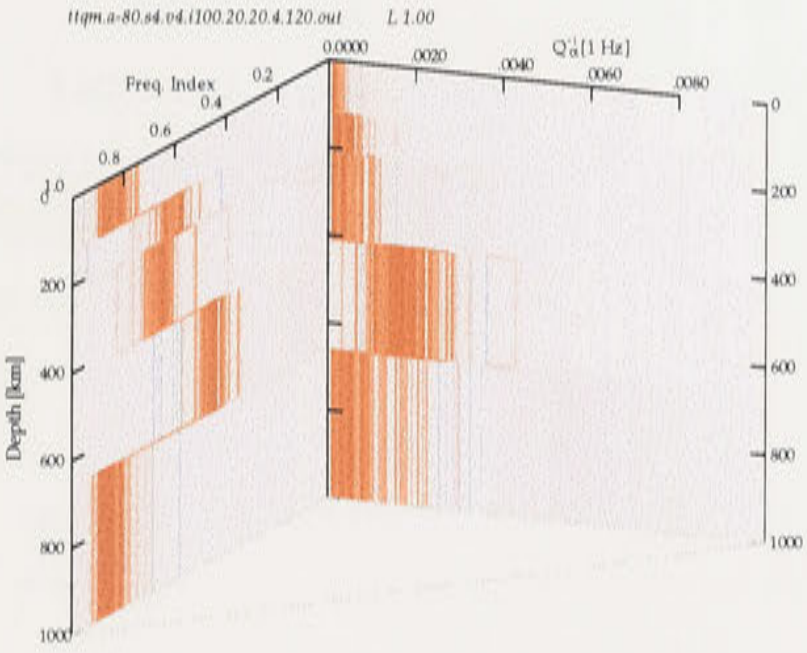

(o) Sl2 Az-80 11.71° < Δ < 35.15°

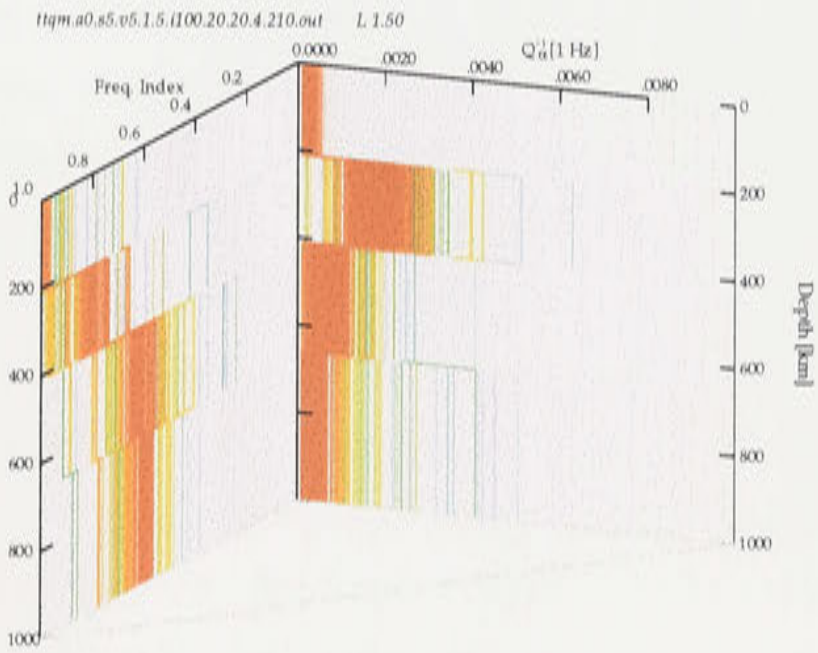

(p) Sl3 Az0 7.15° < Δ < 26.48°

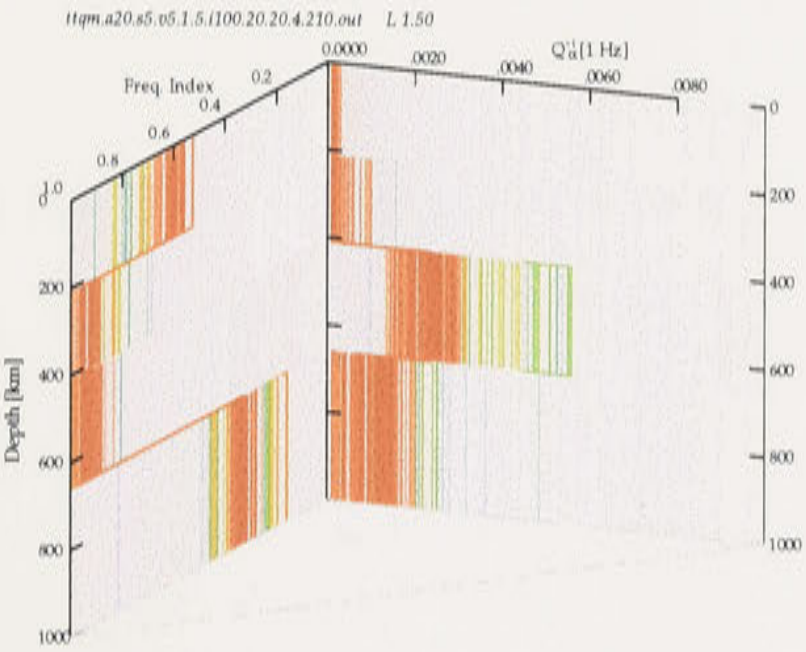

(q) Sl3 Az20 4.29° < Δ < 35.5°

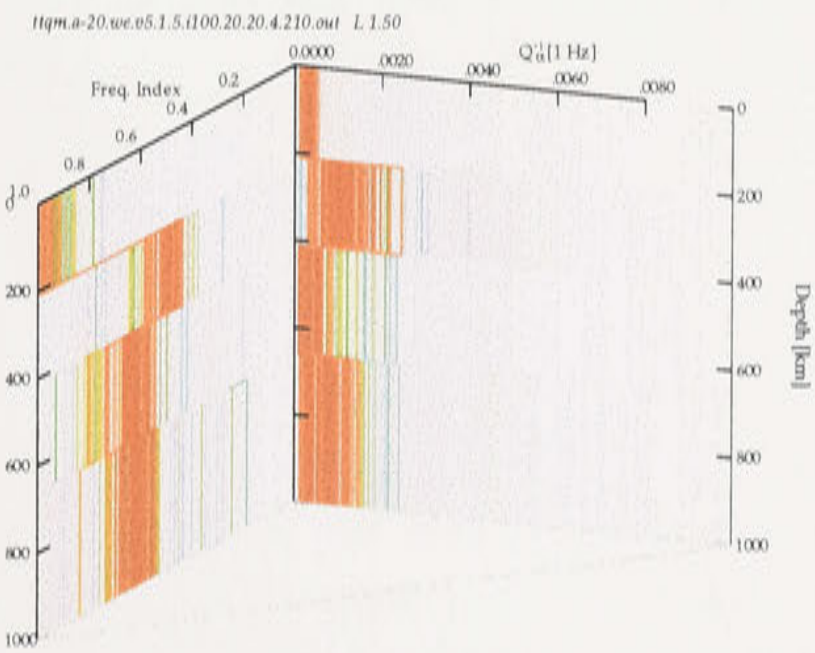

(r) Sl3 Az-20 2.2° < Δ < 37.89°

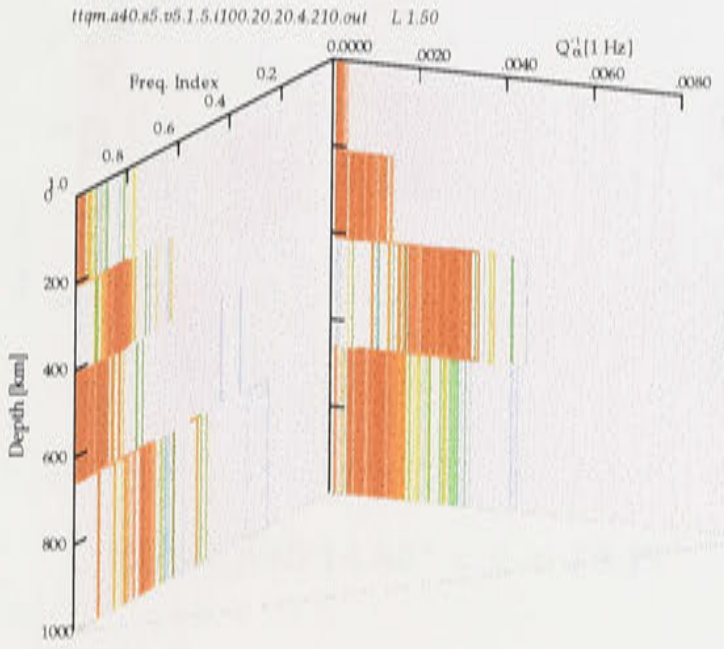

(s) Sl3 Az40 10.92° < Δ < 35.85°

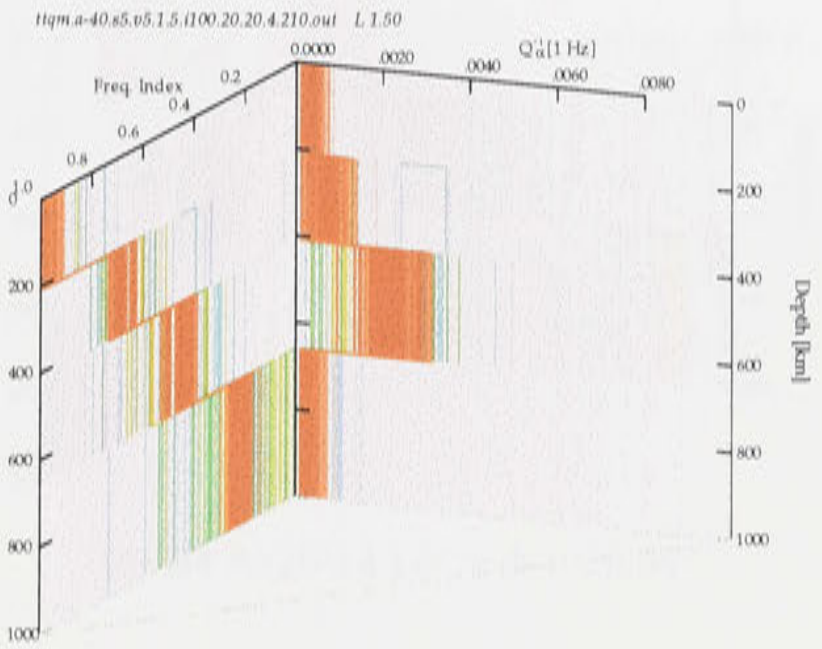

(t) Sl3 Az-40 0.98° < Δ < 30.89°

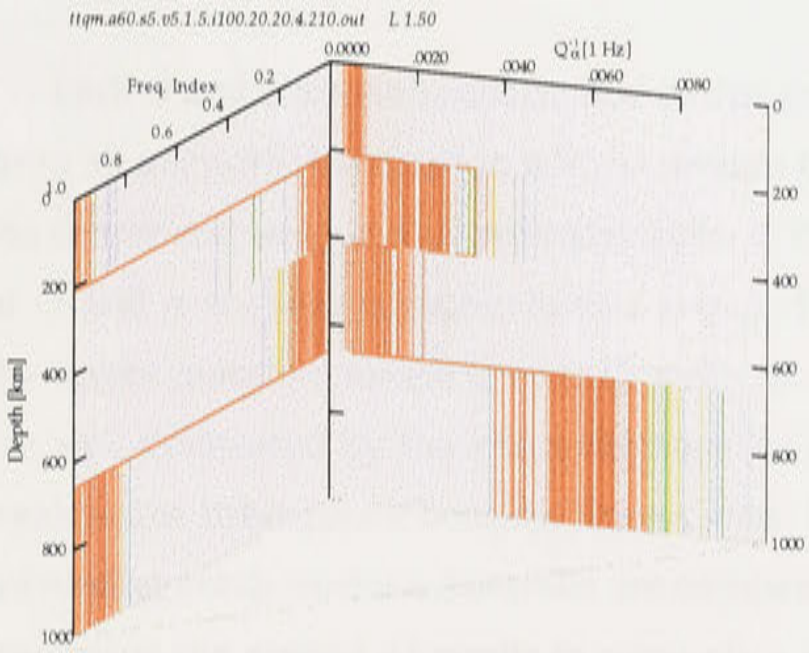

(u) Sl3 Az60 13.6° < Δ < 38.49°

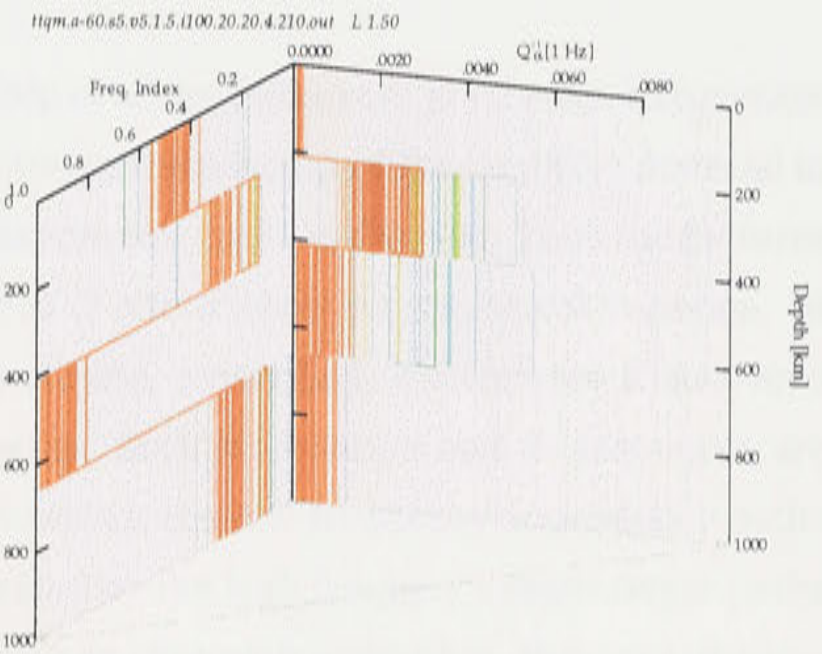

(v) Sl3 Az-60 3.26° < Δ < 31.35°

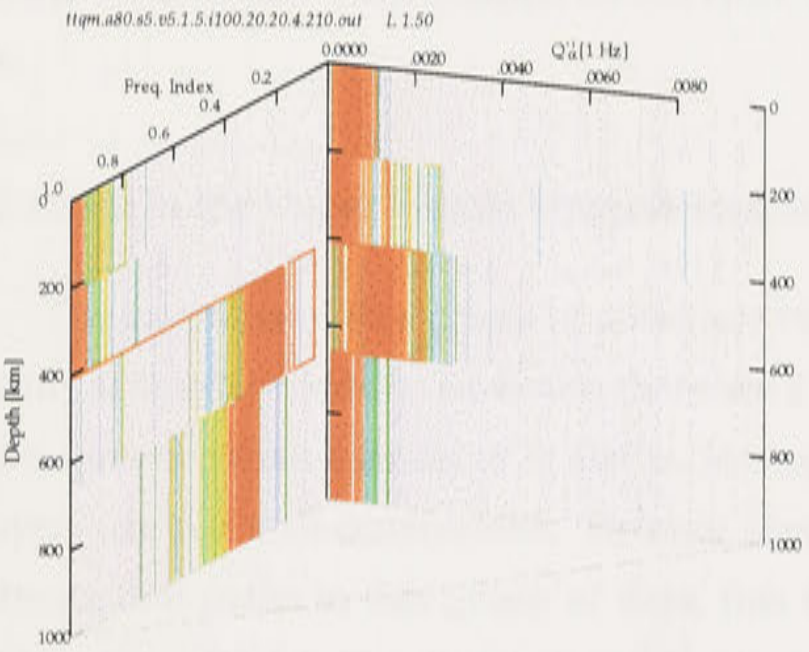

(w) Sl3 Az80 2.81° < Δ < 28.43°

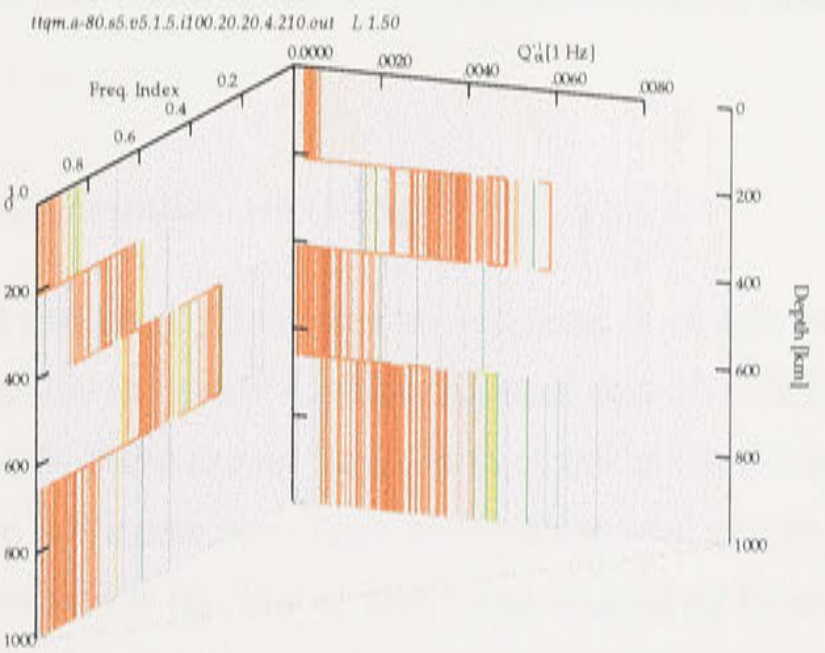

(x) Sl3 Az-80 4.03° < Δ < 41.17°

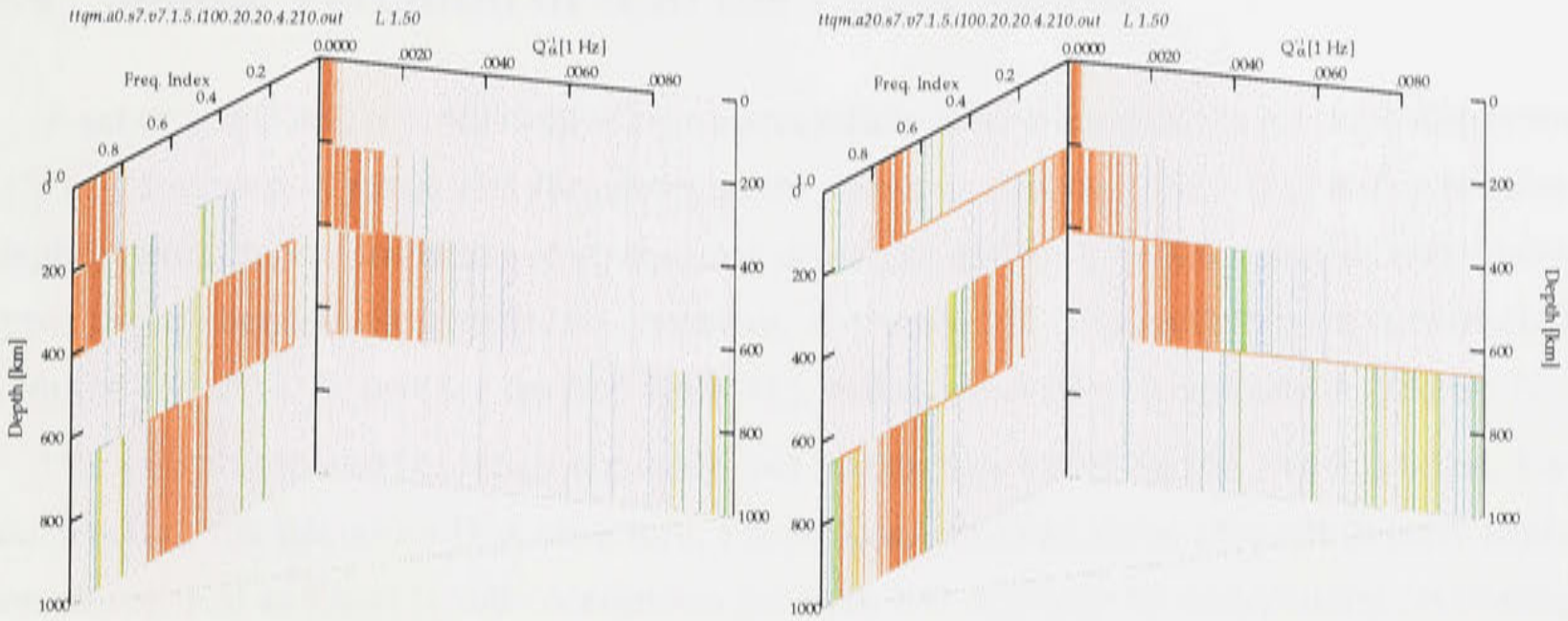

(y) Sl4 Az0 $14.86° < \Delta < 23.15°$ **(z)** Sl4 Az20 $14.14° < \Delta < 22.54°$

Figure 9.5: A set of 1-D Q and α profiles inverted from the SKIPPY data by NA. Epicentral distance range in the caption of each subfigure indicating the data constraints on depth coverage.

Both Q and α are well constrained in this group of slices, because of good raypath coverage from all azimuth distribution which traverse through the outcrop of Precambrian material in the center and west and an extensive zone of Phanerozoic rocks in the east. Thus the features of Q and α are very complex in this group. Both Q and α show strong lateral variation. In the upper mantle beneath the north western Australia, particularly beneath the KIMBA area are well delineated by the short distance raypaths. Both attenuation and its frequency are weak in the lithosphere beneath KIMBA area. However, the low frequency dependence paths traversing north western Australia are compensated by the high frequency dependence paths traversing the central Australia in some slice, such as slice with azimuth 0. However, the low frequency dependence paths and the high frequency dependence paths are distinguished in many other slices. Thus I expect to see clear lateral variation in in the 3-D models of Q and α.

Q and α in the Upper Mantle beneath Western Australia - *sl4* Group

The raypaths in this group of slices are very limited. There are no raypaths available in many azimuth corridors. However, there are 5 paths in the slice with azimuth 0 and 20 which allow me to obtain a model of Q and α. Meanwhile there are no long distance paths the deep layers are not well constrained. Because there are some very high attenuation and strong attenuation paths in this group of data, this turns out the low Q and large α derived from this group of data. This is consistent to the velocity variation and geological background in this area.

9.4 Spatial Variation of α in the Upper Mantle

A set of 1-D Q and α profiles have been successfully constructed by the NA inversion from δt^*_{sp} as a function of range and frequency in the previous section. The 1-D Q and α profiles display strong spatial variation of attenuation structure and its frequency dependence in the upper mantle beneath the Australian continent. A pseudo 3-D Q model has been constructed from the set of 1-D Q profiles derived from δt^*_{sp} estimates at fixed frequency in chapter 7.

It is also possible to construct a pseudo-3-D α structure based on the 1-D α profiles. For constructing the pseudo 3-D α structure, I have again derived three raypath density functions in vertical and horizontal coordinates for each 1-D α profile by undertaking raytracing for each raypath which contributes to the construction of this 1-D profile. I have then conducted a grid search and obtain α values in a particular cell by averaging the 1-D α profiles, which overlapping in this cell, weighted by the two sets of raypath density functions. The parameterisation of the grid search and the way to derive the ray density functions are same as I did in chapter 7. The pseudo 3-D α model is displayed in fig 9.6.

There is a strong depth dependence in α displayed in fig 9.6, as well as the lateral variation. In general, the α is small in shallow part of the Earth, then α increases with depth to its largest value in layer 210-410km, then α decreases in the lower mantle. The α across over the range from 0.02 to 0.98. The α is smaller than 0.5 in most part of the Earth which is consistent with the published results [Tan et al., 2000; Romanowicz and Durek, 2000]. The large α found in the northwestern region at depths greater than 660 km need more investigation to confirm. My synthetic tests suggest that the α in deep mantle could not be well recovered because it is masked by the top layers.

Recent investigation on seismic wave attenuation in the laboratory by [Tan et al., 2000] suggests that the viscoelastic behaviour, attributed to diffusional process, is grainsize sensitive with the dissipation and associated dispersion increasing with decreasing grainsize. This conclusion is under the assumption of α is not dependent to the grainsize sensitive parameter and the grainsize sensitive parameter is not dependent on frequency. What factors actually control the variation of α within the Earth is an interesting question and will need more investigation to answer.

The 3-D α displayed in figure 9.6 and 3-D Q model displayed in figure 7.7 are reasonably consistent in terms of high Q associated with small α and low Q associated with large α. But the high Q block in the layer 210-410km beneath the southeastern part of Australia and high Q block in the deep mantle beneath the northwestern part of Australia are not consistent with the large α in the same region. There are a few possible reasons for this: one is the nature of the Earth, another possibility may the limitations of raypath coverage in these two regions. This leaves room for further investigations.

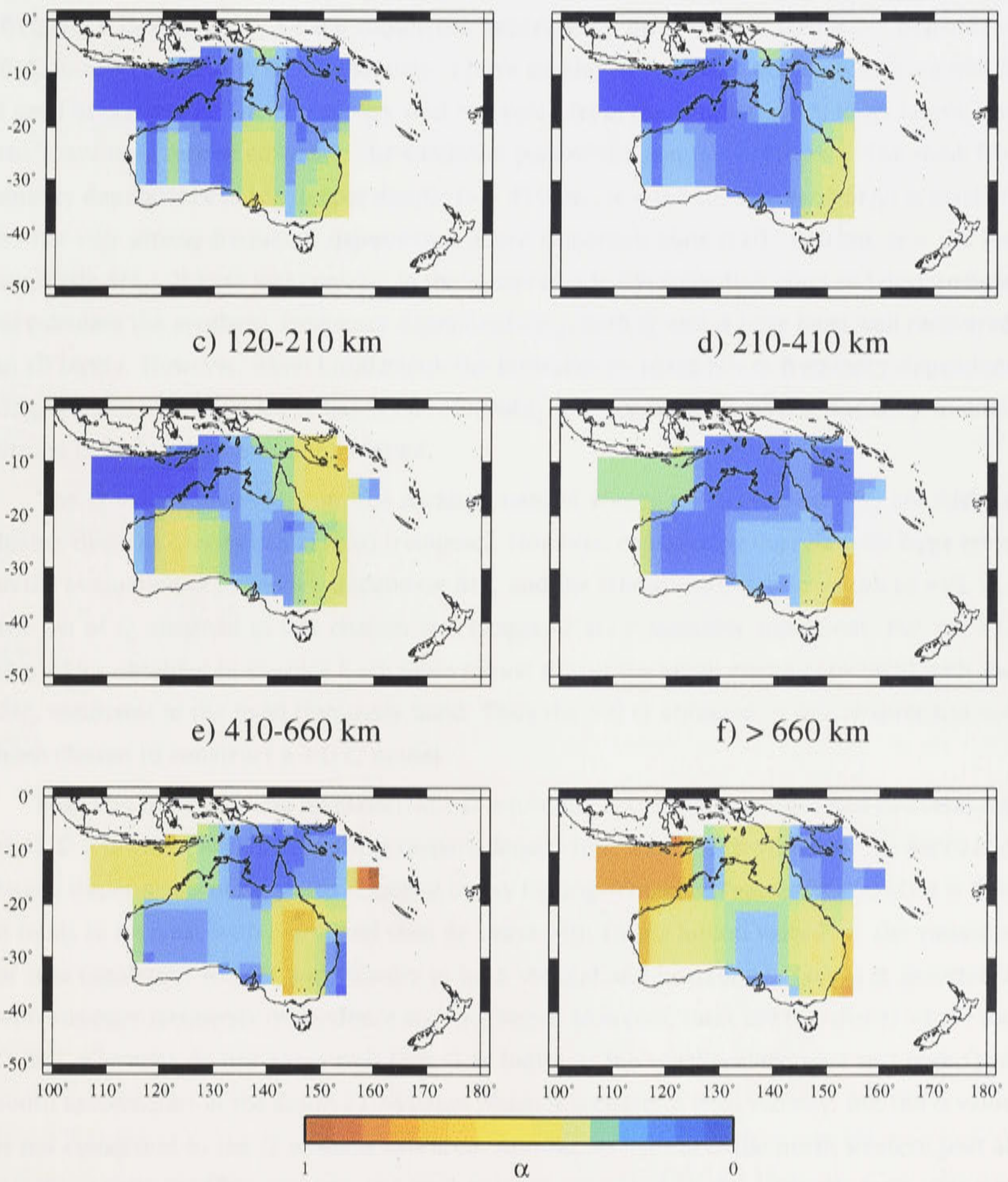

Figure 9.6: 3-D α model in the upper mantle beneath the Australia region.

9.5 Discussion

In this chapter, a set of 1-D Q and α models has been constructed by successfully using NA with frequency dependent δt^*_{sp} estimates in the six subfrequency bands up to 6 Hz from the digital broadband SKIPPY seismic data.

Based on my experience of successfully using NA to invert Q from δt^*_{sp} estimates at fixed frequency in chapter 7, I have conducted experiments on synthetic frequency dependent δt^*_{sp} to invert Q and α simultaneously. I have employed the same parameterisation which I used in chapter 7. The Q was very well recovered from the synthetic δt^*_{sp} in all layers, but the α are only recovered well in the shallower part of the mantle (< 410 km). The weak frequency dependence in the deeper mantle (> > 410 km , α = 0.2 for synthetic δt^*_{sp}) is masked by the very strong frequency dependence above transition zone (210 - 410 km, α = 0.6 for synthetic δt^*_{sp}). If I use less contrast in the values of α in the transition zone and deep mantle to calculate the synthetic frequency dependent δt^*_{sp}, both Q and α have been well recovered in all layers. However, when I undertook the inversion by using NA to frequency dependent δt^*_{sp} from SKIPPY data, the α has been reasonably well constrained even in the deep mantle. Strong lateral variation in α is revealed.

The Q values inverted from the measurement of frequency dependent δt^*_{sp} are slightly higher than the Q obtained at fixed frequency. However, considering the relatively large error in the estimation of frequency dependent δt^*_{sp} and the attempt to obtain α values as well, the two set of Q obtained in this chapter and chapter 7 are reasonably consistent. But the 1-D Q profiles obtained in chapter 7 are more robust due to the small errors associated with the δt^*_{sp} estimates in the fixed frequency band. Thus the 1-D Q obtained in this chapter has not been chosen to construct a 3-D Q model.

Based on the successful inversion on 1-D α profiles, 3-D α has been obtained by averaging the 1-D α profiles, weighted by three raypath density functions which represent the depth and lateral dependence of ray paths obtained by ray tracing. The main feature of the 3-D α is that it tends to increase with depth and then decrease with strong lateral variation. The variation of α is consistent with Q and velocity in both vertical and horizontal. Low Q is associated with stronger frequency dependence and vice versa. However, there are two places where the Q and α results do not agree well Low Q is found in the northeastern part and high Q in south eastern part at the depth 210-410 km which is consistent with velocity. But the α value is not consistent to the Q in these two area. Another exception is the north western part at depths greater than 660 km, but, as I have pointed out based on the synthetic tests, α is not well recovered in the deep mantle.

Appendix A

Seismic Ray Theory and Methods for Travel Time and t^* Calculation

The ray method present a powerful tool for solving wave propagation problems in laterally varying media with inhomogeneous isotropic and/or anisotropic structures. The basic advantage is the applicability of the ray method to inhomogeneous media and its efficiency in such computations. Another great virtue of the ray method is the physical insight which it yields into the wave propagation process. Individual wave phases can be separated in the wavefield and it can be possible to follow the way by which energy of these waves propagate though the medium.

The basic limitation of the ray method in the fact that it is only approximate. It is applicable to smooth media, in which the characteristic dimensions of inhomogeneities are long compared with the wave length. The ray method can yield distorted results or no results in some special regions, such as caustic regions, critical regions, transition zones between the illuminated and shadow regions. The ray method can not describe reliably the interference of two waves propagation in an inhomogeneous medium with nearly same phase velocity (e.g. shear wave coupling in inhomogeneous anisotropic media).

The ray method was not developed originally for the applications in seismology. The seismic ray methods owes a lot to optics and radiophysics. First seismological application of the ray concepts date to the end of the last century. Then only kinematics, specifically travel times were used. The studied structure were simply radially symmetric Earth. The first attempts to use also dynamics (amplitudes and waveforms) were probably by Sir H. Jeffreys. The series solutions of the elastic dynamic equation were first suggested by Babič (Babič, 1956) and Karal and Keller (Karal and Keller, 1959). In seismological applications, the ray methods was mainly used to investigate the inner structure of the each from travel time curves of seismic body waves, and to compute rays and theoretical travel times of seismic waves in various type of media for ultimate comparison with observed data.

In geometric optics a ray is refracted according to Snell's law. For a spherically symmetric medium:

$$\frac{r_1 \sin i_1}{V_1} = \frac{r_2 \sin i_2}{V_2} \tag{A.1}$$

An important consequence of this equation is that the equality $r \sin i/V$ is a constant through the length of the ray regardless of the local waves speed of the layer. It is therefore a convenient parameter for describing the ray, and is called the ray parameter.

$$p = \frac{r \sin i}{V(r)} \tag{A.2}$$

p identifies a ray traveling between two points on or inside the earth. An important equation allows us to calculate the ray parameter from a sets of travel time tables.

$$p = \frac{r \sin i}{V(r)} = \frac{dT}{d\Delta} \tag{A.3}$$

Calculating the ray path, or ray tracing, in more complicated media is a difficult numerical problem. For spherically symmetric media only an integral is requires. the ray path must lie in a diametric plane, and therefore I need only consider the problem in two dimensions. Once the path is found in a plane, the plane itself can be rotated to the correct orientation with respect to the earth. Within the plane the ray is specified as a function $\theta(r)$, where θ is the angular distance from some reference point and r is the radius.

From Fermat's principle, I can derive a second order differential equation for rays which is equivalent to the equation for acoustic wave propagation.

The travel time dt along a ray segment $d\mathbf{r}$ is given by

$$dt = \frac{|d\mathbf{r}|}{v} \tag{A.4}$$

where $d\mathbf{r}$ is taken small enough for v to be effective constant. If I now perturb this ray, such that $d\mathbf{r} - d(\mathbf{r} + d\mathbf{r})$, the ray will traverse a different velocity $v + \delta v$ and

$$dt + \delta dt = \frac{|d\mathbf{r} + d\delta\mathbf{r}|}{v + \delta v} = |d\mathbf{r} + d\delta\mathbf{r}|[\frac{1}{v} + \delta(\frac{1}{v})] \tag{A.5}$$

By expansion, one easily determines that

$$|d\mathbf{r} + d\delta\mathbf{r}| = |d\mathbf{r}| + \frac{|d\mathbf{r} + d\delta\mathbf{r}|}{dr} = \mathbf{n} \cdot (d\mathbf{r} + d\delta\mathbf{r}) \tag{A.6}$$

I therefore have, to first order:

$$\delta dt = \frac{1}{v}\mathbf{n} \cdot d\delta\mathbf{r} + \delta(\frac{1}{v})\mathbf{n} \cdot d\mathbf{r} \tag{A.7}$$

I find the total travel time perturbation δT of a ray between two fixed points A and B by integration:

$$\delta T = \int_A^B \delta(\frac{1}{v})\mathbf{n} \cdot d\mathbf{r} + \int_A^B \frac{1}{v}\mathbf{n} \cdot d\delta\mathbf{r} \tag{A.8}$$

$$\delta \mathbf{r} = \int_A^B \delta(\frac{1}{v})\mathbf{n} \cdot \frac{d\mathbf{r}(s)}{dl} + \int_A^B \frac{1}{v}\mathbf{n} \cdot \frac{d\delta\mathbf{r}(s)}{dl} dl \tag{A.9}$$

In the first integral I may write $\delta(1/v) = \delta\mathbf{r} \cdot \nabla(1/v)$. The second integral can be integrated by parts. This produces, since $\delta\mathbf{r} = 0$ in A and B, and $\mathbf{n} = d\mathbf{r}/dl$:

$$\delta T = \int_A^B \delta\mathbf{r} \cdot [\nabla(\frac{1}{v}) - \frac{d}{dl}(\frac{1}{v}\mathbf{n})]dl \tag{A.10}$$

For arbitrary $\delta\mathbf{r}$ I have $\delta T = 0$ so that:

$$\frac{d}{dl}[\frac{1}{v}\frac{dr}{dl}] = \nabla(\frac{1}{v}) \tag{A.11}$$

which is the same equation as the ray equation derived from the differential equation of acoustic wave propagation.

This is a second order differential equation for rays. It is easier for computers to solve first-order systems than second-order. The second-order system can be easily transformed to a first-order system. Put:

$$p_i = \frac{1}{v}\frac{dx_i}{dl} \quad \text{then} \quad \frac{dp_i}{dl} = \frac{\partial}{\partial x}(\frac{1}{v})$$

Starting with $x_i(0)$ and $p_i(0)$ I can trace rays by numerical integration of this system. $x_i(0)$ tells us where the ray starts, $p_i(0)$ is the ray parameter that gives the direction in which it starts out. What I only know is the end point $x_i(S)$ of a ray. The ray length is part of the solution. If I set $s = \eta S$, so that $0 \le \eta \le 1$ then I have

$$\frac{dx_i}{d\eta} = Sv(\mathbf{r})p_i \tag{A.12}$$

$$\frac{dp_i}{d\eta} = S\frac{\partial}{\partial x_i}(\frac{1}{v}) \tag{A.13}$$

with boundary conditions: $x_i(0) = x_i^0$ and $x_i(0) = x_i^s$. This is a nonlinear eigenvalue problem with Dirichlet boundary conditions at $\eta = 0$ and $\eta = 1$. (Chin et al, 1984)

In a medium with horizontal stratification, I have $v(x, y, z) = v(z)$, so that $dp_x/d\eta$ and $dp_y/d\eta$ vanish. From ray equation I then have, for the ray in the x-y plane:

$$constant\ p_x \equiv p = \frac{1}{v}\frac{dx}{dl} \tag{A.14}$$

which shows that Snell's law is valid for waves satisfying the ray theory $\omega \gg 1$. If I follow a segment of a ray, it will traverse a horizontal distance give by

$$X(p) = \int dx = \int \tan\ i\, dz = \int \frac{\sin i}{(1 - \sin^2 i)^{1/2}} dz = \int \frac{vp}{(1 - v^2p^2)^{1/2}} dz \tag{A.15}$$

in a time:

$$T(p) = \int dt = \int \frac{dl}{v} = \int \frac{dz}{v(1 - v^2p^2)^{1/2}} \tag{A.16}$$

In a Earth with spherical symmetry I find in a similar way:

$$T(p) = \int \frac{\eta^2 dr}{r(\eta^2 - p^2)^{1/2}} \tag{A.17}$$

$$\triangle(p) = \int \frac{p dr}{r(\eta^2 - p^2)^{1/2}} \tag{A.18}$$

where $\triangle(p)$ is the angle in radius, $\eta = r/v$, and $p = \eta \sin\theta$ (θ is the angle of the ray with the radius). For model without symmetry (usually called laterally heterogeneous Earth models), the system of differential equation much be solved with numerical methods. Note that the ray parameter, p, can be pulled outside the integral in A.17 because it is constant along the path. Noting the similarity between Δ and T, I can relate the travel time and distance:

$$T(p) = \int \frac{\eta^2 dr}{r(\eta^2 - p^2)^{1/2}} = \int \frac{p^2 dr}{r(\eta^2 - p^2)^{1/2}} + \int \frac{(\eta^2 - p^2)^{1/2}}{r} dr \tag{A.19}$$

$$T(p) = p\Delta(p) + \int \frac{(\eta^2 - p^2)^{1/2}}{r} dr \tag{A.20}$$

In body wave studies, I commonly account for the effects of attenuation by convolving the elastic pulse shape with an attenuation operator parameterised by the value t^*, which is defined by the travel time divided by the quality factor in a region of uniform attenuation:

$$t^* = \int \frac{dt}{Q} \tag{A.21}$$

Combining A.16 and A.21, I can get:

$$t^* = \int \frac{dz}{vQ(1 - v^2p^2)^{1/2}} \tag{A.22}$$

In a Earth with spherical symmetry, t^* function will be:

$$t^* = \int \frac{\eta^2 dr}{rQ(\eta^2 - p^2)^{1/2}} = \int \frac{p^2 dr}{rQ(\eta^2 - p^2)^{1/2}} + \int \frac{(\eta^2 - p^2)^{1/2}}{rQ} dr \tag{A.23}$$

Appendix B

Nonlinear Attenuation Inversion Using a Neighbourhood Algorithm

B.1 Introduction

A new derivative-free search method for finding models of acceptable data fit in a multidemoentional parameter space was used in this research in constructing the frequency dependent Q models. The objective here is to find an ensemble of models that preferentially sample the good data-fitting regions of parameter space, rather than seeking a single optimal model. The new search algorithm makes use of the geometrical constructs known as Voronoi cells to drive the search in parameter space. These are nearest neighbour regions defined under a suitable distance norm. The algorithm is conceptually simple, requires just two 'tuning parameters', and makes use of only the rank of a data fit criterion rather than the numerical value. In this way all difficulties associated with the scaling of a data misfit function are avoided, and any combination of data fit criteria can be used [Sambridge, 1999a].

B.2 Nonlinear Inversion

The new direct search algorithm is used in this research for the inversion of body wave attenuation structure in the upper mantle. This is known to be a non-linear problem, where linearized inversion techniques suffer from a strong dependence on the starting solution. It is shown that the new algorithm produces a sophisticated type of 'self-adaptive' search behaviour, which to our knowledge has not been demonstrated in any previous technique of this kind [Sambridge, 1999a].

B.3 The Use of a Neighbourhood Algorithm

The neighbourhood algorithm is a derivative-free method for searching a multidimensional parameter space for models (attenuation) of acceptable data fit. It is based on some simple geometrical concepts, involves two tunable parameters, and makes use of randomised, or stochastic, sampling of parameter space. I outline the approach below. Full details can be found in Sambridge [1999a].

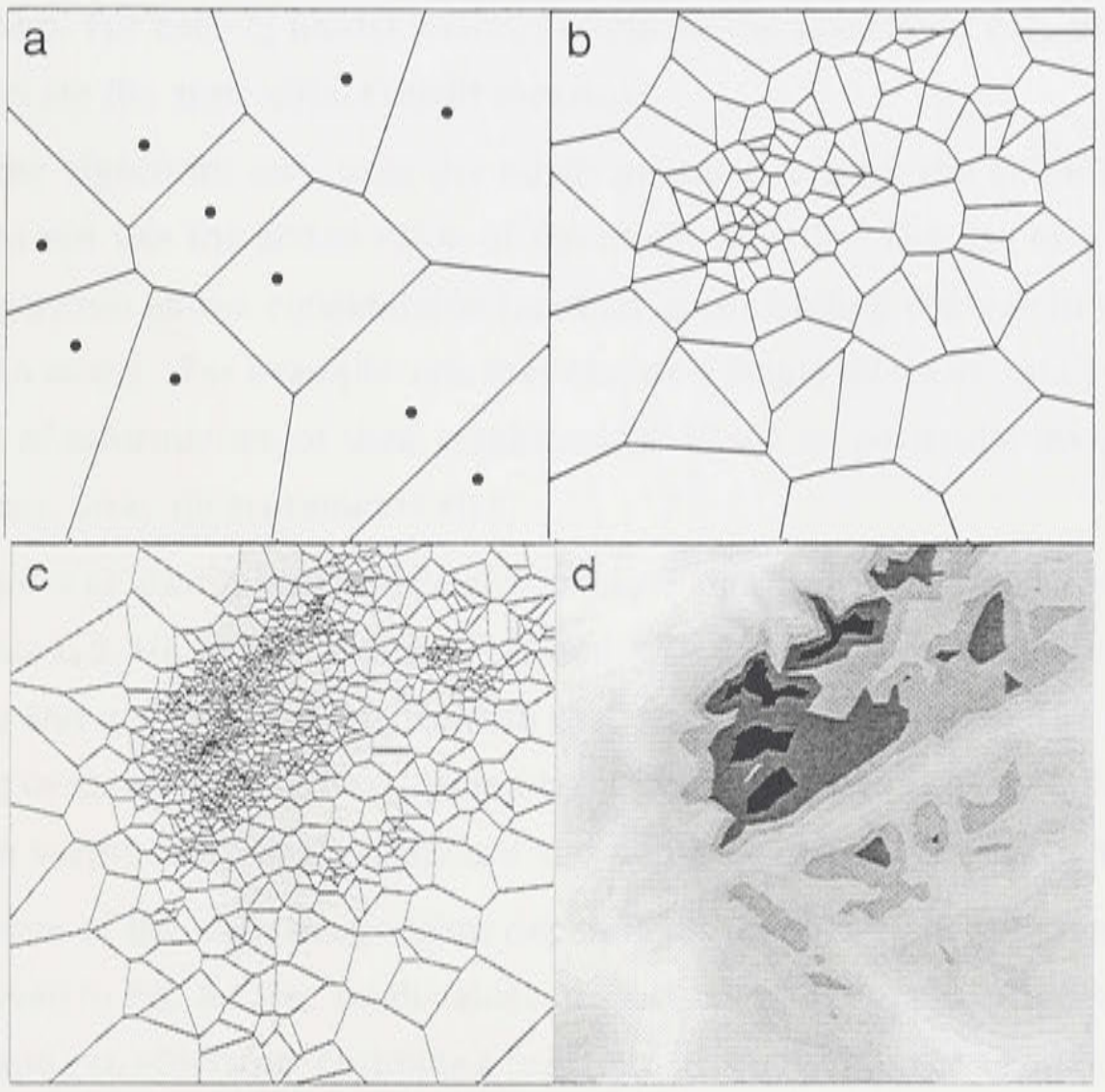

Figure B.1: Example of Voronoi cells, after Sambridge [1999a].

The central idea behind the neighbourhood algorithm is the use of Voronoi cells to guide the search in parameter space. Voronoi cells are simply nearest neighbour regions, as defined by a suitable distance norm (Voronoi, 1908). Also Voronoi cells can be used to enhance any existing direct search algorithm, by intermittently replacing the forward modelling calculating calculations with nearest neighbour calculations.

Here I use the L_2-norm. Fig. B.1 shows examples of Voronoi cells, defined about an irregular set of points in the plane. Each cell is a convex polygon about its defining point. Note that the sides of each cell are formed from the perpendicular bisectors between neighbouring pairs of points. Voronoi cells have many useful properties and have found applications in a number of fields (see Okabe et al, 1992, for a review). From Fig. B.1 I see that the size and shape of Voronoi cells automatically adapts to the density and distribution of the defining points. This is the property which is exploited in the search algorithm. I see from Fig. B.1 that the Voronoi cell defines a neighbourhood about each point.

The neighbourhood attenuation structure algorithm can be summarised as follows: First, an initial population of n_s Q is generated. Usually these follow a uniform random distribution within the parameter space bounds. At each iteration, the current n_r Q with lowest data misfit are determined and a new set of n_s Q are uniformly distributed inside their Voronoi cells, that is, n_s/n_r in each cell. Subsequent iterations are repeated in a similar manner, with the n_r best Q and their Voronoi cells being updated at each iteration. The number of Q models per iteration n_s and the number of Voronoi cells to be occupied N_r are two tuning parameter of the NA procedure. For each Q model tested, I calculate the associated δt^*_{sp} information and use this to generate the appropriate misfit measure.

Note that the algorithm only uses the misfit measure to rank the goodness of fit of Q models. It does not use the actual value of the misfit directly. The use of a rank measure to drive the algorithm allows considerable freedom in controlling the way in which the data influence the NA search. For example, one may choose a single misfit measure combining the different types of information, or their combinations based on particular inversion problem (e.g. arrival times, array measurements etc).

Fig. B.1, shows an example of the neighbourhood algorithm (used for attenuation structure) at iterations 1, 5, 10, and 20, with $n_s = 10$ and $n_r = 2$. Notice how the Voronoi cells adapt to the sampling and quickly focus in the south eastern part of the domain. The precise details of the sampling method are described in Sambridge [1999a]. It turns out that the bookkeeping calculations are surprisingly straightforward and may be handled very efficiently.

The behaviour of the search algorithm depends on the two control parameters, n_s and n_r. As can be seen in Fig. B.1, for small values of n_r it takes on the character of a contracting irregular grid, and can efficiently optimize a function. The power of the approach is due to the fact that at each iteration the sampling is driven by the size and distribution of the Voronoi cells, and these are controlled automatically by all previous samples.

The neighbourhood algorithm makes use of the geometrical constructs known as Voronoi cells to derive the search in parameter space. There are nearest neighbour regions defined under a suitable distance norm. The algorithm is conceptually simple, requires just two 'turning parameters', and makes use of only the rank of a data fit criterion rather than the numerical value. In this way all difficulties associated with the scaling of a data misfit function are avoided, and any combination of data fit criteria can be used. I outline the approach below. Full details can be found in Sambridge [1999a].

Appendix C

Frequently Used Symbols and Notation

Symbol	Description
P	Direct compressional wave
S	Direct shear wave
pP	Depth phase that leaves the focus upward as P (p leg)
sS	Depth phase that leaves the focus upward as S (s leg)
Pg	Compressional wave in the granitic layer of the crust
Sg	Shear wave in the granitic layer of the crust
SmS	Compressional wave reflected at Moho
PcP	P wave reflected at CMB
ScP	S wave reflected at CMB
SV	Radio component of S wave
SH	Transverse component of S wave
Z	Vertical component of S wave
f	Frequency (Hz)
Q	Quality factor
t^*	Attenuation operator
δt^*	Differential attenuation
δt^*_{sp}	Differential attenuation between P and S waves
α	Frequency dependence of attenuation, $Q(f) = Q(f_0)(f/f_0)^{\alpha}$
V	Velocity

Symbol	Description
V_p	P wave velocity
V_s	S wave velocity
$f_c(p)$	P wave corner frequency (Hz)
$f_c(s)$	S wave corner frequency (Hz)
Q_p	Quality factor of P wave
Q_s	Quality factor of S wave
τ	Stress
T	Travel time
δt	Travel time residual
δt_s	Travel time residual of S between observed and synthetic calculated from model *ak135*
δt_p	Travel time residual of P between observed and synthetic calculated from model *ak135*
Δ	Epicentral distance (degree)
$P(t)$	Temporal variations in P wave amplitude
$\tilde{P}_p(f)$	Spectrum of $P(t)$
$SV(t)$	Temporal variations in SV wave amplitude
$\tilde{P}_{sv}(f)$	Spectrum of $SV(t)$
$SH(t)$	Temporal variations in SH wave amplitude
$\tilde{P}_{sh}(f)$	Spectrum of $SH(t)$
$\tilde{P}_{np}(f)$	Noise spectrum of $P(t)$
$\tilde{P}_{nsv}(f)$	Noise spectrum of $SV(t)$
$\tilde{P}_{nsh}(f)$	Noise spectrum of $SH(t)$
R_{ij}	Spectral ration between two phases i and j

(Other symbols are introduced in the text, as required.)

Appendix D

Abbreviations

Abbreviation	Meaning
ak135	Global average velocity model
pkq	Previous velocity model for northern Australia
sk14	Previous velocity model for Australian region
ANU	Australian National University
RSES	Research School of Earth Sciences, ANU
OPRS	Overseas Postgraduate Scolarship
az0sl1	velocity model for sl1 in azimuth 0
az0sl2	velocity model for sl2 in azimuth 0
az0sl3	velocity model for sl3 in azimuth 0
az0sl4	velocity model for sl4 in azimuth 0
az20sl1	velocity model for sl1 in azimuth 20
az20sl2	velocity model for sl2 in azimuth 20
az20sl3	velocity model for sl3 in azimuth 20
az40sl2	velocity model for sl2 in azimuth 40
az60sl3	velocity model for sl1 in azimuth 60
az80sl2	velocity model for sl2 in azimuth 80
az-20sl1	velocity model for sl1 in azimuth -20
az-20sl2	velocity model for sl2 in azimuth -20
az-40sl2	velocity model for sl2 in azimuth -40
az-60sl3	velocity model for sl1 in azimuth -60
az-80sl2	velocity model for sl2 in azimuth -80
Guralp CMG3	Guralp seismometer

Appendix D

Abbreviations

Abbreviation	Meaning
ak135	Global average velocity model
pkq	Previous velocity model for northern Australia
sk14	Previous velocity model for Australian region
ANU	Australian National University
RSES	Research School of Earth Sciences, ANU
OPRS	Overseas Postgraduate Scolarship
az0sl1	velocity model for sl1 in azimuth 0
az0sl2	velocity model for sl2 in azimuth 0
az0sl3	velocity model for sl3 in azimuth 0
az0sl4	velocity model for sl4 in azimuth 0
az20sl1	velocity model for sl1 in azimuth 20
az20sl2	velocity model for sl2 in azimuth 20
az20sl3	velocity model for sl3 in azimuth 20
az40sl2	velocity model for sl2 in azimuth 40
az60sl3	velocity model for sl1 in azimuth 60
az80sl2	velocity model for sl2 in azimuth 80
az-20sl1	velocity model for sl1 in azimuth -20
az-20sl2	velocity model for sl2 in azimuth -20
az-40sl2	velocity model for sl2 in azimuth -40
az-60sl3	velocity model for sl1 in azimuth -60
az-80sl2	velocity model for sl2 in azimuth -80
Guralp CMG3	Guralp seismometer

Abbreviation	Meaning
KIMBA	Potable Digital Broadband Seismic Observation Projects deployed in Kimberly region of Northwestern Australia in 1997-1998
SKIPPY	Potable Digital Broadband Seismic Observation Projects deployed during 1993-1996 covering Australian continent
sl1	SKIPPY data group in slice of Coral Sea area
sl2	SKIPPY data group in slice of Eastern Australia: from Gulf of Carpentaria to south
sl3	SKIPPY data group in slice from Central to western Australia
sl4	SKIPPY data group in slice of Western Australia
NA	Nonlinear geophysical inversion method using a Neighborhood Algorithm

References

Aki, K., 1967, Scaling law of seismic spectrum, *J. Geophys. Res.*, **72**, 1217–1231.

Aki, K., 1980a, Attenuation of shear waves in the lithosphere for frequencies from 0.05 - 25 hz., *Phys. Earth Planet. Inter.*, **21**, 50–60.

Aki, K., 1980b, Scattering and attenuation in the lithosphere., *J. Geophys. Res.*, **85**, 6496–6504.

Anderson, D. L., 1967, The anelasticity of the mantle, *Geophys. J. R. Astron Soc.*, **14**, 135–164.

Anderson, D. L., 1989, *Theory of the Earth*, Blackwell Scientific Publications, Boston, MA, 4th ed.

Anderson, D. L. and Archambeau, C. B., 1964, The anelasticity of the earth, *J. Geophys. Res.*, **69**, 2071–2085.

Anderson, D. L. and Given, J. W., 1982, Absorption band Q model for the earth, *J. Geophys. Res.*, **87**, 3893–3904.

Anderson, D. L. and Hart, R. S., 1978a, Attenuation model of the Earth, *Phys. Earth Planet. Inter.*, **16**, 289–306.

Anderson, D. L. and Hart, R. S., 1978b, Q of the Earth, *J. Geophys. Res.*, **83**, 5869–5882.

Anderson, D. L. and Minster, J. B., 1979, The frequency dependence of Q in the earth and implications for mantle rheology and chandler wobble, *Geophys. J. R. Astron Soc.*, **58**, 431–440.

Bahttacharyya, J., 1998, Comparison between time-domain and frequency-domain measurement techniques for mantle shear-wave attenuation, *Pure appl. geophys.*, **153**, 399–418.

Bahttacharyya, J., Masters, G. and Shearer, P., 1996, Global lateral variations of shear wave attenuation in the upper mantle, *J. Geophys. Res.*, **101**, 22,273–22,289.

Baqer, S. and Mitchell, B. J., 1998, Regional variation of L_g coda Q in the continental united states and its relation to crustal evolution, *Pure appl. geophys.*, **153**, 587–612.

Båth, M., 1984, *Spectral Analysis in Geophysics*, Elasevier Scientific Publishing Company, Amsterdam, Oxford, New York, 1st ed.

Berckhemer, H., Kampfmann, W., Aulbach, E. and Aulbach, H., 1982, Shear modulus and Q of fosterite and dunite near partial melting from forced oscillation experiments, *Phys. Earth Planet. Inter.*, **29**, 30–41.

Bijwaard, H., Spakman, W. and Engdahl, E. R., 1998, Closing the gap between regional and global travel time tomography, *J. Geophys. Res.*, **103**, 30055–30078.

Bock, G., 1991, Long-period S to P converted waves and the onset of partial melting beneath Oahu, hawaii., *Geophys. J. Int.*, 869–872.

Bowman, J. R. and Kennett, B. L. N., 1990, An investigation of the upper mantle beneath northwestern australia using a hybrid seismic array, *Geophys. J. Int.*, **101**, 411–424.

Bowman, J. R. and Kennett, B. L. N., 1991, Propagation of l_g waves in the northern Australian craton: inflence of crustal velocity gradients, *Bull. Seism. Soc. Am.*, **81**, 592–610.

Bowman, J. R. and Kennett, B. L. N., 1993, An investigation of the upper mantle beneath northwestern australia using a hybrid seismic array, *Bull. Seism. Soc. Am.*, **83**, 25–434.

Bulland, R., 1989, The mechanics of locating earthquakes., *Bull. seism. Soc. Am.*, **66**, 173–187.

Bussy, M., Montagner, J.-P. and Romanowicz, B., 1993, Tomographic study of upper mantle attenuation in the Pacific Ocean, *Geophys. Res. Let.*, **20**, 663–666.

Chavez, D. E. and Priestley, K. F., 1986, Measurement of frequency dependent Lg attenuation in the Great Basin., *Geophys. Res. Lett.*, **13**, 551–554.

Clawson, S. R., Smith, R. B. and Benz, H. M., 1989, P-wave attenuation of Yellowstone caldera from three-dimensional inversion of spectral decay using explosion source seismic data, *Geophys. Res. Let.*, **94**, 7205–7222.

Clements, J. R., 1982, Intrinsic Q and its frequency dependence, *Phys. Earth Planet. Inter.*, **27**, 286–299.

Clitheroe, G., Gudmundsson, O. and Kennett, B. L. N., 2000, The crustal thickness of australia, *J. Geophys. Res.*, **105**, 13697–13713.

Cong, L. and Mitchell, B. J., 1998a, L_g coda Q and its relation to the geology and techtonics of the Middle East, *Pure appl. geophys.*, **153**, 587–612.

Cong, L. and Mitchell, B. J., 1998b, Surface velocity and Q structure of the middle eastern crust and upper mantle from surface-wave dispersion and attenuation, *Pure appl. geophys.*, **153**, 503–538.

de Lorenzo, S., 1998, A model to study the bias on Q estimates obtained by applying the rise time method to earthquake data, *Pure appl. geophys.*, **153**, 419–440.

de Souza, J. L. and Mitchell, B. J., 1998, L_g coda Q variations across south Amrica and their relation to crustal evolution of continents, *Pure appl. geophys.*, **153**, 587–612.

Debayle, E. and Kennett, B. L. N., 2000, The Australian continental upper mantle: structure and deformation inferred from surface waves., in press.

Der, Z. A., 1998, High-frequency P- and S- wave attenuation in the Earth, *Pure appl. geophys.*, **153**, 273–310.

Der, Z. A., Lees, A. C. and Cormier, V. F., 1986, Frequency dependence of Q in the mantle underlying the shield areas of Eurasia, part III: The Q model, *Geophys. J. R. Astron. Soc.*, **87**, 1,103–1,112.

Der, Z. A., McElfresh, T. W. and O'Donnell, 1982, An investigation of the regional variation and frequency dependence of anelastic attenuation in the mantle under the United States in the 0.5-4 hz band, *Geophys. J. R. Astron. Soc.*, **69**, 67–99.

Dey, S. C., Kennett, B. L. N., Bowman, J. R. and Goody, A., 1993, Variations in upper mantle structure under northern Australia, *Geophys. J. Int.*, **114**, 304–310.

Douglas, A., 1992, Q for short-period *P*-waves: is it frequency dependent?, *Geophys. J. Int.*, **108**, 110–124.

Dziewonski, A. M., 1979, Elastic and anelastic structure of the Earth, *Rev. Geophys. Space Phys.*, **17**, 303–312.

Dziewonski, A. M. and Steim, J., 1983, Dispersion and attenuation of mantle waves from waveform inversion, *Geophys. J. R. astr. Soc.*, **70**, 503–527.

Engdahl, E. R., van der Hilst, R. and Bulland, R., 1998, Global teleseismic earthquake relocation with improved travel times and procedures for depth determination., *Bull. Seis. Soc. Am.*, **88**, 722–743.

Evans, J. R., 1993, Active source, high-resolution (NeHT) tomography: velocity and Q, in H. M. Iyer and K. Hirahara, eds., *Seismic Tomography Theory and Practice*, chap. 1, 92–132, Chapman and Hall, London.

Farmer, C., 2000, *Earthquake Location by Using NA*, Research School of Earth Sciences, Australian National University, Canberra, Honours Thesis.

Flanagan, M. P. and Wiens, D. A., 1998, Attenuation of broadband P and S waves in tonga: Observation of frequency dependence Q, *Pure appl. geophys.*, **153**, 345–376.

Fleitout, L. and Yuen, D. A., 1984, Secondary convection and the growth of the oceanic lithosphere., *Phys. Earth Plannet. Inter.*, **36**, 181–212.

Goes, S., Govers, R. and Vacher, P. J., 2000, Shallow mantle temperature under europe from P and S wave tomography, *J. Geophys. Res.*, **105**, 11153–11169.

Gordon, R. B. and Nelson, C., 1966, Anelastic properties of the earth, *Rev. Geophys.*, **4**, 457–477.

Gribb, T. T. and Cooper, R. F., 1998a, A high temperatur torsion apparatus for the high-resolution characterization of internal friction and creep in refractory metals and ceramics: Application to the seismic-frequency, dynamic response of Earth's upper mantle, *Rev. Sci. Instrum.*, **69**, 559–564.

Gribb, T. T. and Cooper, R. F., 1998b, Low-frequency shear attenuation in polycrustalline olivine: Grain boundary diffusion and the and the physical significance of the andrade model for viscoelastic rheology, *J. Geophys. Res.*, **103**, 27267–27279.

Gudmundsson, O., Kennett, B. L. N. and Goody, A., 1994, Broadband observations of upper-mantle seismic phases in northern Australia and the attenuation structure in the upper mantle, *Phys. Earth Planet. Inter.*, **84**, 207–226.

Gueguen, Y., Darot, M., Mazot, P. M. and Woirgard, J., 1989, Q^{-1} of fosterite single crystals, *Phys. Earth Planet. Inter.*, **55**, 254–258.

Gueguen, Y., Woirgard, J. and Darot, M., 1981, Attenuation mechanisms and anelasticity in the upper mantle, in F. D. Stacey, M. S. Paterson and A. Nicholas, eds., *Anelasticity in the Earth*, 86–94, Am. Geophys. Union, Washington, D.C.

Gupta, S. C., Teotia, S. S., Rai, S. S. and Gautam, N., 1998, Coda Q estimation in the Koyna region, india, *Pure appl. geophys.*, **153**, 713–731.

Halderman, T. P. and Davis, P. M., 1991, Q_p beneath the Rio Grande and East African rift zones., *J. Geophys. Res.*, **96**, 10,113–10128.

Hanks, T. C., 1981, The corner frequency shift, earthquake source models, and Q, *Bull. Seismol. Soc. Am.*, **71**, 597–612.

Hashida, T. and Shimazaki, K., 1987, Determination of seismic attenuation structure and source strength by inversion of seismic intensity data: Tohoku district, northeastern Japan arc., *J. Phys. Earth*, **35**, 62–92.

Hudson, J. A., 1980, *The Excitation and Propagation of Elastic Waves*, Cambridge University Press, Cambridge, UK.

Humphreys, E. D. and Hager, B. H., 1990, A kinematic model for the late Cenozoic development of southern California crust and upper mantle., *J. Geophy. Res.*, **95**, 19747–19762.

Jackson, D. D. and Anderson, D. L., 1970, Physical mechanisms of seismic-wave attenuation., *Rev. Geophys. Space Phys.*, **8**, 1–63.

Jackson, I., 1991, The petrophysical basis for the interpretation of seismological models for the continental lithosphere, *Geological Society of Australia, Special Publication*, **17**, 81–114.

Jackson, I., 1993, Progress in the experimental study of seismic wave attenuation, *Ann Rev Earth Planet Sci*, **21**, 375–406.

Jackson, I., 2000, Laboratory measurement of seismic wave dispersion and attenuation: Recent progress, in S. I. Karato, A. M. Forte, R. C. Liebermann, G. Masters and L. Stixrude, eds., *Earth's Deep Interior: Mineral Physics and Tomography From the Atomic to the Global Scale*, vol. 117 of *AGU Geophysical Monograph Series,*, 265–289, American Geophysical Union, Washington, D C.

Jackson, I., Gerald, J. D., Faul, U. H. and Tan, B. H., 2000, Seismic wave attenuation in olivine: quantification of grainsize sensitivity and the influence of partial melting., *Fall AGU*.

Jackson, I. and Paterson, 1987, Shear modulus and internal friction of calcite rocks at seismic frequencies: pressure, frequency, and grain size dependence, *Phys. Earth Planet. Inter.*, **45**, 349–367.

Jackson, I., Paterson, M. S. and Fitz Gerald, J. D., 1992, Seismic wave dispersion and attenuation in åheim dunite: an experimental study, *Geophys. J. Int.*, **108**, 517–534.

Jackson, I., Paterson, M. S., Niesler, H. and Waterford, R. M., 1984, Rock anelasticity measurements at high pressure, low strain amplitude and seismic frequency, *Geophys. Res. Lett.*, **11**, 1235–1238.

Jepsen, D. C. and Kennett, B. L. N., 1990, Three-component analysis of regional seismograms, *Bull. Seism. Soc. Am.*, **80**, 2032–2052.

Johnston, D. H. and Töksoz, M. N., 1981, Definition and Terminology, in M. N. Töksoz and D. H. Johnston, eds., *Seismic Wave Attenuation*, No.2 Geophysics reprint series, chap. 1, 1–5, Society of Exploration Geophysicists, Oklahoma.

Jordan, T. H. and Sverdrup, K. A., 1981, Teleseismic location techniques and their application to earthquake clusters in the south-central pacific., *Bull. seism. Soc. Am.*, **71**, 1105–1130.

Kaiho, Y. and Kennett, B. L. N., 2000, Three-dimensional seismic structure beneath the australian region from refracted wave observations, *Geophys. J. Int.*, **142**, 651–668.

Kampfmann, W. and Berckhemer, H., 1985, High temperature experiments on the elastic and anelastic behavior of magmatic rocks, *Phys. Earth Planet. Inter.*, **40**, 223–247.

Kanamori, H., 1967, Spectrum of short-period core phases in relation to the attenuation in the mantle., *J. Geophys. Res.*, **72**, 2181–2186.

Kanamori, H. and Anderson, D. L., 1977, Importance of physical dispersion in surface wave and free oscillation problems: Review, *Review of geophysics and space physics*, **15**, 105–112.

Karato, S. I., 1998, A dislocation model of seismic wave attenuation and micro-creep in the earth: Harold jeffreys and the rheology of the solid earth, *Pure appl. geophys.*, **153**, 239–256.

Karato, S. I. and Spetzler, H. A., 1990, Defect microdynamics in minerals and solid-state mechanisms of seismic wave attenuation and velocity dispersion in the mantle, *Review of geophysics*, **28**, 399–421.

Karato, S. I., Zhang, S. and Wenk, H. R., 1995, Superplasticity in earth's lower mantle; evidence from seismic anisotropy and rock physics., *Science*, **270**, 458–461.

Kennett, B. L. N., 1975, The effects of attenuation on seismograms, *Bull. Seism. Soc. Am.*, **65**, 1643–1651.

Kennett, B. L. N., 1983, *Seismic Wave Propagation in Stratified Media*, Cambridge University Press.

Kennett, B. L. N., 1991a, *IASPEI 1991 Seismological Tables*, Research School of Earth Sciences, Australian National University.

Kennett, B. L. N., 1991b, The removal of free surface interactions from three-component seismograms, *Geophys. J. Int.*, **104**, 153–163.

Kennett, B. L. N., 1991c, Seismic velocity gradients in the upper mantle, *Geophys. Res. Lett.*, **18**, 1115–1118.

Kennett, B. L. N., 1993, Seismic structure and heterogeneity in the upper mantle, in K. Aki and R. Dmowska, eds., *Relating Geophysical Structure and Progresses, The Jeffreys Volume*, Geophysical Monograph 76, IUGG Volume 16, chap. 6, 53–66, IUGG & AGU, Washington,DC.

Kennett, B. L. N., 1994, Representations of the seismic wavefield, *Geophys. J. Int.*, **118**, 344–357.

Kennett, B. L. N., 1997, The upper mantle beneath Australia, *AGSO Journal of Australian Geology and Geophysics*, **17**, 49–54.

Kennett, B. L. N., 1998, *Seismic Wave Propagation and Seismic Tomography*, Research School of Earth Sciences, The Australian National University.

Kennett, B. L. N. and Bowman, J. R., 1990, The velocity structure and heterogeneity of the mantle, *Phys. Earth. Planet. Inter.*, **59**, 429–465.

Kennett, B. L. N., Engdahl, E. R. and Bulland, R., 1995, Constraints on seismic velocities in the Earth from traveltimes, *Geophys. J. Int.*, **122**, 108–124.

Kennett, B. L. N., Gudmundsson, O. and Tong, C., 1994, The upper mantle S and P velocity structure beneath northern australia from broadband observations., *Phys. Earth. Planet. Inter.*, **86**, 85–98.

Kennett, B. L. N. and Nolet, G., 1990, The interaction of the *S* wavefield with upper mantle heterogeneity, *Geophys. J. Int.*, **101**, 751–762.

Kennett, B. L. N. and van der Hilst, R., 1998, Seismic structure of the mantle: subduction zone to craton, in I. Jackson, ed., *The Earth's Mantle : Composition, Structure, and Evolution*, chap. 8, 381–404, Cambridge University Press, Casmbridge.

Lay, T. and Helmberger, D. V., 1981, Body wave amplitude patterns and upper mantle attenuation variations across north america, *Geophys. J. R. Astr. Soc.*, **66**, 691–731.

Lay, T. and Wallace, T. C., 1995, *Modern Global Seismology*, Academic Press, San Diego,CA, 1st ed.

Leblanc, G. S. J., 1967, Truncated crustal transfer function and fine structure of determination., *Bull. Seismol. Soc. Am.*, **57**, 719–733.

Li, X.-D. and Romanowicz, B., 1991, Global mantle model developed using nonlinear asymptotic coupling theory, *J. Geophys. Res.*, **101**, 22,245–22,272.

Liu, H. P., Anderson, D. L. and Kanamori, H., 1976, Velocity dispersion due to anelasticity: Implications for seismology and mantle composition, *Geophys. J. R. Astron. Soc.*, **47**, 41–58.

Lu, C. and Jackson, I., 1998, Seismic-frequency laboratory measurements of shear mode viscoelasticity in crustal rocks II: thermally stressed Quartzite and Granite, *Pure appl. geophys.*, **153**, 441–474.

Madariaga, R., 1976, Dynamics of an expanding circular fault., *Bull. Seismol. Soc. Am.*, **66**, 639–666.

Mamada, Y. and Takenaka, H., 2000, S-wave attenuation in the focal regional of the 1997 northwestern Kagoshima earthquake, Japan, *EOS, Transactions, American Geophysical Union 2000 Spring Meeting*, **81**, S307, published as a supplement to EOS, May 9, 2000.

Marquering, H. and Snieder, R., 1996, Shear-wave velocity structure beneath europe, the northeastern atlantic and western asia from waveform inversions including surface-wave mode coupling., *Geophys. J. Int.*, **124**, 283–304.

Martynov, V. G., Vernon, F. L., Mellors, R. J. and Pavlis, G. L., 1999, High-frequency attenuation in the crust and upper mantle of the northern Tien Shan, *Bull. Seism. Soc. Am.*, **89**, 215–238.

Masters, G. and Gilbert, F., 1983, Attenuation in the earth at low frequencies, *Philos. Trans. R. Soc. London, Ser. A*, **308**, 479–522.

Mills, J., 1977, *Rayleigh wave group velocities and attenuation coefficients*, Ph.D. thesis, Australian National University, Canberra.

Minster, J., 1981, Anelasticity and attenuation, in A. Dziewonski and E. Boschi, eds., *Physics of the Earth's interior*, 152–212, North-Holland, Amsterdam.

Minster, J. B. and Anderson, D. L., 1981, A model for dislocation-controlled rheology for the mantle, *Phil. Trans. Roy. Soc. London*, **299**, 319–356.

Mitchell, B. J. and Cong, L., 1998a, L_g coda Q and its relation to the structure and evolution of continents: a global perspective, *Pure appl. geophys.*, **153**, 639–654.

Mitchell, B. J. and Cong, L., 1998b, L_g coda Q in australia and its relation to crustal structure and evolution of continents, *Pure appl. geophys.*, **153**, 655–664.

Morozov, I. B., Morozova, E. A., Smithson, S. B. and Solodilov, L. N., 1998, 2-D image of seismic attenuation beneath the deep seismic sourding profile "Quartz," Russia, *Pure appl. geophys.*, **153**, 311–344.

Myers, J S Shaw, R. D. and Tyler, I. M., 1996, Tectonic evolution of proterozoic australia, *Tectonics*, **15**, 1431–1446.

Nakanishi, I., 1993, Surface wave tomography: velocity and Q, in H. Iyer and K. Hirahara, eds., *Seismic Tomography Theory and Practice*, 92–132, Chapman & Hall, London.

Nakanishi, I. and Anderson, D. L., 1984, Measurement of mantle wave velocities and inversion for lateral heterogeneity and anisotropy–ii. analysis by the single-station method., *Geophys. J. R. Astron. Soc.*, **78**, 573–617.

Parker, R. L., 1994, *Geophysical Inverse Theory*, Princeton Univ. Press, Princeton.

Press, W. H., Teukolsky, S. A., Vetterling, W. T. and Flannery, B. P., 1995, *Numerical Recipes in C*, Cambridge University Press, Cambridge.

Priestley, K., Qiu, X. and McKenzie, D. P., 1997, The lithospheric structure of southern africa, *Terra Abstracts*, **9(1)**, 84, a.99 (XQ, DPMcK, KP).

Priestley, K. F., 1988, Anelastic attenuation of the upper mantle beneath eastern Kazakh, U.S.S.R. in the 0.5 to 8.0 Hz band., *Seismological Research Letters.*, **59**, 45.

Priestley, K. F. and Chavez, D. E., 1985, Lg attenuation in the Basin and Range Province., *Earthquake Notes.*, **55**, 25.

Richards, P. G. and Menke, W., 1983, The apparent attenuation of a scattering medium, *Bull. Seismol. Soc. Am.*, **73**, 1005–1022.

Roecker, S. W., Tucker, B., King, J. and Hatzfeld, D., 1982, Estimates of Q in Central Asia as a function of frequency and depth using the coda of locally recorded earthquakes., *Bull. Seismol. Soc. Am.*, **72**, 129–150.

Romanowicz, B., 1995, A global tomographic model of shear attenuation in the upper mantle, *J. Geophys. Res.*, **100**, 12375–12394.

Romanowicz, B., 1998, Attenuation tomography of the Earth's mantle: A review of current status, *Pure appl. geophys.*, **153**, 257–272.

Romanowicz, B. and Durek, J. J., 2000, Seismological constraints on attenuation in the Earth: A review, in S. I. Karato, A. M. Forte, R. C. Liebermann, G. Masters and L. Stixrude, eds., *Earth's Deep Interior: Mineral Physics and Tomography From the Atomic to the Global Scale*, vol. 117 of *AGU Geophysical Monograph Series*, 161–179, American Geophysical Union.

Romanowicz, B., Roult, G. and Kohl, T., 1987, The upper mantle degree two pattern: constraints from Geoscope fundamental spheroidal model eigenfrequency and attenuation measurements, *Geophys. Res. Lett.*, **14**, 1219–1222.

Roth, E. D., Wiens, D. A., Dorman, L., Hildebrand, J. and Webb, S. C., 1999, Seismic attenuation tomography of the tonga-fiji region using phase pair methods., *J. Geophys. Res.*, **104**, 4795–4809.

Roth, E. D., Wiens, D. A. and Zhao, D., 2000, An empirical relationship between seismic attenuation and velocity anomalies in the upper mantle, *Geophys. Res. Lett.*, **27**, 601–604.

Roult, G., Romanowicz, B. and Montagner, J. P., 1990, 3-D upper mantle shear velocity and attenuation from fundamental mode free oscillation data, *Geophys. J. Int.*, **101**, 61–80.

Sailor, R. and Dziewonski, A., 1978, Measurements and interpretation of normal mode attenuation, *Geophys. J. R. Astron. Soc.*, **53**, 559–574.

Sambridge, M., 1988, *Seismic inversion for earthquake location and 3-D velocity structure*, Ph.D. thesis, Australian National University, Canberra.

Sambridge, M. and Gallagher, K., 1993, Earthquake hypocenter location using genetic algorithms, *Bull. Seism. Soc. Am.*, **83**, 1467–1491.

Sambridge, M. S., 1999a, Geophysical inversion with a neighbourhood algorithm -I. Searching a parameter space, *Geophys. J. Int.*, **138**, 479–494.

Sambridge, M. S., 1999b, Geophysical inversion with a neighbourhood algorithm -II. Searching a parameter space, *Geophys. J. Int.*, **138**, 727–746.

Sambridge, M. S. and Kennett, B. L. N., 1986, A novel method of hypocentre location., *J. R. astr. Soc.*, **87**, 679–697.

Sanders, C., 1993, Local earthquake tomography: attenuation - theory and results, in H. Iyer and K. Hirahara, eds., *Seismic Tomography Theory and Practice*, 92–132, Chapman & Hall, London.

Sarker, G. and Abers, G. A., 1998, Comparison of seismic body wave and coda wave measures of Q, *Pure appl. geophys.*, **153**, 665–684.

Sato, H., 1995, Laboratory seismic studies: A search for mechanical, thermal and chemical structures of the earth, *J. Phys. Earth*, **43**, 421–455.

Sato, H. and Feher, M. C., 1998, *Seismic Wave Propagation and Scattering in the Heterogeneous Earth*, Springer-Verlag, New York.

Sato, H., Muro, K. and Hasegawa, A., 1998, Three-dimensional mapping of magma source and transport regions from seismic data: the mantle wedge beneath northeastern Jpan, *Pure appl. geophys.*, **153**, 377–398.

Sato, H. and Sacks, I. S., 1989, Anelasticity and thermal structure of the oceanic upper mantle: temperature calibration with heat flow data, *J. Geophys. Res.*, **94**, 5,705–5,715.

Sato, H., Sacks, I. S., Murase, T., E, M. G. and Fukoyama, H., 1989, Q_p-melting temperature relation in peridotite at high pressure and temperature: attenuation mechanism and implications for the mechanical properties of the upper mantle, *J. Geophys. Res.*, **94**, 10,647–10,661.

Sato, R., 1967, Attenuation of seismic waves, *J. Phys. Earth*, **15**, 32–61.

Sen, M. and Stoffa, P. L., 1995, *Global Optimization Methods in Geophysical Inversion*, vol. 4 of *Advances in Exploration Geophysics*, Elsevier, Amsterdam.

Sharrock, D. S., 1995, A two-layer attenuation model for the upper mantle at short periods, *Geophys. Res. Lett.*, **22**, 2,561–2,564.

Sharrock, D. S., Main, I. G. and Douglas, A., 1995, Observations of Q from the northwest Pacific subduction zone recorded at teleseismic distances, *Bull. Seismol. Soc. Am.*, **85**, 237–253.

Shearer, P. M., 1999, *Introduction to Seismology*, University of Cambridge Press, Cambridge.

Sheehan, A. F. and Solomon, S. C., 1988, Joint inversion of shear wave travel time residuals and geoid and depth anomalies for long-wavelength variation in upper mantle temperature and composition along the Mid-Atlantic ridge., *J. Geophys. Res.*, **96**, 19981–20009.

Shimshoni, M., 1970, Computation of the divergence coefficient for seismic phases., *Geophys. J. R. Astron. Soc.*, **21**, 285–294.

Sipkin, S. A. and Jordan, T. H., 1979, Frequency dependence of Q_{ScS}, *Bull. Seismol. Soc. Am.*, **69**, 1,055–1,079.

Smith, S., 1972, The anelasticity of the mantle, *Tectonics*, **13**, 601–622.

Solomon, S. C. and Töksoz, M. N., 1970, Lateral variation of attenuation of P and S waves beneath the United States., *Bull. Seismol. Soc. Am.*, **60**, 819–838.

Suda, N., Shibata, N. and Fukao, Y., 1991, Degree-2 pattern in the upper mantle from apparent complex frequency measurements of fundamental spheroidal modes, *Geophys. Res. Lett.*, **18**, 1119–1222.

Takano, K., 1971, A note on the attenuation of short-period *P*- and *S*-waves in the mantle, *J. Phys. Earth,*, **19**, 155–163.

Tan, B. H., Jackson, I. and Fitz Gerald, J. D., 1997, Grainsize dependence of solid state viscoelasticity in olivine aggregates, *EOS (Trans. Am. Geophys. Union)*, **78**, F466.

Tan, B. H., Jackson, I. and Fitz Gerald, J. D., 2000, High-temperature viscoelasticity of fine-grained polycrystalline olivine., *Phys. Chem. Minerals*, submitted.

Tanimoto, T. and Zhang, Y. S., 1990, Lithospheric thickness and thermal anomalies in the upper mantle inferred from the Love wave data., *Geophys. Res. Lett.*, **17**, 2405–2408.

Taylor, S. R., Bonner, B. B. and Zandt, G., 1986, Attenuation and scattering of broadband *P* and *S* waves across North America, *J. Geophys. Res.*, **91**, 7,309–7,325.

Teng, T. L., 1968, Attenuation of body waves and the *Q* structure of the mantle, *J. Geophys. Res.*, **73**, 2,195–2,208.

Teng, T. L. and Ben-Menahem, A., 1965, Attenuation of body waves and the *Q* structure of the mantle, *J. Geophys. Res.*, **73**, 2,195–2,208.

Tilmann, F. J., McKenzie, D. and Priestley, K. F., 1998, P and S wave scattering from mantle plumes., *J. Geophys. Res.*, **103**, 21,145–21,143.

Titchmarsh, E. C., 1937, *An Introduction to the Theory of Fourier Integrals*, Oxford University Press, Oxford, UK.

Tong, C., Gudmundsson, O. and Kennett, B. L. N., 1994, Shear wave splitting in refracted waves returned from the upper mantle transition zone beneath northern Australia, *J. Geophys. Res.*, **99**, 15783–15797.

Tselentis, G. A., 1998, Intrinsic and scattering seismic attenuation in W. Greece, *Pure appl. geophys.*, **153**, 703–712.

Ugalde, A., Pujades, L. G., Canas, J. A. and Villaseñor, 1998, Estimation of the intrinsic absorption and scattering attenuation in Northeastern Venezuela (Southeastern Caribbean) using coda waves, *Pure appl. geophys.*, **153**, 685–702.

Ulug, A. and Berckhemer, H., 1984, Frequency dependence of *Q* for seismic body waves in the earth's mantle, *Journal of Geophysics*, **56**, 9–19.

van der Hilst, R. D., Kennett, B. L. N., Christie, D. and Grant, J., 1994, Mobile broad-band arrays to study the seismic structure of the lithosphere and mantle beneath australia, *EOS Transactions of the American Geophysical Union*, **75**, 170 & 180,181.

van der Hilst, R. D., Kennett, B. L. N. and Shibutani, T., 1998, Upper-mantle structure beneath australia from portable array deployment, in J. Braun, J. Dooley, B. Goleby, R. van der Hilst and C. Klootwijk, eds., *Structure and Evolution of the Australian Continent*, vol. 26 of *AGU Geodynamics Series*, 39–57, American Geophysical Union, Washington D C.

van der Hilst, R. D., Widiyantoro, S. and Engdahl, E. R., 1997, Evidence for deep mantle circulation from global tomography, *Nature*, **386**, 578–584.

van der Hilst, R. D., Zielhuis, A., Weeks, J. and Kennett, B. L. N., 1995, The SKIPPY project, *Annual Report for 1994, Research School of Earth Sciences, Australian National University*, 23–25.

van der Lee, S. and Nolet, G., 1997, Upper-mantle S velocity structure of North America, *J. Geophys. Res.*, **102**, 22 815–22 838.

Veevers, J. J., 1984, *Phanerozoic Earth Hoistory of Australia*, Oxford geological sciences series; 2, Oxford University Press, Oxford, UK.

Ward, R. W. and Young, C.-Y., 1980, Mapping seismic attenuation within geothermal systems using teleseisms with application to the geysers-clear lake region, *J. Geophys. Res.*, **85**, 5,227–5,236.

Wessel, P. and Smith, W. H. F., 1991, Free software helps map and display data, *EOS*, **72**, 441.

Wessel, P. and Smith, W. H. F., 1995, New version of the Generic Mapping Tools released, *EOS*, **76**, 329.

Widmer, R., Masters, G. and Gilbert, F., 1991, Spherically symmetric attenuation within the earth from normal mode data, *Geophys. J. Int.*, **104**, 541–553.

Woodward, R. L. and Masters, G., 1991a, Global upper mantle structure from long-period differential travel times, *J. Geophys. Res.*, **96**, 6,351–6,377.

Woodward, R. L. and Masters, G., 1991b, Upper mantle structure from long-period differential traveltime and free oscillation data, *J. Geophys. Res.*, **109**, 275–293.

Wu, R. S. and Aki, K., 1985, Multiple scattering and energy transfer of seismic waves - separation of scattering effect from intrinsic attenuation, ii, theory modelling., *Geophys. J. R. Astron. Soc.*, **82**, 57–80.

Wu, R. S. and Aki, K., 1988a, Multiple scattering and energy transfer of seismic waves - Separation of scattering effect from intrinsic attenuation, II, application of the theory to Hindu Kush region., *Pure appl. geophys.*, **128**, 49–80.

Wu, R. S. and Aki, K., eds., 1988b, *Scattering and attenuation of seismic waves.*, vol. 128 of *Pure appl. geophys.*, Birkhaeuser Verlag., Basel, Switzerland.

Wu, R. S. and Aki, K., eds., 1989, *Scattering and attenuation of seismic waves.*, vol. 131 of *Pure appl. geophys.*, Birkhaeuser Verlag., Basel, Switzerland.

Wu, R. S. and Aki, K., eds., 1990, *Scattering and attenuation of seismic waves.*, vol. 132 of *Pure appl. geophys.*, Birkhaeuser Verlag., Basel, Switzerland.

Yomogida, K. and Aki, K., 1987, Amplitude and phase data inversions for phase velocity anomalies in the Pacific Ocean basin., *Geophys. J. R. Astron. Soc.*, **88**, 161–204.

Yoshimoto, K., Sato, H., Iio, Y., Ito, H., Ohminato, T. and Ohtake, M., 1998, Frequency-dependent attenuation of high-frequency P and S waves in the upper crust in Western Nagano Japan, *Pure appl. geophys.*, **153**, 489–502.

Yoshimoto, K. and Wu, R.-S., 2000, Scattering and intrinsic attenuation of high-frequency seismic waves in southern California, *EOS, Transactions, American Geophysical Union 2000 Spring Meeting*, **81**, S307, published as a supplement to EOS, May 9, 2000.

Zielhuis, A. and Nolet, G., 1994, Shear-wave velocity variations in the upper mantle beneath central Europe, *Geophys. J. Int.*, **117**, 695–715.

Zielhuis, A. and van der Hilst, R. D., 1996, Upper-mantle shear velocity beneath eastern Australia from inversion of waveforms from SKIPPY portable arrays, *Geophys. J. Int.*, **127**, 1–17.

Appendix C

Additional material to meet the points raised by the thesis examiners

C.1 Frequency dependent spectral ratio measurement techniques

In (5.3), the transfer function $A^i_{CR}(f)$ should be termed the receiver response rather than the crustal response, because the crustal component is absorbed into the element representing the effect of the propagation path.

The simplest situation arises when Q can be assumed to be independent of f over some frequency band. I am then able to use a spectral ratio approach to estimate the differential attenuation between P and S waves. For the mantle and crust component I can make a ray theoretical development with a phase delay through the mantle and an attenuation factor (Gudmundsson et al, 1994)

$$A^i_{MC} = \exp\left\{\mathrm{i}2\pi f\tau_i(p_i) - \mathrm{i}\varphi_i(p_i)\right\}\exp\left[-\pi f t^*_i(p_i)\right], \tag{C.1}$$

The phase delay $\tau_i(p_i)$ is the ray integral

$$\tau_i(p_i) = \int_{ray_i}\frac{\mathrm{d}s}{V_i(\mathbf{r})}, \tag{C.2}$$

in terms of the appropriate ray speed v_i for the segments of the path. The phase shift $\varphi_i(p_i)$ will be $-\pi/2$ for a turning ray but will have a more complex form for a post-critical reflection. The summary attenuation parameter $t^*_i(p_i)$ is also a ray integral,

$$t^*_i(p_i) = \int_{ray_i}\frac{\mathrm{d}s}{Q_i(\mathbf{r})V_i(\mathbf{r})}. \tag{C.3}$$

In a stratified medium the ray parameter p_i will be a constant along the ray path and the integrals in (C.2), (C.3) will take the form of layer sums.

Consider then the spectral ratio between two body-wave phases i and j, which can be represented in the form

$$R_{ij}(f) = \frac{A_S^i(f)A_I^i(f)A_R^i(f)A_M^i(f)A_G^i(p_i,\xi_i)A_P^i(p_i,\xi_i)}{A_S^j(f)A_I^j(f)A_R^j(f)A_M^j(f)A_G^j(p_i,\xi_i)A_P^j(p_i,\xi_i)}. \tag{C.4}$$

The spectral ratio can be recast into a form which isolates the mantle dependence on attenuation

$$A_{ij}(f) = c_1(f)c_2C_M(f)\exp\left[\pi f t_j^* - \pi f t_i^*\right]. \tag{C.5}$$

The phase term C_M extracts the path dependence

$$C_M = \exp\left\{\mathrm{i}2\pi f[\tau_i(p_i) - \tau_j(p_j)] - \mathrm{i}[\varphi_i(p_i) + \varphi_j(p_j)]\right\}. \tag{C.6}$$

The remaining frequency dependent terms are included in

$$c_1(f) = \frac{A_\phi^i(f)A_{INS}^i(f)A_{CR}^i(f)}{A_\phi^j(f)A_{INS}^j(f)A_{CR}^j(f)}. \tag{C.7}$$

Whereas c_2 represents the ratio of those terms on frequency

$$c_2 = \frac{A_{GS}^i(p_i,\xi_i)A_R^i(p_i,\xi_i)}{A_{GS}^j(p_j,\xi_j)A_R^j(p_j,\xi_j)} \tag{C.8}$$

In my applications I will work with the P and S arrivals and assume a common source time function and instrument response. The receiver response is expected to be very similar for the two phases so that c_1 will be close to unity and a very weak function of frequency.

When I take the logarithm of the spectral ratio (C.5) I obtain

$$\ln A_{ij}(f) = \ln c_1(f) + \ln c_2 + \ln C_M(f) + \left[\pi f t_j^* - \pi f t_i^*\right], \tag{C.9}$$

and the mantle phase term $\ln c_M(f)$ will be purely imaginary. Thus if I consider the real part of the log spectral ratio A_{ij} as a function of frequency I have

$$A_{ij}(f) \approx \ln c_2 + \left[\pi f(t_j^* - t_i^*)\right]. \tag{C.10}$$

Hence I are able to extract the differential attenuation δt_{SP}^* from the slope of the dependence of the logarithmic spectral ratio on frequency. This is the basis of the analysis made by Gudmundsson et al (1994) using broad-band records from the Warramunga array in northern Australia.

The situation becomes more complicated when I allow for frequency dependence of attenuation. Consider the case of a power law relationship between Q and frequency f,

$$Q(f,\mathbf{r}) = Q_0(\mathbf{r})f^{\alpha(\mathbf{r})}, \tag{C.11}$$

I can now define a frequency dependent $t^*(f)$ representing the integrated effect of attenuation along the path:

$$t^*(f) = \int_{ray} \frac{\mathrm{d}s}{Q(f,\mathbf{r})V(f,\mathbf{r})}. \tag{C.12}$$

The presence of intrinsic attenuation induces weak velocity dispersion, but unless Q is very low for an extended depth interval, the influence of this effect is not sufficient to induce significant change in ray path and so I will neglect this effect.

I introduce the term

$$t_0^*(f) = \int_{ray} \frac{\mathrm{d}s}{Q_0(\mathbf{r})V(\mathbf{r})}. \tag{C.13}$$

and can then isolate the frequency dependence of $t^*(f)$ in the form

$$t^*(f) = t_0^* \frac{\int_{ray} \mathrm{d}s f^{-\alpha(\mathbf{r})}[Q_0(\mathbf{r})V(\mathbf{r})]^{-1}}{\int_{ray} \mathrm{d}s[Q_0(\mathbf{r})V(\mathbf{r})]^{-1}} = t_0^* Y(f), \tag{C.14}$$

where $Y(f)$ depends on the ray path. If there is no dependence of the frequency exponent with depth, then $Y(f)$ has a simple power law dependence on frequency.

The analogue of the relation (C.9) is now

$$\ln B_{ij}(f) = \ln c_1(f) + \ln c_2 + \ln c_M(f) + \left[\pi f t_{0j}^* Y_i(f) - \pi f t_{0i}^* Y_j(f)\right], \tag{C.15}$$

and the real part of the logarithmic spectral ratio R_{ij} satisfies

$$R_{ij}(f) \approx \ln c_2 + \left[\pi f (t_{0j}^* Y_j(f) - t_{0i}^* Y_i(f))\right]. \tag{C.16}$$

For P and S waves I anticipate that the majority of attenuation will occur in shear, so that the frequency exponent $\alpha(\mathbf{r})$ will arise from the frequency imaginary part of the shear modulus and be the same for both phases. However, the ratio between the P and S wavespeeds is not constant and so the ray paths taken by the two phases will differ. As a result the frequency dependence of $Y_P(f)$ and $Y_S(f)$ for the same source-station pair can differ.

With the simplifying assumption that the frequency dependence is independent of depth $Y_i(f) = f^{-\alpha}$ and then

$$A_{ij}(f) \approx \ln c_2 + \left[\pi (t_{0j}^* - t_{0i}^*) f^{1-\alpha}\right]. \tag{C.17}$$

If I were able to neglect $\ln c_2$ I would have a simple power law dependence on frequency which could be extracted from the slope of $\ln R_{ij}$ with respect to frequency.

I have found that, to a good approximation, the double logarithm of the spectral ratio between P and S phase at the same station, $\ln A_{SP}$, is close to linear in frequency. The resulting slope provides an estimate of the average frequency exponent γ of Q along the path from source to receiver. I use the notation γ for this empirically determined quantity, because of the various approximations I have employed.

When the frequency dependence of Q does not vary strongly with depth I would expect the quantity γ to be close to the true exponent α.

C.2 The instrumental response and crustal transfer functions

The calculation of the crustal transfer function, the ratio of surface motion and wave motion at the base of crust, $A_{CR}(\omega)$, and the instrumental response, $A_{INS}(\omega)$, are discussed by Teng & Ben-Menahem (1965). These are known factors, when the crustal structure at the recording site, the phase velocity of the concerned signal, and the instrumental characters are given.

Furthermore, the crustal transfer function, has been calculated for many crustal structure and angles of incidence i by various authors. Kanamori (1967) has shown that, e.g. for a 4-layer crust and steep incidence ($i = 10° - 20°$), the ratio of vertical surface motion and P wave amplitude in the frequency range 0-1 Hz assumes an roughly constant average level 2.5 with variations of ±20%, and similar for the ratio of the horizontal ground motion and SV amplitude. Leblanc (1967) has shown that the average of 20 transfer functions of different crustal models varies in the range $0.4 < f < 1.6$ Hz by less than $\pm 1 dB$ about a frequency independent mean value. This is considered a sufficient justification to approximate $A^{\beta}_{CR}(\omega)$ and $A^{\alpha}_{CR}(\omega)$ by frequency independent mean values. It is therefore a reasonable assumption that the crustal transfer function $A^{\alpha}_{CR}(\omega)$ $A^{\beta}_{CR}(\omega)$ take a constant value and are frequency independent in the frequency range 0.01 - 2.0 Hz, and $A^{\alpha}_{CR}(\omega)/A^{\beta}_{CR}(\omega) = n(\approx 1)$.

C.3 Presenting 3-D Q structure and adequate data coverage

The reliability of the 3-D Q and α model is represented by the density of tone in the ray path density diagrams fig 7.8 as a function of depth. From fig 7.8, it is found that the densest raypath distribution is focused in the area around northern Australia, particularly northwestern Australia. The Q and α structure in the areas which correspond to the lightest tone are less reliable because of poor data coverage. An alternative presentation was considered using the Hue, Saturation, Brightness model of color representation in which the colour saturation would be used to indicate the reliability of the results. It proves to be rather difficult to find a satisfactory presentation and so the use of the separate ray density diagram was employed. The results at the largest depths have rather limited constraints but are presented to provide an indication of the likely behaviour.

For the inversion for the frequency exponent α there is no simple relation between the frequency dependence as seen along a path and the frequency dependence as seen in the suite of 1-D models. The assumption has been made that the same style of inversion can be carried out as for Q itself but the results must be regarded as representative of the 3-D variations of α rather than a full model for the frequency exponent.

C.4 Comparisons of the laboratory and observed values of y

A detailed review and summary of laboratory measurement of attenuation and dispersion is given in section 2.2.2 (pp 21-24). In section 2.3.3 (pp 24-25), I have also discussed the application of laboratory results to the seismological models for the Earth's interior. The typical value of y measured from laboratory are 0.15-0.25 in the frequency range 0.01-1 Hz [Jackson, 1993, 2000]. The seismological observed values of y was reviewed and summarised in section 2.1.4 (pp 17-19). The frequency bands and values of y vary from author to author, in the mantle the common values of y lie the range from 0.2-1.0 for the frequency band from 0.01 - 2 Hz. The estimated values of the frequency exponent, which are typically 0.1-0.3 for the cratons fit quite well with the low temperature results of Jackson. At higher temperatures the frequency dependence becomes more pronounced in the laboratory work (see Jackson, 2000) and it is likely that the values of y from 0.5-0.9 for the more attenuative paths reflect the influence of enhanced temperature.